

**Relationship Between Microstructure, Texture and Ridging in Ferritic
Stainless Steels**

by

Guillaume Lefebvre

M.Sc Materials Engineering, ENSIACET Toulouse, France, 2008

A THESIS SUBMITTED IN PARTIAL FULFILLMENT OF
THE REQUIREMENTS FOR THE DEGREE OF

DOCTOR OF PHILOSOPHY

in

The Faculty of Graduate and Postdoctoral Studies

(Materials Engineering)

THE UNIVERSITY OF BRITISH COLUMBIA

(Vancouver)

March 2014

© Guillaume Lefebvre, 2014

Abstract

The influence of cold rolling and final annealing on the development of ridging during tensile deformation of an industrial AISI 445 ferritic stainless steel has been investigated. The relationship between microstructure, (micro)-texture and ridging was evaluated by comparing full-field crystal plasticity calculations (VPFFT) to experimental measurements of surface roughness and microstructure. Results showed that the major parameter responsible for ridging is the through-thickness fraction of orientations with high out-of-plane shear strain rate. This was found to dictate the amplitude of the surface displacement and the spacing between corrugations observed on the sheet surface. To examine the origins of these regions, the process of annealing from the cold rolled state to the final product was next characterized by means of electron back-scattered diffraction (EBSD), with a focus on the formation of regions with similar shearing behaviour as defined by the crystal plasticity calculations. The combined effect of preferential nucleation and growth advantage of $\{111\}\langle 112\rangle$ orientations from deformed $\{111\}\langle 112\rangle$ grains is able to explain the bulk texture change from the deformed to the recrystallized state. On a microscopic scale, these orientations (within $\pm 15^\circ$ of the ideal orientation) have low out-of-plane shearing intensity of both negative and positive sign. Their nucleation and growth during annealing leads to the replacement of large grains with high out-of-plane shearing intensity with finer grains having lower out-of-plane shearing tendency. As a consequence, both the intensity and the spatial distribution of orientations with various out-of-plane shearing tendency are modified, leading to a reduction of ridging. As the final processing stage of the steel sheet (cold rolling and final annealing) reduces the non-random distribution of grains having a particular out-of-plane shearing tendency (“clustering”) and because ridging is still present in the final product, it was concluded that ridging originates in the upstream process. A generalized description of the origins of ridging and the heredity of microstructure and texture from the slab to the final product is proposed based on simplified crystal plasticity calculations and microstructure observations of the casting and the transfer bar.

Preface

The majority of the experimental work presented in this thesis has been carried out in the Department of Materials Engineering at the University of British Columbia Vancouver between January 2009 and May 2013. This included all the experimental design, material heat treatment, sample preparation and most of the microstructural characterization. Part of this microstructural characterization, however, has also been performed by the author at the University of British Columbia (Okanagan) and at the Aperam Research Centre in Isbergues (France). In all of these experiments (described below) the author planned the experiments, prepared the samples at UBC Vancouver for measurements and carried out the analysis and interpretation on the raw datasets.

X-ray diffraction measurements were performed at the Aperam Research Centre (Isbergues, France) in collaboration with Mr. S. Tachel. Half of the experiments were made during a visit of the author in January 2010 when the author worked directly with Mr. Tachel to perform the measurements. The second half of the measurements was made by Mr. Tachel alone.

Electron Backscatter diffraction characterization of one sample (AISI 409) was performed by Dr. D. Barbier at Arcelor Mittal Research Centre (Maizieres-les-Metz, France) in July 2010. While Dr. Barbier made the measurement himself and provided the raw experimental data, all analysis was performed by the author. Part of the experimental surface roughness characterization for this material (effect of tensile direction on surface roughness, presented in this work in section 5.3.1), was performed by C. W. Sinclair. These data, combined with the crystal plasticity calculations performed by the author and presented in section 5.4.2, have been published (Lefebvre, G., C. W. Sinclair, R. A. Lebensohn, and J.-D. Mithieux. (2012) “Accounting for Local Interactions in the Prediction of Roping of Ferritic Stainless Steel Sheets.” *Modelling and Simulation in Materials Science and Engineering* 20, no. 2. The organization of the manuscript was initially planned with Sinclair and all of the co-authors (Sinclair, Lebensohn and Mithieux) contributed to editing the draft of the manuscript (e.g. the section on “Full-field simulations using the VPFFT code” was co-developed by the author with R.A. Lebensohn).

Table of Contents

Abstract	ii
Preface	iii
Table of Contents.....	iv
List of Tables.....	vi
List of Figures	vii
Acknowledgments.....	xviii
Chapter 1: Introduction.....	1
Chapter 2: Literature Review	3
2.1. Characteristics of Ferritic Stainless Steels.....	3
2.2. Crystallographic Texture of Ferritic Stainless Steels	4
2.3. Ridging: Its Characteristics and Relation to Microstructure	6
2.4. Microstructural Features Associated with Ridging.....	12
2.5. Effect of Thermo-Mechanical Processing on Microstructure Development	24
2.5.1. Introduction.....	24
2.5.2. Cold Rolling.....	28
2.5.3. Final Annealing of Cold Rolled Sheet	32
2.5.4. Practical Routes for Reducing Ridging via Process Control During Cold Rolling and Annealing.....	37
2.5.5. Casting	39
2.5.6. Hot Rolling	41
2.5.7. Practical Routes for Reducing Ridging via Process Control During Casting and Hot Rolling	43
2.6. Effect of Chemical Composition on Microstructure, Texture and Ridging	46
2.6.1. Introduction.....	46
2.6.2. Effect of Carbon.....	47
2.6.3. Effect of Chromium.....	48
2.6.4. Effect of Titanium and Niobium.....	49
2.7. Summary of the Literature Review	50
Chapter 3: Scope and Objectives	51
Chapter 4: Experimental Procedure and As-Received Materials.....	52
4.1. Methodology for Materials Characterization.....	52
4.1.1. Optical Microscopy and Measurement of Recrystallized Fraction.....	52
4.1.2. Scanning Electron Microscopy and EBSD (Electron Backscattered Diffraction)	52
4.1.3. Bulk Texture Measurements.....	53
4.1.4. Surface Roughness Measurements.....	54
4.2. Thermo-Mechanical Processing	57
4.2.1. Cold Rolling.....	57
4.2.2. Annealing.....	57
4.3. Materials.....	59

Chapter 5: Characterization of the Spatial Heterogeneity of Microstructure and its Link to Ridging.....	63
5.1. Introduction.....	63
5.2. VPFFT Model.....	64
5.3. Characterization of Microstructure and Ridging Behaviour: Experiments	69
5.3.1. Microstructure of the AISI 409 Steel	69
5.3.2. Presentation of the UA-445-R Material	72
5.3.3. Presentation of the A-445-R Material	74
5.4. Numerical Prediction of Ridging from Experimental Microstructures.....	76
5.4.1. Introduction.....	76
5.4.2. Predicted Ridging Behaviour of AISI 409	78
5.4.3. Predicted Ridging Behaviour of AISI 445	80
5.4.4. Effect of Neighbourhood: Mean-field Simulations Applied to the AISI 409 material.....	84
5.5. Correlating Microstructure to the Spatial Heterogeneities Responsible for Ridging.....	91
5.6. Conclusion	103
Chapter 6: Microstructure and Texture Evolution During the Final Annealing	105
6.1. Introduction.....	105
6.2. Effect of Cold Rolling Reduction and Annealing Conditions on Texture and Recrystallization Kinetics	106
6.3. Annealing of the Annealed Hot Band AISI 445 after Cold Rolling.....	111
6.3.1. Methodology	111
6.3.2. Early Stages of Recrystallization (<30% Recrystallized).....	115
6.3.3. Intermediate Stages of Recrystallization	123
6.3.4. End of Recrystallization (>75% Recrystallized)	129
6.4. Influence of Annealing on the Spatially Heterogeneous Distribution of Texture.....	139
6.5. Conclusion	146
Chapter 7: On the Origin of Ridging and the Heredity of Texture and Microstructure.....	147
7.1. Introduction.....	147
7.2. Texture and Microstructure Evolution on Roughing	148
7.2.1. Characterization of the Slab	148
7.2.2. Roughing.....	148
7.2.3. Comparison with the Experimental Transfer Bar	151
7.3. Relation to Ridging	154
7.4. Conclusion	160
Chapter 8: Conclusions and Future Work.....	161
8.1. Conclusions.....	161
8.2. Future Work.....	162
Bibliography.....	165
Appendix A: Experimental surface roughness measurements.....	179
Appendix B: Input for VPFFT simulations	182

List of Tables

Table 2.1: Principal characteristics of the common surface roughness profiles: ridging in ferritic stainless steels, roping in aluminum alloys and orange peel effect.....	11
Table 2.2: Typical composition range and effect of alloying elements in Ferritic Stainless Steels. From [4] and [6].	47
Table 4.1: Nominal composition (in wt.%) for the ferritic stainless steel grades studied in this work.	60
Table 5.1: Summary of the characteristic dimensions of ridging for the three materials as experimentally measured and predicted using the VPFFT model. The repeating patterns are obtained from the auto-correlation functions.	84
Table 5.2: Arithmetical mean deviation values between the binomial distribution and the experimental distribution of shearing behaviour for the three cases presented in Figure 5.24.	101
Table 6.1: Annealing conditions tested for the study of recrystallization at 800°C after 80% cold rolling reduction. The number of measured EBSD maps for each condition and their recrystallized fraction are also indicated. The advancement of recrystallization is also presented (early stage <25%, intermediate stage between 25% and 75%, end stage >75%).	115
Table A.1: Characterization of the repeatability of surface roughness measurement on R_a , R_q and R_{max}	181

List of Figures

Figure 2.1: Fe-Cr phase diagram showing the presence of a γ -austenite loop for lower chromium content, (b) Influence of carbon addition and (c) influence of nickel addition to the Fe-Cr system on the stabilization of the γ -loop (γ -stabilizer) [6].....4

Figure 2.2: Classical crystallographic orientations observed during the processing of ferritic steel sheets represented in the $\phi_2=45^\circ$ section of the Euler space. The corresponding unit cell (cube) geometry is also shown for these orientations as though being viewed along ND (except for the high index orientation $\{223\}\langle 582\rangle$).....6

Figure 2.3: The appearance of ridging in ferritic stainless steel sheet following (a) tensile deformation parallel to the rolling direction and (b) deep drawing.7

Figure 2.4: Two-dimensional profilometry measurements from surface samples tested in tension to 15% elongation. The direction of tension was varied from 0° (tension parallel to RD) to 90° (tension parallel to TD). Adapted from [24].8

Figure 2.5: Example of (a) a tensile sample and (b) the corresponding 3-D surface roughness map measured after 15% elongation in tension by contact profilometry, obtained by multiple linear surface roughness measurements along the TD which are re-combined and properly aligned to obtain the three dimension profile [23].....9

Figure 2.6: (a) Profilometric surface roughness measurement showing the correlation between the top and the bottom surfaces following tensile testing parallel to RD, adapted from [24]. The spacing between the traces is not indicative of the actual thickness of the sheet. (b) Similar observation but showing two-dimensional surface roughness measurements on the top and bottom surfaces of the same sheet illustrating the exact correlation of the surface roughness [23].10

Figure 2.7: Schematic representation of the surface roughening (roping) observed in Aluminum alloys after tensile testing parallel to the transverse direction [26].11

Figure 2.8: Optical microscopy of etched surfaces revealing clustering of grains having similar orientations aligned with the rolling direction based on the density of etch pits as a function of the orientation. (a)-(c) sample exhibiting intermediate level of ridging (rolling direction is vertical), (d)-(f) sample exhibiting strong ridging (rolling direction is horizontal) [23]. (g) The 2 variants of $\{hkl\}\langle 110\rangle$ (α -fibres proposed to be at the origins of ridging in the model proposed by Takechi et al.) are distinguished by the shape of their etching patterns [21]. (a)-(f) are hot rolled, cold rolled and annealed 430 grades Ferritic Stainless. (g) is from a cold rolled 17%-Cr Stainless Steel.13

Figure 2.9: Correlation between the etch pits patterns revealed after etching of the undeformed grip and ridged surface on the gauge length of the 430 Ferritic Stainless Steel sample [23]. Arrows point to features that appear to have similar patterns in the etched and ridged regions.....14

Figure 2.10: Schematic of the basic features of ridging according to Chao (a) and (b), based on the differences of through thickness compression of the two texture components, and according to Wright (c) and (d), based on compressive forces resulting in buckling of the $\{001\}\langle 110\rangle$ bands. The tensile axis (TA) is parallel to the rolling direction (RD).	16
Figure 2.11: Takechi model for origin of ridging where (a) alternating clusters along the transverse direction (TD) of grains of the different $\{111\}\langle 110\rangle$ variants are aligned along the rolling direction (RD). When the tension axis (TA) is aligned with RD, the two variants undergo opposite out-of-plane shear resulting in (b) the overall corrugations of the sheet. The out-of plane shear is caused by the activation of a specific and non compensated slip system (represented by the blue arrows) [42]......	17
Figure 2.12: Correspondence between surface of etched sample (underlain) and EBSD maps (colour) where the EBSD maps show only grains having $\langle 111\rangle//ND$ as blue [23]......	18
Figure 2.13: EBSD maps showing apparent banding of specific orientations given by their Euler angles and volume fraction ($V\%$) [44].	19
Figure 2.14: (a) Absolute intensity of out-of-plane shear strain rate calculated by VPSC as a function of orientations represented in the $\varphi_2=45^\circ$ section of the Euler space. The behaviour of each grains was estimated by assuming them to be embedded in a very compliant matrix (Sachs-like behaviour) [37]. (b) Intensity of the “in-plane shear ratio” defined by $s=\gamma_{23}/d\varepsilon_{11}$, (where 1 is RD, 2 is TD and 3 is ND) using simple relaxed Taylor conditions [23]. The color code for shear intensity is superimposed on the experimental ODF from a sample exhibiting high ridging, represented by iso-intensity diagrams in φ_2 sections (plotted every 5°).	21
Figure 2.15: Out-of-plane shearing map created from an EBSD data set taken at mid-thickness on the sheet plane. This map represents the spatial distribution of out-of-plane shear intensity calculated with VPSC. Bands of similar shearing behaviour aligned with the RD are visible [37].	23
Figure 2.16: Simplified schematic of the industrial process for stainless steel production, from casting to final annealing. The characteristic dimensions and temperatures along the different steps are highlighted as well [5].	25
Figure 2.17: Inverse Pole Figure (IPF) EBSD maps made on the transverse plane of the hot band of a 17%Cr ferritic stainless steel showing the inhomogeneous recrystallization behaviour. (a) ND IPF and (b) RD IPF (crystal axis represented by the stereographic triangle are parallel to the normal direction of the sheet and to the rolling direction of the sheet respectively) [49].	27
Figure 2.18: Example of texture evolution close to the surface ($s=0.8$) (a)-(c) and at the centre ($s=0$) (d)-(f) of a 17%Cr ferritic stainless steel sheet during cold rolling (80% reduction) and annealing (1h at 700°C), from [17].	28

Figure 2.19: (a) EBSD ND Inverse Pole Figure map made on the transverse plane of a cold rolled (50% reduction) and partially annealed (10s at 750°C) 409 grade ferritic stainless steel sheet, and (b) {200} pole Figures corresponding to the selected deformed grains in (a). Results show that deformed γ -fibre grains (blue grains 1={111}<110> and grain 5=close to {111}<110>) are alternating with deformed α -fibre grains (pink-red grains 2={001}<110>, grain 3 and 4=close to {112}<110>) [63].	30
Figure 2.20: Effect of crystallographic orientation along the α -fibre on the stored energy available for recrystallization, measured by different methods: Taylor factor TEM [73]), and X-ray [75]). From [87]. Refer to text for details about the different methods.	32
Figure 2.21: Transmission Electron Microscope bright field images from the transverse plane of the sub-structure developed by cold rolling (50% reduction) and recovery (10 seconds at 750°C) of a 409 grade ferritic stainless steel sheet. (a) Homogeneous sub-structure composed of elongated, well aligned cells developed within α -fibre grains (indicated by arrows), and (b) heterogeneous sub-structure showing a nuclei (at the centre) arising from abnormal sub-grain growth and surrounded by equiaxed cells with various sizes inside a deformed γ -fibre grain [63].	33
Figure 2.22: (a) Band contrast EBSD map of a partially recrystallized Ti-stabilized 409 ferritic stainless steel after cold rolling to 50% reduction and annealed at 700°C for 200s. Unrecrystallized grains 1, 2 and 3 belongs to the α -fibre (close to {001}<110> as shown on (b) the {100} pole Figure from unrecrystallized regions. (c) is the {100} pole Figure of the recrystallized grains exhibiting γ -fibre orientations [93].	35
Figure 2.23: Structure of a continuously cast slab (445 grade Ferritic Stainless Steel) showing the presence of large columnar grains near the surface, growing along the normal directions to the surfaces and equiaxed and smaller grains in the centre region. Secondary columnar grains within the equiaxed region are also visible. Picture courtesy of Aperam.	41
Figure 2.24: (a) Effect of stirring intensity on ratio of the size of the equiaxed grains zone, and (b) corresponding effect on ridging amplitude [114].	44
Figure 2.25: Effect of carbon in solid solution on ridging height, as a function of the processing route defined in [107]. The severity of ridging decreases for every route when the carbon content is increased.	48
Figure 4.1: Ideal sine wave with a period of 5mm (left), the same curve shifted by different amount along the horizontal axis (centre) and the corresponding auto-correlation function (right) showing correlated patterns every 5 mm.	56
Figure 4.2: Temperature measured from a thermocouple attached to the surface of a sample annealed under argon for the 3mm hot band cold rolled between 40% and 80%. Samples were annealed in a furnace at 1010°C during one minute per mm thickness.	58

- Figure 4.3: Example of isothermal treatment performed in the Gleeble 3500 on a sample cold rolled to 80% reduction. The initial heating rate was 100°C/s, followed by a slower heating rate of 10°C/s during the last 20°C (2s) before the isothermal plateau at 800°C for 30s. In the insert, detail of the two-step heating rate is shown.59
- Figure 4.4: EBSD characterization of the un-annealed hot band for the AISI 445 grade. (a) ND inverse pole figure map on the ND plane at mid thickness showing large elongated grains along RD. In this case, the color code (represented by the stereographic triangle) corresponds to crystallographic directions being parallel to the ND of the sheet. (b) ND inverse pole figure on the RD plane covering the full thickness of the hot band and showing microstructure and texture gradients through thickness, as represented by the $\varphi_2=45^\circ$ section of the Euler space for (c) the top surface (25% of the thickness), (d) the central layers (50% of the thickness) and (e) the bottom surface (25% of the thickness).61
- Figure 4.5: EBSD characterization of the annealed hot band for the AISI 445 grade. (a) ND inverse pole figure map on the ND plane at mid thickness showing a well recrystallized microstructure. (b) ND inverse pole figure on the RD plane covering the full thickness of the hot band and showing microstructure and texture gradients through thickness, as represented by the $\varphi_2=45^\circ$ section of the Euler space for (c) the top surface (25% of the thickness), (d) the central layers (50% of the thickness) and (e) the bottom surface (25% of the thickness).62
- Figure 5.1: Schematic of a microstructure superimposed to a regular grid of Fourier points. Each point belonging to a grain is assigned an orientation. The grain boundaries have been reconstructed based on the difference of orientations between neighbouring points. The horizontal direction correspond to the transverse direction of the sheet, the vertical direction corresponds to the normal direction of the sheet, and the microstructure is assumed to be extruded along the third dimension (the rolling direction).67
- Figure 5.2: EBSD ND inverse pole figures maps for the AISI 409 ferritic stainless steel taken from (a) the ND plane at mid-thickness, and (b) the RD plane, covering approximately 75% of the sheet thickness. (c) texture corresponding to (b) after calculation of the ODF and represented in the $\varphi_2=45^\circ$ section of the Euler space. ...70
- Figure 5.3: Two-dimensional profilometry measurements from the surface sample of the AISI 409 after tension to 15% where the tensile axis was parallel to the (a) prior RD, (b) 45° to RD and (c) prior TD. For these three cases the tensile direction is vertical, and the scale bar is in microns [23]. (d) is a one-dimensional surface obtained following the procedure described in section 4.1.4 and it's corresponding auto-correlation function.71
- Figure 5.4: EBSD ND inverse pole figures maps for the un-annealed AISI 445 hot band after 80% reduction and annealing (1010°C for 45s) taken from (a) the ND plane at mid-thickness, and (b) the RD plane, covering the entire thickness. (c) texture corresponding to (b) after calculation of the ODF and represented in the $\varphi_2=45^\circ$ section of the Euler space.73

Figure 5.5: (a) Line scan surface roughness measured on the surface of the un-annealed AISI 445 hot band after 80% cold rolling, annealing at 1010°C for 45s and deformation by 15% elongation along the previous RD (b) Auto-correlation function revealing the major wavelength characteristic of ridging.....	74
Figure 5.6: EBSD ND inverse pole figures maps for the annealed hot band AISI 445 ferritic stainless steel after 80% cold rolling reduction and annealing (1010°C for 45s) taken from (a) the ND plane at mid-thickness, and (b) the RD plane, covering the entire thickness. (c) is the texture corresponding to (b) after calculation of the ODF and represented in the $\phi_2=45^\circ$ section of the Euler space.....	75
Figure 5.7: (a) Line scan surface roughness measured on the surface of the annealed AISI 445 hot band after 80% cold rolling, annealing at 1010°C for 45s and deformation by 15% elongation along the previous RD. (b) Auto-correlation function revealing the major wavelength characteristic of ridging.....	76
Figure 5.8: Simulated effect of tensile testing direction on surface roughness after 15% elongation (extrapolated from a single step of 1%) along RD (blue curve) and along TD (grey curve) on the AISI 409 ferritic stainless steel. Right is the auto-correlation function corresponding to the tension along RD.	79
Figure 5.9: Comparison of surface roughness as measured experimentally (top) and calculated (bottom) for the AISI 409 deformed in tension to 15% along RD. Both amplitude and wavelength are in excellent agreement [93]......	79
Figure 5.10: Map of the spatial distribution of out-of-plane shear strain components ϵ_{12} after 1% elongation parallel to RD (top). The intensity of this component is represented by the grey scale above the map.	80
Figure 5.11: Surface roughness for the UA-445-R material (un-annealed hot band AISI 445 grade cold rolled 80% and annealed at 1010°C for 45s), calculated after 1% elongation parallel to RD and extrapolated to 15% (top), the corresponding map of spatial distribution of out-of-plane shear strain rate in s^{-1} (centre) and the auto-correlation function corresponding to the surface roughness profile (bottom).	82
Figure 5.12: Surface roughness for the A-445-R material (annealed hot band AISI 445 grade cold rolled 80% and annealed at 1010°C for 45s), calculated after 1% elongation parallel to RD and extrapolated to 15% (top), the corresponding map of spatial distribution of out-of-plane shear strain rate in s^{-1} (centre) and the auto-correlation function corresponding to the surface roughness profile (bottom).	83
Figure 5.13: Out-of-plane shear strain distribution predicted by (a) VPSC (mean-field) and (b) VPFFT (full-field) after 1% tensile deformation along RD.	85
Figure 5.14: Spatial distribution of out-of-plane shear strain intensity calculated with VPFFT (a) and VPSC (b). The color black represents regions with large negative shear strain intensity ($-0.006 < \epsilon_{12} < -0.002$), the color grey represents regions with low shear strain intensity ($-0.002 < \epsilon_{12} < 0.002$) and the color white represents regions with large positive shear strain intensity ($0.007 > \epsilon_{12} > 0.002$).	86

- Figure 5.15: Histogram of the nature of the interfaces between regions of different shearing behaviour (black=high negative shear strains, grey=low shear strains, white=high positive shear strains). Differentiation has been made depending on the directionality of the neighbours (TD vs. ND).87
- Figure 5.16: Section $\varphi_2=45^\circ$ of the Euler space representing the ODF calculated from (a) the regions having positive shear strain rate, and (b) the regions having negative shear strain rate, assuming orthotropic symmetry. The color scaling corresponds to shear strain rates.....89
- Figure 5.17: Section $\varphi_2=45^\circ$ of the extended Euler space representing the ODF calculated from the regions having positive shear strain rate (top) and the regions having negative shear strain rate (centre), assuming the sample symmetry to be triclinic. At the bottom is the combined ODF from the two previous subsets, also assuming triclinic sample symmetry.....90
- Figure 5.18: Intensity of the out-of-plane shear strain rate calculated for each orientation of the $\varphi_2=45^\circ$ section of the Euler space on a regular grid (5° along φ_1 and Φ). The calculations were performed with the VPSC model assuming that each orientation was a single crystal deformed under relaxed Taylor conditions.....90
- Figure 5.19: Effect of through thickness distribution of shearing orientations in clusters on surface roughness developed during tensile deformation. Each region defining a ‘cluster’ is composed of 33% of shearing orientations surrounded by a matrix representative of the recrystallized bulk texture. Shearing orientations are distributed within (a) the central 33% of the thickness and (b) the full thickness. (c) Surface roughness profiles for different through thickness spatial distribution showing an identical behaviour for the conditions tested.92
- Figure 5.20: Effect of grain size on surface roughness developed during tensile deformation. The RVE is populated with (a) 1000 seeds (10 grains through the thickness) and (b) 25000 seeds (55 grains through the thickness). Clusters are composed of shearing orientations and are surrounded by a matrix representative of the recrystallization bulk texture. (c) Surface roughness profiles for different grain sizes showing an identical behaviour for the conditions tested.93
- Figure 5.21: Effect of dilution of clusters by introduction of different orientations. a) Initial Takechi model [21] composed of blocks of each of the two $\{111\}\langle 110\rangle$ orientations, b) introduction of anti-shearing orientations in each block (orientations with same intensity of shearing but opposite sign), and c) effect of introduction of different orientations on the amplitude of ridging, calculated as the R_a value. The colors in (a) and (b) are randomly chosen for the two $\{111\}\langle 110\rangle$ variants.....95
- Figure 5.22: Distribution of the out-of-plane shear strain rate intensity (a) for the ideal Takechi model (each cluster is composed of a unique variant of $\{111\}\langle 110\rangle$), (b) when 10% of “anti-shearing” orientation are randomly introduced in clusters, (c) when 30% of “anti-shearing” orientation are randomly introduced in clusters and (d) when 50% of “anti-shearing” orientation are randomly introduced.96

Figure 5.23: Schematic of the effect of the out-of-plane shear strain rate on the RD plane. In vertical section through the thickness, the shear components are summed up, leading to a local vertical displacement. Adjacent sections along TD provide a cumulative effect leading to the overall undulations. Adapted from [30].98

Figure 5.24: Illustration of how the simulated surface roughness (bottom) was used to calculate the incremental displacement (Δ) associated with each surface nodal point (top).99

Figure 5.25: Histograms of the frequency of having k ($k=[0,\dots,20]$) positive vertical displacement in a bin containing 20 adjacent vertical sections along TD for (a) the AISI 409 grade, (b) the UA-445-R, (c) the A-445-R. The red dots represent the theoretical probability given by a binomial distribution for a random distribution.100

Figure 5.26: Histograms of the frequency of shear strain rate for (a) the UA-445-R materials and (b) the A-445-R, from Figures 5.11 and 5.12 respectively. (c) is the difference between (b) and (a), showing that the data in (a) contains a higher fraction of points with high shear strains and (b) has a higher fraction of points with low shear strains.....102

Figure 6.1: Evolution of bulk texture as a function of cold rolling reduction for the AISI 445 annealed hot band. The $\varphi_2=45^\circ$ section of the Euler space with the triclinic symmetry is represented here. The texture measurements were made at the mid-thickness on the ND plane after (a) 40% cold rolling reduction, (b) 60% cold rolling reduction and (c) 80% cold rolling reduction.....107

Figure 6.2: Evolution of bulk texture of the fully recrystallized sheet of AISI 445 annealed hot-band following cold rolling and annealing to full recrystallization. The $\varphi_2=45^\circ$ section of the Euler space (triclinic symmetry) is represented. XRD measurements were made at mid-thickness on the ND plane. (a) 40% cold rolling reduction, annealed at 1010°C during 110s, (b) 60% cold rolling reduction, annealed at 1010°C during 75s and (c) 80% cold rolling reduction, annealed at 1010°C during 40s. Annealings were performed in the tube furnace...108

Figure 6.3: Evolution of the intensity along the two common fibre texture in ferritic stainless steels: (a) α -fibre after deformation, (b) γ -fibre after deformation, (c) α -fibre after annealing, and (d) γ -fibre after annealing. The intensity is in multiple of random.109

Figure 6.4: Recrystallization kinetics following 40%, 60% and 80% cold rolling and (a,b) annealed at 850°C and (c,d) 800°C. The solid lines in (a) and (c) show JMAK fits for the data. These fits were obtained using the double log graphs in (b) and (d) [93]. In (b) and (c), X represents the overall fraction recrystallized.110

Figure 6.5: Detail of a partially recrystallized microstructure showing a recrystallized grain with high aspect ratio (grain A). Grain B also exhibits low internal misorientation ($<3.5^\circ$) but because of its large aspect ratio, the grain is considered as restored and non recrystallized. The white areas correspond to mis-indexed pixels.112

Figure 6.6: Rodrigues space for representation of misorientations. (a) Fundamental zone for cubic symmetry (left), showing also the decomposition of the space into sub-volumes corresponding to the cubic-cubic system (right, in red), from [37]. (b) Example of one of the section of the sub-volume corresponding to the cubic-cubic system showing the characteristic features used in the following sections for the analysis of misorientations ($r_3=0.25$).....	114
Figure 6.7: Selection of EBSD maps (ND inverse pole figure maps) for the early stages of recrystallization, taken on the TD plane after 80% cold rolling of the annealed hot band and annealing at 800°C for 5s, corresponding to 5.6% recrystallization. (a) full map where white regions are mis-indexed points, such as precipitates, (b) recrystallized grains, (c) deformed grains. Each map is accompanied by its corresponding ODF.....	117
Figure 6.8: Selection of EBSD maps (ND inverse pole figure maps) for the early stages of recrystallization, taken on the ND plane after 80% cold rolling of the annealed hot band and annealing at 800°C for 10s, corresponding to 16.4% recrystallization. (a) full map where white regions are mis-indexed points, such as precipitates, (b) recrystallized grains, (c) deformed grains. Each map is accompanied by its corresponding ODF.....	118
Figure 6.9: (a) Detail from Figure 6.7(d) showing nucleation in bands. The red line is where (b) the misorientation profile across these bands was taken. (c) EBSD map on the TD section showing that these bands are inclined by 30-35° from the RD, in agreement with [159].	119
Figure 6.10: Misorientations between recrystallized $\{111\}\langle 112 \rangle$ grains and their deformed neighbours, represented in sections of Rodrigues space for constant r_3 values, for the microstructures presented in Figure 6.8. (a) $(111)[1-21]$ variant for the material annealed 5s (Figure 6.8(a-c)), (b) $(111)[-1-12]$ variant for the same material annealed 5s, (c) $(111)[1-21]$ variant for the material annealed 10s (Figure 6.8(d-f)), (d) $(111)[-1-12]$ variant for the same material annealed 10s.	121
Figure 6.11: (a) to (d) Histograms of the misorientation angles between recrystallized grains and their neighbouring deformed grains, obtained from the data used to calculate the MODFs presented in Figure 6.10 respectively. (a) also presents the MacKenzie plot in red dots (distribution of misorientation angles for a randomly textured polycrystal), showing that the misorientation distribution is non random.	122
Figure 6.12: Misorientation between recrystallized grains having one of the $\{111\}\langle 110 \rangle$ orientations and their neighbouring deformed grains for the material annealed for 10s (Figure 6.8(d-f)). (a) MODF and (b) histogram of misorientation angles for the $(111)[1-10]$. The results are similar to those presented for the $\{111\}\langle 112 \rangle$ orientations (Figure 6.10 and Figure 6.11).	123

- Figure 6.13: Selection of EBSD maps (ND inverse pole figure maps) for the early stages of recrystallization, taken on the ND plane after 80% cold rolling of the annealed hot band and annealing at 800°C for 30s, corresponding to 51.7% recrystallization. (a) full map where white regions are mis-indexed points, such as precipitates, (b) recrystallized grains, (c) deformed grains. Each map is accompanied by its corresponding ODF.125
- Figure 6.14: Selection of EBSD maps (ND inverse pole figure maps) for the early stages of recrystallization, taken on the TD plane after 80% cold rolling of the annealed hot band and annealing at 800°C for 70s, corresponding to 66.4% recrystallization. (a) full map where white regions are mis-indexed points, such as precipitates, (b) recrystallized grains, (c) deformed grains. Each map is accompanied by its corresponding ODF.126
- Figure 6.15: Misorientations between recrystallized $\{111\}\langle 112 \rangle$ grains and their deformed neighbours, represented in sections of Rodrigues space for constant r_3 values, for the microstructures presented in Figure 6.14. (a) $(111)[1-21]$ variant for the material annealed 30s (Figure 6.14(a-c)), (b) $(111)[-1-12]$ variant for the same material annealed 30s, (c) $(111)[1-21]$ variant for the material annealed 70s (Figure 6.14(d-f)), and (d) $(111)[-1-12]$ variant for the same material annealed 70s.127
- Figure 6.16: (a) to (d) Histograms of the misorientation angles between recrystallized grains and their neighbouring deformed grains, obtained from the data used to calculate the MODFs presented in Figure 6.15 respectively. (a) also presents the MacKenzie plot in red dots (distribution of misorientation angles for a randomly textured polycrystal), showing that the misorientation distribution is non random.128
- Figure 6.17: Detail of the origins of the 35° around $\{110\}$ misorientation. (a) Inverse pole figure map from the AISI 445 annealed hot band after 80% cold rolling reduction and annealing at 800°C for 30s (63.6% recrystallized) showing deformed grains with a $\{112\}\langle 110 \rangle$ orientation, surrounded by recrystallized grains belonging to the γ -fibre. (b) $\{200\}$ and $\{110\}$ pole figures of the deformed grains. (c) Pole Figure and Orientation Distribution Function of the recrystallized grains surrounding the deformed $\{112\}\langle 110 \rangle$ grains, showing that these grains belong to the γ -fibre.129
- Figure 6.18: Selection of EBSD maps (ND inverse pole figure maps) for the early stages of recrystallization, taken on the TD plane after 80% cold rolling of the annealed hot band and annealing at 800°C for 70s, corresponding to 79.8% recrystallization. (a) full map where white regions are mis-indexed points, such as precipitates, (b) recrystallized grains, (c) deformed grains. Each map is accompanied by its corresponding ODF.131
- Figure 6.19: Selection of EBSD maps (ND inverse pole figure maps) for the early stages of recrystallization, taken on the TD plane after 80% cold rolling of the annealed hot band and annealing at 800°C for 200s, corresponding to 91.4% recrystallization. (a) full map where white regions are mis-indexed points, such as precipitates, (b) recrystallized grains, (c) deformed grains. Each map is accompanied by its corresponding ODF.132

- Figure 6.20: Misorientations between recrystallized $\{111\}\langle 112 \rangle$ grains and their deformed neighbours, represented in sections of Rodrigues space for constant r_3 values, for the microstructures presented in Figure 6.19. (a) $(111)[1-21]$ variant for the material annealed 70s (Figure 6.19(a-c)), (b) $(111)[-1-12]$ variant for the same material annealed 70s, (c) $(111)[1-21]$ variant for the material annealed 200s (Figure 6.19(d-f)), (d) $(111)[-1-12]$ variant for the same material annealed 200s...133
- Figure 6.21: (a) to (d) Histograms of the misorientation angles between recrystallized grains and their neighbouring deformed grains, obtained from the data used to calculate the MODFs presented in Figure 6.157 respectively. (a) also presents the MacKenzie plot in red dots (distribution of misorientation angles for a randomly textured polycrystal), showing that the misorientation distribution is non random.134
- Figure 6.22: Microtexture evolution of specific crystallographic orientation during recrystallization. (a) Number fraction of recrystallized grains, (b) average grains size, (c) maximum grain size and (d) total area fraction, as a function of the overall fraction recrystallized. Solid lines are used only to illustrate trends in the data.....138
- Figure 6.23: (a) Characterization of a deformed grain belonging to the α -fibre. Such grains usually present a large gradient of orientations (b) accompanied by a misorientation profile (c) characterized by small point-to-point misorientations (average 1.1°) that can however add up and generate large misorientation gradients when compared to the point of origin (in this case 50° over $450 \mu\text{m}$).140
- Figure 6.24: (a) Characterization of a deformed grain belonging to the γ -fibre. Such grains usually present little gradient of orientations (b) accompanied by a misorientation profile (c) characterized by larger point-to-point misorientations (average 2.3°). The cumulative profile (with regards to the point of origin) is more chaotic and does not present cumulative misorientation over large distance. 141
- Figure 6.25: Schematic of recrystallization during annealing in ferritic stainless and its effect on the spatial distribution of sign of shearing tendency.....142
- Figure 6.26: Spatial distribution of shear strain rate (s^{-1}) during recrystallization, for recrystallized grains. The intensity was calculated using the method described at the end of section 5.4. The scale on each figure is in μm . (a) is obtained after 15.6% recrystallization, (b) after 49.7% recrystallization and (c) after 73.9% recrystallization. (d) is the intensity of shear strain rate for the deformed grains for the microstructure presented in (a).....143
- Figure 6.27: Rotation field of orientations during plain strain compression, using the VPSC model with $n^{\text{eff}}=10$. (a) Pancake shaped grains embedded in a deformation texture (strong α -fibre and weak γ -fibre) and (b) equiaxed grains embedded in a random texture. A deformation of 1% was simulated and a scaling factor of 15 was applied for representation. The color corresponds to the change of section for φ_2 : blue is for $\varphi_2 < 45^\circ$ and red is for $\varphi_2 > 45^\circ$ 145

Figure 7.1: Initial ODFs produced for simulating (a) the surface and (b) the centre of the slab, plotted on the $\varphi_2=45^\circ$ section of the Euler space using the software MTEX.....	150
Figure 7.2: Final textures obtained after 5 steps of 0.32 strain (80% rolling) for (a) the surface in plane strain compression, (b) the surface of the slab with introduction of shear, and (c) the centre of the slab in plain strain compression, plotted on the $\varphi_2=45^\circ$ section of the Euler space using the software MTEX.	150
Figure 7.3: EBSD characterization of the transfer bar. (a) Inverse pole figure map of the transverse section (the horizontal direction is RD, the vertical direction is ND), (b) texture of the two surfaces combined and (c) texture of the central region. The centre was considered to be the region surrounded by the red box.	152
Figure 7.4: Detail of the microstructure of the transfer bar on the sheet plane at mid-thickness, revealing a mixture of large deformed grains and smaller recrystallized grains (courtesy of Aperam, Isbergues).....	153
Figure 7.5: Detail from Figure 7.4(a) showing the bulging (circled) of an α -fibre grain close to $\{001\}\langle 110\rangle$ (as indicated by (c)) into adjacent grains whose orientation is close to $\{111\}\langle 112\rangle$ (as indicated by (b)).....	154
Figure 7.6: Detail from Figure 5.2(a) showing the alternation of bands of grains with γ -fibre orientation (surrounded in blue) and grains with non γ -fibre orientations (surrounded in red).....	155
Figure 7.7: Schematic of the microstructure (and texture) evolution during hot rolling, from the slab to the un-annealed hot band.....	156
Figure 7.8: Multi-scale schematic characterization of ridging in the final product.....	158
Figure 7.9: (a) Microstructure of the cast slab for the grade AISI 445 E2 showing no columnar grains, figure provided by Aperam, Isbergues. (b) Band contrast EBSD map on the ND plane at mid-thickness and its corresponding texture on the section $\varphi_2=45$ of the Euler space using orthotropic sample symmetry. The contours represent intensities of 2, 3 and 4, from [170].	159
Figure A.1: Schematic of the surface roughness measurements on the surface of a deformed sample.	179
Figure A.2: Raw data for a surface roughness measurement of the AISI 409 material, and polynomial fits (6 th order and 8 th order).	180
Figure A.3: Final surface roughness profiles after correction by the two polynomial fits and filtering. Also are included the amplitude parameters using the same color code as the corresponding curves.	180
Figure B1: Definition of the deformation and boundary conditions for the VPFFT simulations in the fft.in input file	183
Figure B2: Definition of the activity of slip systems and hardening law in the bcc.sx3 input file	184

Acknowledgments

I believe the success of any work is not only the fruit of one's own efforts, but also the result of the people who accompanied us during the journey. I would thus like to thank and acknowledge some of the numerous people who helped me through this Ph.D thesis and made life so much easier, especially when coming from somewhere else and starting a new life away from home. Don't feel offended if your name is not here, I'm just limited by the number of pages!

First of all, I would like to thank Prof. Chad Sinclair for his continuous and enormous support, patience, encouragement and help. Working under your supervision was a great experience during which I learned so much. I would also like to thank Prof. Warren Pool for welcoming me into his department, as well as Prof. Matthias Militzer and Prof. David Embury for their feedback and very fruitful discussions. The discussions' topics ranged from the work we were doing to other numerous aspects - the knowledge out there is simply amazing! Additionally, a great thank you goes to Jean-Denis Mithieux and Francis Chassagne from Aperam research Center, Isbergues, France, for the industrial aspect of the project, their great input, and their contribution to this work. Thanks also, to Jean-Hubert Schmitt for combining both the academic, and the industrial aspect of the study, Thank you for all the great ideas and discussions.

I would also like to thank all the various colleagues (and nonetheless, excellent friends) who made the department (and Ampel). More specifically Guillaume ("the one with light brown hair, glasses, and badly shaved"! Wait, it's just like me... well, the other Guillaume), who I met on the other side of the globe after going to secondary school with him back home (talk about a small world and coincidences), and his wife Colette, Tom ("oh oui oh oui"), David, Guilhem, Quentin, Ludi (why are there so many French people here?), Jenny, Sina, Tegar, Hamid, M.J., and Beth. I really enjoyed our Friday trips to the pub and amazing conversations about everything and anything over a pint of good beer.

Other than the academic side to my time in the program, being in Vancouver definitely changed me. I had the opportunity, the chance, and the privilege to live at St. John's College, an international graduate college. Where else can you meet people from over 40 different countries, learn about their culture, eat their food, and engage in

uncountable discussion topics? I will be forever indebted and thankful for all the great people I met and the friendships I made. I can't name them all here, but some MUST have their name mentioned, because they really mean a lot to me. So, Sarah, Nicole, Abhijit, Gaby, Andrew, Alex, Bieke, Niusha, Kristof, Ian, Michelle, Illiana, Adinda, Felipe, Kara, Dawn, no words can express my gratitude and how much I owe you because you really supported me throughout the entire process even (and especially) through the dark times.

I cannot forget those whom I left in France and are still very dear to me: Quentin and Aurelia, Flomich and Klervi, FloS and Karine, Yann, Aymeric, Mehdi, Juliette and Regis, Gros and Aline, Tom and Melanie, Bernard, Laureline and Thibaut, Clio and Arnaud, Laetitia, Morgan, Alexandra and Maxime, plus many others. I hope to see you all soon!

Finally, I cannot thank my parents (and extended family) enough for their unlimited support and care. Such an adventure wouldn't have been possible without you all, and I know it's hard to see each other frequently, but you are always in my thoughts.

Chapter 1: Introduction

Developing new, less expensive steel grades that can compete with other materials (austenitic stainless steels) on the basis of mechanical and functional performance is an ongoing challenge for producers. Such considerations are driving the development of ferritic stainless steels for applications in both industrial and consumer products [1] [2]. Ferritic stainless steels are particularly valuable in aggressive environments, such as in car exhaust systems, due to their excellent mechanical behaviour at elevated temperature, corrosion resistance and relative low cost [1] [3] [4] [5]. Over the past 20 years ferritic stainless steel use in exhaust systems has increased drastically, replacing previously used aluminized carbon steel owing to the improvements in lifespan afforded by improved corrosion [3]. For similar reasons, ferritic stainless steels play an important role in the food industry, in the manufacture of domestic electrical appliances (e.g. dish washers, food processors and meat grinders) and in architectural cladding [1] [5] [4]. In these applications the aesthetic appeal of the bright surface of stainless steels is equally important to inert chemical behaviour and good mechanical properties.

Any effect that deteriorates the surface appearance of ferritic stainless steels reduces their desirability in many of these applications. One of the most troublesome phenomenon for producers of ferritic stainless steels is a defect known as ridging (sometimes also called roping¹) that appears on otherwise defect free material following deep drawing or stretching operations. This phenomenon is characterized by the appearance of raised ridges that mark the otherwise smooth, shiny visual appearance of a formed part. Owing to the undesirable visual appearance of parts exhibiting ridging, these parts have to be sold as lower value added products or they have to be further processed, with added expense, so as to remove the surface roughness by polishing.

While ridging is a phenomenon that has been known and studied for more than 50 years it has only been recently that advances in experimental and modelling techniques

¹ While “ridging” and “roping” were initially used interchangeably for ferritic stainless steels and aluminum alloys [WuL102] [44], most authors seem to have agreed to associate the term “roping” with the specific surface roughening developed during stretching of aluminum sheets and the term “ridging” with the surface roughening developed during stretching of ferritic stainless steels. In this work, only the term “ridging” will be used for the sake of simplicity and consistency with the literature [26].

have provided us with a toolset that can allow for a proper quantitative description of its origins. While this has allowed for a better fundamental understanding of the origins of roping, there is still a need to link this with the processing schedule of the steel. For steel producers this is a major challenge since, at the moment, it is difficult to know for a given coil of steel whether it will exhibit strong ridging prior to experimentally evaluating it.

Based on this need, stainless steel manufacturer Aperam has been actively involved in attempting to study and control ridging in their products. The present project was launched in collaboration with Aperam having the specific aim to quantify,

- 1) The relationship between microstructure, texture and ridging in industrially processed ferritic stainless steel sheet.
- 2) The dependence of these microstructure/microtexture features with the final steps of industrial sheet processing (cold rolling and annealing).

To accomplish these tasks, a newly developed crystal plasticity tool was applied to predict ridging based on experimentally measured microstructures. Based on the results of these simulations, experimental studies on the annealing behaviour of ferritic stainless steels have been used to look at the origins of the microstructural features deemed responsible for ridging. Finally, some thoughts on the overall relationship between processing and ridging have been given.

Chapter 2: Literature Review

2.1. Characteristics of Ferritic Stainless Steels

Stainless steels are alloyed to contain a minimum of 10.5 wt.% chromium, chromium being principally added to increase corrosion resistance due to the formation of a passive chromium oxide layer on the steel surface [6] [7] [8]. Stainless steels can be further divided into different sub-groups depending on how they are alloyed into austenitic, ferritic, martensitic and duplex grades [4] [6].

Ferritic stainless steels are characterized as having a fully body centered cubic (b.c.c.) crystal structure at room temperature [6]. Typically, the chromium content of ferritic grades ranges from 13 wt.% to 30 wt.% [4]. Unlike other stainless steels ferritic grades contain very little nickel, if any. This combination of high chromium content (ferrite stabilizer) and very low nickel and carbon contents (austenite stabilizers) stabilizes the α -ferrite phase over a wider range of temperature by reducing the size of the γ -austenite loop present in the Fe-Cr phase diagram (Figure 2.1(b) and Figure 2.1(c) [4] [6]). Further stabilization of the ferrite phase can be achieved by introducing other alloying elements such as titanium, niobium or zirconium. These elements strongly react with carbon and nitrogen to form carbo-nitrides, removing the interstitial elements from solid solution and thus further reducing the size of the γ -loop [4]. Such stabilized ferritic stainless steels are ferritic at all temperatures up to the melting point. As a consequence, there is no austenite to ferrite transformation during thermo-mechanical processing.

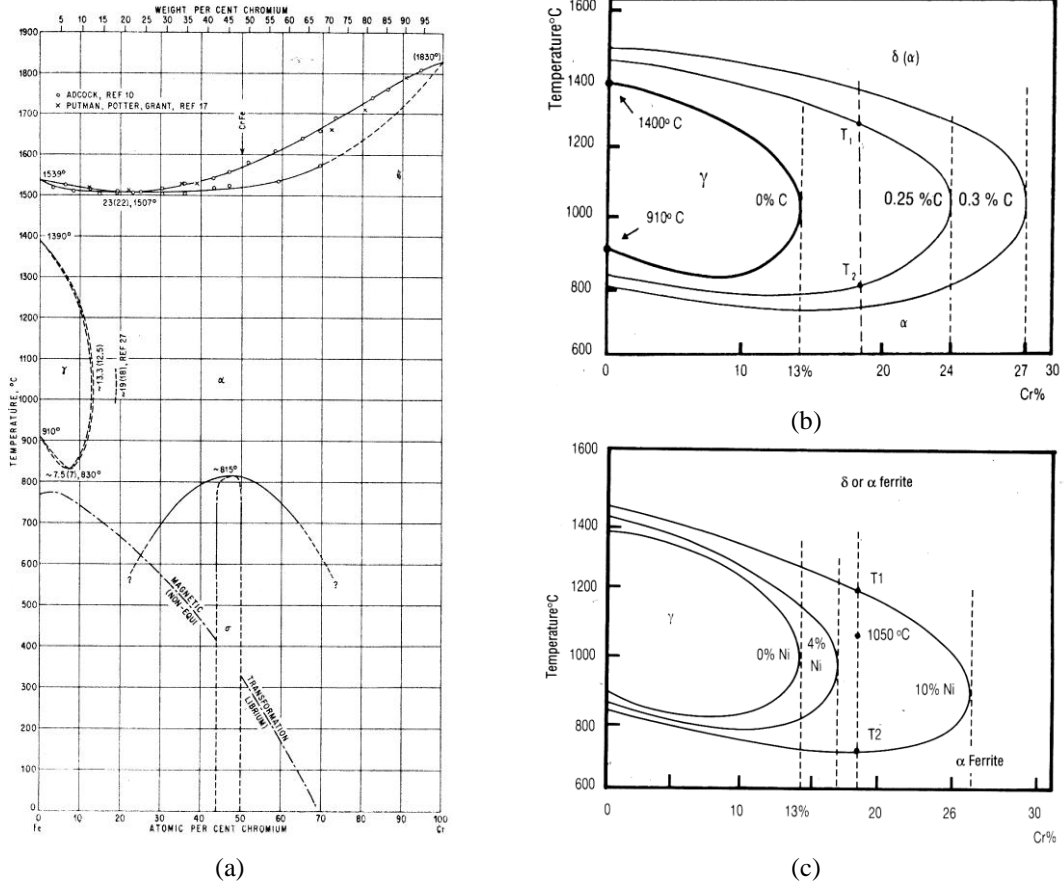


Figure 2.1: (a) Fe-Cr phase diagram showing the presence of a γ -austenite loop for lower chromium content [174], (b) Influence of carbon addition and (c) influence of nickel addition to the Fe-Cr system on the stabilization of the γ -loop (γ -stabilizer) [6].

2.2. Crystallographic Texture of Ferritic Stainless Steels

As will be discussed later, the phenomenon of ridging is strongly dependent on the crystallographic texture developed during thermomechanical processing. Modification to the texture must be done carefully, however, as texture also plays an important role in determining the formability of these steels [9] [10] [11].

As reviewed by [10] [12] [13] the crystallographic orientation of particular texture components of sheet material is often represented in a simplified way using the Miller indices associated with the plane of the sheet and the direction parallel to the rolling direction. In this notation, $\{hkl\}\langle uvw \rangle$ refers to grains having a crystallographic plane of

type $\{hkl\}$ parallel to the plane of the sheet and a crystallographic direction of type $\langle uvw \rangle$ parallel to the rolling direction of the sheet.

While the above notation provides a quick and simple indication of particular orientations by providing a simple visualization of the relationship between crystallographic orientations and the macroscopic directions of the sample, a more precise description of the crystallographic orientation of a grain, or orientations in a polycrystal is needed [14] [15]. Among the various ways of doing this, the most common is Euler angles. Using the Bunge convention $(\varphi_1, \Phi, \varphi_2)$ any orientation can be described in a space spanned by $0 \leq \varphi_1 \leq 360$, $0 \leq \Phi \leq 180$, $0 \leq \varphi_2 \leq 360$. However, owing to the cubic symmetry of bcc crystals, the unique portion of this space is reduced to $0 \leq \varphi_1 \leq 360$, $0 \leq \Phi \leq 90$ and $0 \leq \varphi_2 \leq 90$. Further, if the orthotropic symmetry of the sheet is considered then the unique portion of the space is further reduced to $0 \leq \varphi_1 \leq 90$, $0 \leq \Phi \leq 90$ and $0 \leq \varphi_2 \leq 90$ [15]. While the use of Euler space is common, it does have some limitations and thus, for some purposes other representations (e.g. Frank-Rodrigues space or Axis-Angle space) may be preferred [14] [15].

The processing of ferritic stainless steel sheet by hot rolling, cold rolling and annealing favours the alignment of specific orientations, or groups of orientations with the macroscopic RD (rolling direction), ND (normal direction) and TD (transverse direction) of the sheet. Such a group of orientations is called “fibre”. Ferritic steel sheet products (whether stainless or not) tend to develop two important fibres:

- **α -fibre:** Comprised of all orientations having a $\langle 110 \rangle$ parallel to RD.
- **γ -fibre:** Comprised of all orientations having a crystal plane $\{111\}$ parallel to the sheet plane (plane normal to ND).

While these two fibre textures are most commonly associated with ferritic stainless steel sheet, the former being particularly associated with the as-cold rolled texture and the later with the as-recrystallized texture [9] [13] [16], there are other orientations that can be important as well:

- **The rotated cube orientation, $\{001\}\langle 110 \rangle$:** This orientation (and those close to it), is part of the α -fibre. It has a particularly strong resistance to recrystallization [10] [17].

- **The Goss orientation, $\{110\}\langle 001 \rangle$:** This orientation is associated with strong shear deformation, such as that experienced in the near-surface region of sheet materials [18] [19].

All of these major texture components can be found in a cut through Euler space having $\phi_2=45^\circ$ (Figure 2.2). For this reason, the texture of ferritic steel is often represented in the $\phi_2=45^\circ$ section alone.

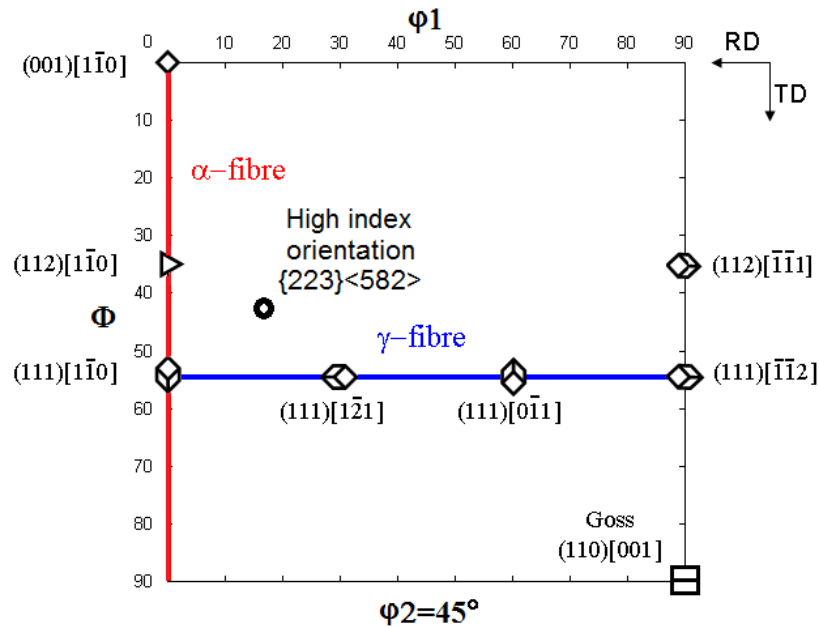


Figure 2.2: Classical crystallographic orientations observed during the processing of ferritic steel sheets represented in the $\phi_2=45^\circ$ section of the Euler space. The corresponding unit cell (cube) geometry is also shown for these orientations as though being viewed along ND (except for the high index orientation $\{223\}\langle 582 \rangle$).

2.3. Ridging: Its Characteristics and Relation to Microstructure

The phenomenon of “ridging” is most typically described based on its effect on the visual appearance of the sheet’s surface. Ridging is observed as an anisotropic roughening of the sheet surface during stretching operations, such as tension or deep drawing, performed on the final product following cold rolling and annealing [20] [21]

[22]. During tensile stretching the sheet develops raised ‘ridge-like’ features that run parallel to the previous rolling direction and appear almost continuous along the length of the sample, as can be seen on Figure 2.3(a). On deep drawn parts, such as the cup shown in Figure 2.3(b), the ridges give the appearance of scratches or dark marks on the surface of the part. As noted in chapter 1, ferritic stainless steels are often selected for their attractive visual appearance. The appearance of these ridges or marks on the surface of formed parts is therefore detrimental to their end use.

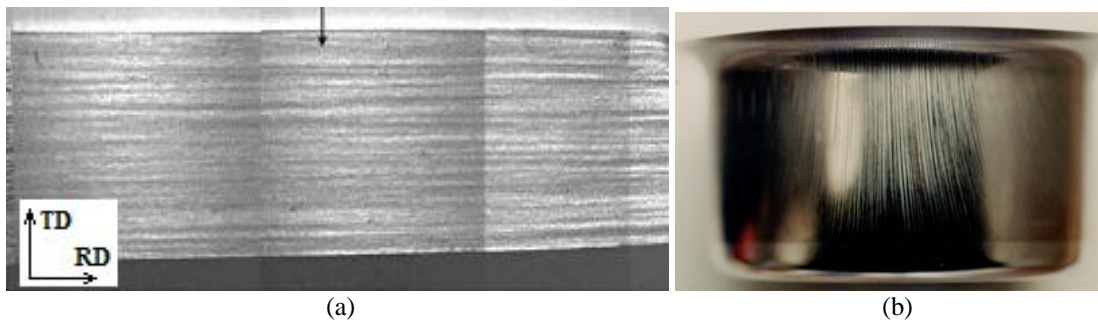


Figure 2.3: The appearance of ridging in ferritic stainless steel sheet following (a) tensile deformation parallel to the rolling direction and (b) deep drawing.

If one periodically measures the amplitude of the surface roughness associated with ridging during a tensile test, it is found that it increases roughly linearly with tensile strain [23]. Moreover, it is found that the amplitude, for a given level of tensile strain, depends on the macroscopic direction along which the tensile test is performed [24] [25]. As shown in Figure 2.4 the maximum ridging amplitude is obtained when the tensile axis is parallel to the rolling direction (RD) of the sheet. The amplitude progressively decreases as the tensile direction is rotated away from the RD, with very low or, in some cases, no perceptible ridging when the tensile direction is aligned with the transverse direction (TD) of the sheet. Regardless of the tensile direction, the ridges are always observed to run parallel to the rolling direction of the sheet.

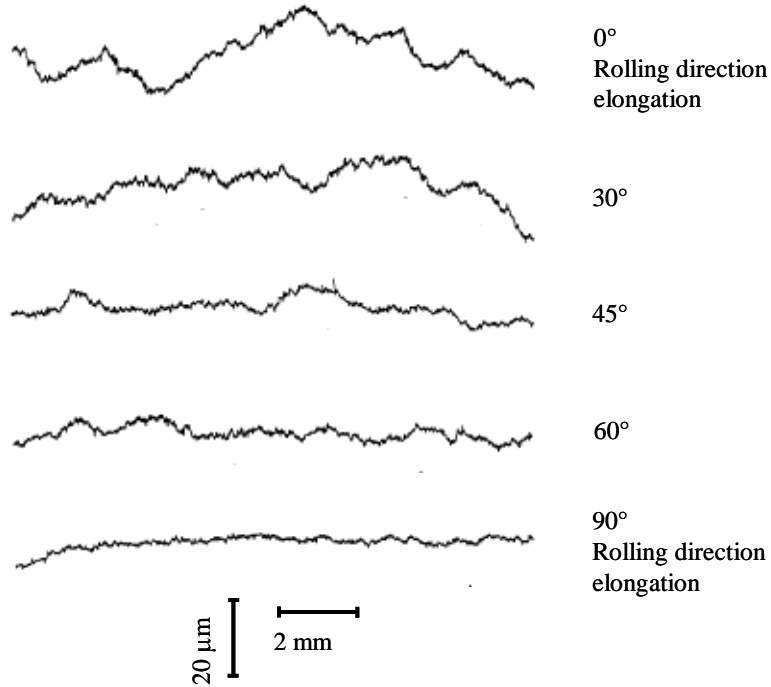


Figure 2.4: Two-dimensional profilometry measurements from surface samples tested in tension to 15% elongation. The direction of tension was varied from 0° (tension parallel to RD) to 90° (tension parallel to TD). Adapted from [24].

In industry it is common to characterize the surface roughness due to ridging by qualitative visual inspection or by quantitative profilometry (see e.g. Figure 2.5). From profilometry measurements, typically made following 15% tensile deformation [21] [22] [26], the amplitude² of the ridges is found to vary between approximately 10 - 50 micrometres (e.g. Figure 2.6). While the average amplitude of the ridges can be quantified readily, the wavelength of the ridges (parallel to the transverse direction of the sheet) is less well defined. Qualitatively, the visual appearance of the surface suggests that the separation between ridges is on the order of 1 to 5 millimetres [21] [24] [27] (e.g. Figure 2.6), though quantitative Fourier analysis of surface roughness data shows a wide range of wavelengths [23].

As mentioned above, the ridges appear almost continuous along the length of the sample, often reaching several centimetres in length parallel to the rolling direction. From

² A simple quantitative measurement of ridging amplitude is usually made by measuring the surface roughness along the transverse direction of the sample using a profilometer. Different filters can be applied to the 1-D measurement to remove undesired wavelengths according to the norm ISO 4284-1997, and the values for amplitude given in this work correspond to the maximum height of the roughness profile, which is the distance between the highest peak and the deepest valley for a given length of measurement.

this observation it must be concluded that ridging is a phenomenon occurring on a scale much larger than that typical of the microstructure (e.g. the grain size). Despite this, as will be shown later in Section 2.4, the microstructure plays a crucial role in determining the characteristic appearance of ridging in ferritic stainless steel samples.

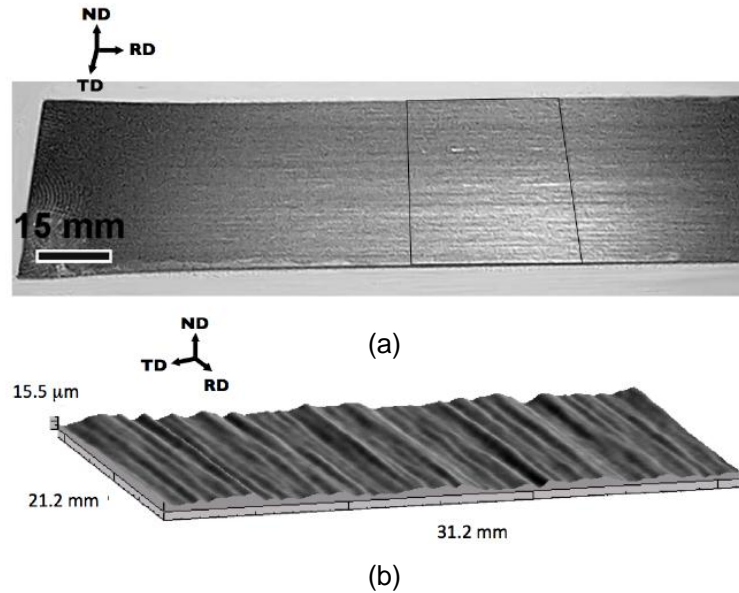


Figure 2.5: Example of (a) a tensile sample and (b) the corresponding 3-D surface roughness map measured after 15% elongation in tension by contact profilometry, obtained by multiple linear surface roughness measurements along the TD which are re-combined and properly aligned to obtain the three dimension profile [23].

While visual inspection might lead one to the conclusion that ridging is a surface defect, this is not in fact the case. Unlike surface roughening arising from the orange peel effect [28], ridging is the consequence of a cooperative bulk deformation of the material. This is revealed most clearly when surface roughness measurements are made on the top and bottom surfaces of the same steel sheet (Figure 2.6). Such measurements clearly reveal a correlation between the surface roughness on the top and bottom surfaces of the sheet. As can be seen in Figure 2.6 ‘peaks’ on one side of the sheet coincide with valleys on the other side, and vice versa [21] [22] [24] [29] [30]. Thus, rather than a surface roughening, ridging is actually a coordinated ‘corrugation’ of the sheet material in the ND-TD plane.

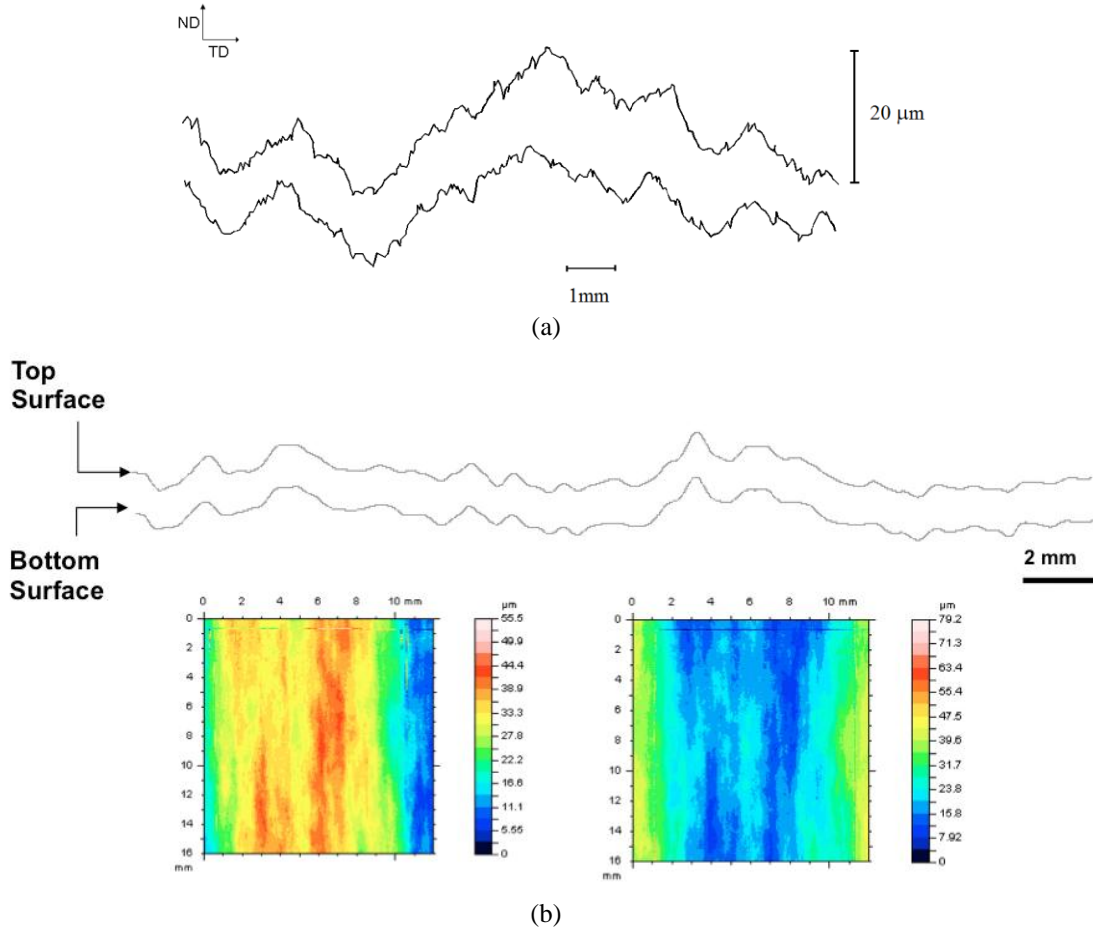


Figure 2.6: (a) Profilometric surface roughness measurement showing the correlation between the top and the bottom surfaces following tensile testing parallel to RD, adapted from [24]. The spacing between the traces is not indicative of the actual thickness of the sheet. (b) Similar observation but showing two-dimensional surface roughness measurements on the top and bottom surfaces of the same sheet illustrating the exact correlation of the surface roughness [23].

A similar, but distinct phenomenon is also observed following the tensile deformation of aluminum alloys. The phenomenon of roping in aluminum alloys has some strong similarities with ridging of ferritic stainless steels. Both phenomena appear during stretching operations, leading to the formation of ridges (or ropes) apparent on the surface of the sheet and aligned with the RD. Moreover, in both cases the characteristic dimensions of the surface roughness is much larger than the scale of the microstructure [26] [31]. Closer inspection though, reveals that the microstructural origins of the two phenomena are quite different. The amplitude of ridging in steels is strongest when tension is performed parallel to the RD. In contrast, the amplitude of roping in aluminum alloys is strongest when tensile stretching occurs parallel to the TD [26]. Differentiating

these phenomena further is the observation that the surface roughness measured on the top and bottom surfaces of aluminum sheets rarely shows strong correlation, as seen on Figure 2.7 [26]. This lack of surface roughness correlation suggests that, unlike in the case of ridging, roping is a phenomenon controlled by deformation in the near-surface region of the sheet. The similarities and differences between ridging, roping and the orange peel effect are highlighted in Table 2.1.

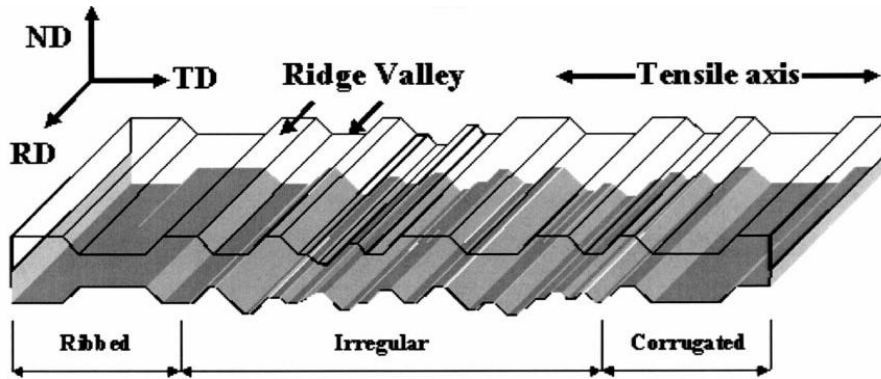


Figure 2.7: Schematic representation of the surface roughening (roping) observed in Aluminum alloys after tensile testing parallel to the transverse direction [26].

Table 2.1: Principal characteristics of the common surface roughness profiles: ridging in ferritic stainless steels, roping in aluminum alloys and orange peel effect.

		Ridging in ferritic stainless steels	Roping in Al alloys	Orange peel effect [28]
Relationship top and bottom surfaces		Corrugated surfaces [22]	No correlation [26]	No correlation
Dimensions	Length (parallel to RD)	Few centimetres [21]	Few centimetres [26]	Grain size (few μm)
	Wavelength (parallel to TD)	1-5 mm [21] [27]	1-2 mm [32]	Grain size (few μm)
	Amplitude	10-50 μm [21] [27]	5-30 μm [26]	Grain size (few μm)

2.4. Microstructural Features Associated with Ridging

Owing to the connection between the raised ridges on ferritic stainless steel sheet and its rolling direction, it has long been believed that a connection should exist between microstructural inhomogeneity and ridging. Grain size heterogeneity [33], segregation of alloying elements such as chromium, carbon or molybdenum [34] [35] and texture heterogeneity [20] [21] [22] [29] [30] [36] have all been cited as possible sources for ridging. While these different microstructural features may impact ridging, it is now accepted that ridging is caused by the strong plastic anisotropy exhibited by regions containing grains having particular types of crystallographic orientation. These bands of grains result in a coordinated deformation that gives rise to a pattern of deformation on a scale larger than the size of an individual grain [20] [21] [22] [29].

Early evidence for the clustering of grains having similar orientations was provided by etch pitting experiments [20] [21]. Based on the shape of individual etch pits, and their contribution to the mesoscopic appearance of the surface when viewed under the optical microscope, it was possible to observe large clusters of grains (viewed in planes perpendicular to the ND) such as illustrated in Figure 2.8 (Eau Regale/Aqua Regia etchant). Such experiments, though qualitative, were interpreted as providing evidence of clusters of grains oriented parallel to the RD, each cluster being comprised of one family of $\{hkl\}\langle 110 \rangle$ crystallographic orientation [21], as seen in Figure 2.8(g). Various observations have shown, however, that the pattern of etch pits can vary significantly through the thickness of the material. For example, it is often observed that the etch pit patterns in the near-surface regions of ferritic stainless steels are much more random than those found near the centre of the sheet (Figure 2.8(a-c), medium level of ridging). In other materials, however, similar spatial distributions of etch pits have been observed to be more homogeneous through thickness (Figure 2.8(d-f), high level of ridging). The observation of clustering of etch pits in the centre of the sheet but not necessarily at the sheet surface has led some to argue that ridging originates within the centre of the sheet [37].

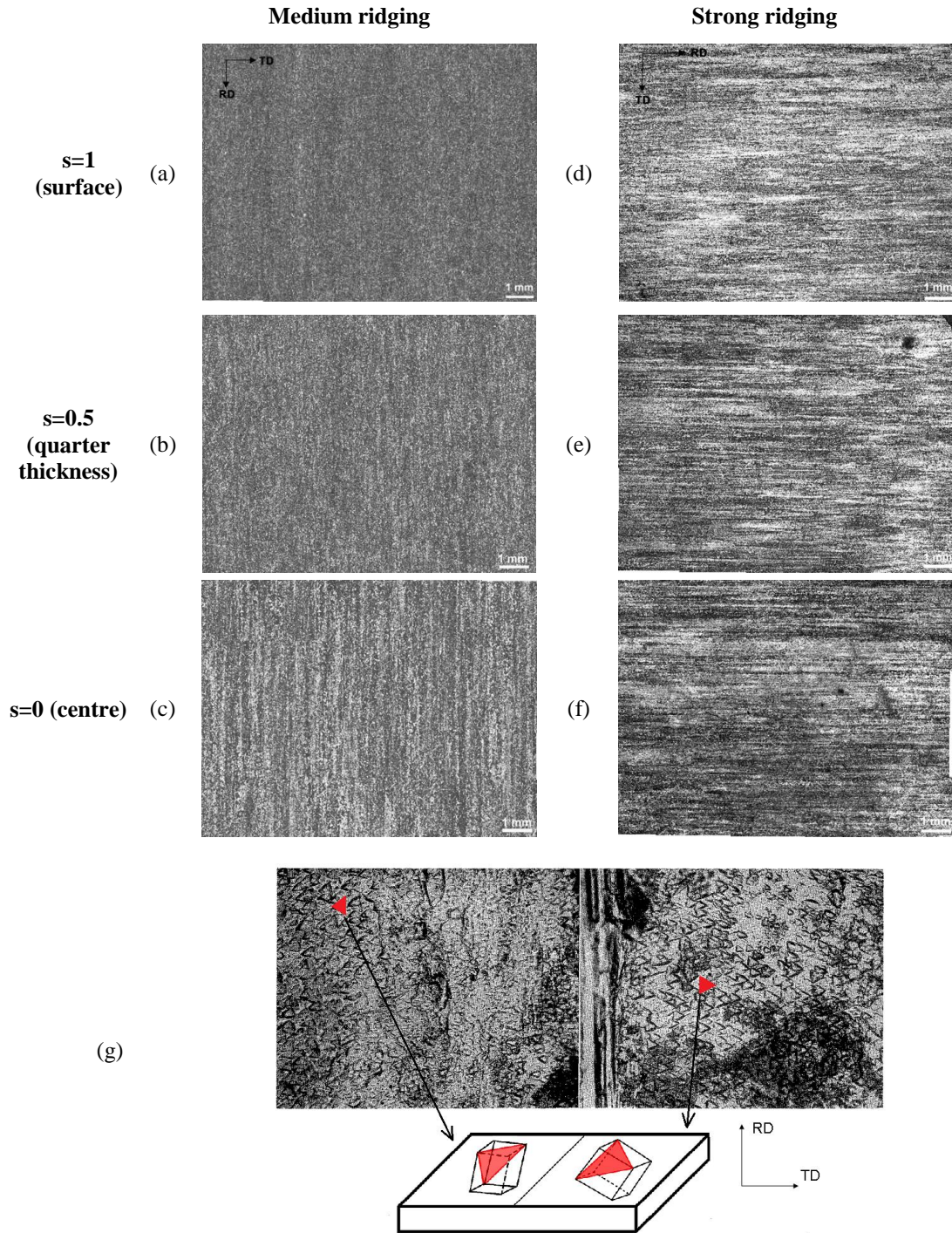


Figure 2.8: Optical microscopy of etched surfaces revealing clustering of grains having similar orientations aligned with the rolling direction based on the density of etch pits as a function of the orientation. (a)-(c) sample exhibiting intermediate level of ridging (rolling direction is vertical), (d)-(f) sample exhibiting strong ridging (rolling direction is horizontal) [23]. (g) The 2 variants of $\{hkl\}\langle 110 \rangle$ (α -fibres proposed to be at the origins of ridging in the model proposed by Takechi et al.) are distinguished by the shape of their etching patterns [21]. (a)-(f) are hot rolled, cold rolled and annealed 430 grades Ferritic Stainless. (g) is from a cold rolled 17%-Cr Stainless Steel.

Regardless of this detail, it does appear that some correlation between the etch pits and ridging can be found. Figure 2.9 shows a tensile sample whose grip region was polished and etched to reveal the etch pit pattern. While the correlation with the ridging profile on the gauge length of the sample itself is not perfect, one can find some strong qualitative similarities in the spacing and continuity of the etch and ridging patterns.

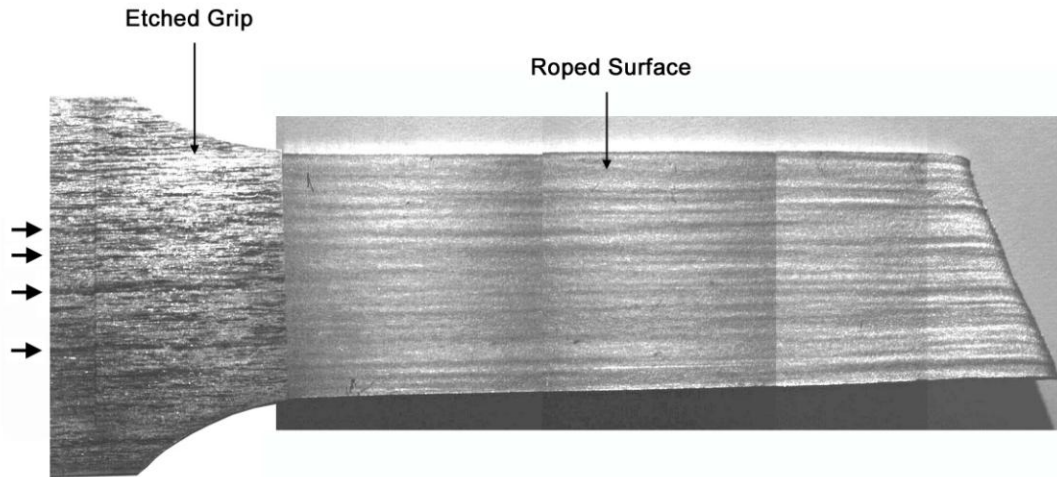


Figure 2.9: Correlation between the etch pits patterns revealed after etching of the un-deformed grip and ridged surface on the gauge length of the 430 Ferritic Stainless Steel sample [23]. Arrows point to features that appear to have similar patterns in the etched and ridged regions.

These etch pit experiments helped motivate three early models for ridging. These models were built upon the idea of clusters of grains oriented parallel to RD having their $\langle 110 \rangle$ direction parallel to the tensile axis. These models were motivated by the knowledge that such $\langle 110 \rangle$ oriented grains exhibit particularly strong plastic anisotropy owing to the orientation of the $\langle 111 \rangle$ slip directions with respect to the tensile axis. The anisotropic behavior of such grains has been used to explain other phenomenon, including 'grain curling' observed in $\langle 110 \rangle$ textured bcc wires and anisotropic sample shapes observed in compressed FCC materials [38] [39]. If one imagines a cubic unit cell being stretched parallel to a $\langle 110 \rangle$ direction, two of the potential $\langle 111 \rangle$ slip directions are perpendicular to this loading axis and cannot accommodate the imposed extension. The other two $\langle 111 \rangle$ slip directions are in the same plane as the $\langle 110 \rangle$ tensile direction. Operation of these two $\langle 111 \rangle$ slip directions will fully accommodate the extension

parallel to $\langle 110 \rangle$ while giving an equal but opposite contraction along a $\langle 100 \rangle$ direction and no strain parallel to the $\langle 110 \rangle$ direction perpendicular to the loading axis (see Figure 2.10(b)). Such deformation leads to plane strain deformation of these grains. In the case of $\{001\}\langle 110 \rangle$ grains tensile testing leads to zero strain in the TD direction.

Chao was the first to combine the idea of microtexture and the strong plastic anisotropy of $\{hkl\}\langle 110 \rangle$ grains to explain the origins of ridging [20]. In this model (Figure 2.10(b)) it was assumed that the microstructure could be described as bands or clusters of “cube-on-face” (CF) oriented grains ($\{001\}\langle 110 \rangle$) embedded in a matrix of “cube-on-corner” (CC) orientated grains ($\{111\}\langle 110 \rangle$) (Figure 2.10(a)). As mentioned above, the cube-on-face $\{001\}\langle 110 \rangle$ grains deform in plane strain with extension parallel to RD, contraction parallel to ND and zero strain parallel to TD. It was argued by Chao that the cube-on-corner $\{111\}\langle 110 \rangle$ oriented grains prefer to deform in plane strain but with zero strain parallel to the ND direction and contraction parallel to the TD direction. As will be seen below, this view is not actually correct as an important shear strain is also expected during the deformation of these grains. While this model predicts the correct type of surface profile, it predicts a ‘ribbed’ through-thickness microstructure rather than the corrugated profile found experimentally.

A second competing model [22] was proposed on the basis that an inhomogeneous buckling of individual grains could lead to ridging (Figure 2.10(c) and Figure 2.10(d)). In this case Wright envisioned the presence of bands of grains having a $\{001\}\langle 110 \rangle$ orientation in a matrix composed of $\{111\}\langle 112 \rangle$ orientations (Figure 2.10(c)). Wright argued that in order to accommodate the plastic incompatibility arising from the lack of contraction of $\{001\}\langle 110 \rangle$ grains parallel to TD and contraction of the surrounding $\{111\}\langle 112 \rangle$ oriented grains, the $\{001\}\langle 110 \rangle$ grains could undergo an inhomogeneous buckling. While this model admitted the correct corrugated profile of the sheet, and (it was argued) could explain the effects of tensile direction on the amplitude of roping, it requires a very specific configuration. Indeed, it was later shown that in the limit of very long $\{001\}\langle 110 \rangle$ grain clusters or in the case of $\{001\}\langle 110 \rangle$ grain clusters that are fully embedded within a three-dimensional matrix of $\{111\}\langle 112 \rangle$ orientations no buckling would be expected [27].

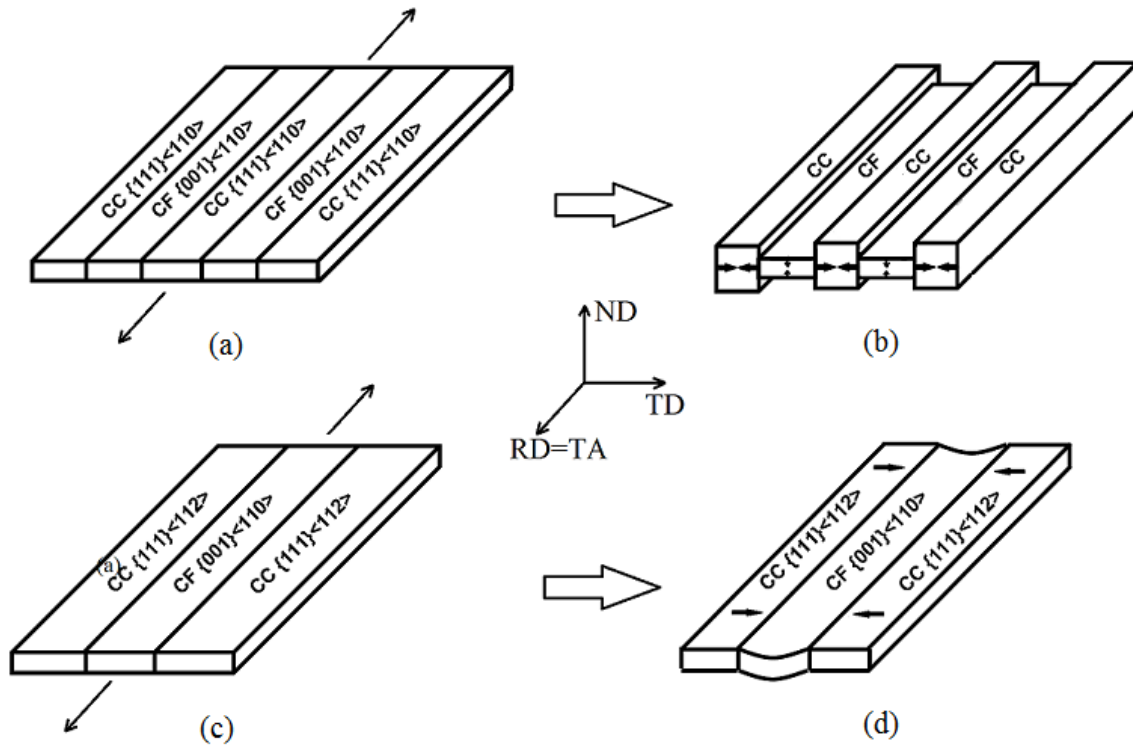


Figure 2.10: Schematic of the basic features of ridging according to Chao (a) and (b), based on the differences of through thickness compression of the two texture components, and according to Wright (c) and (d), based on compressive forces resulting in buckling of the $\{001\}\langle 110\rangle$ bands. The tensile axis (TA) is parallel to the rolling direction (RD).

Along with the above mentioned flaws in the Chao and Wright models, another discrepancy between their models and experiments is the fact that they rely on the presence of orientations (the $\{001\}\langle 110\rangle$ orientation) which is not a strong component of the experimentally measured texture in final sheet products [40]. A third model, developed almost at the same time as the Chao model but much less widely discussed in the early literature, provides a remedy to some of these problems.

The Takechi model [21] starts from a similar starting idealized microstructure as the Chao and Wright models but considers alternating clusters or bands of $\{111\}\langle 110\rangle$ oriented grains. In this case two variants (rotated by 180° from each other about ND) of the same $\{111\}\langle 110\rangle$ orientation are assumed to occupy the bands. A schematic of this model microstructure is presented Figure 2.11(a). Upon imposing tension parallel to the rolling direction, the deformation of each grain (or band of grains) is accommodated by the activation of 3 slip systems. The slip system represented by the black arrow in Figure 2.11 is perpendicular to the tensile axis and, as a consequence, is not activated.

Elongation will be accommodated by the activation of the slip systems represented by the red arrows, whose vertical and lateral components (along the sheet normal and along the transverse direction) cancel each other, resulting in no thinning or no contraction of the sheet. The contraction is accommodated by the activation of the slip system represented by the blue arrow, resulting in an unbalanced ‘out-of-plane shear’ (i.e. a shear in the ND-RD plane in the ND direction) that leads to a rigid rotation of the crystal. Rotations in opposite directions result from the symmetrically equivalent orientations, leading to the corrugated profile usually observed (Figure 2.11(b)). This is to be contrasted with Chao’s original assertion that the deformation of $\{111\}\langle 110\rangle$ grains is purely plane strain in the RD-ND-TD coordinate system. This is only true if you consider the macroscopic strain arising from an equal mixture of the two $\{111\}\langle 110\rangle$ variants shown in Figure 2.11 [27] [41].

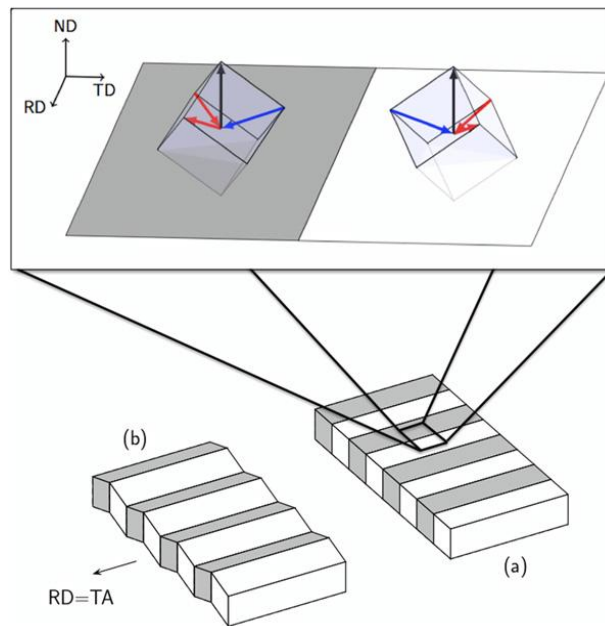


Figure 2.11: Takechi model for origin of ridging where (a) alternating clusters along the transverse direction (TD) of grains of the different $\{111\}\langle 110\rangle$ variants are aligned along the rolling direction (RD). When the tension axis (TA) is aligned with RD, the two variants undergo opposite out-of-plane shear resulting in (b) the overall corrugations of the sheet. The out-of plane shear is caused by the activation of a specific and non compensated slip system (represented by the blue arrows) [42].

Recent crystal plasticity Finite Element Method (CPFEM) calculations have provided basic validation of the concepts underlying the Takechi model, particularly

confirming the role of out-of-plane shearing in the development of through-thickness corrugation [27]. Moreover, these CPFEM calculations have revealed that the presence of large colonies of $\{111\}\langle 110\rangle$ or $\{112\}\langle 110\rangle$ grains through the full sheet thickness are not necessary for the appearance of ridging. Instead it was found to be sufficient to have smaller clusters located at the centre of the sheet in order to create surface ridges.

Just as with the Chao and Wright models, the major criticism that can be made of the Takechi model is its reliance on an extremely over simplified view of the microstructure of ferritic stainless steel sheet. It has been the development and advancement of electron back-scattered diffraction (EBSD) that has played a vital role in advancing our understanding of the microstructure, microtexture and ridging. Recent EBSD observations have allowed for a fully quantitative description of the spatial distribution of grains with particular crystallographic orientations over areas of several square millimetres [27] [29] [30] [33] [36] [37] [43] [44]. Indeed, one can show a one-to-one correlation between the etching pattern viewed on the ND plane of a sheet and EBSD maps made from the same area (Figure 2.12), where clear regions (lightly etched) appear to be $\langle 111\rangle$ oriented grains while dark etching grains are non $\langle 111\rangle$ oriented grains.

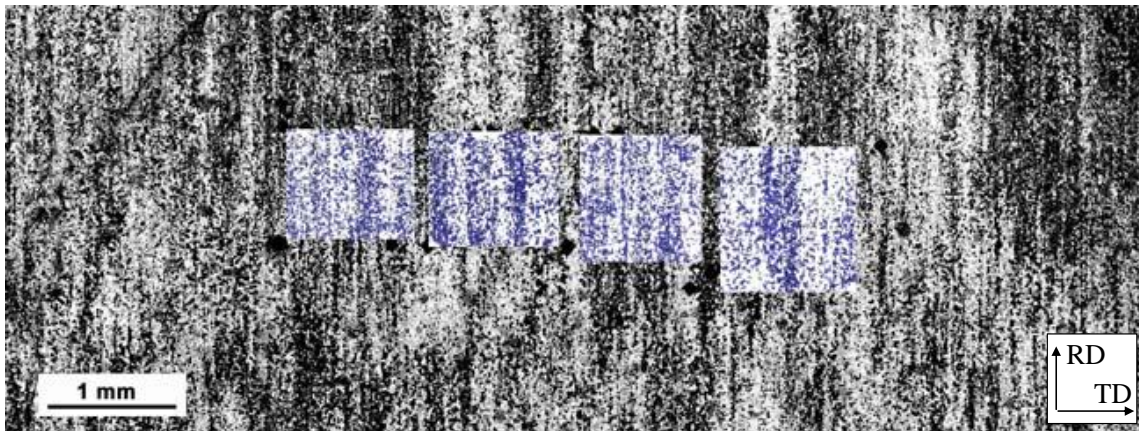


Figure 2.12: Correspondence between surface of etched sample (underlain) and EBSD maps (colour) where the EBSD maps show only grains having $\langle 111\rangle//ND$ as blue [23].

The most important conclusion reached from early EBSD studies of ferritic stainless steel sheet was that, while bands of grains with particular orientations can often be identified, providing a fully quantitative description of their extent and composition (in terms of spread of orientations) tends to be difficult. Such bands are composed of not

one but multiple orientations and so how they appear in EBSD maps depends sensitively on how the maps are constructed (Figure 2.13). One can see that different bands appear in maps depending on how the data is separated based on orientation. One can also see that the separation of these bands parallel to TD is much smaller than the wavelength of ridging observed experimentally [44].

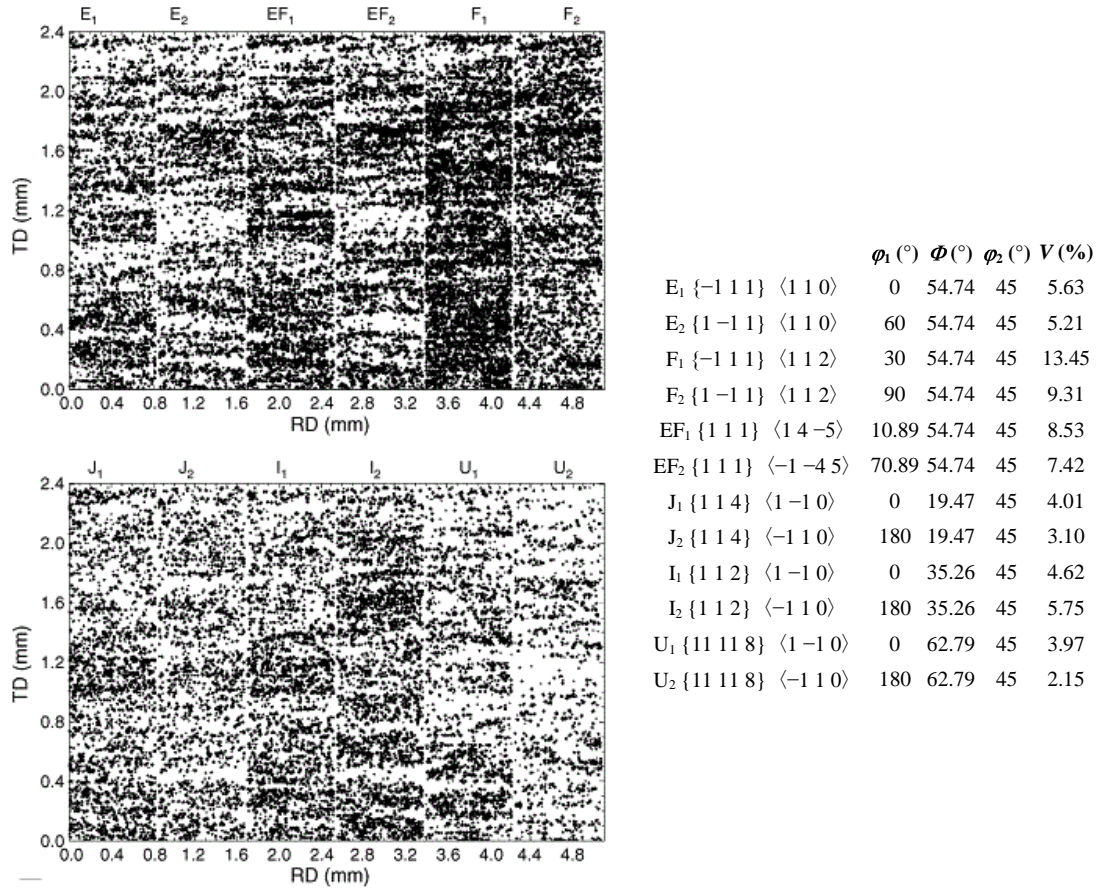


Figure 2.13: EBSD maps showing apparent banding of specific orientations given by their Euler angles and volume fraction (V%) [44].

From EBSD measurements, banding of grains could be most easily observed if maps were plotted showing all grains having a $\langle 111 \rangle$ direction within 10° - 20° of ND (i.e. γ -fibre grains, and especially orientations E₁, E₂, EF₁ and EF₂) (Figure 2.13). Such maps reveal bands of grains separated by approximately 100-200 μm parallel to TD and several hundred micrometres in length parallel to RD. While the dimensions of the bands parallel to RD appear coherent with expectations, the separation between bands parallel to TD is

much smaller than the typical wavelength of ridges measured on the surface of samples, the ridging wavelength being closer to 1 – 5 mm. More careful analysis of the orientations of grains within these $\langle 111 \rangle$ //ND grains reveals a complex mix of grain orientations, far from the idealized grain clusters or bands envisioned in the Chao, Wright or Takechi models.

As briefly noted above, modern crystal plasticity simulation tools have provided an important link between the oversimplified Chao, Wright and (most notably) Takechi models and experimental EBSD observations, allowing for a proper physical description of the mechanisms leading to plastic deformation as well as increasingly allowing for a more realistic treatment of microstructure on the scale that is required to describe roping. A notable example of this work is that performed by Wu et al. using CPFEM calculations starting from an experimentally measured EBSD map (measured on the plane normal to the ND direction with dimensions of 0.816 mm//RD and 2.376 mm//TD) as input microstructure for the simulations [44]. In these calculations, a far-field biaxial tensile stress in the RD-TD plane was considered with an imposed strain parallel to the rolling direction. The normal stresses perpendicular to the sheet surface were assumed to be zero (i.e. plane stress conditions were assumed). From these simulations, an inhomogeneous displacement of the surface was found, showing characteristics similar to ridging behaviour. It was found that the displacement of the surface parallel to ND was dominated by the contribution from out-of-plane shearing, consistent with the basic idea underlying the Takechi model, despite the fact that the clusters in the simulations were composed of a complex mix of different crystallographic orientations (see Figure 2.13). These results clearly point to the fact that, while the out-of-plane shearing identified by Takechi is the important contribution to the inhomogeneous deformation causing ridging, this out-of-plane shearing can arise from a wide range of crystalline orientations. This has been summarized by means of simple relaxed Taylor [23] and Sachs-like [37] calculations of the shearing tendency of all possible crystallographic orientations. Figure 2.14(a) shows the (absolute) normalized amplitude of out-of-plane shearing strain rate as a function of the crystallographic orientation in the $\varphi_2=45^\circ$ section of Euler space, and Figure 2.14(b) shows the calculated ratio of the out-of-plane shear to the tensile strain

$s=\gamma_{23}/d\varepsilon_{11}$, (where direction 1 is RD, direction 2 is TD and direction 3 is ND) for every orientation in the reduce Euler space. As predicted by Takechi, the $\{111\}\langle 110\rangle$ orientations have a high shearing tendency but so do a wide range of orientations spreading, for example, upwards along the α -fibre.

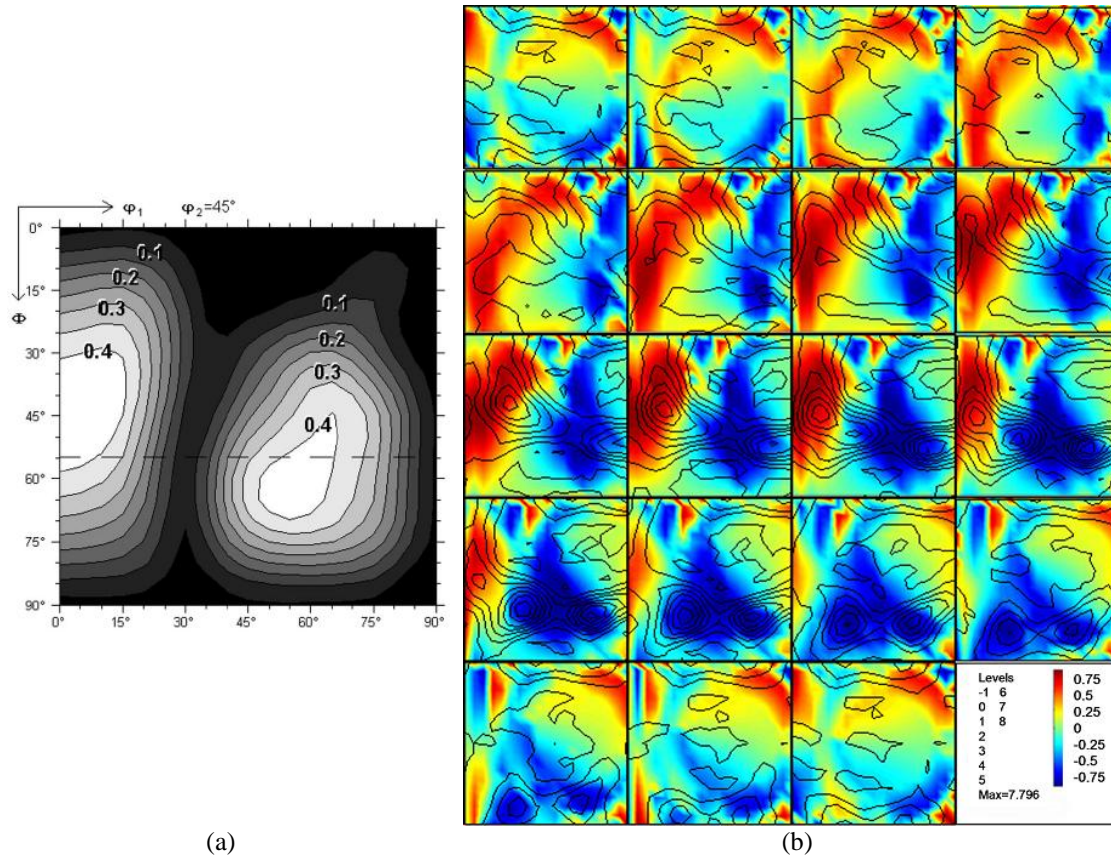


Figure 2.14: (a) Absolute intensity of out-of-plane shear strain rate calculated by VPSC as a function of orientations represented in the $\phi_2=45^\circ$ section of the Euler space. The behaviour of each grains was estimated by assuming them to be embedded in a very compliant matrix (Sachs-like behaviour) [37]. (b) Intensity of the “in-plane shear ratio” defined by $s=\gamma_{23}/d\varepsilon_{11}$, (where 1 is RD, 2 is TD and 3 is ND) using simple relaxed Taylor conditions [23]. The color code for shear intensity is superimposed on the experimental ODF from a sample exhibiting high ridging, represented by iso-intensity diagrams in ϕ_2 sections (plotted every 5°).

While the microstructure area investigated by Wu et al. [44] was relatively large (0.816 mm/RD and 2.376 mm/TD), it was still small relative to the wavelength of ridging (1–5 mm). This means that attempting to make a quantitative comparison between the CPFEM results and experiments is difficult. Indeed, no attempt for a

quantitative comparison with experimental surface roughness measurements was made in this work [44].

As a computationally less expensive alternative to CPFEM, mean-field crystal plasticity simulations have also been used in an attempt to predict ridging behaviour from experimentally measured microstructures. Wu et al., for example, developed a simplified ridging model (applied both to roping in aluminum alloys [45] and ridging in stainless steels [46]) where the deformation of each individual grain is computed based on the assumption that the local stresses are the same as the far-field imposed stresses. Sinclair [23] used a relaxed Taylor type of calculation to also calculate the out-of-plane shearing tendency for individual grains in an EBSD map (Figure 2.14(b)). Others have turned to self-consistent crystal plasticity models, notably the Los Alamos Viscoplastic Self-Consistent (VPSC) model, as an intermediate tool compared with full-field CPFEM simulations or simplified Taylor and Sachs mean-field calculations. In VPSC simulations each individual grain is considered embedded within a homogeneous matrix having the average behaviour of all of the grains. The mechanical behaviour of this homogeneous matrix has to be obtained self-consistently with the calculation of the stresses and strains accommodated by each individual grain. In this case, the local stresses and strains on an individual grain tend to be between those predicted from upper bound Taylor or lower bound Sachs like models [47] [48].

Engler et al. [37] performed such VPSC calculations using as input the texture data obtained from a large scale EBSD measurement made on the ND plane of a ferritic stainless steel sheet. The resulting out-of-plane shearing was computed for each grain and re-plotted back on the originally measured EBSD map (Figure 2.15). Despite the fact that the VPSC calculations do not retain the information about the local neighbourhood of each individual grain, these simulations gave qualitatively similar results to the full-field CPFEM calculations made by Wu et al. [44].

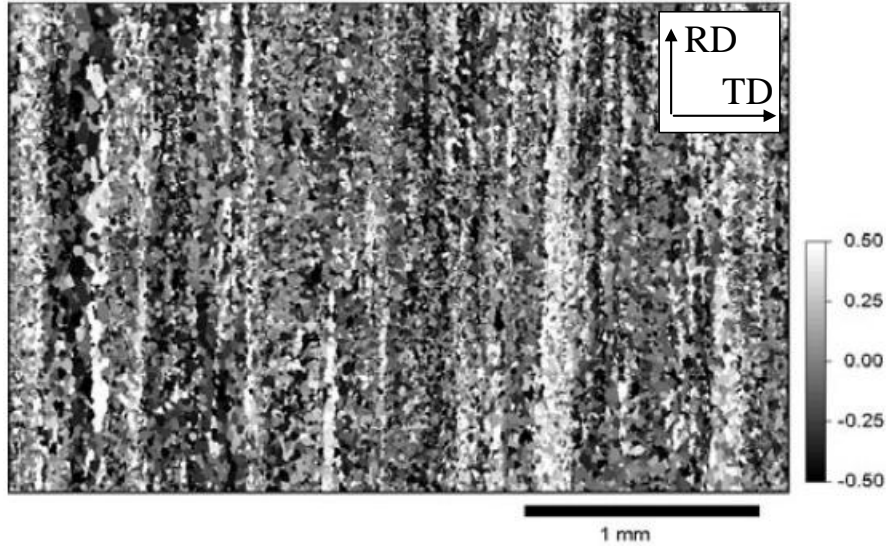


Figure 2.15: Out-of-plane shearing map created from an EBSD data set taken at mid-thickness on the sheet plane. This map represents the spatial distribution of out-of-plane shear intensity calculated with VPSC. Bands of similar shearing behaviour aligned with the RD are visible [37].

While the full-field and mean-field crystal plasticity simulations described above have all improved our understanding of the link between real, experimentally measured microstructures and the mechanism leading to ridging, a major limitation in all cases has been the fact that the calculations have been performed purely on data collected from two dimensional EBSD measurements most often from the ND plane. As noted above, it has been shown that the appearance of clusters via etch pit experiments can vary depending on the position through thickness at which the measurement is made. Engler et al. explicitly mentioned that, due to a lack of clusters near the surface of the sheet, it was expected that only the center half of the sheet contributes to ridging [37]. This, however, raises the immediate question of whether the near surface regions affect the amplitude or wavelength of ridging. Very little work has been done to examine the effect of the spatial distribution of clusters through thickness and ridging. Brochu et al. [36] attempted to make a simplified model to account for experimentally observed texture heterogeneities through the sheet thickness, including a lack of clusters through the full thickness of the sheet. In their model, the thickness of the sheet was sub-divided into small domains and the net deformation in this column of material calculated as the sum of the deformations in each of the domains. While highly over-simplified, this model is notable as it was the first to attempt such a correlation between ridging and through thickness microstructure.

More recently Sinclair [41] used VPSC to examine the shearing behaviour of individual grains, as a function of their shape, volume fraction and crystallographic orientation, when fully embedded within a matrix of well-defined orientation. The key finding of this work was that even when present in dilute quantities, grains having orientations with a strong tendency to shear do continue to shear even when completely surrounded by grains that have no tendency to shear. Moreover, such strongly shearing grains (e.g. $\{111\}\langle 110\rangle$ type) will actually tend to impose their deformation on their surroundings by causing non-shearing grains (e.g. $\{111\}\langle 112\rangle$ type) to shear. Thus, this result clearly shows that fully embedded three-dimensional grains, like the simplified three-dimensional microstructures considered in the prior work noted above, should also be expected to produce out-of-plane shearing, even when the surroundings would appear unfavourable for it. A second important observation was that, for a fixed aspect ratio of the width to thickness of a grain in the RD plane, the shearing (more strictly the rotation arising from the shearing) was nearly independent of the length of the grain parallel to RD (tensile direction). Thus, in this case, the length of the clusters parallel to RD is important from the perspective of the apparent continuity of the ridges formed on the surface, but not important in terms of the amplitude of the surface roughening resulting from ridging. This point will be used to justify some of the important assumptions made regarding the simulations performed later in this thesis.

2.5. Effect of Thermo-Mechanical Processing on Microstructure Development

2.5.1. Introduction

The above-reviewed work points to the presence of non-randomly distributed grains being the source of ridging observed after stretching ferritic stainless steel sheet. These ‘clusters’ consist of grains having a similar tendency for out-of-plane shearing and as such tend to have particular types of crystallographic orientation.

As ridging is observed on the final sheet product, it has long been believed that modifying the final processing steps, particularly cold rolling and/or annealing, could be effective at reducing or eliminating ridging [17] [49]. With this in mind, there has been a

significant amount of work performed to attempt to relate texture and microstructure to the processing parameters involved in these last steps of sheet production. Others have, however, pointed to results suggesting that the upstream processing (hot rolling and casting) appear to also have an important impact on ridging [27] [43].

In this section, the evolution of microstructure and texture during these four processing steps will be reviewed in reverse order to how they are performed industrially (Figure 2.16). The review will therefore start from the cold rolling and annealing steps then move upstream to the hot rolling and casting steps.

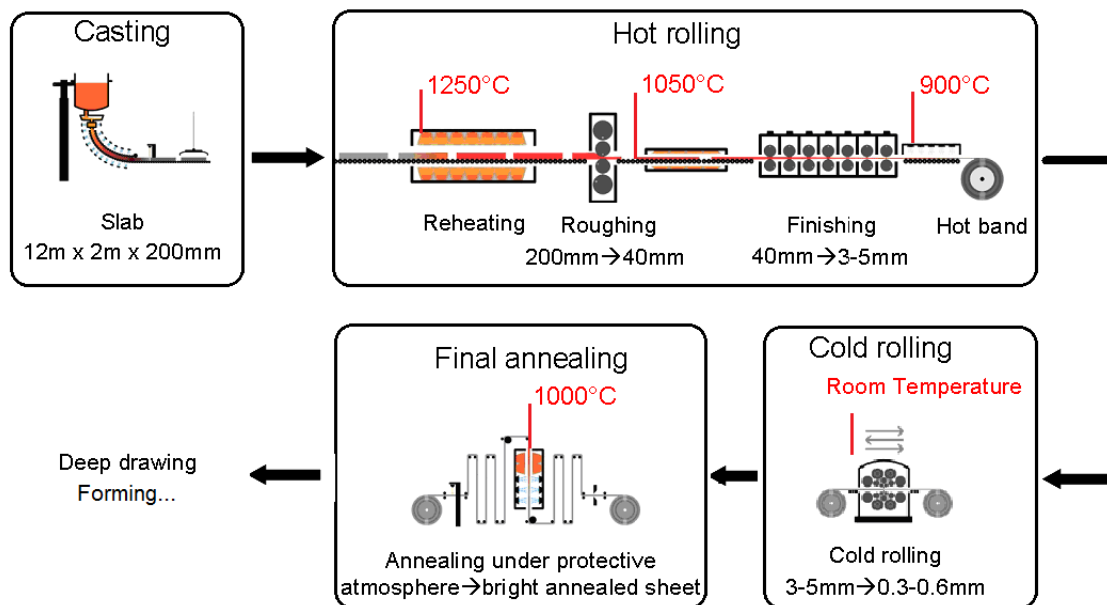


Figure 2.16: Simplified schematic of the industrial process for stainless steel production, from casting to final annealing. The characteristic dimensions and temperatures along the different steps are highlighted as well [5].

Ferritic stainless steels present very similar deformation [10] [50] [51] [52] and annealing [10] [12] [51] [55-61] behaviour to that of other ferritic low carbon and interstitial free steels, due to their common crystal structure. Given that there is a much more extensive literature related to these non-stainless steels, the discussion presented here will attempt to use both sets of literature to give an overview of the microstructure and texture characteristic of ferritic steels.

The material that enters the cold rolling mill is in the form of ‘hot band’, 2 - 5 mm thick sheet material that has been previously hot rolled, coiled and (sometimes) annealed. Ferritic stainless steel ‘hot band’ is heterogeneous in its microstructure and texture, having large microstructural and texture gradients through-thickness [49] [50]. Performing an annealing treatment on the as-hot rolled material can change some aspects of the microstructure and texture, though as will be seen later, these changes tend to be much smaller than those obtained on annealing of the cold rolled sheet [60]. Here, the microstructure and texture associated with un-annealed hot band will be considered since this is the case most often studied in the literature.

The near-surface of ferritic stainless steel hot band (defined by $0.5 < s < 1$)³ most often consists of recrystallized grains, elongated along RD, whose average dimensions are about 40 μm parallel to the normal direction and 100 μm or more parallel to the rolling direction [17] [49]. As seen in Figure 2.17 a wide grain size distribution exists at this stage of processing. The texture in this region can be described as mainly consisting of {110}<001>-Goss (major component) and {112}<111> (minor component) orientations, as can be seen on Figure 2.18(a) [17] [49]. The microstructure within the middle half of the sheet ($0 < s < 0.5$) is very different, grains tending to be highly elongated, well recovered and having a texture composed of a strong α-fibre, dominated by the {001}<110> and {112}<110> orientations, though it often also exhibits a weaker γ-fibre (see Figure 2.18(d)) [13] [17] [49] [50] [64-66].

From Figure 2.18, it can be seen that during cold rolling, all layers see the formation of an α-fibre whose intensity increases as one gets closer to the centre, as well as an incomplete and weaker γ-fibre (especially {111}<110>). During annealing, the bulk texture sees the replacement of the α-fibre by a γ-fibre whose intensity increases as one gets closer to the centre [17]

³ The *s*-parameter is classically used to describe the fractional through thickness position and is defined by $s = \frac{a}{1/2 \cdot d}$, where *a* is the distance between the centre of the sheet and the position of interest. The sample thickness is defined as *d*, so that *s* varies from 0 at the sheet centre to 1 at the surface.

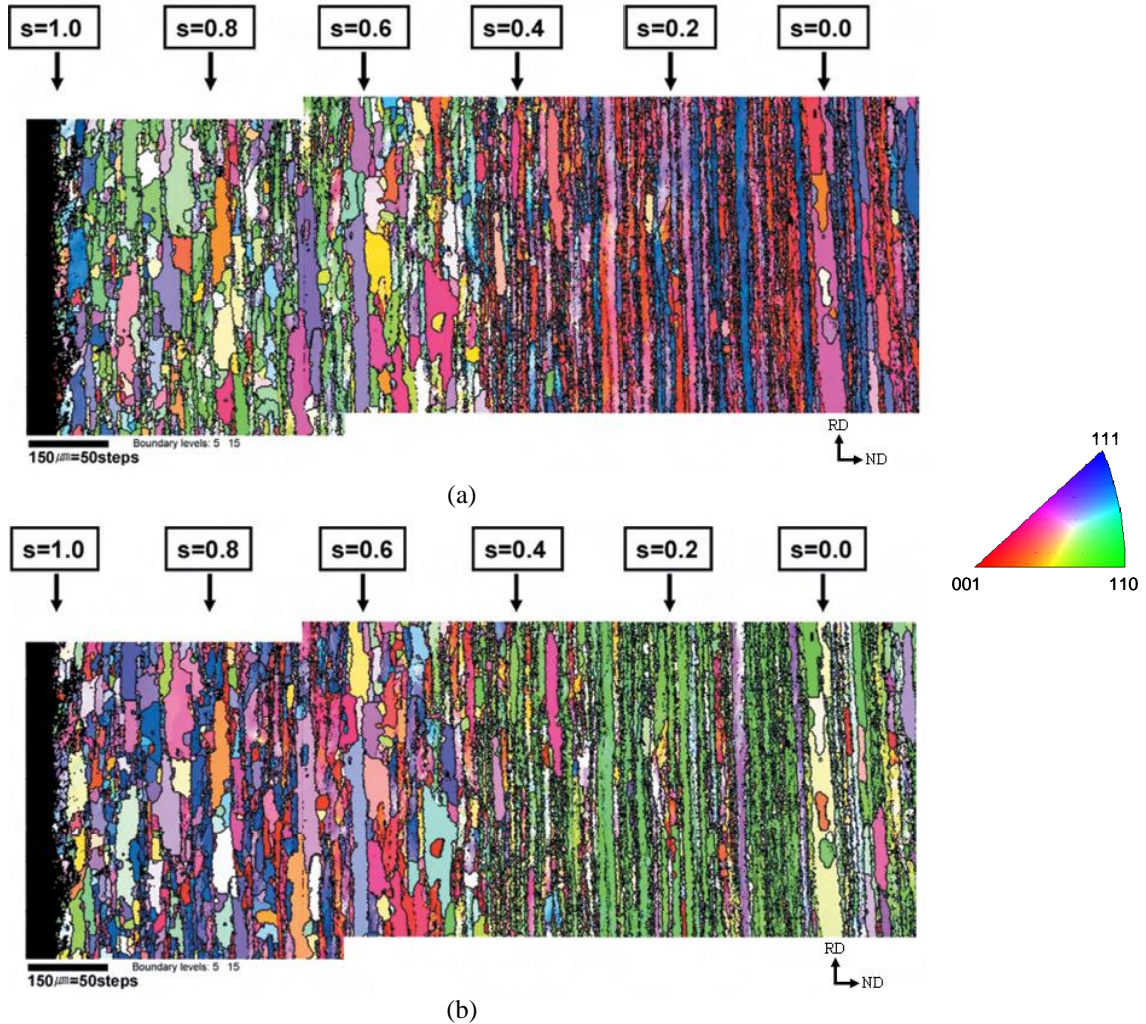


Figure 2.17: Inverse Pole Figure (IPF) EBSD maps made on the transverse plane of the hot band of a 17%Cr ferritic stainless steel showing the inhomogeneous recrystallization behaviour. (a) ND IPF and (b) RD IPF (crystal axis represented by the stereographic triangle are parallel to the normal direction of the sheet and to the rolling direction of the sheet respectively) [49].

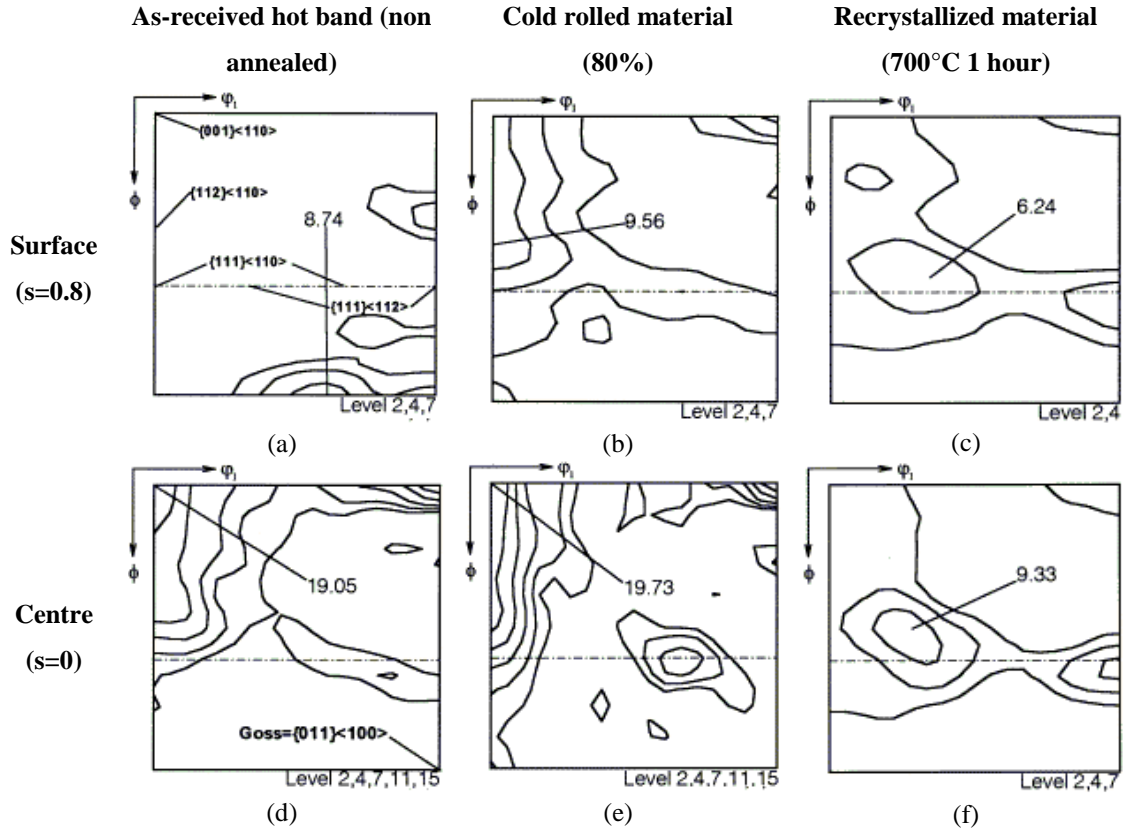


Figure 2.18: Example of texture evolution close to the surface ($s=0.8$) (a)-(c) and at the centre ($s=0$) (d)-(f) of a 17%Cr ferritic stainless steel sheet during cold rolling (80% reduction) and annealing (1h at 700°C), from [17]

As will be seen in the next sections, the through thickness gradients of microstructure and texture in the hot band are responsible for gradients of texture in the cold rolled and annealed product.

2.5.2. Cold Rolling

Upon cold rolling, the already elongated microstructure in the central region of the hot band becomes even more strongly elongated, forming a sort of ‘pancaked’ grain structure [10] [64]. Cold rolling leads to a significant strengthening of the α -fibre in this region with particular strengthening at orientations such as $\{001\}\langle 110\rangle$, $\{112\}\langle 110\rangle$, $\{111\}\langle 110\rangle$ or any combination of these three components. If a γ -fibre exists in the hot band prior to cold rolling, it too will be strengthened upon cold rolling, particularly the $\{111\}\langle 110\rangle$ orientation (e.g. Figure 2.18(e)) [13] [17] [43] [61] [63] [65] [66]. Such texture changes have been previously explained by means of relaxed Taylor calculations,

where relaxation of the shear strains parallel to the rolling plane is assumed [13] [51]. The results of these simulations show that orientations belonging to the α -fibre, while not being stable end orientation, have very low rotation rates.

Similar calculations have also been used for the prediction of the texture changes during cold rolling of the surface layer of the sheet. These reveal that slight deviations from the exact Goss orientation lead to re-orientation towards the $\{111\}\langle 112\rangle$ orientation on the γ -fibre or towards the $\{001\}\langle 110\rangle$ on the α -fibre [13] [51]. Such near-surface textures have been observed, being composed of especially $\{001\}\langle 110\rangle$ or $\{111\}\langle 112\rangle$ orientations (e.g. Figure 2.18(b)) [13] [17] [49] [61] [65].

The effect of total amount of cold rolling reduction on texture has also been studied [153] [10] [13] [51] [63]. It was observed that the intensity of the α -fibre (especially between $\{001\}\langle 110\rangle$ and $\{111\}\langle 110\rangle$) increases with the amount of reduction in all layers, with clear development of maxima at $\{001\}\langle 110\rangle$ and $\{112\}\langle 110\rangle$. Increasing the level of cold rolling deformation also affects the γ -fibre, depending on the position in the thickness. While the intensity of the $\{111\}\langle 110\rangle$ orientation increases in all layers, the intensity of the $\{111\}\langle 112\rangle$ orientation generally decreases towards the sheet centre ($s=0$) and increases in the sub-surface layers ($s=0.8$) [13] [51]. This effect can be explained by the initial texture gradient in the hot band, and the rotation rates of orientations during plane strain compression [13] [51].

As a consequence, following cold-rolling, a highly elongated microstructure is generated with pancake-shaped grains having a strong α -fibre and a weaker γ -fibre intensity [49] [62] [63]. The texture and microstructure gradients initially present in the hot band before cold rolling tend to disappear with cold rolling. Reduction of through thickness heterogeneities is usually associated with lower levels of ridging (c.f. section 2.4) [17] [49]. The remaining difference between the centre and the surface of the cold rolled sheet is the intensity of the α -fibre. It is commonly observed that for a given amount of reduction, the strength of the α -fibre increases from the surface to the centre of the cold rolled sheet (e.g. Figure 2.18(b) and Figure 2.18(e)) [17] [49] [68]. Micro-texture analysis has revealed that the cold rolled sheet consists of a “sandwich” structure where grains having orientations belonging to the α -fibre and grains belonging to the γ -fibre alternate through thickness [62] [63] Figure 2.19). As briefly stated in section 2.4, most

of the work done by EBSD for orientation clustering measurement has been done on the ND plane [37] [43] [44] [46] [49] [69]. Other observations have also been done on the TD plane, where the banded structure is easily observable [43] [62] [63]. However, very little work has been done on the RD plane [36] [43]. The importance of the plane of observation for the characterization of ridging will be returned to later.

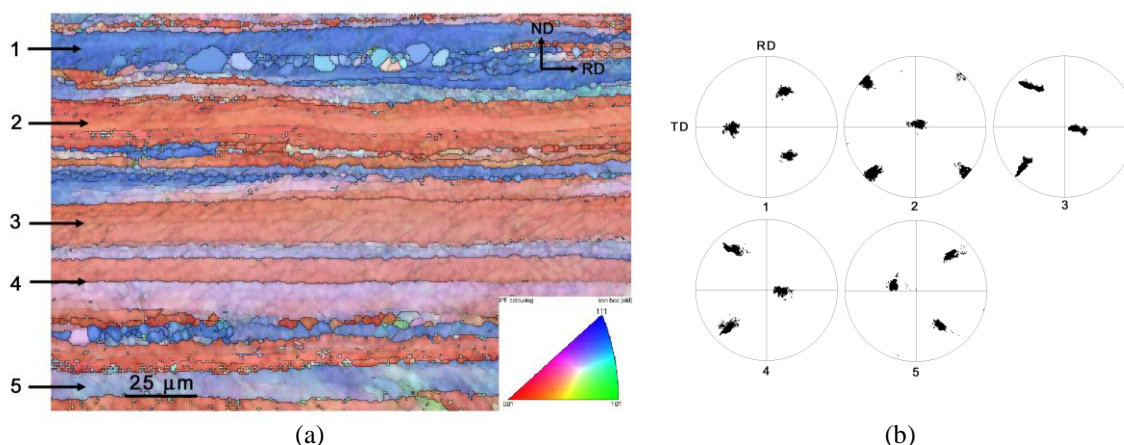


Figure 2.19: (a) EBSD ND Inverse Pole Figure map made on the transverse plane of a cold rolled (50% reduction) and partially annealed (10s at 750°C) 409 grade ferritic stainless steel sheet, and (b) {200} pole Figures corresponding to the selected deformed grains in (a). Results show that deformed γ -fibre grains (blue grains 1= $\{111\}\langle 110\rangle$ and grain 5=close to $\{111\}\langle 110\rangle$) are alternating with deformed α -fibre grains (pink-red grains 2= $\{001\}\langle 110\rangle$, grain 3 and 4=close to $\{112\}\langle 110\rangle$) [63].

It is well known that texture, particularly microtexture, strongly influences the annealing/recrystallization behaviour of cold rolled ferritic stainless steel sheet [40] [53] [70]. Many studies have pointed to the very different microstructures of the α -fibre and γ -fibre type grains as viewed in the optical microscope [20] [54], EBSD [54] [59] [63] [71] [72], transmission electron microscope [55] [63] [73] [74] [75] and with EBSD [63] [76]. Two important points need to be noted; (i) differences in microstructure between different orientations only appear after a critical amount of deformation (e.g. 50% plain strain compression in [72]), and (ii) most of the observations on deformed samples have actually been made on recovered samples, as the quality of EBSD patterns is very poor in the as-deformed state [77]. When recovery is not performed, a correlation between microstructure and texture seems extremely difficult, as grains with similar orientation can exhibit different type of microstructure, and a given type of microstructural feature

can be associated with different orientations [78]. The effect of recovery on microstructure as a function of orientation will be presented in the following section.

In concert with these microstructural studies, more macroscopic measurements by either X-ray diffraction (e.g. [75] [79]) or neutron diffraction (e.g. [80]) have been used in an attempt to assess the ‘stored energy’ of different grain orientations, this ‘stored energy’ being correlated to stored dislocation content and therefore to the recrystallization behaviour of individual grains [9] [74] [75] [81]. The ‘stored energy’ is also often related to the Taylor Factor [82] [83], which gives an indication of the activity of the slip systems of a given grain/orientation. The relationship between orientation (classically along the α -fibre since this is the major fibre generated during cold rolling) and stored energy has been studied by different authors, either by estimating it as a function of subgrain size and misorientation between adjacent cells in the deformed materials [73], or by X-ray or neutron diffraction line broadening [75] [79] [80]. Even though the exact details of the evolution of the stored energy as a function of the orientation are dependent on the method used, some similarities can be noticed. It has been observed that the stored energy increases gradually as the orientation moves away from $\{001\}\langle 110\rangle$ along the α -fibre (increasing Φ angle, going towards $\{110\}\langle 110\rangle$) (Figure 2.20). These experimental measurements have been compared with the predicted evolution of the Taylor factor (M) (calculated by using a fully constrained, plain strain deformation model) [82] [83] where the differences between the trends in the two have been explained by the over simplification of the Taylor model in the case of the deformation of polycrystals due to the assumption of uniform strain in all grains [80]. The very low stored energy of the $\{001\}\langle 110\rangle$ orientation has been attributed to the relatively simple slip system arrangement that allows the imposed plane strain deformation to be accomplished by the operation of as few as two slip systems (see Section 2.4). This appears to correspond, at least qualitatively, with what is found experimentally. Grains oriented near $\{001\}\langle 110\rangle$ tend to exhibit low levels of internal misorientation as measured by EBSD and tend to be highly resistant to recrystallization [63] [84] [85].

The low stored energy of the $\{001\}\langle 110\rangle$ orientation is an important issue as it is proposed to be partly responsible for the sluggish recrystallization behaviour in b.c.c.

steels which can seriously impact the formability, even for low levels of under-recrystallization [62] [77].

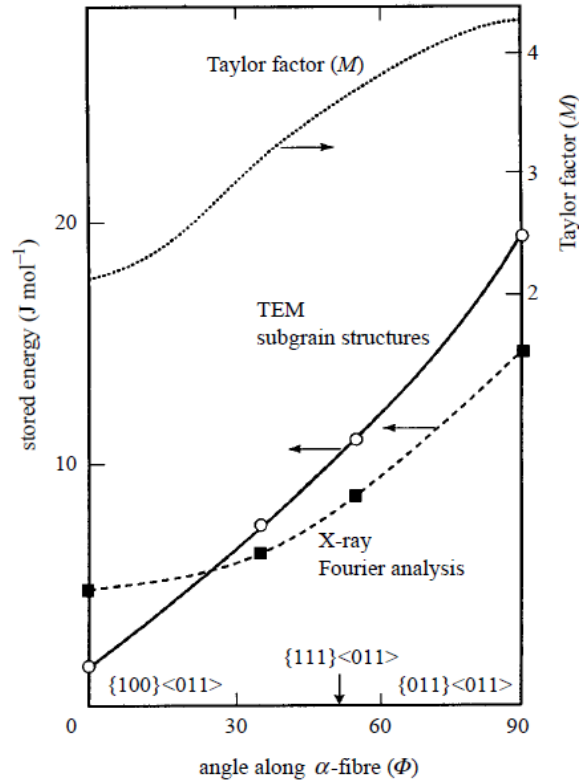


Figure 2.20: Effect of crystallographic orientation along the α -fibre on the stored energy available for recrystallization, measured by different methods: Taylor factor TEM [73]), and X-ray [75]). From [87]. Refer to text for details about the different methods.

2.5.3. Final Annealing of Cold Rolled Sheet

Final annealing is one of the most important ways to control the final microstructure and texture of sheet steels. Final microstructure, texture as well as recrystallization kinetics highly depend on the structure and texture of the deformed material [88]. As mentioned earlier, the substructure of α -fibre and γ -fibre grains are different, this difference being most clearly visible after some amount of recovery has occurred. While the α -fibre grains present a substructure composed of lightly misoriented, large cells often $>2 \mu\text{m}$ in size, the γ -fibre grains are composed of multiple sets of micro-bands forming highly misoriented small cells ranging from $0.2\text{-}2 \mu\text{m}$ in size [59] [63] [77]. Recovered α -fibre grains form subgrains that are elongated along the

rolling direction and constrained by very flat and parallel boundaries [55] [62] [63] (Figure 2.21(a)). Misorientation profiles measured from EBSD maps show that such recovered α -fibre grains generally exhibit low misorientations [54] [59], but that these misorientations can accumulate progressively over long distances parallel to the rolling direction (orientation gradients are estimated to be $0.2\text{-}0.5^\circ/\mu\text{m}$ along the rolling direction in α -fibre grains) [63] [76] [77].

In contrast, recovered γ -fibre orientated grains are composed of smaller, well recovered and roughly equiaxed subgrains that have a more heterogeneous size distribution [55] [54] [63] [77] (Figure 2.21(b)). Misorientation profiles measured across recovered γ -fibre grains reveal a more “chaotic” behaviour compared to α -fibre grains, where point-to-point misorientation often presents large jumps (up to 10°) between adjacent cells [54] [62] [63] [72] [77].

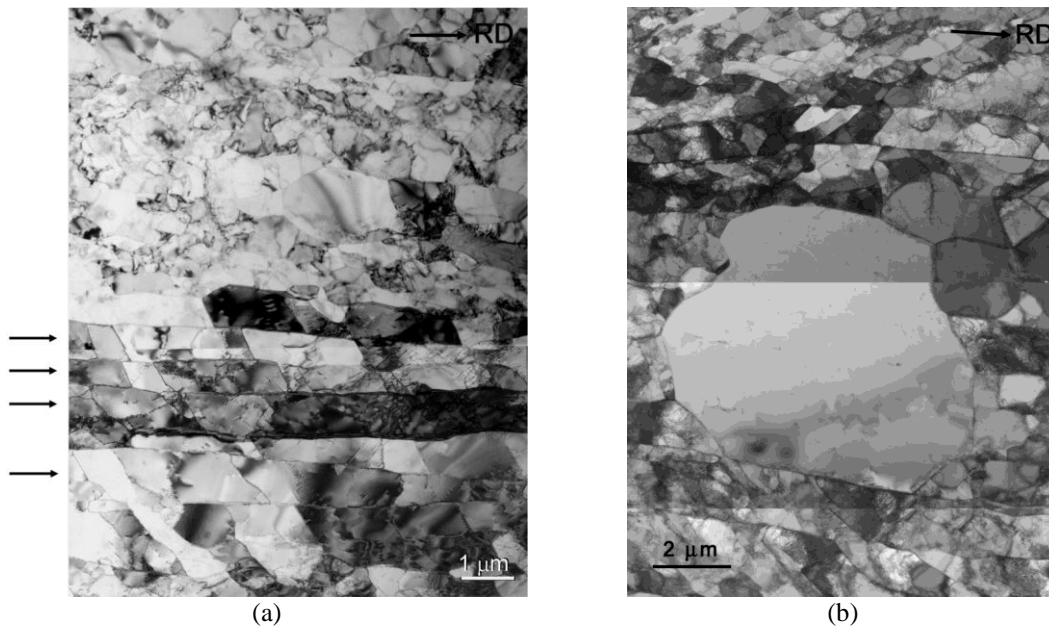


Figure 2.21: Transmission Electron Microscope bright field images from the transverse plane of the sub-structure developed by cold rolling (50% reduction) and recovery (10 seconds at 750°C) of a 409 grade ferritic stainless steel sheet. (a) Homogeneous sub-structure composed of elongated, well aligned cells developed within α -fibre grains (indicated by arrows), and (b) heterogeneous sub-structure showing a nuclei (at the centre) arising from abnormal sub-grain growth and surrounded by equiaxed cells with various sizes inside a deformed γ -fibre grain [63].

Such clear distinctions are not always possible [54], and disagreements on the details of the microstructural features exist in the literature. For instance, Hutchinson [87], referring to the earlier work of Every & Hatherly [75] presented an opposite description of the substructure, where equiaxed cells were associated with α -fibre grains and elongated cells associated with γ -fibre grains. These discrepancies are not easily explained but may point to the importance of the interaction between neighbouring deforming grains during cold rolling.

It was noted above that, from a macroscopic point of view, γ -fibre grains exhibit a high degree of lattice curvature associated with a high stored dislocation density and correspondingly high stored energies. As shown above, this is translated upon recovery into relatively large subgrain-to-subgrain misorientations, particularly when contrasted with the α -fibre grains that are reported to have low stored energy. This view is also consistent with the larger range of subgrain size observed in the γ -fibre oriented regions. Both of these factors provide favourable conditions for the ‘nucleation’ of recrystallized grains by means of abnormal subgrain growth⁴ [17] [63] [68] [166]. The α -fibre grains, having a low stored energy and low subgrain-to-subgrain size spread, have been reported to undergo recrystallization ‘nucleation’ by strain induced boundary migration (SIBM) at the interface between α -fibre and γ -fibre grains [57] [59] [63] [76]. Recrystallization proceeds with the growth of these new nuclei within the deformed γ -grains by the consumption of neighbouring cells, reducing the overall stored energy of the material [10] [55]. There seems, however, to be no specific growth advantage for special orientations in this stage of recrystallization [57] [89], and the effect of this phenomenon seems limited compared to the abnormal sub-grain growth happening in γ -fibre grains.

Due to the pancaked grain morphology of heavily cold rolled ferritic stainless steels, there is a physical separation between the α -fibre and γ -fibre grains. At intermediate stages of recrystallization (such as represented in Figure 2.22) this can lead to a drastic slowing of the recrystallization as the growth of recrystallized γ -fibre grains (particularly those close to $\{111\}\langle 112\rangle$ and $\{111\}\langle 110\rangle$) slows at α -fibre/ γ -fibre

⁴ The oriented nucleation has also been observed in other b.c.c. steels and has been proposed as the main mechanism responsible for recrystallization in these materials [53] [55] [57] [73] [83] [86] [90].

interfaces leading to the so-called “sluggish” recrystallization kinetics classically observed in ferritic steels [56] [62] [63] [71] [90] [91].

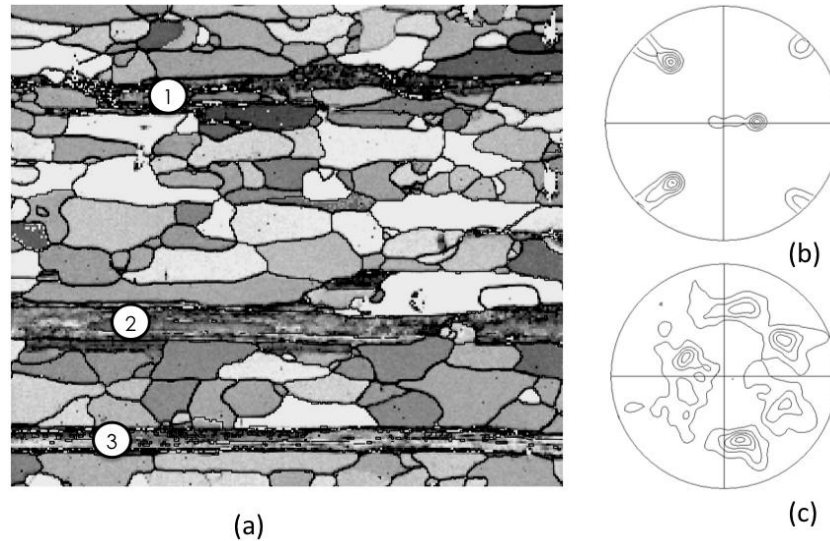


Figure 2.22: (a) Band contrast EBSD map of a partially recrystallized Ti-stabilized 409 ferritic stainless steel after cold rolling to 50% reduction and annealed at 700°C for 200s. Unrecrystallized grains 1, 2 and 3 belongs to the α -fibre (close to $\{001\}\langle 110\rangle$ as shown on (b) the $\{100\}$ pole Figure from unrecrystallized regions. (c) is the $\{100\}$ pole Figure of the recrystallized grains exhibiting γ -fibre orientations [93].

This slowing has been attributed to three factors; the flat nature of these interfaces [92], the low stored energy in the α -fibre grains [56] [77] [71] and the role of precipitates lying on the α -fibre/ γ -fibre boundaries [63] that act as pinning sites for the migrating interfaces. This slowing of the recrystallization is clearly observed in the macroscopic kinetics of recrystallization, this being seen clearly when viewed in a JMAK plot [62] [63]. This has been examined both experimentally and by means of modelling [92] [93]. In these studies it has been shown that the particular microstructural topology in the α -fibre and γ -fibre grains can play a significant role on the recrystallization kinetics.

As a consequence of the processes described above, the fully recrystallized material is characterized by a strengthened γ -fibre and weakened α -fibre compared to the cold rolled state [13] [17] [60] [62] [63] [67]. The intensity of the γ -fibre has been shown to increase with increasing amount of rolling reduction [63] [66] [76]. In the case of

stabilized ferritic stainless steels and IF-steels, the maximum texture intensity is found to be located between the γ -fibre and α -fibre, on a shifted γ -fibre where orientations are described as $\{334\}\langle 483\rangle$, $\{554\}\langle 225\rangle$, $\{557\}\langle 583\rangle$ or $\{223\}\langle 582\rangle$ [13] [17] [51] [60] [62] [65] [68]. Raabe has attempted to explain the development of this shifted texture based on a selective particle drag model [13] [65]. During annealing, there is a competition between the retarding force applied on the moving grain boundary by small particles (Zener effect), which is proportional to the grain boundary energy⁵, and the driving force for recrystallization (reduction of stored energy). For ferritic stainless steels the deformed grains (mainly composed of $\{112\}\langle 110\rangle$) are replaced by recrystallized grains having orientations close to the γ -fibre. In the particular case of recrystallized orientations on the shifted γ -fibre mentioned above, these orientations are close to having a misorientation of 27° $\langle 110\rangle$ with the average deformed texture of $\{112\}\langle 110\rangle$, which is a coincidence site boundary ($\Sigma 19a$) thought to have a low energy [64]. Because the retarding force exerted by a particle is directly proportional to the energy of the boundary, Raabe has argued that in the case of these orientations on the shifted γ -fibre, the Zener drag force would be smaller than the driving force for recrystallization. As a consequence, these orientations having coincident boundaries present a “favourable” configuration for growth. This is of interest in the case of ridging as the orientations on the shifted γ -fibre lie in region of high shearing tendency, as can be seen in Figure 2.14(b).

While the description above has focused on the bulk texture and its relation to recrystallization, detailed EBSD observations made on the fully recrystallized material show that the major texture components are not randomly distributed in space within the material. Instead, there is a tendency to form bands along the rolling direction where grains belonging to the γ -fibre alternate on the ND plane with bands of grains whose orientations are more random but globally close to the α -fibre [27] [37] [43]. This was clearly illustrated in Figure 2.12, which showed the correspondence between clusters of γ -fibre oriented grains and etch pits on the ND surface of a fully recrystallized 409

⁵ Classically, the Zener retarding pressure is given by $P_z = \frac{3 \cdot \gamma(g) \cdot f}{2 \cdot r}$, where $\gamma(g)$ is the grain boundary energy, f is the volume fraction of stable particles, and r is the average particle radius.

stainless steel. While this clustering has been widely reported in the literature [17] [20] [21] [27] [36] [37] [44] there have been few studies that have aimed to explain how this non-random spatial distribution of grains with certain orientations is influenced by the processing conditions. Moreover, while it is known that the clusters are revealed if EBSD data is partitioned based on γ -fibre vs non γ -fibre oriented grains this is only a relatively coarse description. Given that some γ -fibre orientations have a high shearing intensity while others have a low (or no) shearing tendency it is necessary to be able to further specify the makeup of these clusters if their relation to ridging is to be fully characterized.

2.5.4. Practical Routes for Reducing Ridging via Process

Control During Cold Rolling and Annealing

Many previous attempts have been made to reduce ridging by changing the final microstructure of ferritic stainless steel sheet during cold rolling and annealing. In most cases these attempts have focused on approaches that change the bulk texture of the material and/or eliminate the ‘orientation clusters’ described above.

One method that has been shown to be capable of changing the as-rolled texture and microstructure is strain path changes. For example, Huh et al. [49] showed that changing the rolling direction by 45° during hot rolling led to significant changes in the texture and microtexture of the final sheet following cold rolling and annealing. It was found that a much weaker cold rolled texture was developed in this case, having a particularly weak α -fibre (compared to the classically cold rolled material). After the final annealing treatment, the sheet exhibited a weaker and more uniform γ -fibre compared to the conventionally cold rolled material. This process also led to a change of the microtexture as evidenced by a significantly reduced surface roughness measured following tensile testing of the final sheet material.

Another method that has been shown to be effective at reducing or even eliminating ridging is to cold roll starting from a two-phase microstructure. While stabilized ferritic stainless steel grades are fully ferritic at all temperatures, unstabilized grades (e.g. AISI 430) have a two-phase mix of austenite and ferrite at elevated temperature. If the material is quenched from a sufficiently high temperature a mix of ferrite and martensite is formed. While such a dual-phase microstructure is often found in

the hot band of unstabilized ferritic grades, hot band annealing prior to cold rolling removes the martensite replacing it with a mix of ferrite and carbides [69]. If, however, the ferrite-martensite mix is retained and cold rolled one finds a very different microstructure and texture in the final product. In this case the martensite acts as hard ‘particles’ leading to significant local misorientations developed at the ferrite-martensite interfaces [69]. Upon annealing this leads to particle stimulated recrystallization [64] [69] at the ferrite-martensite interface. This process results in (i) the breaking up of the elongated microstructure typical of the hot band and (ii) a much more random bulk texture owing to the particle stimulated nucleation [69] [94]. As a consequence, ridging can be made to be extremely low in such materials if the distribution of martensite is homogeneous [95].

One strong argument against processes like cross-rolling or martensite-ferrite rolling for ridging control is that they both result in an overall weakening of the recrystallized γ -fibre texture. As mentioned earlier, a strong, uniform γ -fibre is highly desirable in ferritic steels as it gives rise to a high Lankford parameter, low in-plane anisotropy and correspondingly a high deep drawing capability [10] [11] [17]. Already, ferritic stainless steels tend to have a weaker γ -fibre and therefore lower formability compared with low carbon steels with whom they compete in many applications.

A processing route that can improve both the formability and ridging performance of ferritic stainless steels involves the use of intermediate annealing steps between cold rolling passes. This leads to a reduction of the sharpness of the final texture and shifts the most prominent orientation from the shifted γ -fibre (e.g. $\{223\}\langle 582\rangle$) towards a more uniform and strong γ -fibre [17]. The change in texture depends on exactly the number of rolling and annealing steps performed and how much strain is imposed between each annealing step [96]. While this process was mainly investigated as a way of improving the texture for highly formable steels it was also found to be very effective at reducing or eliminating ridging [17]. In this case one can understand that the multiple rolling and annealing steps helps to break-up the bands apparent on traditionally one-step cold rolled and annealed sheet. This suggests that the bands themselves are not generated by recrystallization but instead, that recrystallization tends to randomize the spatial distribution of orientations in the final product.

From an industrial point of view, increasing the number of processing steps by having several cold rolling and annealing steps is not particularly attractive given the additional cost of adding these extra steps. There remains, therefore, a desire to find ways of modifying the classical one-step cold rolling and annealing process to reduce ridging. What the above experiments suggest, however, is that cold rolling and annealing are likely not the origins of ‘clusters’ and ridging. Instead it appears that this process can reduce ‘clustering’ and ridging, though their efficiency at doing this appears to be low during classical processing. Furthermore this suggests that to find the ultimate origins of ridging one should look further upstream at the processes of hot rolling and casting.

2.5.5. Casting

As mentioned above, after the downstream processes of cold rolling and final annealing, bands of grains with similar orientations are observed in the ND plane of the sheet. The dimensions of these bands (about 100-200 μm along the TD) are, however, at least one order of magnitude smaller than the observed wavelength of the corrugations associated with ridging (1-5 mm). It has also been shown (section 2.4) that grains with a similar tendency for out-of-plane shearing during stretching cluster together. The dimension of these bands resembles more closely the dimensions of the corrugations observed during ridging.

Ridging has been observed, however, on sheet directly after hot rolling (hot band) before cold rolling and annealing [97]. This observation suggests that the microstructural features that cause ridging are actually present before cold rolling and annealing. With this in mind, it is important to examine the microstructure and texture evolution during the upstream processes of casting and hot rolling to understand the origins of the features leading to ridging.

During casting, liquid metal is solidified into the form of a large slab having a thickness of around 200 mm (see Figure 2.23) [98]. Different types of casting exist, among which the more common are ingot casting and continuous casting [6]. As continuous casting allows for low-cost continuous production of slab, it is the most widely used method for casting. For this reason the microstructure and texture evolution during continuous casting will be focussed on in this section.

During continuous casting liquid metal is poured into a cooled mould. At contact the liquid metal starts solidifying, forming a solid skin or shell composed of small equiaxed recrystallized grains with diameter of about 500 μm [99]. Between the two solid shells, the liquid metal is subjected to thermal gradients that favour the formation of columnar grains by favoured growth of the dendrites perpendicular to the length of the slab. It is observed that the columnar grains formed close to the surfaces are strongly textured with a $\langle 001 \rangle$ direction parallel to the column direction (a so-called $\{001\} \langle uvw \rangle$ fibre) [43] [85] [99] [100]. Columnar grains can be as long as several centimetres [99] [101] and their diameter largely varies from 450 μm [84] [85] [100] to a couple of millimetres [99]. With further solidification, nucleation of new grains starts towards the centre of the slab creating a more isotropic microstructure composed of equiaxed grains [102]. The size of equiaxed grains usually reaches a couple of millimetres [99] [103]. It is important to note the similarities between the cast grain size, both in the equiaxed and columnar regions, and the characteristic dimensions of the corrugations in ridging (especially the wavelength which is around 1-5mm), this has been used to suggest a possible connection between these two phenomena [27] [69] [104]. The fact that so many processing steps exist between casting and the final product, however, makes this a very speculative hypothesis. Experimental measurements of the texture in the equiaxed central layers of continuously cast ferritic stainless steels revealed that the texture is very weak and almost random [99] [103]. Reappearance of columnar grains among the equiaxed region is also commonly observed in ferritic stainless steels [105] [106]. The origin of these secondary columnar grains is explained by the absence of magnetic stirring in certain regions of the slab [105] or by crystal sedimentation where recrystallized grains “fall” by gravity and accumulate in the lower region of the slab [106]. This results in an asymmetric grain structure with regard to the centre line. A typical microstructure of the slab is represented in Figure 2.23.

The presence of the secondary columnar grains within the equiaxed region is an additional source of heterogeneity, which, as will be showed later (section 7.2), is detrimental for the appearance of ridging.

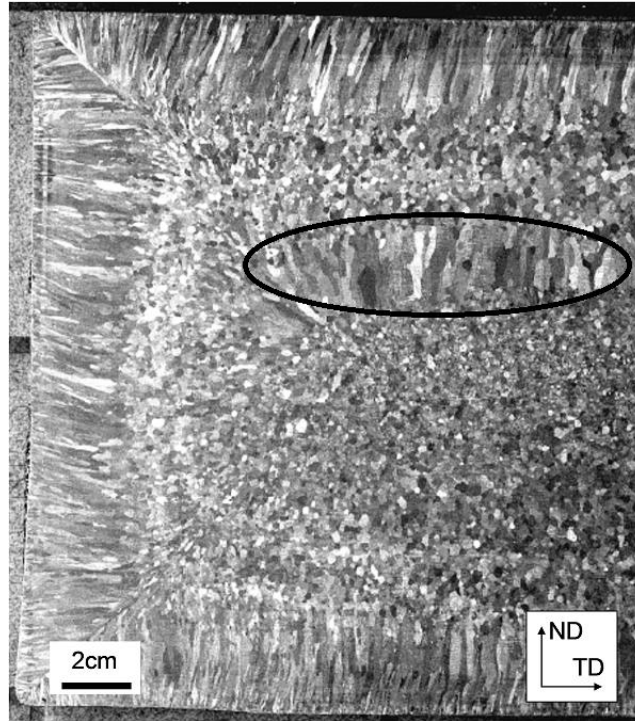


Figure 2.23: Structure of a continuously cast slab (445 grade Ferritic Stainless Steel) showing the presence of large columnar grains near the surface, growing along the normal directions to the surfaces and equiaxed and smaller grains in the centre region. Secondary columnar grains within the equiaxed region are also visible. Picture courtesy of Aperam.

2.5.6. Hot Rolling

Hot rolling is typically composed of two consecutive steps (see Figure 2.16). The first step, roughing, involves the first rolling passes of the as-cast slab and consists of a small number of passes with high amount of deformation per pass. During roughing, the temperature decreases from approximately 1250°C to 1050°C due to air cooling. After roughing, the ‘transfer bar’ is about 40 mm thick and undergoes the finishing step of hot rolling to reach a final thickness of about 3-5 mm. After passing the finishing mills, the hot band has cooled down to about 900°C and is further quenched to 700-750°C before being coiled [98].

Because the temperature during roughing is well above the recrystallization temperature, continuous dynamic recrystallization is expected [64]. It is very difficult to experimentally follow the microstructure and texture evolution during industrial hot rolling, as it is practically impossible to obtain samples other than at the end of roughing and finishing. Most of the literature on hot rolling is therefore based on laboratory

experiments using different conditions than those used industrially. For instance, the inter-pass conditions can be significantly different, leading to a change in thermal history that can affect recrystallization behaviour. Additional reheating in-between passes can thus be necessary in the laboratory, affecting the global microstructure and texture evolution. While there is no literature that quantitatively describes the differences between industrial processing and laboratory processing, Pouillard et al. [107] noted that laboratory processing tends to generally result in weaker roping compared to what is observed after industrial processing.

The surface of the sheet during hot rolling is subjected to strong friction due to the contact with the rolls and is consequently deformed significantly in shear [51]. Because of the lower temperature caused by the contact with the mills, thermal transfer with ambient air and simultaneous water cooling, dynamic recovery is lower near-surface and the stored energy and dislocation density is higher [13]. The combined effect of high dislocation density and low recovery leads to recrystallization of the surface layers during the final passes. The resulting texture is weak with a slight preference for the formation of $\{110\}\langle 001\rangle$ -Goss and $\{112\}\langle 111\rangle$ texture components [13] [19] [50] [51] [61].

The central portion of the hot rolled product has a very different behaviour. The deformation mode can be approximated to plane strain compression (similar to the case of cold rolling) [50] [51]. As the temperature is higher compared to the surface of the sheet, extensive recovery takes place [13]. As mentioned in section 2.1 unlike carbon steels, no austenite-ferrite phase transformation takes place during hot rolling. As a result, the microstructure generated during hot rolling at the centre of the sheet is composed of extremely elongated and pancake shaped grains [13]. As mentioned at the beginning of the Section 2.5.1 (see Figure 2.17), these unrecrystallized grains have a strong α -fibre, with a maximum intensity close to $\{001\}\langle 110\rangle$ and spreading towards $\{112\}\langle 110\rangle$, accompanied by a weak γ -fibre [13] [50] [51] [61]. This maximum intensity close to $\{001\}\langle 110\rangle$ has been previously explained to arise from the $\{001\}\langle uvw\rangle$ columnar grains from the cast material, these grains not being replaced by new grains during phase transformation or recrystallization [50] [99].

A more careful study of the behaviour of columnar and equiaxed grains during deformation reveals that the presence of columnar grains are especially detrimental for

ridging [27] [108]. Indeed, samples cut from columnar regions of a slab systematically exhibit a higher degree of ridging after hot rolling, cold rolling and annealing compared to samples cut from the equiaxed region of the slab. This result has been explained as the consequence of a strong $\{001\}\langle 110\rangle$ component arising from the cast $\{001\}\langle uvw\rangle$ fibre texture in the columnar structure of the slab [108]. As mentioned in section 2.5.2, the $\{001\}\langle 110\rangle$ orientation is very stable during deformation and, most importantly, during annealing. As a result, grains coming from the columnar regions of the slab will generate extremely elongated grains that are hard to recrystallize, these therefore having a high probability of remaining throughout the whole process. This results in a more banded structure in the final product, and consequently higher level of ridging [43].

For this reason, different solutions have been proposed to limit the fraction of columnar grains in the slab. Other solutions aimed at reducing the formation of elongated grains before cold rolling, mainly by favouring recrystallization of the hot band. These will be discussed in the next section.

2.5.7. Practical Routes for Reducing Ridging via Process Control During Casting and Hot Rolling

One of the most efficient and commonly used methods to reduce the volume fraction of columnar grains is electro-magnetic stirring during casting [109]. Electro-magnetic stirring results in a more uniform cast microstructure by inducing a rotational flow of the liquid metal, favouring the nucleation of equiaxed grains at the expense of columnar grains. A detailed description of the forces and motions generated by magnetic stirring are described in [109] while various explanations for the preferential formation of equiaxed grains can be found in [110] [111] [112] [113].

It has been observed that the fraction of equiaxed grains increases with increasing stirring intensity (e.g. Figure 2.24(a)), and correspondingly a decrease in ridging amplitude was reported (e.g. Figure 2.24(b)) [114] [115]. Ridging is not, however, completely prevented by a fully equiaxed slab, as shown on Figure 2.24(b). The ridging amplitude decreasing with increasing fraction of equiaxed grains up to 60-70% of equiaxed grains. Beyond this the amplitude of ridging saturates towards a non-zero

minimum value. It is also seen that the effect of stirring intensity is amplified and helped by the superheat ($\Delta T(^{\circ}\text{C})$).

Not only does the electromagnetic stirring decrease the fraction of columnar grains, it also decreases the size of the equiaxed grains [116]. Decreasing the size of initial grains in the slab is beneficial in the case of ridging as it limits the maximum size of grains throughout the downstream processes of rolling and annealing.

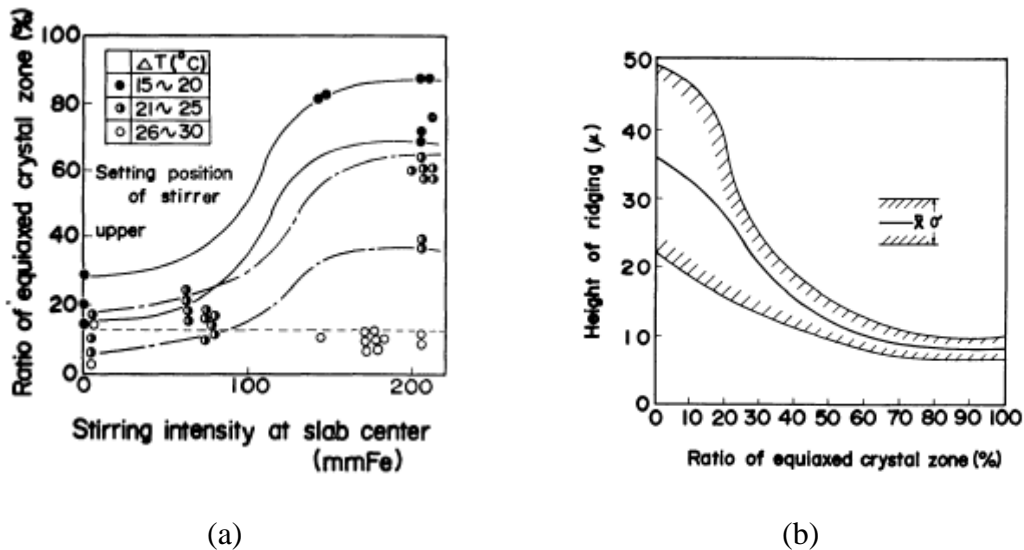


Figure 2.24: (a) Effect of stirring intensity on ratio of the size of the equiaxed grains zone, and (b) corresponding effect on ridging amplitude [114].

It is interesting to note (Figure 2.24) that a complementary effect to electromagnetic stirring arises from changes to the superheat temperature. The superheat temperature is defined by the difference between the temperature of the molten steel and the liquidus temperature. It is found that the lower the superheat, the higher the ratio of equiaxed to columnar grains [114]. The optimum slab microstructure (minimum fraction of columnar grains) is obtained with a combination of low superheat temperature and high stirring intensity [105] [113] [114].

Another effective way of promoting a large fraction of equiaxed grains in the slab is by heterogeneous nucleation by precipitation in the liquid. Experimentally, it was observed that increasing the amount of titanium from 0.1 wt.% to 0.4 wt.% in a 430 ferritic stainless steel) increased the equiaxed grain fraction from 21% to 69% [117].

Titanium is known for its affinity with carbon and nitrogen [118] [119] [120], with which it creates very stable Ti(C,N) precipitates at high temperature. Thermodynamic calculations have shown that the formation of TiN occurs at high temperature, when the metal is still liquid [67] [117]. Titanium nitride precipitates serve as heterogeneous nucleation sites, leading to the formation of an equiaxed grain structure when they are homogeneously distributed within the slab. Homogeneous distribution of titanium nitride within the molten steel is favoured by electro-magnetic stirring [114]. Similar results have been observed with the addition of a Fe-Ti-N master alloy [121]. In this case, an addition of 2.5 wt.% of the master alloy in a classical 409 Ferritic stainless steel has raised the fraction of equiaxed grains from 14% to 100%, while decreasing the slab grain size from 1500 μm to 300 μm .

Other secondary parameters also effect the formation and growth of columnar or equiaxed grains. These parameters include, but are not limited to casting speed, stirring mode and position of the stirrer. Attempting to control the microstructure in this way is, complex, however, as interactions exist between all these parameters. A clear and concise summary of these inter-relationships can be found in [114].

Compared with more common non-stainless low carbon steels, extra-low carbon and interstitial free (IF) steels, the lack of phase transformation during hot rolling of ferritic stainless steels results in the formation and retention of hard to recrystallize α -fibre grains, especially those having orientations close to $\{001\}\langle 110 \rangle$. Because of the potential for significant recovery during hot rolling and coiling, the level of stored energy remaining to drive recrystallization of the hot rolled sheet is low. In addition, phase transformation, by introducing new grains with different orientations, tends to randomize the spatial distribution of orientations and disrupt the elongations of features [10]. During cold rolling, this elongated microstructure is further accentuated. To promote the breakdown of the elongated hot rolled microstructure prior to cold rolling, researchers have investigated lowering the hot rolling finishing temperature [122] [123]. When low finishing temperatures are coupled with hot band annealing, recrystallization of the α -fibre grains can be achieved leading to a weakening of the texture [124] and a reduction of the elongation of the microstructure in the hot band [60] [107] [122]. A recrystallized

hot band allows for a weaker α -fibre, finer microstructure and more uniform γ -fibre after cold rolling and final annealing [60]. Ultimately, this results in a final recrystallized condition having a better formability [60] and lower ridging [107] [122] [124] [125].

Another route examined as a way to modify the micro-texture of the hot band is asymmetric rolling. Asymmetric rolling involves a mill having rolls operating at different speeds or having different roll diameters [126] [127] [128]. This asymmetry leads to a change in the strain path and thus a change in the texture formation [127]. Asymmetric rolling introduces extra shear components in the plane of rolling and in the direction of rolling [128] which can cover the whole thickness of the sheet, as observed both by texture measurements through thickness and by observation of deformed markers introduced in the sheet [129] [130]. The introduction of shear deformation throughout the whole thickness has been shown to lead to faster recrystallization of ferritic stainless hot band and the formation of a strong γ -fibre [130]. It results in a final product presenting a refined and homogeneous microstructure with improved formability, especially if the sheet is rotated 180° around the RD between passes [127] [130], though this is not very practical under industrial conditions.

2.6. Effect of Chemical Composition on Microstructure, Texture and Ridging

2.6.1. Introduction

The previous sections have focused on describing how the different processing steps involved in the production of ferritic stainless steel sheet can impact on the presence of clusters of grains having the correct deformation tendency and spatial correlation to explain the phenomenon of ridging. It is also known that the microstructure and texture of sheet products are strongly influenced by chemical composition. While the effects of individual alloying elements are relatively straightforward to examine in simple binary alloys, their role in highly alloyed steels is much more complex as synergistic effects between elements are common. In this section, the main effects of the alloying elements common to the ferritic stainless steels studied in this thesis (chromium, carbon and the

stabilizing elements niobium and titanium, see Table 2.2) are discussed in relation to their potential effects on ridging.

Table 2.2: Typical composition range and effect of alloying elements in Ferritic Stainless Steels. From [4] and [6].

Element	C	Cr	Ti	Nb
Range (wt.%)	0.02-0.75	11-29	0.1-1	
Effect	Stabilizes austenite.	Stabilizes ferrite. Increases corrosion resistance.	Stabilize ferrite. Prevent sensitization. Improve functional properties (formability, high temperature strength, creep properties).	

2.6.2. Effect of Carbon

In the case of non-stabilized ferritic stainless steels (e.g. AISI 430) an increase in carbon content has been shown to drastically decrease ridging amplitude (Figure 2.25) [107]. By increasing the carbon in ferritic stainless steels a reduction of the intensity of the hard to recrystallize $\{001\}\langle 110 \rangle$ component of the hot rolled texture was observed. As noted above, this texture component tends to be associated with the retention of the highly elongated aspect of the hot rolled microstructure. It was proposed that the beneficial addition of carbon was due to the stabilization of the austenite phase (see Figure 2.1(b)) leading to partial phase transformation during hot rolling [122]. The formation of austenite with higher strength than ferrite [131] leads to inhomogeneous strain partitioning during rolling. The extra strain carried by the ferrite can promote dynamic recrystallization and break down the elongated structure generated during hot rolling [69].

The beneficial effects of carbon on ridging and recrystallization are, however, generally counterbalanced by a loss of formability [10] [132]. Carbon, both in solid solution and in the form of carbide precipitates, suppresses the formation of a sharp $\{111\}$ //ND texture during annealing. As has been previously discussed, this is highly advantageous for high deep drawing [10].

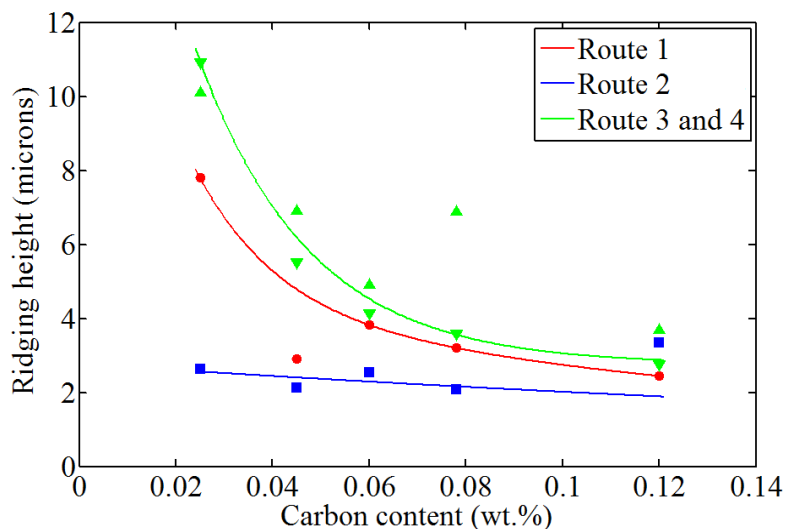


Figure 2.25: Effect of carbon in solid solution on ridging height, as a function of the processing route defined in [107]. The severity of ridging decreases for every route when the carbon content is increased.

2.6.3. Effect of Chromium

Chromium content also illustrates complex interactions between chemistry, processing and microstructure. When hot rolling is performed with long inter-pass times in order to promote recrystallization, it was observed that ridging was decreased with increased chromium additions. When the slab is classically hot rolled (with short inter-pass time), the effect of chromium was less clear, though a slight tendency for increasing ridging height with chromium addition was observed [107]. Such contradictory results are difficult to interpret, and were not explained by the authors. One must be careful of drawing direct conclusions in this case.

Historically ridging was thought to be due to segregation, with chromium being particularly responsible [34] [35] [133] [134] due to observed etching patterns caused by segregation patterns⁶. The direct link between chromium segregation and ridging has largely been dismissed however [34], in favour of the idea that if an effect exists it likely has more to do with the effects of segregation on limiting or suppressing the recrystallization of hard-to-recrystallize cube of face ($\{001\}\langle 110\rangle$) orientations [34].

⁶ In the works from Suzuki et al., the banding observed was denominated 'stripe pattern', and is caused by the difference in corrosion resistance due to Cr segregation

2.6.4. Effect of Titanium and Niobium

Additional alloying elements are classically added to the steel to modify mechanical properties and to improve the welding properties and the corrosion resistance [135]. As observed in [134] the depletion of chromium caused by precipitation of carbides at grain boundaries is responsible for a decrease of inter-granular corrosion (IGC) resistance known as sensitization [136] [137]. To prevent sensitization, the amount of carbon in solid solution needs to be reduced, either by reducing the total net amount of carbon, or by introducing stabilizing elements such as titanium and niobium [137]. These elements preferentially form carbonitrides ($\text{Ti}(\text{C},\text{N})$ and $\text{Nb}(\text{C},\text{N})$) which are thermodynamically more stable than $\text{Cr}(\text{C},\text{N})$. As a consequence, chromium is left in solution and the corrosion resistance is increased.

Additions of stabilizing elements are also beneficial for the formability of the sheet, a detailed review being given by [10]. It has been shown that both the addition of Nb [138] and Ti [139] improved the plastic strain ratio (or Lankford coefficient r) by favouring a more intense and uniform γ -fibre in the final product. The effect of stabilizing elements on texture evolution is relatively complex and depends on whether the element is in solid solution, favouring the ideal γ -fibre [138] [139], or in the form of precipitates that favour the appearance of high index orientations that are detrimental in terms of ridging [65].

The addition of Ti, as mentioned in section 2.5.7, also effects ridging by promoting the nucleation of stable precipitates in the liquid during casting. These act as heterogeneous nucleation sites leading to an expansion of the equiaxed zone in the slab, and to a reduction of ridging in the final product.

Although the addition of stabilizing elements is beneficial for the refinement of the initial structure, for the IGC behaviour and for the formability of the final product, they have been shown to have a negative effect on recrystallization kinetics in the final product. They lead to a slowing of recrystallization and grain growth [146-148] due to Zener pinning and solute drag. This can lead to under-recrystallization and

misinterpretation of the effect of alloying elements on formability⁷ [140]. Under-recrystallization can significantly effect ridging as it is known that the last grains to recrystallize belong to the α -fibre where the out-of-plane shearing tendency is high (see section 2.5.3).

2.7. Summary of the Literature Review

The main characteristics of ridging in ferritic stainless steels have been reviewed in relation to the microstructural features that have been associated with it in the past. Microstructure and texture evolution during cold rolling and annealing in these steels are now relatively well known, but their effect and relationship to the formation and evolution of ‘clusters’ is unclear. The term ‘cluster’ has been used to define elongated features having either a similar orientation or a similar deformation behaviour, but no clear definition has even been given. The lack of a clear definition is most likely the reason why no description of the correlation between microstructural observations and the formation of ridges at the surface of the sheet during deformation has been made. Furthermore, no tool developed so far has been able to give a fully quantitative prediction of both the amplitude and the wavelength of the corrugation for a given microstructure.

⁷ The observed lower Lankford coefficient in the work of [140] has been attributed to the addition of niobium. The actual reason should, however, be attributed to the fact that the sheet was not fully recrystallized, as explained by [138]

Chapter 3: Scope and Objectives

The literature review has shown that there is a common idea that some form of microstructural heterogeneity, often vaguely referred to as ‘clustering’, is responsible for the phenomenon of ridging. While this idea is broadly applied in the literature, there isn’t a clear definition or description which can be used to identify such ‘clusters’ in real materials. The objective of this thesis is to quantify the non-random distribution of microstructural features responsible for ridging and to relate the processing history of the material to the mechanical and spatial characteristics of this non-randomness. Starting from the hypothesis that this non-random distribution is related to a collective mechanical response of groups of grains, as illustrated originally by the simplified model of Takechi, evidence of such behaviour in real and idealized microstructures will be sought.

As a starting point, real experimental microstructures (two-dimensional sections) will be used as input to a crystal plasticity simulation tool that allows for large scale, spatially resolved calculations and therefore a direct prediction of both local strains as well as surface roughness. Using these results it is possible to observe and quantify the connection between the behaviour of a single grain and the collective behaviour of many grains to give the overall surface roughness profile. To test hypotheses about the connection between local and global behaviour, idealized microstructures will also be produced and simulated.

From these results, a better understanding of the heterogeneities responsible for ridging will be obtained. This will be used to identify the formation of the non-random distribution of orientations and mechanical behaviours during the annealing of cold rolled sheet product, simulating the last stage of industrial processing. These experiments will look at the effects of annealing temperature and time as well as the effect of cold rolling reduction. One industrial steel grade will be examined starting from two hot rolled states.

Finally, a brief discussion will be given to the potential effect of modifying upstream processing (casting and hot rolling) on the susceptibility of the material to ridging. Here a small number of experimental observations are combined with crystal plasticity simulations to give some ideas for future directions of process modification to reduce ridging.

Chapter 4: Experimental Procedure and As-Received Materials

4.1. Methodology for Materials Characterization

4.1.1. Optical Microscopy and Measurement of Recrystallized Fraction

Since one of the objectives of this thesis is to evaluate the effect of annealing on the evolution of microstructure, one needs to be able to evaluate the fraction recrystallized. The majority of fraction recrystallized measurements were made using optical microscopy. Samples were prepared for optical metallography by mechanically grinding the surface with SiC emery paper to 1200 grit followed by a final polishing using 6 μm and 1 μm diamond paste. The polished surface was then electrochemically etched in nitric acid (68%) at room temperature with a current density of $\sim 400 \text{ mA/cm}^2$ (1.2V) for about 30s to reveal the grain boundaries. Following electrochemical etching, the sample was rinsed under running water and then cleaned in an ultrasonic bath of denatured alcohol. Micrographs were taken using a Nikon EPIPHOT 300 series inverted microscope equipped with a digital camera.

The fraction recrystallized was determined from optical micrographs on the transverse plane (containing the RD and ND directions) over the full thickness of the sheet using the point counting method defined by ASTM E562-11. In order to have sufficient statistics (between 5 and 20 fields of observation according to the norm), the fraction recrystallized was calculated on multiple regions covering the full thickness and a minimum of 1.5 mm along RD.

4.1.2. Scanning Electron Microscopy and EBSD (Electron Backscattered Diffraction)

Samples for backscattered images and EBSD analysis were prepared following the mechanical polishing procedure described above. Electropolishing was then performed using 95 vol.% acetic acid and 5 vol.% perchloric acid at room temperature.

Electropolishing was performed with a current density of $\sim 50 \text{ mA/cm}^2$ (15V) for about 45 seconds. The sample was then rinsed under running water and in an ultrasonic bath of denatured alcohol. Back scattered electron (BSE) imaging was performed in a Hitachi S-570 Scanning Electron Microscope while EBSD measurements were performed using either:

- A Tescan Mira3 XMU Field Emission Scanning Electron Microscope equipped with the EBSD system Oxford AZtecHKL (HKNordlysMax² EBSD detector)
- A Zeiss Sigma VP Field Emission Scanning Electron Microscope equipped with the DigiView IV EBSD Camera and combined with the Orientation Imaging Microscopy (OIM) Data Analysis software.

All EBSD measurements were made on a regular square grid and data post-processing was performed using TSL OIM Analysis 6 software. The as-measured data were cleaned using a single step grain dilation. A grain was defined as a group of EBSD points containing at least five pixels distributed in at least two rows and separated by a grain boundary, defined by a misorientation of more than 5° between adjacent pixels. It was observed that amongst the multiple clean-up methods proposed by TSL, the one chosen here allows for re-indexation of mis-indexed points, while preventing the creation of artefacts (new grains that would appear just from the cleaning method but should not be present in the microstructure) that could occur during the cleaning of groups of mis-indexed pixels.

The texture was characterized from EBSD data by calculating the orientation distribution function (ODF) using a series expansion with $L_{\text{max}}=22$ (number of terms in the expansion). Results were plotted in the Euler space assuming triclinic sample symmetry (i.e $\varphi_1=360^\circ$, $\Phi=90^\circ$ and $\varphi_2=90^\circ$ as explained in section 2.2).

4.1.3. Bulk Texture Measurements

Bulk texture measurements were made at the sheet mid-thickness by mechanically grinding a sample measuring $30 \times 30 \text{ mm}^2$ using a procedure similar to that described in section 4.1.2. Three incomplete $\{200\}$, $\{110\}$ and $\{211\}$ pole figures were measured by X-ray diffraction using a X'pert Pro MRD XL diffractometer with $\text{Co-K}\alpha$ (1.78901 \AA)

radiation at 45kV and 20mA. Data points were collected on a 5°x5° grid. The raw data was first background corrected for incoherent scattering and fluorescence. Two background measurements were taken at 2θ-5° and 2θ+5° as a function of the tilt angle and averaged. This background was then subtracted from the raw data in order to improve the peak-to-background ratio. Following the background correction, the data was corrected for defocusing [15]. Calculation of the ODF was performed using the software MTEX [152]. As for microtexture measurements, triclinic sample symmetry was assumed.

4.1.4. Surface Roughness Measurements

Characterization of surface roughness was performed using contact profilometry. The raw surface profile was first refined by applying a form removal using a least square 8th order polynomial plane, according to equation (4.1)

$$y_{corr}(x) = y(x) - (a_8 \cdot x^8 + a_7 \cdot x^7 + a_6 \cdot x^6 + a_5 \cdot x^5 + a_4 \cdot x^4 + a_3 \cdot x^3 + a_2 \cdot x^2 + a_1 \cdot x + a_0) \quad (4.1)$$

where $y(x)$ indicates the initial roughness at the position x and a_n - a_0 indicate the coefficients of the 8th order polynomial plane. Then a Gaussian filter was used to remove high-frequency noise (wavelength smaller than 80 μm), according to equation (4.2):

$$y_{flt}(x) = y_{corr}(x) \cdot \sqrt{\frac{a}{\pi}} \cdot \exp(-a \cdot x^2) \quad (4.2)$$

where a is a function of the cut-of wavelength (taken here as 0.08 mm).

Three amplitude parameters are classically used for ridging characterization in industry and therefore have been calculated from experimentally measured and numerically predicted surface roughness profiles:

- Arithmetical mean deviation: $R_a = \frac{1}{N} \sum^N |y(x)|$ (N is the number of points measured along the profile, $y(x)$ is the position of the x-th points on the surface profile).
- Root mean square deviation: $R_q = \sqrt{\frac{1}{N} \sum^N y^2(x)}$ (equivalent to the standard deviation of roughness).
- Maximum profile peak height: $R_{\max} = \max(y(x)) - \min(y(x))$.

The estimation of the wavelength was done by calculating the auto-correlation function of the surface roughness (cross-correlation of the surface roughness profile with itself). The auto-correlation function is a way to quantify the correlation of the position of two points separated by a distance d . It can be calculated using:

$$I(d) = \frac{1}{L} \int_0^L y(x) \cdot y(x+d) \cdot dx \quad (4.3)$$

or more conveniently as [173]:

$$I(x) = FFT^{-1}(\hat{y}(\xi) \cdot \overline{\hat{y}(\xi)}) \quad (4.4)$$

where ‘ $\hat{\cdot}$ ’ indicates the Fourier transform, ‘ ξ ’ denotes frequency and ‘ $\bar{\cdot}$ ’ is the complex conjugate of the Fourier transform.

Figure 4.1 shows a sinusoidal function (period of 5 mm) and its auto-correlation function. As can be seen on the right hand side of Figure 4.1, the auto-correlation functions have peaks in intensity at exactly 5 mm, 10 mm and 15 mm. This result can be understood by imagining that we superimpose the sinusoidal function on itself and shift one of the curves horizontally over the other. The correlation between the two curves rapidly decreases as the shift increases to reach a minimum at 2.5 mm (where the two

curves exactly cancel). By shifting further, the correlation between the two profiles increases again to reach a maximum at 5 mm, corresponding to a translation of exactly one period. The multiplicity of the periods are obviously also marked by a peak in intensity on the auto-correlation curve.

As a consequence the auto-correlation function is more representative of repeating patterns rather than actual wavelengths. In the case of surface roughness measurements, the auto-correlation function helps one to see characteristic spacing of the underlying repeating features that make up the ‘ridges’ on the surface of a tested sample and how clearly coordinated such ridges are in their spacing

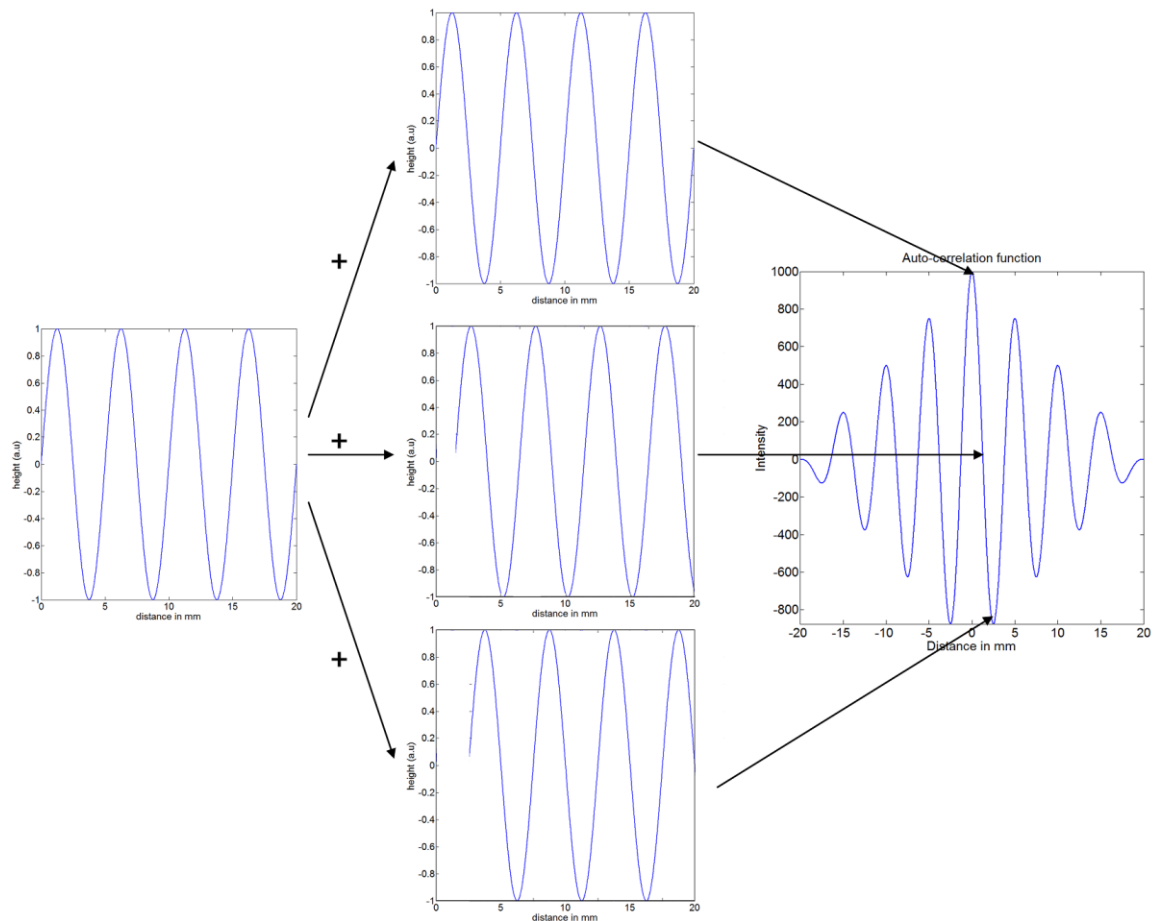


Figure 4.1: Ideal sine wave with a period of 5mm (left), the same curve shifted by different amount along the horizontal axis (centre) and the corresponding auto-correlation function (right) showing correlated patterns every 5 mm.

4.2. Thermo-Mechanical Processing

4.2.1. Cold Rolling

Cold rolling was carried out on the as-received hot band using a laboratory scale rolling mill at room temperature. The diameter of each roll was 150mm and their speed of rotation was 14 revolutions per minute. The gap between the two rolls was progressively reduced so that the reduction per pass was close to 5%. Approximately 25 passes were performed to achieve a reduction of 80% and a final sheet thickness of 0.65 mm. The direction of rolling was kept constant and aligned with the direction of the previous hot rolling. A high level of rolling reduction (80%) was chosen as it has been shown that the propensity for ridging increases with cold rolling reduction [142].

4.2.2. Annealing

Two different annealing procedures have been used during this project. The first treatment was used to mimic industrial annealing and consisted of annealing in a tube furnace under flowing argon at 1010°C for one minute per millimetre of sheet thickness. This was recommended by Aperam, who use this procedure to simulate industrial continuous annealing. The sample was rapidly inserted in the furnace after the temperature was stabilized and the time recorded starting from when the sample was fully inserted. After annealing, the samples were cooled to room temperature in air. Figure 4.2 presents the temperature profiles measured from a thermocouple welded to the surface of samples for different sheet thicknesses annealed under these conditions. It can be seen that for the annealing times used the sample is being continuously heated, which is consistent with the industrial conditions.

The second type of annealing treatment was done using resistive heating in the Gleeble 3500 thermo-mechanical simulator under vacuum (the pressure in the chamber was $< 2.7 \times 10^{-6}$ mbar). Rectangular samples (60 mm along RD and 15 mm along TD) were used. Both ends of the samples were held between water cooled copper grips.

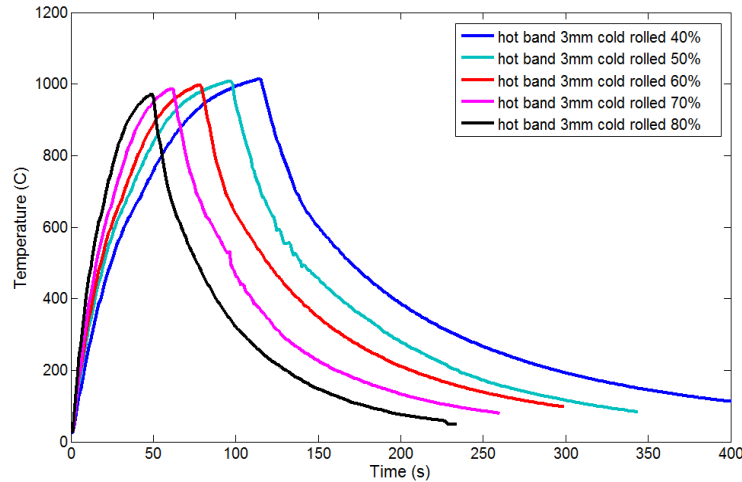


Figure 4.2: Temperature measured from a thermocouple attached to the surface of a sample annealed under argon for the 3mm hot band cold rolled between 40% and 80%. Samples were annealed in a furnace at 1010°C during one minute per mm thickness.

A high heating rate (100°C/s) was used in the Gleeble so as to ensure the sample spent most of its time at the desired temperature. Samples were held at 800°C, 850°C and 900°C for times ranging from 1s to 2000s (33 min). Temperature control was ensured by monitoring a spot-welded K-type thermocouple at the centre of the sample. To avoid temperature overshoot a lower heating rate (10°C/s) was imposed for the final 20°C before reaching the desired isothermal temperature. At the end of annealing, the samples were allowed to cool (natural cooling) within the Gleeble. An example of these annealing treatments is presented in Figure 4.3 where it can be seen that the temperature measured by the central thermocouple is maintained to within 1°C of the programmed temperature up to the point where power is turned off. A second thermocouple, placed 7.5 mm away from the central thermocouple shows that the temperature along the length of the sample is non-uniform. Because of thermal gradients generated by the Gleeble, it was important to make sure that all observations were conducted in the homogeneous temperature region of material. To do this, the temperature profile along the length of the sample (where the temperature gradient is the strongest) was first estimated by placing thermocouples at different locations along the sample. It was observed that the temperature varied by no more than 5°C within +/5 mm of the central thermocouple. Observations were further limited to this region, as close as possible to the central thermocouple.

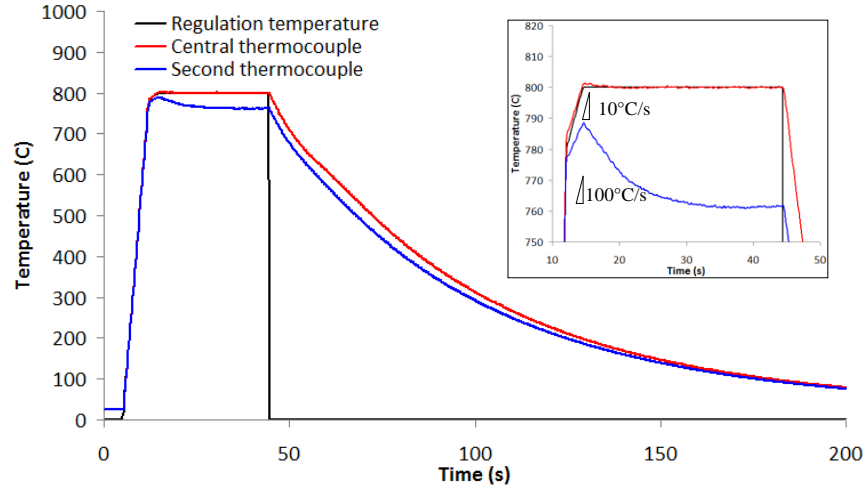


Figure 4.3: Example of isothermal treatment performed in the Gleeble 3500 on a sample cold rolled to 80% reduction. The initial heating rate was 100°C/s , followed by a slower heating rate of 10°C/s during the last 20°C (2s) before the isothermal plateau at 800°C for 30s. In the insert, detail of the two-step heating rate is shown.

4.3. Materials

Three distinct materials were used in this study. An AISI 409 alloy was specifically selected in the form of a final sheet product as it was a material that had been previously shown to exhibit extremely strong ridging. The other two materials represent two variations of the same AISI 445 alloy (denoted E1 by Aperam) obtained as hot rolled plate. One batch was received just following coiling. The second batch was received after hot band annealing. These two states were selected so as to allow comparison of the effect of the microstructure and texture on the microstructure evolution on further processing.

The nominal composition of both these steels is given in Table 4.1. The AISI 409 grade was provided by the Aperam Stainless Steel Research Center (Isbergues, France) in the form of cold rolled and annealed sheet with a thickness of 1.4 mm. This material, though supplied by Aperam, was produced by another company. The precise thermo-mechanical route was therefore unknown. The AISI 445 grade was manufactured and provided by Aperam in the form of hot rolled plate (100 cm in length, 70 cm in width and 3.1 mm in thickness).

Table 4.1: Nominal composition (in wt.%) for the ferritic stainless steel grades studied in this work.

Composition (wt.%)	C	Cr	Nb	Ti	Si	Mn	Cu	N	Fe
409	0.01	11.30	-	0.19	0.45	0.3	-	-	Bal.
445	0.015	20.20	0.45	-	0.25	0.25	0.45	0.02	Bal.

The AISI 409 grade was received in the form of a final sheet product. Its microstructure will be presented in a later section, when direct comparison of final microstructure and ridging will be required.

The un-annealed AISI 445 hot band presented a large gradient in microstructure and texture through its thickness. The centre (~ 50% of the total thickness of the hot band) was mainly unrecrystallized and composed of very large (larger than 700 μm along RD and around 200-300 μm along TD) pancake-shaped grains (Figure 4.4(a) and Figure 4.4(b)). The texture in the sheet center was found to be composed of a strong α -fibre with a weaker γ -fibre (Figure 4.4(d)).

The near surface regions (each representing about 25% of the total thickness) were found to be composed of small recrystallized grains (average grain size 6 μm) mixed with large unrecrystallized grains (with dimensions similar to the dimensions of the grains near the centre) whose orientations were more typical of shear deformation [18] [19]. (Figure 4.4(c) and Figure 4.4(e)).

The annealed hot band also presented a strong gradient of microstructure and texture through its thickness (Figure 4.5(b)). In this case, however, the material was found to be fully recrystallized throughout the thickness (Figure 4.5(a) and Figure 4.5(b)).

While the centre was found to be composed of grains with an average equal area diameter (EQAD) grain size of 49 μm (Figure 4.5(a)) having a strong α -fibre and weaker γ -fibre (Figure 4.5(d)), the surfaces regions were found to be composed of smaller grains (EQAD grain size of 33 μm , Figure 4.5(b)) whose texture was characteristic of the friction induced shear deformation at the plate surface (Figure 4.5(c) and Figure 4.5(e)).

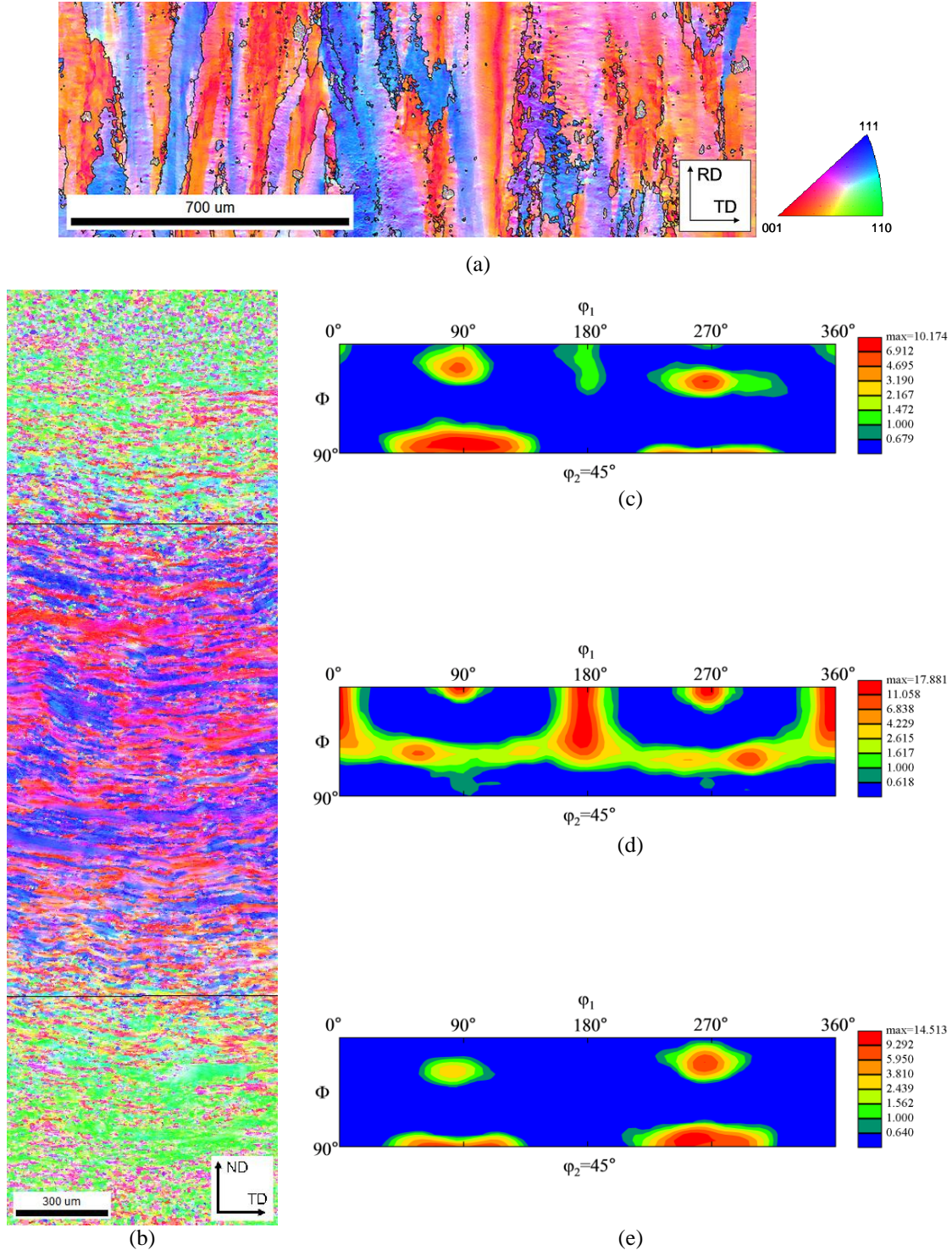


Figure 4.4: EBSD characterization of the un-annealed hot band for the AISI 445 grade. (a) ND inverse pole figure map on the ND plane at mid thickness showing large elongated grains along RD. In this case, the color code (represented by the stereographic triangle) corresponds to crystallographic directions being parallel to the ND of the sheet. (b) ND inverse pole figure on the RD plane covering the full thickness of the hot band and showing microstructure and texture gradients through thickness, as represented by the $\phi_2=45^\circ$ section of the Euler space for (c) the top surface (25% of the thickness), (d) the central layers (50% of the thickness) and (e) the bottom surface (25% of the thickness).

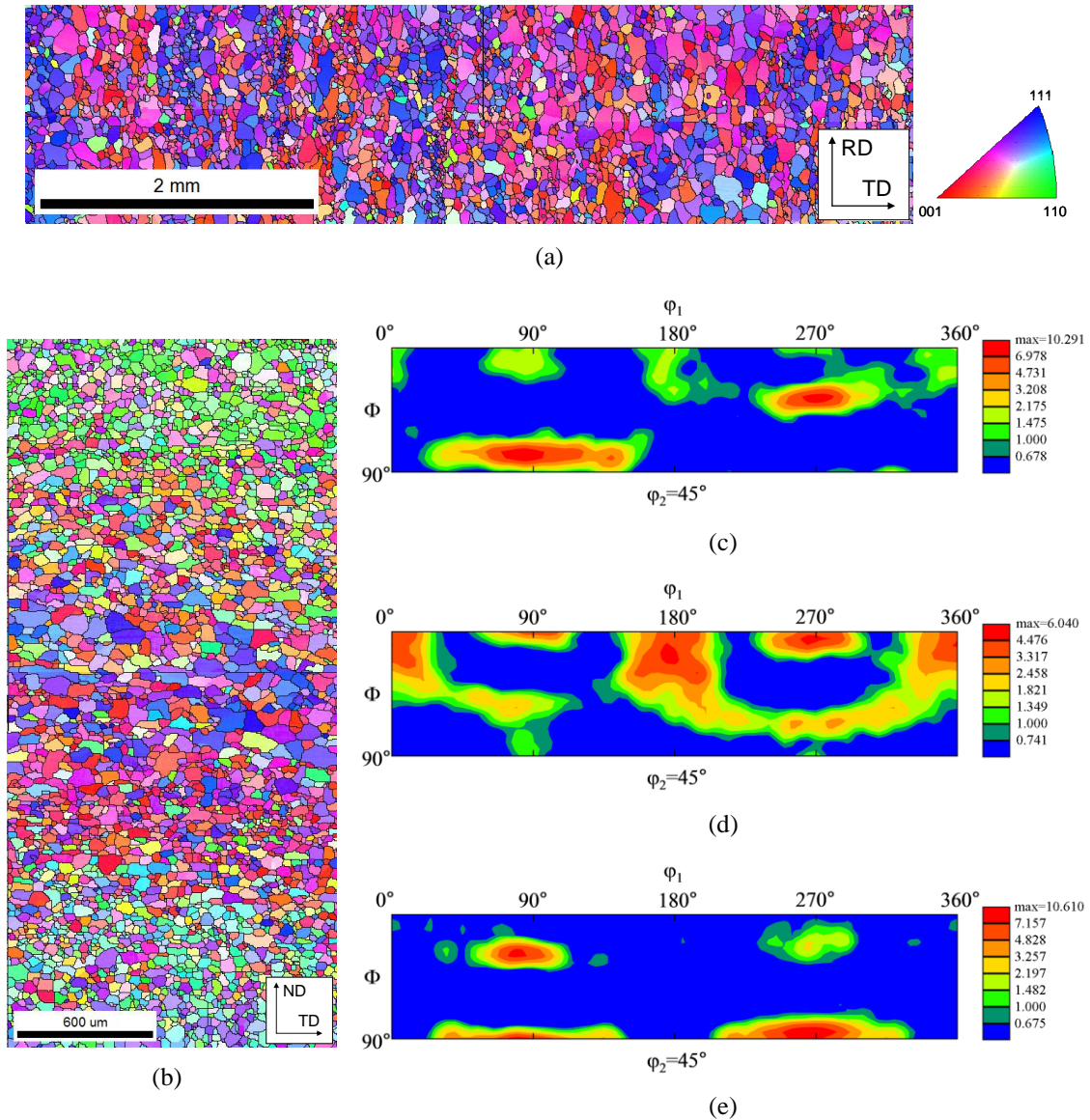


Figure 4.5: EBSD characterization of the annealed hot band for the AISI 445 grade. (a) ND inverse pole figure map on the ND plane at mid thickness showing a well recrystallized microstructure. (b) ND inverse pole figure on the RD plane covering the full thickness of the hot band and showing microstructure and texture gradients through thickness, as represented by the $\phi_2=45^\circ$ section of the Euler space for (c) the top surface (25% of the thickness), (d) the central layers (50% of the thickness) and (e) the bottom surface (25% of the thickness).

In the following chapter, the samples processed from the un-annealed hot band (after cold rolling and annealing) will be referred as to UA-445-R materials, and the samples processed from the annealed hot band will be referred as to A-445-R materials.

Chapter 5: Characterization of the Spatial Heterogeneity of Microstructure and its Link to Ridging

5.1. Introduction

As noted in the literature review, ridging has been described as being a consequence of ‘clusters’ of grains in the final product. This idea of ‘clusters’, while widely reported [20] [21] [22] [29] [36], has yet to be quantified. Here a ‘cluster’ will be defined as an aggregate of continuously connected grains sharing a similar deformation behaviour. With this definition in mind, crystal plasticity simulations have been used to help identify the potential presence of these clusters in real microstructures. These results are used to quantify the link between the identified non-random distribution of orientations and the amplitude and wavelength of ridging.

Previous attempts to link microstructure with ridging using crystal plasticity simulations relied on either viscoplastic self-consistent (VPSC) or crystal plasticity finite element (CPFEM) calculations applied to measured microstructures and microtextures [37] [44]. Both types of models showed the importance of grains having large out-of-plane shearing and linked their presence to ridging based on the Takechi model [21]. None of these prior studies, however, were able to make a quantitative prediction of the surface roughness. Simulations using VPSC use a ‘mean field’ assumption and thus assume that each orientation is embedded in a homogeneous effective medium whose properties are those of the average polycrystal. As a consequence, no spatial information is directly included in the calculations and no interaction between neighbouring grains is taken into account [37] [41]. Simulations performed using FEM calculations (which can incorporate the spatial information of real microstructures) have been restricted to simplified microstructures on scales much smaller than the scale of ridging due to restrictions on computational resources [44].

In both cases, most simulations have focused on the relationship between microstructure and ridging based on two-dimensional microstructures measured from

within the sheet plane. In doing this the effect of the strong through thickness microstructure and microtexture gradients described in the literature review are ignored.

In this chapter, an efficient full-field viscoplastic model based on solving Green's function using the Fast Fourier Transform (FFT) algorithm, the VPFFT model [143], has been used to overcome the limitations of prior self consistent (lack of spatial information) and CPFEM (limited simulation domain size) simulations⁸. The VPFFT model is able to use large experimental EBSD data sets as input, thus allowing for an accurate description of the local environment of individual grains. Artificial microstructures can also be designed and used for input to allow for the study of individual parameters and their influence on both wavelength and amplitude of ridging.

In section 5.2, a description of the VPFFT model is given. In section 5.3, the experimental microstructures and ridging behaviours of the 409 and 445 steels are presented. Starting from these experimental results, section 5.4 presents the prediction of surface roughness and local deformation using the VPFFT model with experimental microstructure as input. Finally, section 5.5 discusses these results with a focus on the relationship between the microstructure and ridging

5.2. VPFFT Model

The VPFFT model was first developed by Moulinec and Suquet [144] [145] and later adapted to the case of polycrystalline plasticity by Lebensohn et al. [143]. A detailed description of this model can be found in [143] [146]. Here the key concepts will be briefly reviewed.

The VPFFT method considers a representative volume element (RVE) composed of Fourier points distributed on a regular grid with periodic boundary conditions. Each Fourier point is assigned an orientation and the mechanical response of the polycrystal is calculated by solving the equations for equilibrium of stresses and compatibility of deformation at each point in the microstructure.

The efficiency of this model arises because of the use of the Green's function (denoted $G_{ij}(x-x')$) to solve for mechanical equilibrium and compatibility in Fourier

⁸ This work has been submitted and published in the journal "Modelling and Simulation in Materials Science and Engineering" [42].

space. The Green's function gives the displacement in the i -direction at a point x due to an applied force in the j -direction at a point x' . In the VPFFT model it is the deviations from a uniform and homogeneous distribution of stresses and strains (equal to the macroscopic stresses and strains) that are calculated. In this case, the Cauchy stress field is given by [143],

$$\sigma_{ij}(x) = L_{ijkl}^0 \cdot \dot{\epsilon}_{kl}(x) + \phi_{ij}(x) - p(x) \cdot \delta_{ij} \quad (5.1)$$

where δ_{ij} is the Kronecker delta, $p(x)$ is the hydrostatic pressure field, L_{ijkl}^0 is a linear reference stiffness and $\phi_{ij}(x)$ is the so-called polarization field defined as,

$$\phi_{ij}(x) = \sigma'_{ij}(x) - L_{ijkl}^0 \cdot \dot{\epsilon}_{kl}(x) \quad (5.2)$$

or, in other words, it is the deviation of the deviatoric stress field away from the field predicted by the linear reference stiffness. The linear reference stiffness, L_{ijkl}^0 is computed at the start of each deformation step by making a 'Taylor' calculation (i.e. assuming that the local strains are equal to the macroscopic strains everywhere) and using this to calculate the local stresses [143] [146].

The VPFFT algorithm uses the polarization field to calculate the 'local fluctuation velocity field', i.e. the deviation of the velocity field away from the macroscopic velocity, by convolution of the derivative of G_{ij} with ϕ_{ij} ,

$$\tilde{v}_k(x) = \int_{\mathbb{R}^3} G_{ki,j}(x-x') \cdot \phi_{ij}(x') \cdot dx' \quad (5.3)$$

When transformed into the Fourier space, equation (5.3) becomes:

$$\hat{\tilde{v}}_k(x) = (-i\xi_j) \cdot \hat{G}_{ki}(\xi) \cdot \hat{\phi}_{ij}(\xi) \quad (5.4)$$

where '^' indicates the Fourier transform and ξ denotes frequency. If the polarization field is known (or can be guessed), equation (5.4) can be used to calculate the fluctuation of the velocity field in Fourier space, which in turn can be inversely transformed to provide the fluctuation field in real space ($\tilde{v}_i(x)$). The change in position for each point in the simulation domain can then be obtained as:

$$\Delta x_i = (\dot{E}_{ij} \cdot X_j + \tilde{v}_i(x)) \cdot \Delta t \quad (5.5)$$

where Δt is the time increment corresponding to a single deformation step, \dot{E}_{ij} is the macroscopically imposed strain rate $\dot{E}_{ij} = \frac{\partial \dot{X}_i}{\partial x_j}$, and X_j is the position of the Fourier point before deformation, the subscript indicating the direction (i.e. x, y or z).

Since at the outset of the calculation the polarization field is not known, an initial guess has to be made for it. From this initial guess, the local strain rates are computed and their average compared to the macroscopically imposed strain rate. If these are not sufficiently close, then a new estimate for the polarization field is calculated based on the prior calculated strain rates (equation (5.2)) and the process repeated until convergence is obtained. Upon convergence, the full strain rate state is calculated at each point in the microstructure. The VPFFT code was then modified for the purpose of ridging prediction to estimate the vertical displacement of the surface. For each column of Fourier points, the contribution from the strain rate tensor to the vertical displacement of each point in this column has been summed up and reported as the final position of the surface, leading to the description of the surface roughness.

The main advantage of the VPFFT calculations over other full-field techniques is the speed of the calculations. For the same RVE containing 32^3 elements, a recent study showed that VPFFT simulations of rolling and wire drawing took several hours, while the corresponding finite element computations took several days [147]. A drawback of the VPFFT model, however, is that the simulation points must always be on a regular grid. This contrasts with the fact that the local variations in predicted strain will tend to make an initially regular grid of points become irregular even after the first deformation step. To overcome this, the VPFFT model used here takes the displacement of each calculation (Fourier) point to be that corresponding to the macroscopically imposed strain when updating the microstructure after deformation. Given that the present calculations consider relatively small plastic strains (< 0.15), errors arising from this are believed to be small.

Simulations were performed on two-dimensional microstructures in the RD plane. Because of the periodic boundary conditions imposed by VPFFT, each grain in the RD plane is actually considered to be columnar, with its long axis being parallel to the RD

direction [148]. A schematic of such a two-dimensional microstructure used for VPFPT simulations is presented in Figure 5.1. While this configuration may be expected to give an over-estimation of the tendency for shearing and rigid rotation about RD due to the lack of constraint in RD, Sinclair [41] has previously shown that the elongation along this direction only has limited effect on the shearing intensity, and that the effect rapidly saturates with the length of grains along RD.

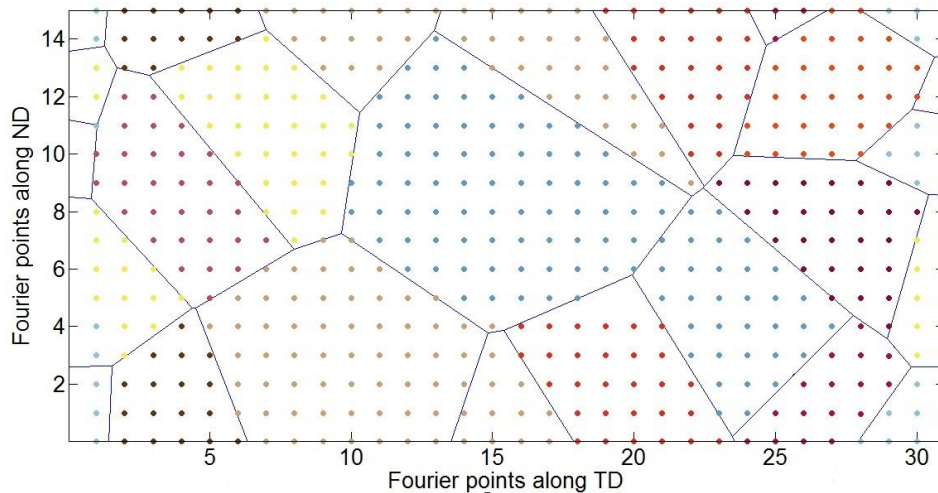


Figure 5.1: Schematic of a microstructure superimposed to a regular grid of Fourier points. Each point belonging to a grain is assigned an orientation. The grain boundaries have been reconstructed based on the difference of orientations between neighbouring points. The horizontal direction correspond to the transverse direction of the sheet, the vertical direction corresponds to the normal direction of the sheet, and the microstructure is assumed to be extruded along the third dimension (the rolling direction).

As noted in the literature review, very few studies have considered deformation in the RD plane. Prior simulations have typically been performed on microstructures in the ND plane where orientation banding is more readily observed in EBSD maps (e.g. Figure 2.12). The decision to focus on the RD plane in this study can be attributed to three facts. First, this plane allows for a complete description of the through thickness texture and microstructure gradients, as it is known that different layers along the thickness can exhibit different properties [23] [27] [43]. Secondly, this plane captures the texture and microstructure evolution along TD, which is the direction along which different bands of orientations have been seen to alternate [37] [42] [44]. Finally, as noted above, it has been previously argued that banding of orientations along the RD is not the most critical

factor in determining the tendency of grains to undergo out-of-plane shearing [41]. Of course, using fully three dimensional microstructures for the crystal plasticity simulations would be ideal to provide a one-to-one correlation to experimental results but this would require volumes on the order of several centimetres cubed to be quantified experimentally and simulated numerically. To retain a resolution sufficient to capture each grain in the material this would require tens of millions of data points, this far exceeds the current experimental and numerical capabilities available for this study. For instance, a representative volume of material whose dimensions are 0.6 mm//ND x 10 mm//TD x 10 mm//RD with a step size of 5 μm would represent a total of 480 million points.

To simulate ND surfaces that are traction-free, as in a typical tensile test, the bottom five layers of Fourier points in the RVE have been assigned properties that have infinite compliance (i.e. the stresses on these points are zero) [146]. This has the effect of separating the two surfaces of the simulation domain allowing for the independent deformation of the surfaces of the material to mimic roughening of the surface observed experimentally. This value was chosen as a compromise between steep stress/strain gradients generated during the deformation (lower number of points in this ‘gas-layer’) and the wish to not disregard the behaviour of many layers of material, since the surface roughness is really the result of the whole through thickness deformation (higher number of points in this ‘gas-layer’).

Simulations of uniaxial tensile tests were performed imposing a macroscopic strain rate of 10^{-2} s^{-1} along the axis of tension, and a macroscopic strain rate of $-0.5 \times 10^{-3} \text{ s}^{-1}$ in the other two directions normal to the tensile direction. In these simulations all shear strain rate components were fixed to be zero. Slip was considered to occur on $\{110\}\langle 111 \rangle$ and $\{112\}\langle 111 \rangle$ slip systems. For all slip systems, an identical critical resolved shear stress (CRSS) was considered with no hardening (see Appendix B), and microstructure and texture evolutions were not updated. Because it is experimentally observed that the amplitude of ridging is directly proportional to the amount of tensile strain [23], only one step of 1% tensile strain was computed. The surface displacements were then scaled to allow for comparison with experimental results measured at 15% tensile strain.

5.3. Characterization of Microstructure and Ridging

Behaviour: Experiments

Because of the efficiency of the VPFFT model, it is possible to use real microstructures as the input to the model. Here, the experimental microstructures of the AISI 409 and the two AISI 445 steels are described in their final, fully recrystallized state. In the case of the AISI 409 steel this was the as-received state of the material. For the AISI 445 materials, the microstructures presented here were obtained following cold rolling and annealing. These microstructures will subsequently be used as input to the VPFFT model.

5.3.1. Microstructure of the AISI 409 Steel

Large EBSD maps were measured on the ND (at mid-thickness) and RD plane (covering 75% of the full thickness). From the ND plane map (Figure 5.2(a)), the grain size, measured as the equivalent area diameter (EQAD), was estimated to be 34 μm . A gradient of grain size is observed, however, through thickness with smaller grains (20 μm) near the surfaces of the sheet (Figure 5.2(b)).

The ND-inverse pole figure map, plotted in the ND plane (Figure 5.2(a)), exhibits the often observed (cf. Figure 2.12 from the literature review) banding of grains with near γ -fibre orientations (in blue on that map). These bands of grains appear roughly parallel to RD and alternate with bands having a weaker texture, but a higher than average occurrence of grains having $\langle 001 \rangle$ parallel to ND (in red on the map). The microstructure and microtexture viewed in the RD plane, on the other hand, shows no obvious spatial banding of grain orientations.

Large samples for tensile testing (250 mm gauge length by 50 mm gauge width) were prepared from this material. Tensile tests were performed at room temperature to 15% elongation at a strain rate of 10^{-3} s^{-1} . Tensile tests parallel to, at 45° to and perpendicular to RD were performed and surface roughness was measured on one side of each sample using a Taylor-Hobson Talysurf contact profilometer. The results from these measurements are presented again in Figure 5.3. It can be seen from these three

measurements that the ridges (when present) are always aligned with the previous rolling direction (in agreement with the literature), but their amplitude strongly decreases as the direction of tension moves away from the rolling direction. The amplitude is found to be maximum when the tensile axis is parallel to the previous RD and is much lower when the tensile axis is at 45° from RD. When the tensile test is performed along TD, the surface roughness is weak and isotropic, this being similar to the so-called orange peel effect observed generally in other polycrystalline materials [28].

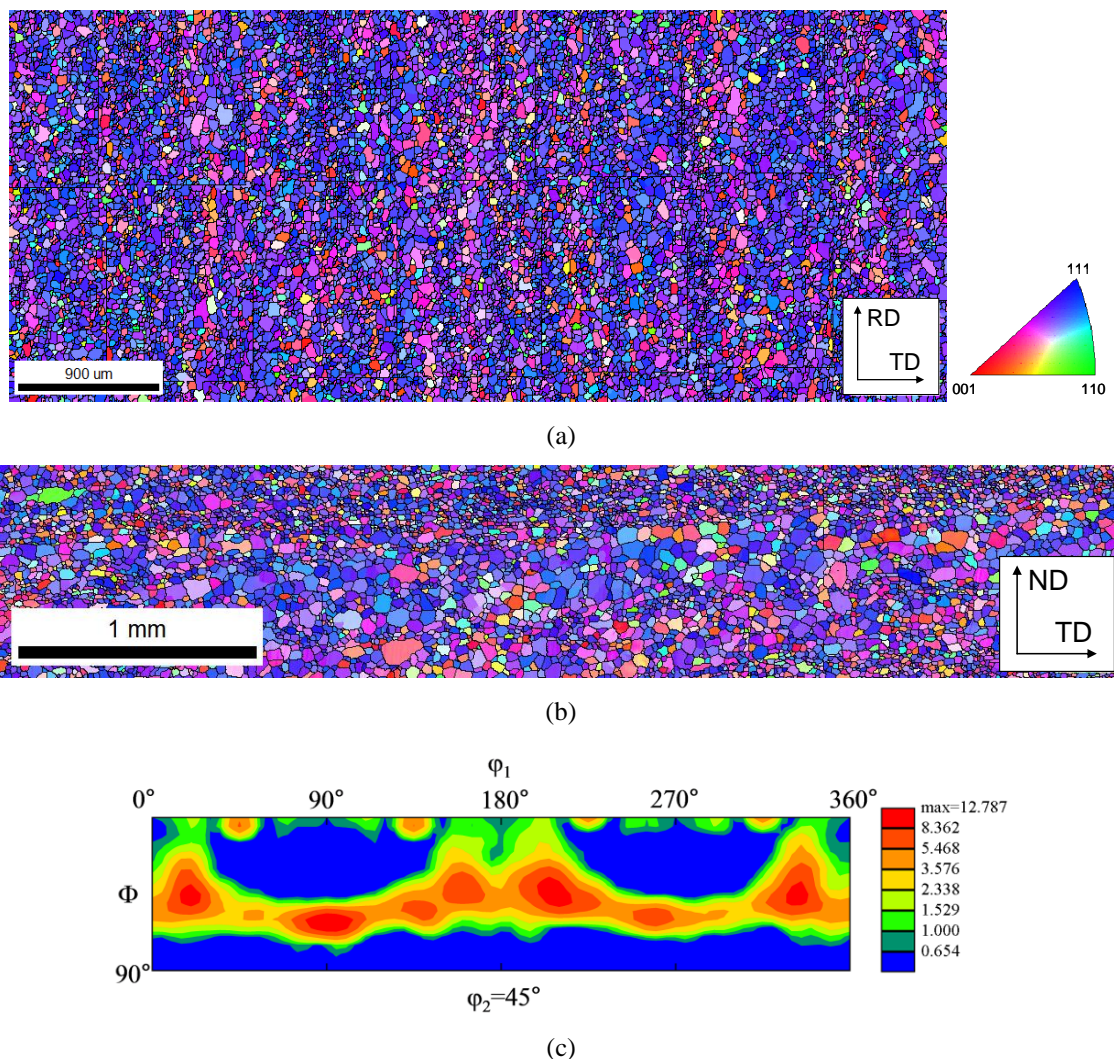


Figure 5.2: EBSD ND inverse pole figures maps for the AISI 409 ferritic stainless steel taken from (a) the ND plane at mid-thickness, and (b) the RD plane, covering approximately 75% of the sheet thickness. (c) texture corresponding to (b) after calculation of the ODF and represented in the $\phi_2=45^\circ$ section of the Euler space.

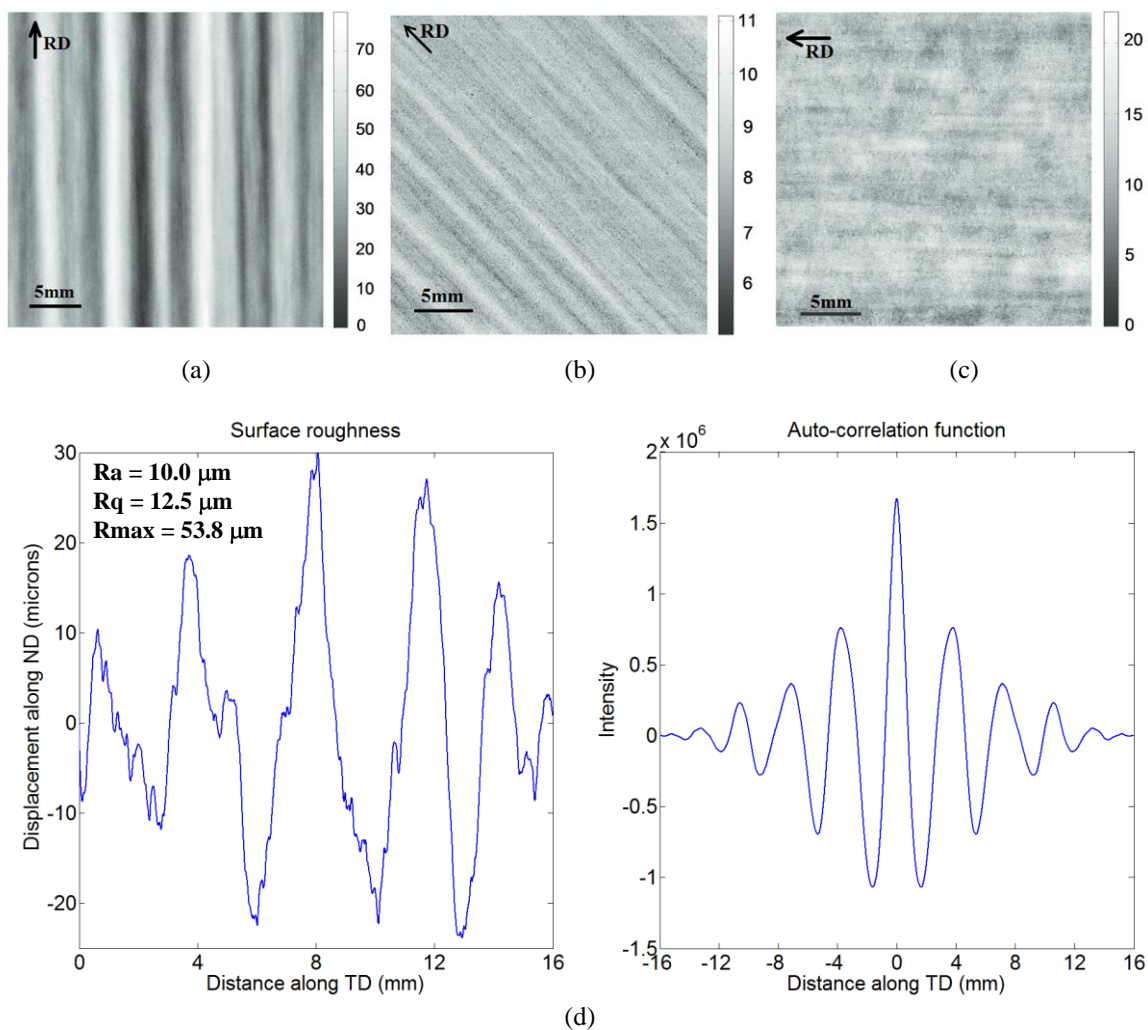


Figure 5.3: Two-dimensional profilometry measurements from the surface sample of the AISI 409 after tension to 15% where the tensile axis was parallel to the (a) prior RD, (b) 45° to RD and (c) prior TD. For these three cases the tensile direction is vertical, and the scale bar is in microns [23]. (d) is a one-dimensional surface obtained following the procedure described in section 4.1.4 and its corresponding auto-correlation function.

Figure 5.3(d) is a one-dimensional surface roughness profile after tensile test parallel to RD obtained by profilometry and corrected using the procedure described in section 4.1.4. The amplitude parameters are $R_a = 10.0 \mu\text{m}$, $R_q = 12.5 \mu\text{m}$ and $R_{\text{max}} = 53.8 \mu\text{m}$. The auto-correlation function reveals that there is a repeating pattern at approximately 3.8 mm.

5.3.2. Presentation of the UA-445-R Material

The un-annealed hot band was cold rolled 80% and annealed at 1010°C for 45s so as to obtain a fully recrystallized material. Large EBSD maps were measured on the ND (at mid-thickness) and RD planes (covering the full thickness). From the ND plane (Figure 5.4(a)) the microstructure appears similar to the AISI 409 (presence of elongated features) with, however, a smaller average grains size (EQAD) of 20 μm . The grain size distribution of the UA-445-R material, unlike the AISI 409, is homogeneous through the thickness of the sheet (Figure 5.4(b)).

The texture of this material (Figure 5.4(c)) is composed of a shifted γ -fibre with a maximum intensity towards the high index orientations, such as observed in the case of the AISI 409 (Figure 5.2(c)).

Large samples for tensile testing (125 mm gauge length by 25 mm gauge width) were prepared from this material. Tensile tests were performed parallel to RD at room temperature to 15% elongation at a strain rate of 10^{-3} s^{-1} . The surface roughness was measured by a single line scan on one side of this sample using the SurfTest SJ-310. The raw surface profile was refined using the procedure presented in section 4.1.4 and the result is presented Figure 5.5. Repeating features were found at 3.2 mm according to the auto-correlation function (Figure 5.5(b)) and the amplitude parameters were calculated as $R_a = 5.1 \mu\text{m}$, $R_q = 6.6 \mu\text{m}$ and $R_{\text{max}} = 35.6 \mu\text{m}$.

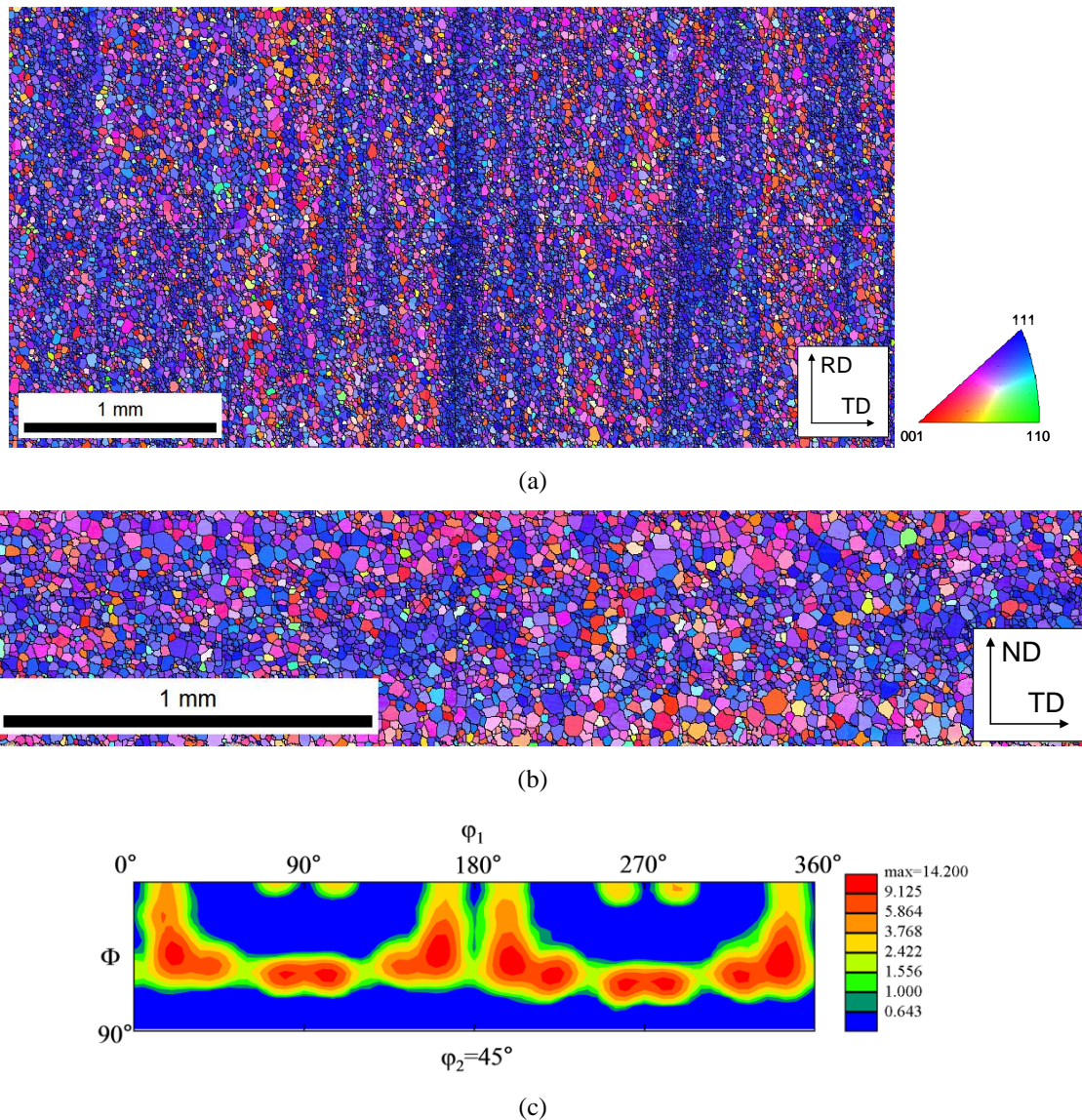


Figure 5.4: EBSD ND inverse pole figures maps for the un-annealed AISI 445 hot band after 80% reduction and annealing (1010°C for 45s) taken from (a) the ND plane at mid-thickness, and (b) the RD plane, covering the entire thickness. (c) texture corresponding to (b) after calculation of the ODF and represented in the $\Phi_2=45^\circ$ section of the Euler space.

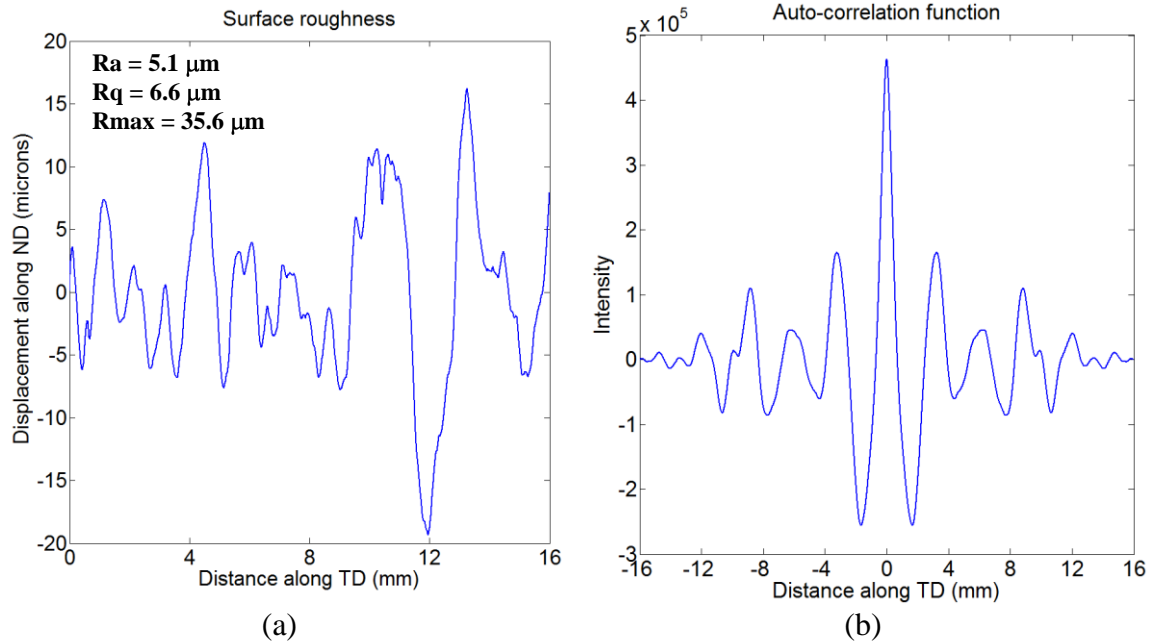


Figure 5.5: (a) Line scan surface roughness measured on the surface of the un-annealed AISI 445 hot band after 80% cold rolling, annealing at 1010°C for 45s and deformation by 15% elongation along the previous RD (b) Auto-correlation function revealing the major wavelength characteristic of ridging.

5.3.3. Presentation of the A-445-R Material

Similar characterization has been applied to the annealed AISI 445 hot band after cold rolling (80% reduction) and annealing (1010°C for 45s), see section 4.2.2. From the ND plane map (Figure 5.6(a)), the grain size, measured as the equivalent area diameter (EQAD), was estimated to be 19 μm, similar to that of the UA-445-R material. From this map, it is observed that the classical banding of grains with near γ -fibre orientations is not as obvious as in the case of the AISI 409 and the UA-445-R materials. The grain size for the A-445-R is found to be uniform through thickness (Figure 5.6(b)).

The texture of this material is similar to the texture of the AISI 409 grade and the UA-445-R material presented in Figure 5.2(c) and Figure 5.4(c) respectively, but presents a more ideal γ -fibre, with no strong shift towards high index orientations. As with the two other materials, there is no obvious orientation banding on the RD plane.

The surface roughness results are presented in Figure 5.7. Repeating features were found at 2.7 mm according to the auto-correlation function (Figure 5.7(b)). One should, however, notice that the amplitude of the auto-correlation function for this surface

roughness profile is about one order of magnitude smaller than for the two previously presented materials. This means that although the auto-correlation function is able to capture patterns that repeat over a certain distance, the correlation is weak compared to those obtained for the AISI 409 and the UA-445-R materials. The amplitude parameters were calculated as $R_a = 3.0 \mu\text{m}$, $R_q = 3.7 \mu\text{m}$ and $R_{\text{max}} = 17.5 \mu\text{m}$.

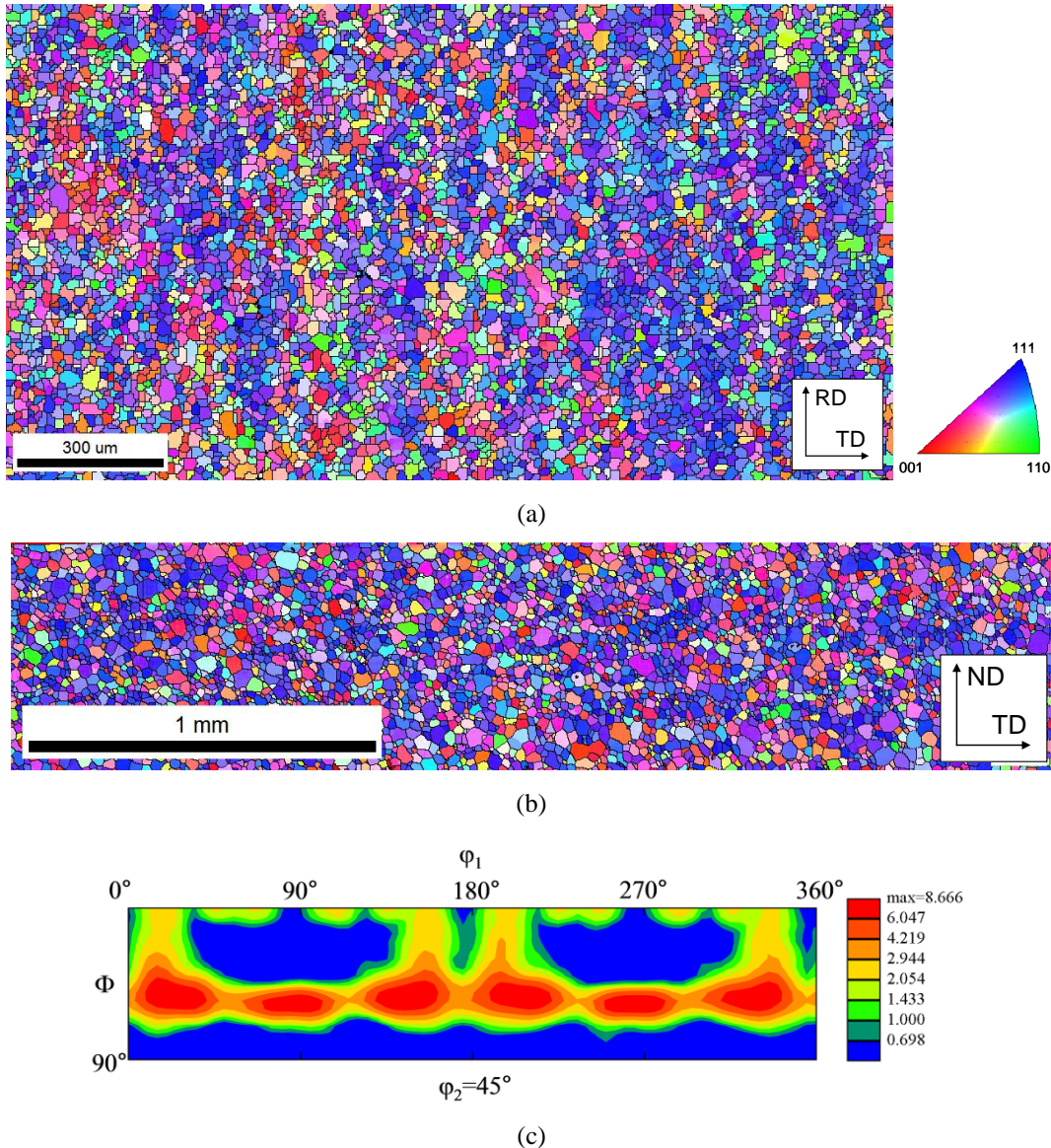


Figure 5.6: EBSD ND inverse pole figures maps for the annealed hot band AISI 445 ferritic stainless steel after 80% cold rolling reduction and annealing (1010°C for 45s) taken from (a) the ND plane at mid-thickness, and (b) the RD plane, covering the entire thickness. (c) is the texture corresponding to (b) after calculation of the ODF and represented in the $\phi_2=45^\circ$ section of the Euler space.

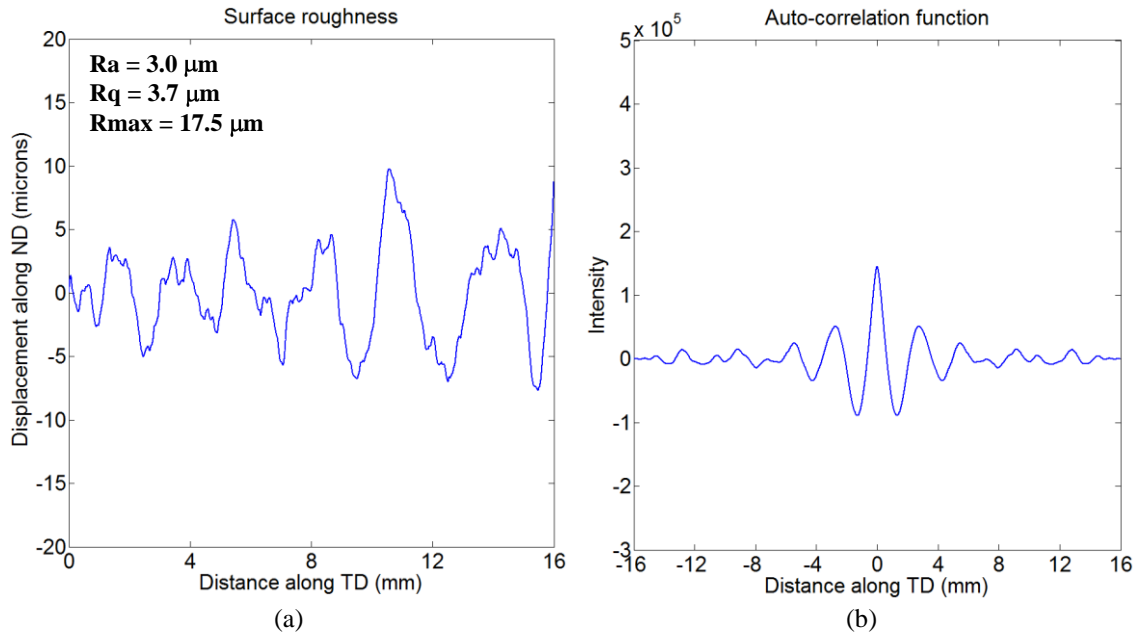


Figure 5.7: (a) Line scan surface roughness measured on the surface of the annealed AISI 445 hot band after 80% cold rolling, annealing at 1010°C for 45s and deformation by 15% elongation along the previous RD. (b) Auto-correlation function revealing the major wavelength characteristic of ridging.

5.4. Numerical Prediction of Ridging from Experimental Microstructures

5.4.1. Introduction

In Figure 5.2(a), Figure 5.4(a) and Figure 5.6(a), a banding of blue γ -fibre grains is apparent to the eye but clearly distinct clusters are difficult to define. One can roughly estimate the size of the bands in these figures to be several millimetres in length parallel to the RD and of the order of 100 μm parallel to TD. The spacing between bands in the TD direction should, however, be contrasted with the spacing between the ridges in Figure 5.3(d), Figure 5.5 and Figure 5.7 (approximately 4 mm, 4 mm and 6 mm respectively). It is thus necessary to resort to numerical simulations if one wants to find correlations between the microstructure and the surface roughness developed during deformation, especially since similar microstructure can present different ridging behaviour, as showed by the previous experimental measurements.

The two-dimensional microstructures presented in Figure 5.2(c), Figure 5.4(c) and Figure 5.6(c) have been used as input for VPFFT calculations with the aim of predicting ridging amplitude and wavelength. The three RVEs were constructed from these maps as a regular grid of Fourier points, with (i) 2^{11} points along TD and 2^9 points along ND (i.e. 1,048,576 EBSD points), corresponding to a cross-section of approximately 4 mm x 1 mm for the AISI 409, (ii) 2^{11} points along TD and 2^8 points along ND (i.e. 524,288 EBSD points), corresponding to a cross-section of approximately 4.9 mm x 610 μm for the A-445-R material and (iii) 2^{11} points along TD and 2^8 points along ND (i.e. 524,288 EBSD points), corresponding to a cross-section of approximately 5.1 mm x 640 μm for the UA-445-R material⁹.

A Matlab routine was specifically developed to serve as an interface between the EBSD outputs that need to be converted in a proper format to be used as input for the VPFFT model. This code re-organizes the EBSD output data and reformats them so that they are compatible with the VPFFT model.

The periodicity in the x-direction (along TD) leads to the formation of a false set of grain boundaries at these two extremities of the RVE. This artefact was found, however, to only affect the behaviour locally at the far left and right sides of the RVE.

At the end of one step of deformation the displacement of each Fourier point was calculated using equation (5.5). In this way the predicted surface roughness is just the displacement of the Fourier points on the top/bottom surfaces of the RVE. The surface roughness profiles on both surfaces were calculated and compared, showing perfect correlations. As a consequence, the surface roughness obtained from the top surface alone will be presented in the following sections. Since it has been proposed that out-of-plane shear strains are responsible for the corrugations observed during deformation, one can further investigate the source of the surface roughness by looking at the spatial distribution of this strain component within the microstructure. From the complete strain field calculated at each point of the RVE, the out-of-plane shear strain ε_{12} (1=TD, 2=ND) has been extracted and mapped back onto the microstructure.

⁹ It can be noted that the RVE chosen for the UA-445 and for the A-445 materials are exactly identical but do not correspond to similar real dimensions. This is due to the step size chosen for both cases which was not identical.

5.4.2. Predicted Ridging Behaviour of AISI 409

The surface roughness following simulated tension to 15% strain in both the RD and TD directions is shown for the AISI 409 alloy in Figure 5.8. Qualitatively, the results show similarities to the experimental surface roughness reported in Figure 5.3. When tension is performed parallel to RD a large wavelength undulation is observed on a scale much larger than the grain size (3.2 mm from the auto-correlation function vs. $34\ \mu\text{m}$)¹⁰. In contrast, roughening with a much smaller amplitude and wavelength was observed for simulations performed with the tensile axis parallel to TD (Figure 5.8).

The calculated and experimentally measured one-dimensional surface roughness profiles for tensile tests parallel to RD are directly compared in Figure 5.9. Although the RVE for the simulation is much smaller than the length of the surface roughness profile measured by profilometry (4 mm vs. 16 mm), an excellent agreement was found both in terms of the simulation's prediction of the large-scale surface roughness wavelength and amplitude.

Figure 5.10 shows the out-of-plane shear strain field after deformation combined with the simulated surface roughness profile. One can immediately recognize two large 'clusters' of grains on this map. In the bottom left hand side of the map there is a large region containing dark grey/black grains exhibiting a large negative shear strain rate. This corresponds exactly to the region exhibiting a large negative slope on the surface roughness profile. On the right hand side, a second region containing light grey/white grains exists, these grains exhibiting a strong positive shear strain rate. These grains correspond to the region exhibiting a positive slope on the surface roughness profile. It is important to note that these apparent groups of grains having similar shearing tendencies are not evident from the raw EBSD data plotted in the form of an inverse pole figure map (i.e. Figure 5.2(c)).

¹⁰ After crystal plasticity calculations, the RVE measured by EBSD reveals exactly one wavelength. This is not an artefact of the simulation but a real result coming from the fact that the EBSD map covered exactly two large clusters of grains having similar deformation (shearing) behaviour.

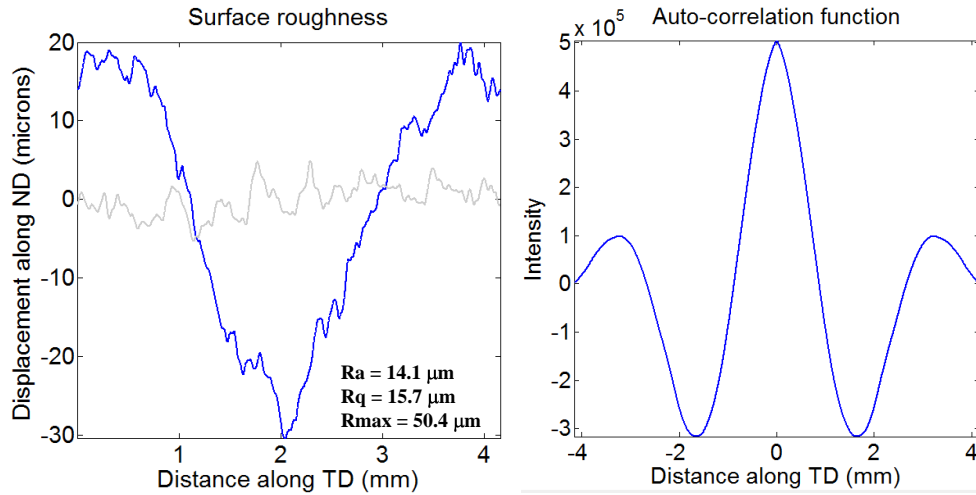


Figure 5.8: Simulated effect of tensile testing direction on surface roughness after 15% elongation (extrapolated from a single step of 1%) along RD (blue curve) and along TD (grey curve) on the AISI 409 ferritic stainless steel. Right is the auto-correlation function corresponding to the tension along RD.

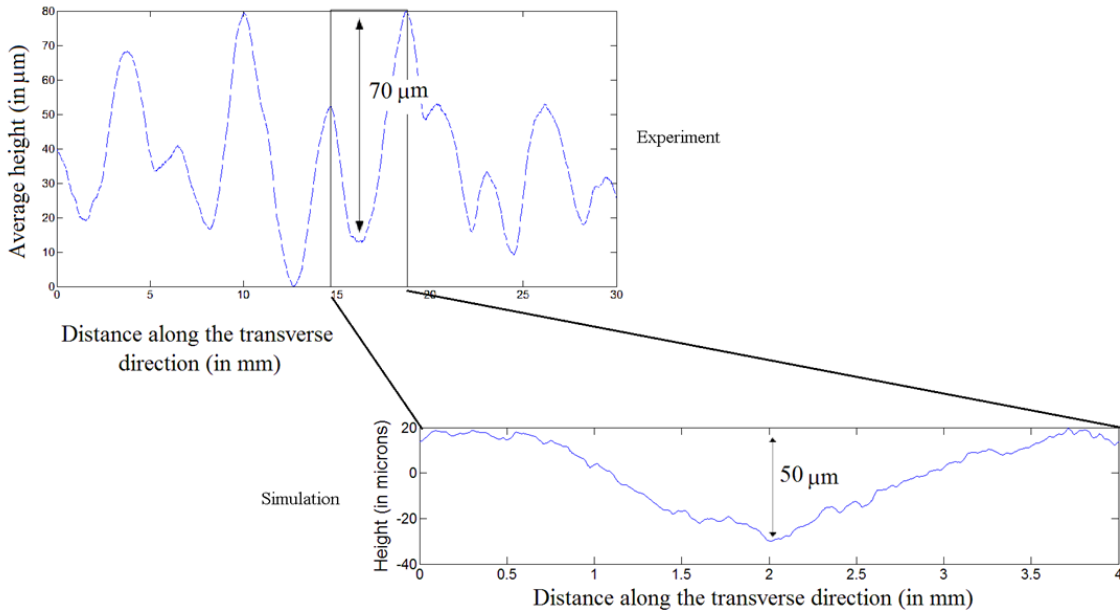


Figure 5.9: Comparison of surface roughness as measured experimentally (top) and calculated (bottom) for the AISI 409 deformed in tension to 15% along RD. Both amplitude and wavelength are in excellent agreement [93].

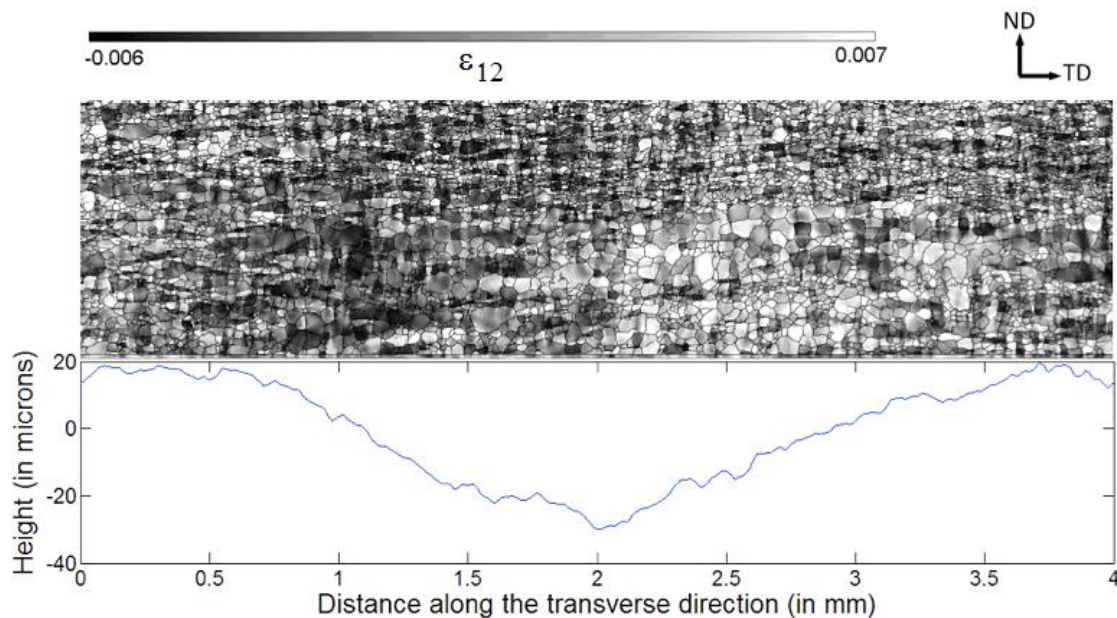


Figure 5.10: Map of the spatial distribution of out-of-plane shear strain components ϵ_{12} after 1% elongation parallel to RD (top). The intensity of this component is represented by the grey scale above the map.

5.4.3. Predicted Ridging Behaviour of AISI 445

The AISI 409 grade exhibits an extremely high level of ridging. It is thus not entirely surprising that large clusters exhibiting similar deformation behaviour could be found. Such strong correlation between microstructure and the surface roughness makes this case similar to the ideal microstructure proposed by Takechi. The two 445 alloys described in this section are more indicative of ridging formed in commercial materials.

The surface roughness predicted at 15% tensile strain and shear strain rate map are shown in Figure 5.11 and Figure 5.12 for the two AISI 445 sheets. Qualitatively it is observed that the surface roughness profiles have a lower amplitude compared to the AISI 409 grade.

Comparing the surface roughness profiles to the maps of out-of-plane shear strain rate (Figure 5.11 top and centre, and Figure 5.12 top and centre respectively), one does not clearly see the sort of clusters shown in Figure 5.10. A closer investigation, however, does show that the UA-445-R material does exhibit regions with higher than average positive and negative shear strain rate and that these correspond to changes in the slope of the surface roughness profile. These specific regions cover almost the entire thickness of

the sheet. Their dimension along TD, however, is smaller than those observed in the 409 grade (about 600 μm compared to 1.5-2 mm for the AISI 409).

Compared to the AISI 409 grade (Figure 5.10) the surface roughness of the AISI 445 grade is seen to be more complex. While the surface profile of the AISI 409 material was shown to exhibit one low frequency undulation (3.2 mm, associated with a large amplitude), with superimposed high frequency undulations, the surface profiles for the AISI 445 exhibits a wider range of wavelength and amplitude. While the auto-correlation function indicates that there is a repeating pattern at 2 mm and 3.1 mm for the UA-445-R and A-445-R materials respectively, there seems to be some undulations with smaller wavelength on the order of 1-1.5 mm.

A summary of all the characteristic dimensions of the surface roughness profiles for the three materials is presented in Table 5.1. Experimental measurements were performed at three locations along the gauge length of the sample and each roughness measurement at a given position was repeated three times for repeatability (see Appendix A).

It is seen that the characteristic dimensions obtained from the experimental surface roughness measurements and from the simulations are different, although the trends are respected for the three materials (stronger ridging for the AISI 409, followed by the UA-445-R, then the A-445-R material). The choice of the polynomial order can affect the estimation of the amplitude parameters: the higher the polynomial order, the smaller R_a , R_q and R_{max} (see Appendix A). Although the methodology used here is similar to what is used in the industry and seems to match the simulations, it is expected to see some variations in the results with the polynomial correction. This could partially explain these differences. In addition, the dimension of the microstructures used for the simulations (4-5 mm along TD) is roughly three times smaller than the dimension of the experimental surface roughness measurements (16 mm along TD). This limits the lower frequency components that can be accessed in the simulated ridging profiles (especially for the AISI 409 which exhibits only one large scale undulation).

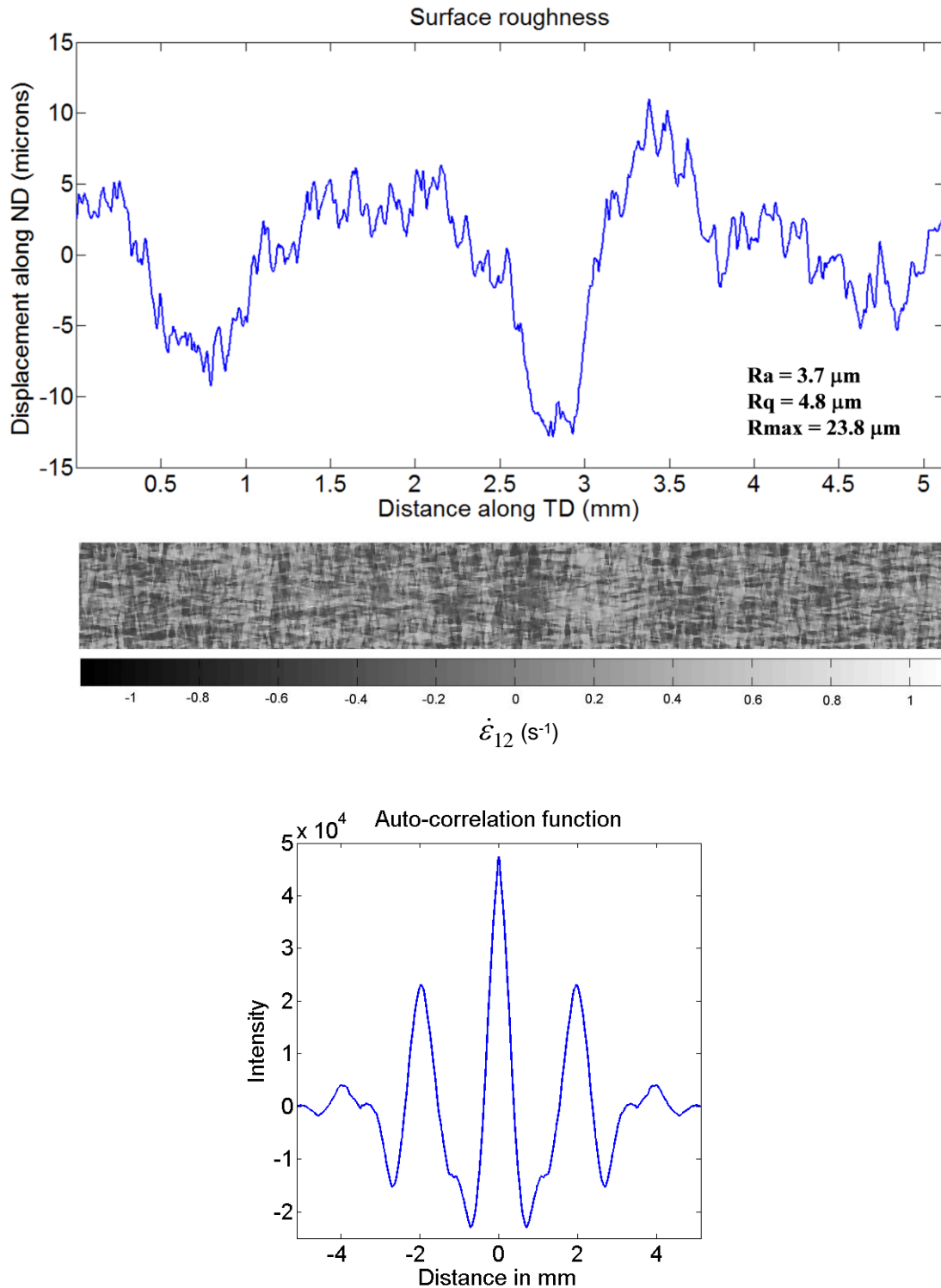


Figure 5.11: Surface roughness for the UA-445-R material (un-annealed hot band AISI 445 grade cold rolled 80% and annealed at 1010°C for 45s), calculated after 1% elongation parallel to RD and extrapolated to 15% (top), the corresponding map of spatial distribution of out-of-plane shear strain rate in s^{-1} (centre) and the auto-correlation function corresponding to the surface roughness profile (bottom).

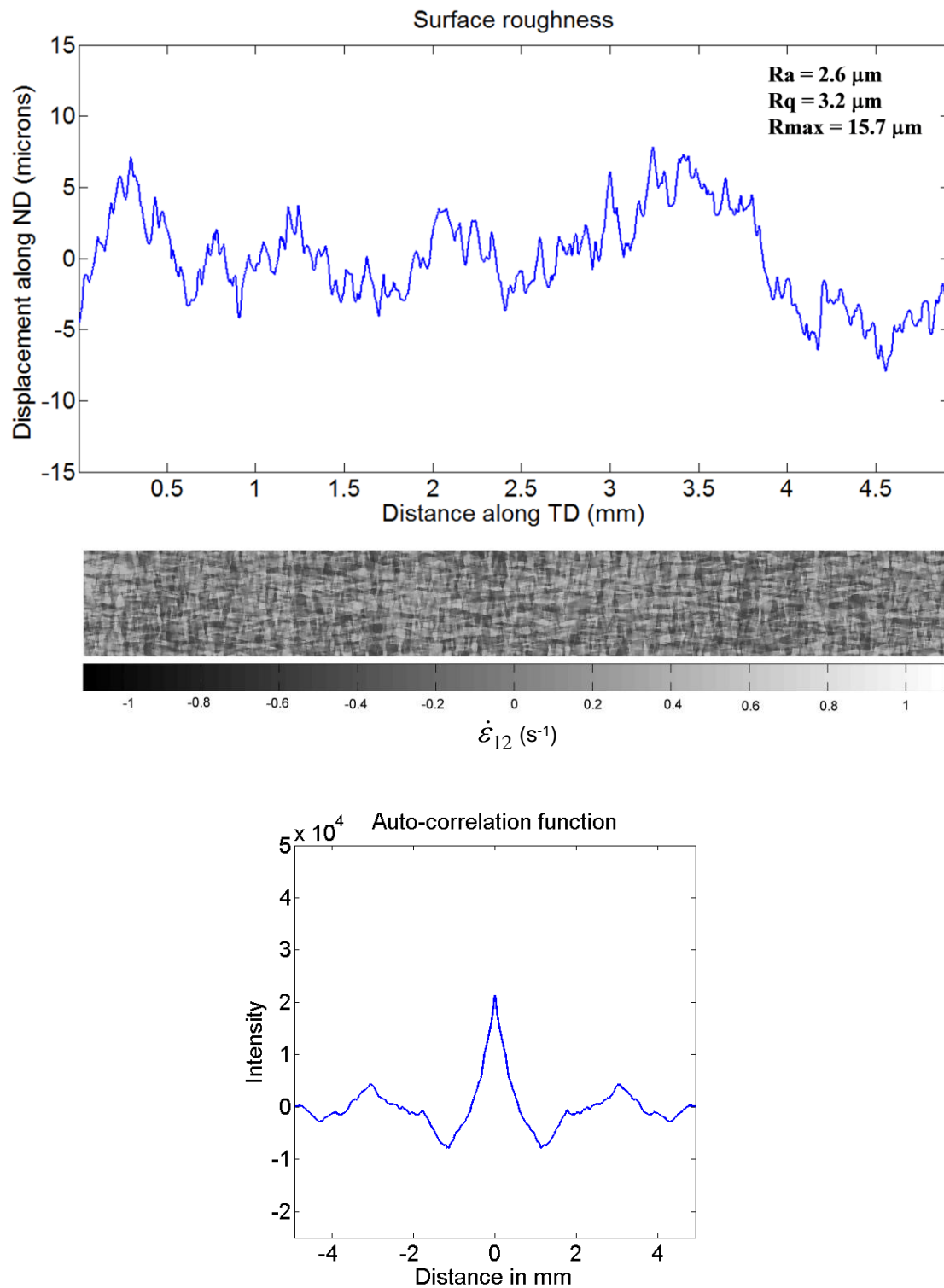


Figure 5.12: Surface roughness for the A-445-R material (annealed hot band AISI 445 grade cold rolled 80% and annealed at 1010°C for 45s), calculated after 1% elongation parallel to RD and extrapolated to 15% (top), the corresponding map of spatial distribution of out-of-plane shear strain rate in s^{-1} (centre) and the auto-correlation function corresponding to the surface roughness profile (bottom).

Table 5.1: Summary of the characteristic dimensions of ridging for the three materials as experimentally measured and predicted using the VPFFT model. The repeating patterns are obtained from the auto-correlation functions.

	AISI 409		UA-445-R		A-445-R	
	Experimental	Simulated	Experimental	Simulated	Experimental	Simulated
R_a	8.6 +/- 2.0 μm	14.1 μm	5.3 +/- 0.4 μm	3.7 μm	2.9 +/- 0.7 μm	2.6 μm
R_q	11.0 +/- 2.5 μm	15.7 μm	6.7 +/- 0.5 μm	4.8 μm	3.5 +/- 0.8 μm	3.2 μm
R_{max}	50.8 +/- 10.0 μm	50.4 μm	33.1 +/- 5.9 μm	23.8 μm	16.9 +/- 1.3 μm	15.7 μm
Repeating patterns	3.6 +/- 0.2 mm	3.2 mm	3.2 +/- 0.1 mm	2.0 mm	2.7 +/- 0.4 mm	3.1 mm

5.4.4. Effect of Neighbourhood: Mean-field Simulations

Applied to the AISI 409 material

For the three materials, the above calculations show a correspondence between the spatial organization of grains having similar shearing tendency and large scale surface roughness, the simulated surface roughness seeming to be in good agreement with that obtained experimentally. One question that arises, however, is whether local grain-to-grain interactions play a significant role in predicting this behaviour. In order to examine this, the simulations performed on the AISI 409 have been compared to predictions made using the mean-field VPSC model [47] [48]. Only this case has been studied since it presents the most obvious deformation clustering.

The VPSC model has been widely used over the past twenty years for the prediction of plastic deformation and texture change in polycrystalline materials. As a consequence, there exists an extensive literature describing this model, and the reader is invited to refer to it for more details [47] [48] [149-151].

The VPSC model differs from the VPFFT model in that it doesn't take into account the spatial distribution of crystallographic orientation. In this model, a grain is considered as an ellipsoidal inclusion embedded in an effective viscoplastic medium whose behaviour is the average behaviour of the bulk material. The calculations are done at the grain level, so the deformation within the grain is uniform.

To perform the VPSC simulations, the same set of crystallographic orientations has been used as in the VPFFT simulations, but as noted above, the VPSC simulations do

not consider their spatial arrangement. Following Engler et al [37], the deformation was simulated using a homogenization parameter of $n^{\text{eff}} = 100$ (see [47] for details). This results in a ‘Sachs’-like, nearly equal stress condition. The out-of-plane shear strain rate component $\dot{\epsilon}_{12}$ was obtained in a similar manner as from the VPFFT simulations (section 5.4.1). To visualize the results of these calculations, the out-of-plane shear strain component was mapped back onto the original microstructure for comparison with the results obtained by VPFFT.

The distributions of shear strain rate intensity obtained with VPFFT and VPSC after 1% tensile deformation along RD are compared in Figure 5.13. It can be seen that the two models predict significant differences in behaviour. The mean-field simulation predicts a large fraction of grains having either very large positive or very large negative shearing strains as well as a large fraction of grains with very low or no shearing strains (Figure 5.13(a)). The full-field simulation, on the other hand, predicts a similar fraction of grains with very low or no shearing, but very few grains with either very large positive or very large negative shearing strains. Instead, there is a relatively high fraction of grains with intermediate positive and negative shearing strains. As a consequence, the effect of considering the environment of a grain is to moderate the very high shearing tendency of individual grains due to the constraints imposed by the surrounding grains. This result is in qualitative agreement with previous simulations [41] where the effect of embedding individual grains within different orientations was studied.

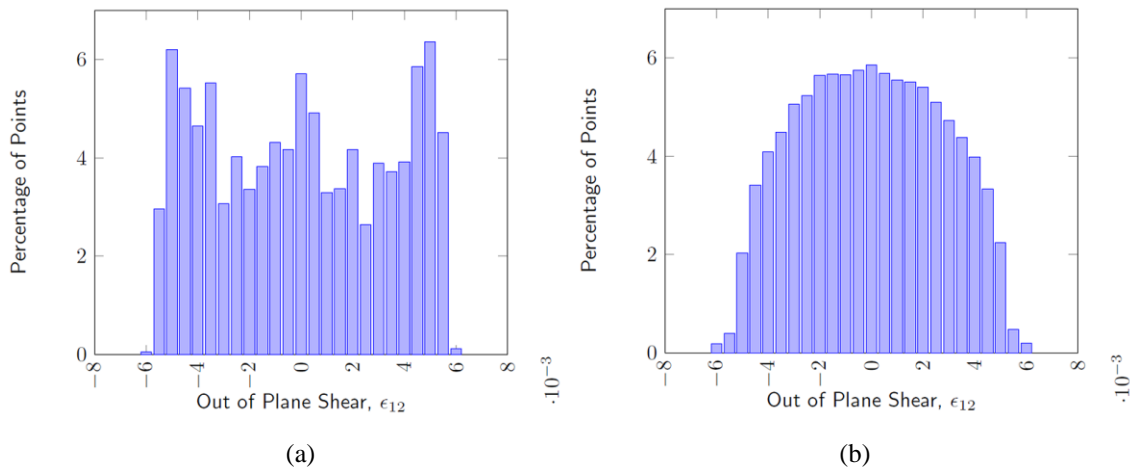


Figure 5.13: Out-of-plane shear strain distribution predicted by (a) VPSC (mean-field) and (b) VPFFT (full-field) after 1% tensile deformation along RD.

To examine these results further, grains have been divided into three groups after simulating 1% tension parallel to RD; those grains exhibiting large negative shearing tendency ($-0.006 < \epsilon_{12} < -0.002$), those exhibiting large positive shearing tendency ($0.007 > \epsilon_{12} > 0.002$) and those exhibiting low shearing tendency ($-0.002 < \epsilon_{12} < 0.002$). The color black was associated with large negative values, grey with low values, and white with large positive values. The spatial distribution of shearing tendency using this scheme is shown for both full-field and mean-field predictions in Figure 5.14. Qualitatively, both simulations reveal similar features, notably the large positively and negatively shearing groups of grains previously highlighted in Figure 5.10. The main difference between the two methods is the fact that there are many cases of black and white (opposite shearing) regions being directly adjacent in the case of the mean-field calculations.

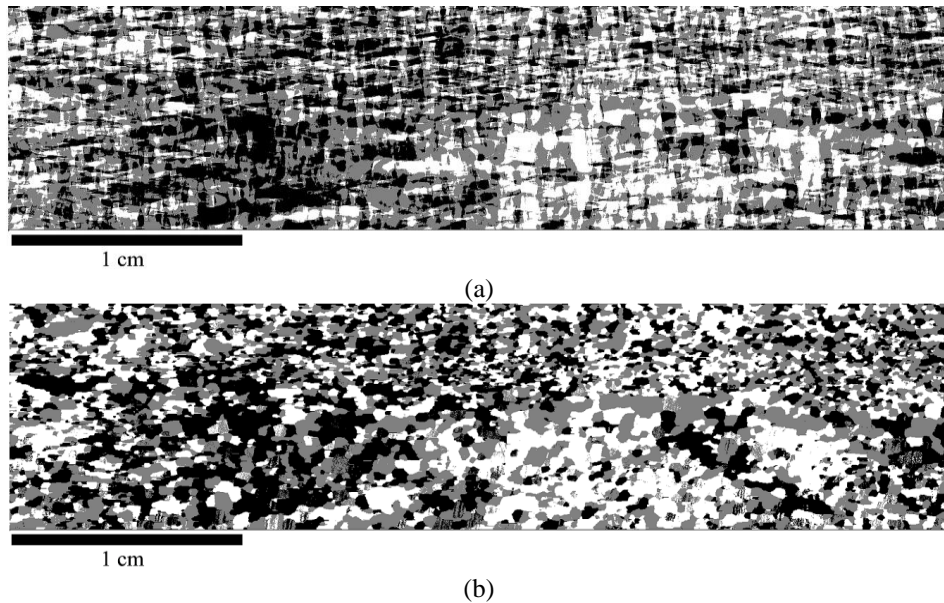


Figure 5.14: Spatial distribution of out-of-plane shear strain intensity calculated with VPFFT (a) and VPSC (b). The color black represents regions with large negative shear strain intensity ($-0.006 < \epsilon_{12} < -0.002$), the color grey represents regions with low shear strain intensity ($-0.002 < \epsilon_{12} < 0.002$) and the color white represents regions with large positive shear strain intensity ($0.007 > \epsilon_{12} > 0.002$).

This has been quantified by counting the number of neighbouring points having different colours (white/grey, white/black, black/grey) in the maps. Each point from the microstructures presented in Figure 5.14 was examined and compared with its four closest neighbours. When neighbouring points belonged to different categories of

shearing intensity, their interface was considered and counted. As seen in Figure 5.15, the total number of black/grey and white/grey interfaces is much larger for the full-field simulation compared with the mean-field simulation. This increase of high shearing/low shearing interfaces (either black/grey or white/grey) is compensated by a large decrease of high positive/high negative (white/black) interfaces, this being consistent with Figure 5.13.

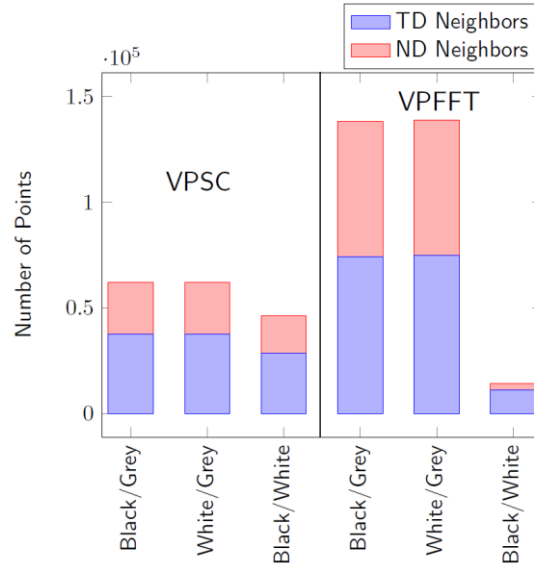


Figure 5.15: Histogram of the nature of the interfaces between regions of different shearing behaviour (black=high negative shear strains, grey=low shear strains, white=high positive shear strains). Differentiation has been made depending on the directionality of the neighbours (TD vs. ND).

These results also highlight the importance of capturing the microstructure in the RD plane when considering the quantitative prediction of ridging. Indeed, in the case of black/white interfaces (regions of high but opposite shearing tendency), the mean field calculation predicts that 39% of them are aligned parallel to ND. When interactions between neighbours are taken into account (VPFFT), this value drops to 22%. This means that the interaction between adjacent grains strongly prevents the shearing tendency of individual grains when they are aligned in the vertical direction (ND) compared to when these grains are aligned along TD. This last observation is consistent with the fact that the deformation of grains with opposite shearing tendency, when aligned parallel to TD, can be easily accommodated, as proposed by Takechi et al [21].

Although ND plane maps usually exhibit significant banding of grains for a specific position through the thickness, the actual shearing behaviour of that layer will depend on the behaviour of the layers directly above and below it. If similar banding of grains having the opposite shearing tendency occurs directly above or below that plane, their individual effects will be cancelled, leading to low levels of ridging. For similar reasons, if a ND plane map does not show significant banding, it does not necessarily mean that the sample will be ridging-free. Thus the cumulative effect of different layers, each of them exhibiting very little banding, can lead to a strong ridging.

Finally, the correlation between orientation and shearing tendency has to be considered. As noted at the beginning of this section, there is no clear indication from the EBSD map in Figure 5.2(c) that clusters of similarly deforming grains exist in Figure 5.14. The VPFFT simulation results were separated into two subsets based on the sign of the out-of-plane shear strain rate for each simulation point. The orientation distribution function (ODF) has been calculated for each of these two sets of data and are represented as $\varphi_2=45^\circ$ sections of Euler space in Figure 5.16. Assuming orthotropic sample symmetry, the points exhibiting opposite shearing sense appear to have statistically identical orientations. In order to clearly see the differences in orientation corresponding to the differences in shearing tendency, one must consider a lower triclinic sample symmetry. The same ODFs considering triclinic sample symmetry are presented in Figure 5.17.

The distinction between orientations with different shearing behaviour is now clear. Some orientations of the ODF are clearly responsible for positive shear strains (φ_1 close to $0-30^\circ$ and close to $330-360^\circ$), whereas other orientations are responsible for negative shear strains (φ_1 close to $150-210^\circ$). It can be noted that these orientations are close to orientations lying on the two α -fibres defined by (i) $\varphi_1=0^\circ$, $0^\circ < \Phi < 54.7^\circ$ and $\varphi_2=45^\circ$ and (ii) $\varphi_1=180^\circ$, $0^\circ < \Phi < 54.7^\circ$ and $\varphi_2=45^\circ$. However, it can be seen on Figure 5.17 that some orientations can shear in both directions (for φ_1 around 90° and for φ_1 around 270° on the γ -fibre). These orientations most likely correspond to orientations having low net shearing tendency (as seen from Figure 2.14) that can be influenced by the surrounding materials, as mentioned in [41].

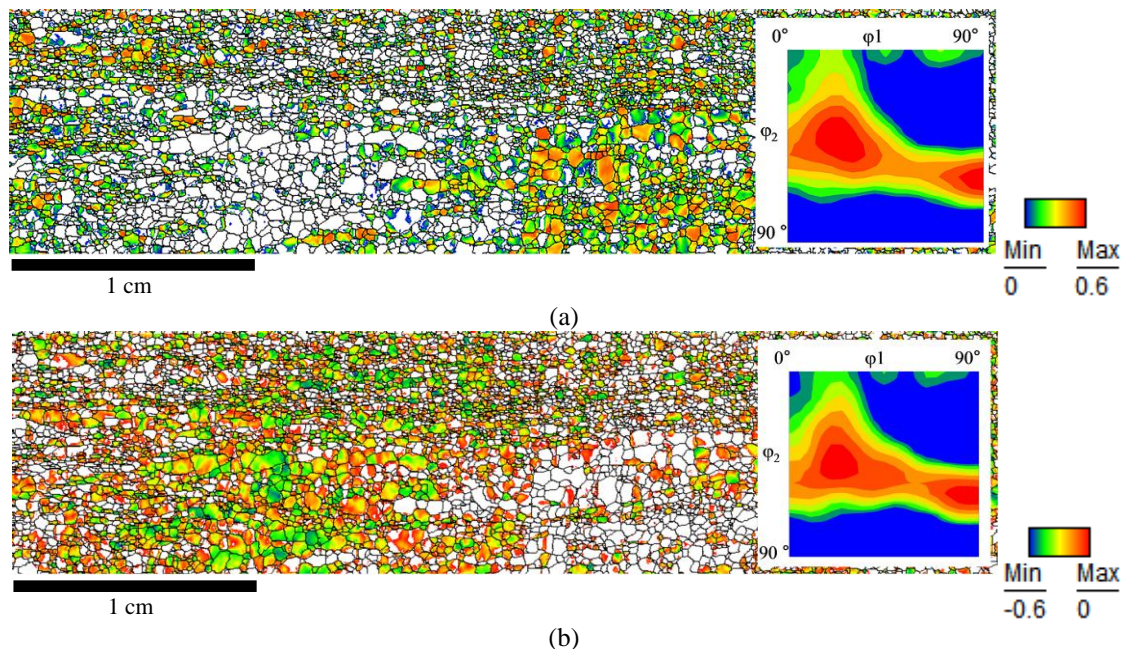


Figure 5.16: Section $\varphi_2=45^\circ$ of the Euler space representing the ODF calculated from (a) the regions having positive shear strain rate, and (b) the regions having negative shear strain rate, assuming orthotropic symmetry. The color scaling corresponds to shear strain rates.

When the ODF from the positively and negatively shearing orientations are combined, the global texture is similar to the bulk texture calculated by XRD on that material, as presented in [42], composed of the typical shifted γ -fibre.

These results can be rationalized when the shearing tendency of individual grains is considered (Figure 5.18). This figure is an extension to the triclinic symmetry of what has been presented in the literature review (Figure 2.14(b)). The shear strain rates were calculated using the VPSC model for multiple orientations on a regular grid (every 5° along φ_1 and Φ) assuming simple relaxed Taylor conditions on single crystals.

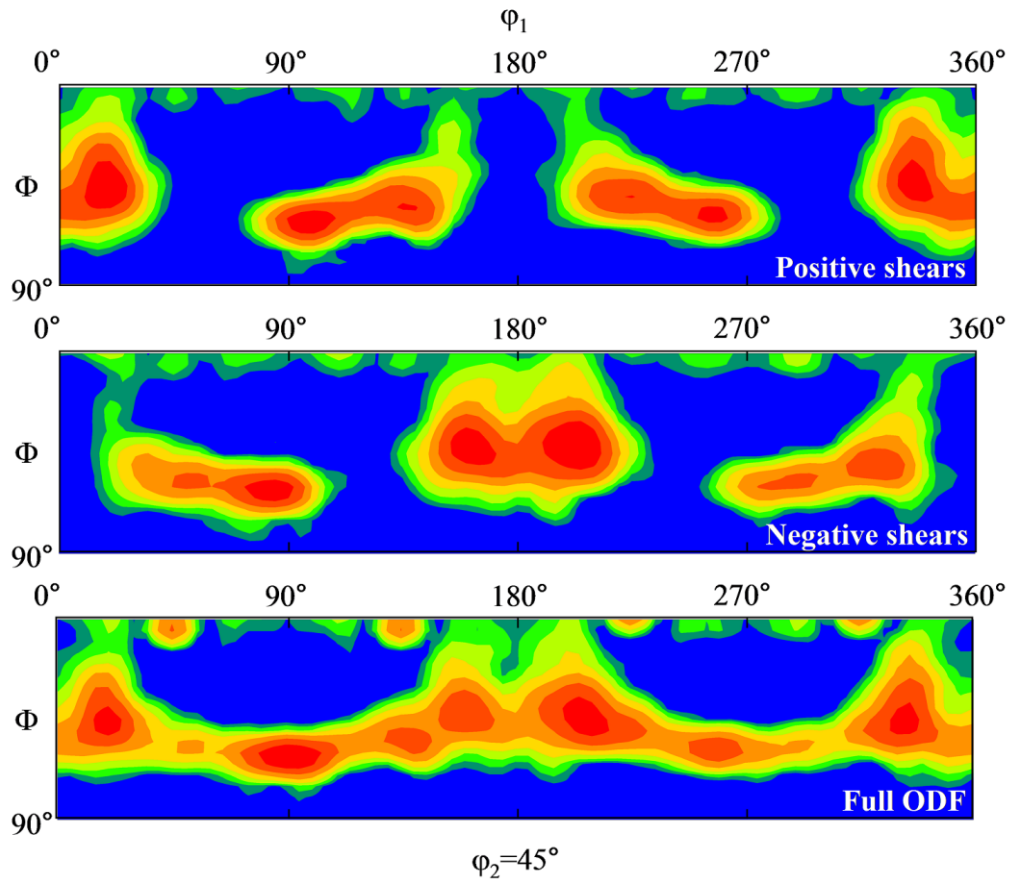


Figure 5.17: Section $\phi_2=45^\circ$ of the extended Euler space representing the ODF calculated from the regions having positive shear strain rate (top) and the regions having negative shear strain rate (centre), assuming the sample symmetry to be triclinic. At the bottom is the combined ODF from the two previous subsets, also assuming triclinic sample symmetry.

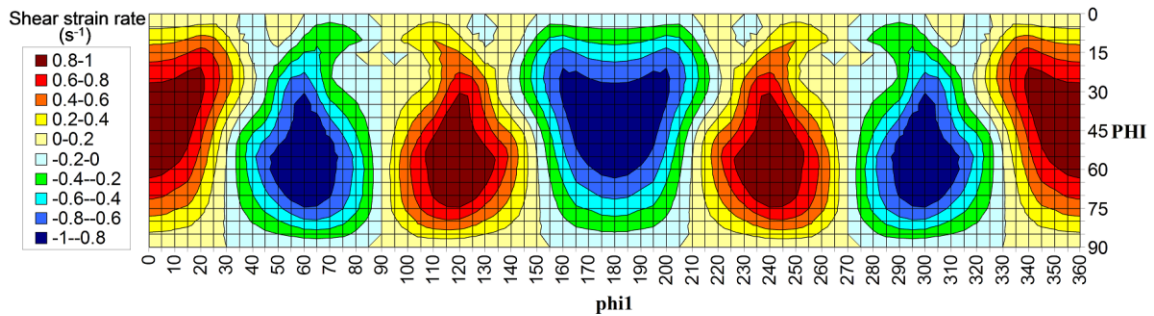


Figure 5.18: Intensity of the out-of-plane shear strain rate calculated for each orientation of the $\phi_2=45^\circ$ section of the Euler space on a regular grid (5° along ϕ_1 and Φ). The calculations were performed with the VPSC model assuming that each orientation was a single crystal deformed under relaxed Taylor conditions.

5.5. Correlating Microstructure to the Spatial Heterogeneities Responsible for Ridging

Despite having fairly similar textures and microstructures, the three materials described above all show quite different ridging behaviour. What is not clear from these simulations and experiments is which features have the most significant role in determining the amplitude and wavelength of ridging. In order to systematically study the effect of individual parameters, synthetic microstructures were created containing well defined clusters in the spirit of the original Takechi model. In this case, the effects of (i) the spatial distribution of orientations within a cluster, (ii) the grain size and (iii) the fraction of positive and negative shearing orientations in a cluster have been evaluated.

A Matlab routine was specifically developed in this work for the generation of the synthetic microstructures. This code is able to generate two-dimensional grain structures using Voronoi tessellations with periodic boundary conditions. A grid of Fourier points (2048x256 points) is then superimposed on the microstructure. The code also assigns crystallographic orientations to each Fourier point and is able to generate various spatial distributions of specific crystallographic orientations assuring a strict control of the non-random distribution of features with specific mechanical behaviour. The VPFFT simulations were then run in a similar manner to those presented in section 5.4 and the results presented after 1% macroscopic tensile strain imposed parallel to RD.

From the results of the simulations on experimental microstructures, one clear difference between the AISI 409 and the two AISI 445 conditions is the presence of large areas where grains with high positive or high negative shear strain rates are next to each other (Figure 5.10 compared to Figure 5.11 and Figure 5.12 centre). This raises the question whether the spatial distribution of orientations through the thickness of the sheet impacts the average through thickness shearing tendency. To study this effect, clusters were artificially introduced within the RVE. It was assumed that each cluster is composed of orientations with high shearing tendency (orientations within 15° of $\{111\}\langle 110\rangle$) and represents one third of the sheet thickness. The rest of the microstructure was randomly assigned orientations representative of the recrystallized bulk texture. The spatial

distribution of orientations in each cluster was varied from a ‘compact cluster’ (where all high shearing orientations are grouped together within the central third of the sheet, as presented in Figure 5.19(a)) to a ‘dilute cluster’ (where the high shearing orientations are distributed throughout the entire thickness, such as presented in Figure 5.19(b)).

The results of these simulations are presented in Figure 5.19(c). It is seen that the surface roughness developed during tensile deformation is independent of the through thickness distribution of shearing orientations within delimited regions along TD (under the condition that all other parameters are kept constant, e.g. intensity of shearing orientation and dimension of the regions along TD).

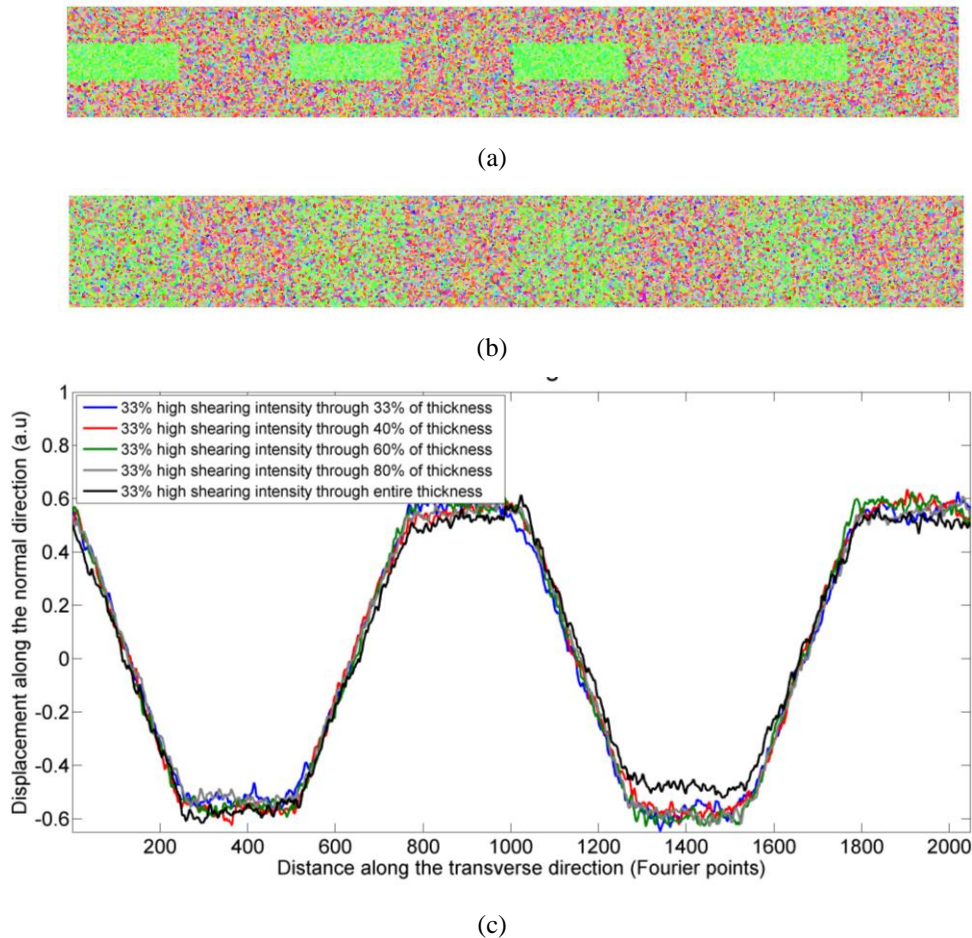


Figure 5.19: Effect of through thickness distribution of shearing orientations in clusters on surface roughness developed during tensile deformation. Each region defining a ‘cluster’ is composed of 33% of shearing orientations surrounded by a matrix representative of the recrystallized bulk texture. Shearing orientations are distributed within (a) the central 33% of the thickness and (b) the full thickness. (c) Surface roughness profiles for different through thickness spatial distribution showing an identical behaviour for the conditions tested.

The second main difference between the high ridging AISI 409 and the low ridging AISI 445 materials is the grain size (34 μm and 19-20 μm respectively). The effect of grain size was estimated by varying the number of seeds in the Voronoi tessellation and keeping the RVE dimensions constant. The number of grains was varied from 1,000 to 25,000, corresponding to 10 to 55 grains through the thickness of the microstructure and these two extreme conditions are represented in Figure 5.20(a) and Figure 5.20(b) respectively. Clusters with high shearing tendency were manually introduced in a similar manner as presented above.

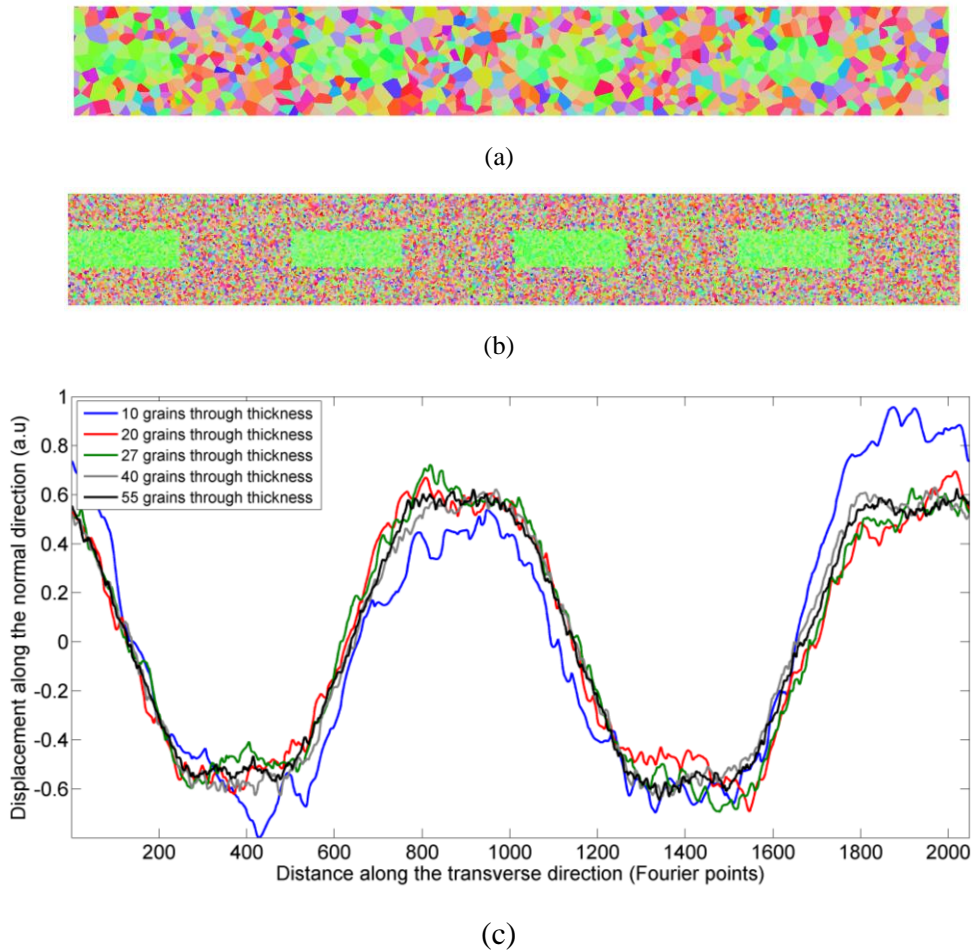


Figure 5.20: Effect of grain size on surface roughness developed during tensile deformation. The RVE is populated with (a) 1000 seeds (10 grains through the thickness) and (b) 25000 seeds (55 grains through the thickness). Clusters are composed of shearing orientations and are surrounded by a matrix representative of the recrystallization bulk texture. (c) Surface roughness profiles for different grain sizes showing an identical behaviour for the conditions tested.

The results of the simulations (Figure 5.20(c)) show that the grain size does not impact the surface roughness after deformation. It can be noted, however, that for the larger grain sizes, the high frequency surface roughness becomes noisier and a second type of undulation (high frequency and low amplitude) is superimposed to the roughness attributed to ridging. There is thus a local effect of grain size on the secondary undulation whose dimension is related to the grain size. This does not appear, however, to influence the surface roughness characteristic of ridging.

A less obvious parameter from the experimental microstructures, but already proven to impact the ability of grains to rotate due to shearing on a mean field level [41], is the fraction of positive and negative shearing orientations in a specific region. This effect was estimated by modifying the initial Takechi (Figure 5.21(a)) model by randomly introducing different types of orientation within a cluster by (i) introduction of grains into a cluster with the same shearing intensity but opposite sign (Figure 5.21(b)), (ii) introduction of random orientations into a cluster, or (iii) introduction of non shearing orientations ($\{111\}\langle 112\rangle$) into a cluster. Microstructures for (ii) and (iii) are not shown since they look similar to those shown in Figure 5.21(b). The resulting effect on ridging amplitude (in terms of R_a value after normalization by the sheet thickness) is presented in Figure 5.21(c).

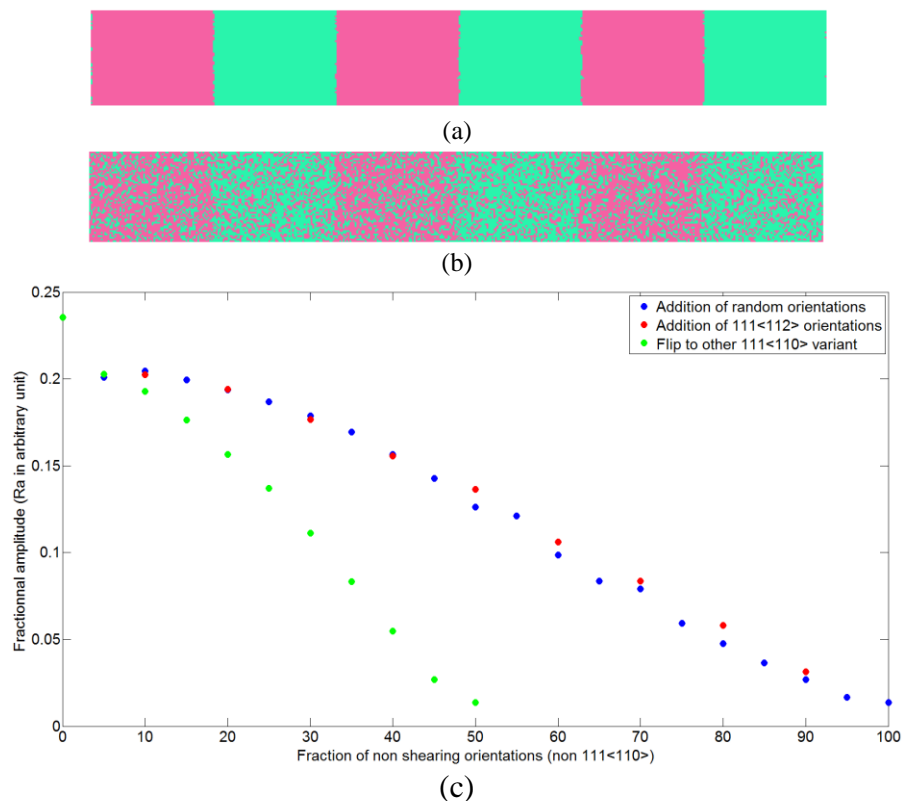


Figure 5.21: Effect of dilution of clusters by introduction of different orientations. a) Initial Takechi model [21] composed of blocks of each of the two $\{111\}\langle 110\rangle$ orientations, b) introduction of anti-shearing orientations in each block (orientations with same intensity of shearing but opposite sign), and c) effect of introduction of different orientations on the amplitude of ridging, calculated as the R_a value. The colors in (a) and (b) are randomly chosen for the two $\{111\}\langle 110\rangle$ variants.

All three cases show a similar trend. The amplitude decreases linearly with increasing ‘dilution’ of the clusters. This behaviour can be explained by the interaction with neighbouring grains which tends to prevent the rotations of grains with high shearing tendency (similarly to what has been shown by Sinclair [41]). It is seen that the introduction of the other variant of $\{111\}\langle 110\rangle$ reduces more drastically the amplitude compared to when random or non-shearing orientations are introduced. This can be explained by their higher shearing tendency. It is expected that the interactions between grains with opposite shearing tendency but with similar intensity are stronger than between a grain with high shearing tendency and a grain with either no or low shearing tendency. In the latter case, the low or no shearing orientations would be ‘dragged along’ by the rotation of the highly shearing grains [41], leading to a lower reduction of the overall shearing. A representation of such interactions can be seen in Figure 5.22 where

histograms of out-of-plane shear strain rate are represented in the case of case (i) above. It appears that introducing orientations with a different shearing behaviour drastically decreases the fraction of grains that strongly shear and increases the fraction of grains with a more moderate shearing tendency. As a consequence, the surface roughness of the sheet decreases as the clusters are ‘diluted’.

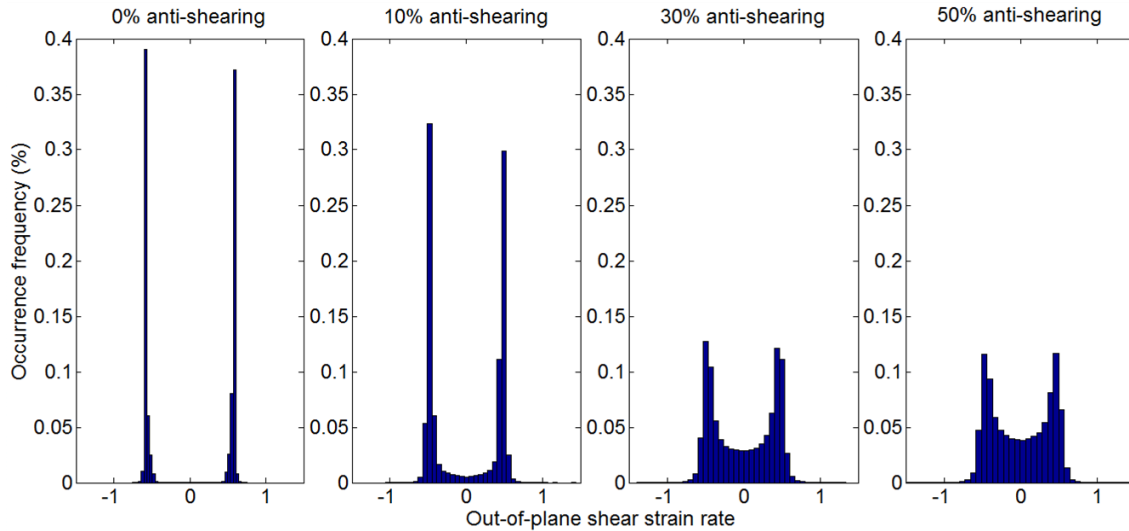


Figure 5.22: Distribution of the out-of-plane shear strain rate intensity (a) for the ideal Takechi model (each cluster is composed of a unique variant of $\{111\}\langle 110\rangle$), (b) when 10% of “anti-shearing” orientation are randomly introduced in clusters, (c) when 30% of “anti-shearing” orientation are randomly introduced in clusters and (d) when 50% of “anti-shearing” orientation are randomly introduced.

This observation, that by reducing the volume fraction of grains with similar shearing tendency within a specified volume of the microstructure decreases the ridging amplitude likely explains the main differences in ridging behaviour between the strongly ridging and clearly clustered AISI 409 material and the more weakly ridging and less clearly clustered AISI 445 alloys. Combining the results of the previous simulations, it is seen that there is no need of clusters as they were defined at the beginning of this section (aggregate of continuously connected grains). Instead, it is required to have regions within the thickness of the microstructure that have, on average, a higher fraction of either positive or negative shearing behaviour. In what follows, the term cluster will therefore not be used. The features responsible for ridges will be referred to as regions

with higher than average fraction of grains having one type of out-of-plane shearing behaviour.

The previous simulations all assume that there exist some regions along TD where the fraction of shearing orientations of one sign is, on average, higher than the fraction of shearing orientations of the other sign. To see how far away the materials studied here are from having such a simple random positive and negative shearing, the distribution, along TD, of the sign of vertical displacements of the surface for the different experimental materials was compared with the surface roughness of a synthetic material where the sign of the vertical displacements were randomly selected along TD. To do this, the RD section was discretized into sections whose vertical displacement is the net behaviour of the cumulative displacements of all points in the thickness. As a consequence, this simplified microstructure is similar to the one proposed by Takechi [21], and the effect of all the grains lying on top of each other superimpose leading to a corrugation of the sheet responsible for the observable ridging, as represented in Figure 5.23 [30].

The sheet thickness of the different materials was thus discretized into columns of points (along ND) and the net vertical displacement of each column was estimated by summing all the vertical components of the strain field at each point (caused both by shearing strains and by normal strains). For each column, a value of +1 or -1 was assigned if the net vertical displacement was positive or negative, respectively. Practically, this was done by comparing the y-position of each point on the surface profile to its neighbour on the left. A positive relative displacement was assigned to this point if its y-position is higher than the y-position of its left neighbour. Alternatively, a negative relative displacement was assigned.

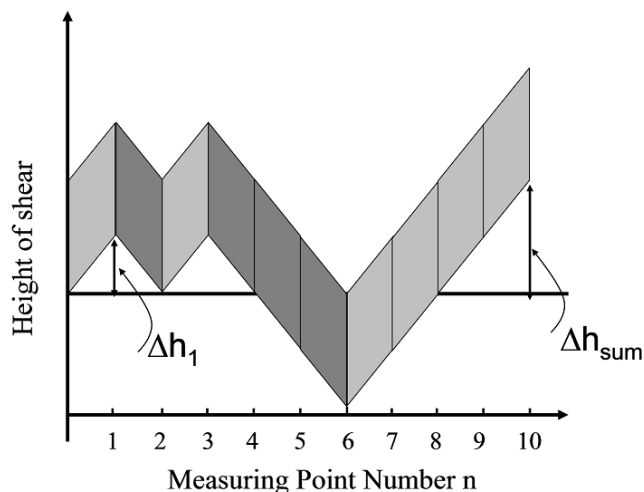


Figure 5.23: Schematic of the effect of the out-of-plane shear strain rate on the RD plane. In vertical section through the thickness, the shear components are summed up, leading to a local vertical displacement. Adjacent sections along TD provide a cumulative effect leading to the overall undulations. Adapted from [30].

The continuity (along TD) of similar vertical displacements (along ND) was estimated by creating bins containing 20 of the previously defined vertical columns¹¹ and by counting the number of positive vertical displacements in each bin. A bin containing a majority of positive vertical displacements will lead to a section of the surface roughness curve with a positive slope (such as the right hand side half of the curve presented in Figure 5.10), whereas a bin containing a majority of negative vertical displacements will contribute to a section of the surface roughness curve with a negative slope (such as the left hand side half of the curve in Figure 5.10). A schematic summarizing this methodology is presented in Figure 5.24.

¹¹ This number of columns in each bin was chosen to take into account the behaviour over 2 to 3 grains (around 40-50 μm) along TD. This assures a minimum distance over TD to look at the adjacent vertical displacements such that the results would not be determined by a single grain.

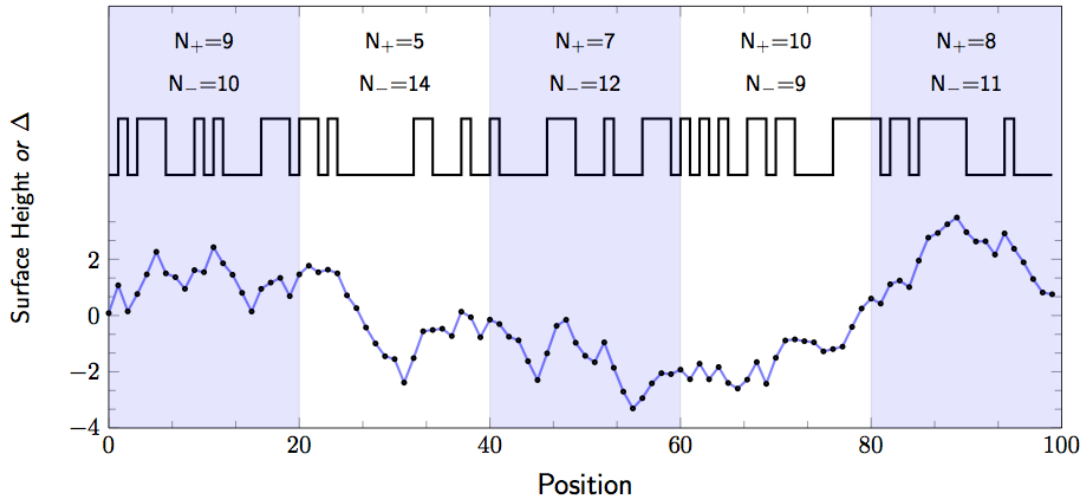


Figure 5.24: Illustration of how the simulated surface roughness (bottom) was used to calculate the incremental displacement (Δ) associated with each surface nodal point (top).

Finally, the histogram representing the frequency of occurrence of having k positive vertical displacements per bin ($k=[0, \dots, 20]$) has been plotted. For each of the materials studied, the results have been compared to the histogram obtained with a random distribution of positive and negative vertical displacements. This random distribution, described as a stochastic process similar to the result of a coin tossing experiments [30], leads to a binomial distribution, where the probability of finding exactly k positive vertical displacements in n trials is given by:

$$P(k) = \binom{n}{k} \cdot p^k \cdot (1-p)^{n-k} = \frac{n!}{k!(n-k)!} \cdot p^k \cdot (1-p)^{n-k} \quad (5.6)$$

where p is the probability of successfully getting a vertical displacement ($1/2$ in the case of a coin tossing experiment).

As seen from the results in Figure 5.25, the net vertical displacements are clearly not randomly distributed along TD. On the contrary, there is a much higher probability of finding multiple similar vertical displacements consecutively in the experimentally measured microstructures compared to a synthetic microstructure where vertical displacements are randomly distributed. This is especially true for the AISI 409 grade which exhibits a high fraction of only positive or negative vertical displacements in bins of 20 columns (corresponding to about $40 \mu\text{m}$). For both AISI 445 grade conditions

(annealed hot band and un-annealed hot band), the distributions are closer to the binomial distribution, although they remain clearly non random. It is surprising to see that despite the different ridging behaviours of the two AISI 445 materials (Figure 5.11 and Figure 5.12), the two histograms of their spatial distribution of shearing tendency along TD are quite similar.

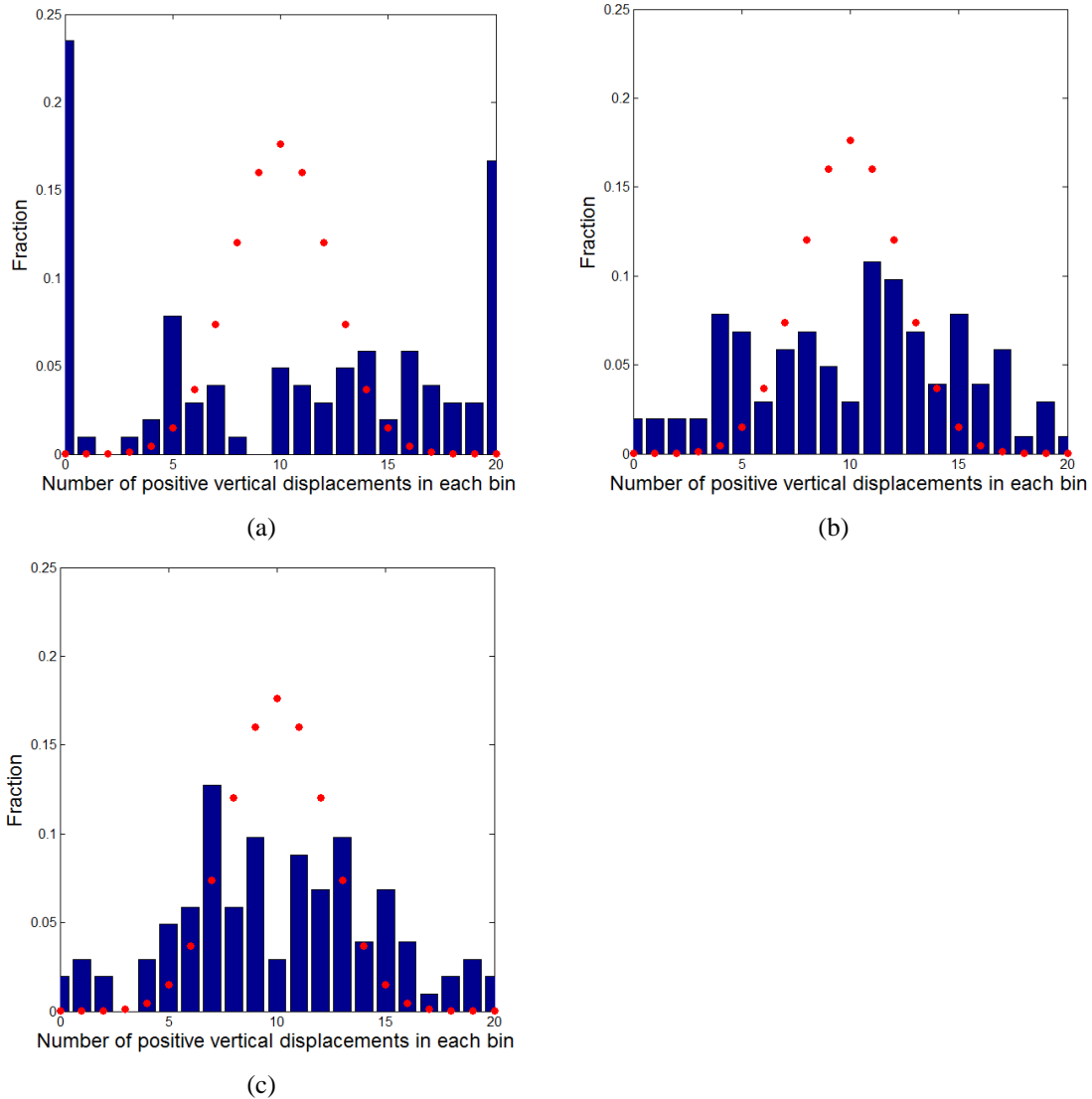


Figure 5.25: Histograms of the frequency of having k ($k=0, \dots, 20$) positive vertical displacement in a bin containing 20 adjacent vertical sections along TD for (a) the AISI 409 grade, (b) the UA-445-R, (c) the A-445-R. The red dots represent the theoretical probability given by a binomial distribution for a random distribution.

A quantitative measure of how far the spatial distribution of shearing behaviours from a random distribution is, can be given by an arithmetical mean deviation:

$$D = \frac{1}{nb} \sum_{k=1}^{nb} \|P(k) - f(k)\| \quad (5.7)$$

where nb is the number of bins, P(k) is the probability previously described in equation (5.6) and f(k) is the frequency of finding k positive displacement in the experimentally measured microstructures. The results for the 3 cases studied (the AISI 409 and the two AISI 445) are presented in Table 5.2.

Table 5.2: Arithmetical mean deviation values between the binomial distribution and the experimental distribution of shearing behaviour for the three cases presented in Figure 5.24.

Material	AISI 409	UA-445-R	A-445-R
D	0.1729	0.0596	0.0501

As can be seen, the AISI 409 exhibits a large D value, corresponding to a large deviation from the random case, whereas the two AISI 445 final products exhibit very similar and much lower D values.

This suggests that the differences in ridging behaviour of the two materials UA-445-R and A-445-R does not come from the spatial distribution of orientations with similar shearing tendency but instead from the fact that the material processed from the un-annealed hot band material is composed of more orientations with higher shearing tendency than the material processed from the annealed hot band. This result is first confirmed by the bulk texture (e.g Figure 5.4 vs Figure 5.6), which shows that the UA-445-R material contains a higher volume fraction of orientations on the shifted γ -fibre compared to the A-445-R material, those orientations having a higher shearing tendency compared to orientations closer to $\{111\}\langle 112 \rangle$ (Figure 5.18). The importance of the difference in the intensity of shearing of orientations in this case can also be seen if the data contained in the out-of-plane shearing maps (Figure 5.11 centre and Figure 5.12 centre) is plotted as histograms as shown in Figure 5.26. Here it can be seen that the UA-445-R material (Figure 5.26(a)) has a higher fraction of grains with high positive and

high negative out-of-plane shearing compared with the A-445-R material (Figure 5.26(b)), as can be seen by the plot of the difference in fraction (Figure 5.26(c)).

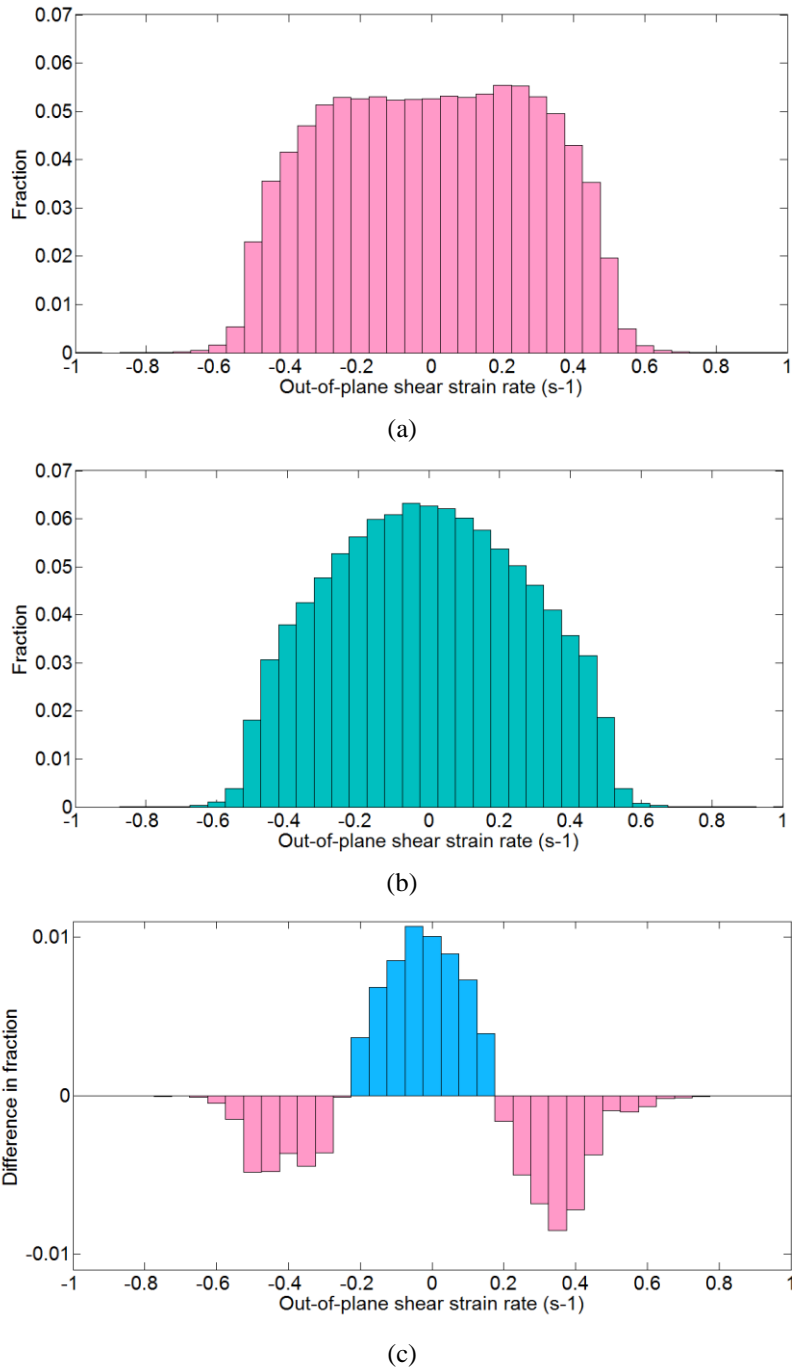


Figure 5.26: Histograms of the frequency of shear strain rate for (a) the UA-445-R materials and (b) the A-445-R, from Figures 5.11 and 5.12 respectively. (c) is the difference between (b) and (a), showing that the data in (a) contains a higher fraction of points with high shear strains and (b) has a higher fraction of points with low shear strains.

This effect cannot, however, be generalized to every ridging case. Indeed, if one compares the bulk texture of the AISI 409 and of the UA-445-R materials (Figure 5.2(c) and Figure 5.4(c) respectively) and the spatial distribution of their shearing tendency along the TD (Figure 5.25(a) and Figure 5.25(b) respectively), one sees that the major parameter responsible for the difference in ridging between these two materials is the difference in the spatial distribution of grains with similar shearing tendency rather than the difference in the intensity of the shearing, since the bulk textures are very similar.

The comparison between these three materials shows that ridging is a complex phenomenon that can not be simply explained by either a parameter indicative of the non-random distribution of features or by shearing intensity considerations. It is rather an intricate combination of both which highly depends on other parameters such as alloy composition and process history.

The severity of ridging can be reduced either by decreasing the volume fraction of highly shearing orientations in a given region of material, or by randomizing the distribution of shearing along TD. Both cases lead to an apparent decrease of clustering (as observed on the out-of-plane shear strain rate distribution maps, Figure 5.10, Figure 5.11 and Figure 5.12), and have been experimentally seen to reduce ridging.

5.6. Conclusion

VPFIT simulations have been used to successfully reproduce the basic aspects of the surface roughness developed during the tensile deformation of ferritic stainless steel sheets from experimental microstructures when the microstructure was measured on the RD plane. Comparison between calculated surface roughness and experimentally measured surface roughness with a profilometry showed agreement, both in terms of amplitude and distance between repeating patterns. In the case of samples exhibiting strong ridging, this technique revealed the presence of large clusters of grains presenting either strong positive or negative out-of-plane shear strain rate corresponding to sharp changes in the slope of the surface roughness. For samples with low ridging levels, it was seen that such ‘clusters’ are not necessarily present, but there still exists some regions of

the microstructure which present a non-random spatial distribution of grains having positive or negative shearing behavior. It was also seen that strong interactions between neighboring grains can drastically reduce the shearing behavior of strongly out-of-plane shearing orientations, especially when the neighboring grains are oriented along ND.

Synthetic microstructures have been generated to estimate the effect of individual parameters on the amplitude and wavelength of the corrugations. The results showed that the amplitude is strongly dependant on the fraction of shearing orientations along the normal direction, and do not depend on the spatial distribution of these orientations through the thickness, nor on the grain size. The distance between repeating patterns is determined by the distance along TD over which the fraction of shearing orientations of one sign is on average larger than the volume fraction of shearing orientations of the other sign.

These results show that it can be hard to visualize ‘clusters’ with sharp boundaries and that ridging can still be present even when no visually obvious banding exists (Figure 5.19). This is an important point as most of the studies on ridging focus on the observation of ‘clusters’, although clusters are never clearly defined. These results suggest that spending time and resources to observe clusters is a delicate issue that can potentially lead the observer to incorrectly attribute ridging to features in the microstructure that are not the ones directly responsible for it.

Chapter 6: Microstructure and Texture Evolution During the Final Annealing

6.1. Introduction

In the previous chapter it was shown that the distribution of out-of plane shearing is non-uniformly distributed for the three materials studied. This, combined with the bulk texture, was shown to be the most important characteristic governing ridging behaviour. The difference in ridging observed for the materials obtained from the un-annealed and the annealed AISI 445 hot band points to the effect of multiple annealing steps in reducing ridging by texture modification, consistent with previous work [17].

As mentioned in the literature review (section 2.5.2), it is well accepted that recrystallization of ferritic steels occurs by the preferential replacement of deformed α -fibre oriented grains with recrystallized γ -fibre or shifted γ -fibre oriented grains. Information on how the spatial distribution of grains with different textures develops during recrystallization remains, however, unknown. This is important if one wants to understand and control the ridging response shown in Chapter 5.

In this chapter the recrystallization behaviour of the material processed starting from the annealed AISI 445 hot band following cold rolling (80% reduction) is focused on. This material most closely matches that produced industrially and therefore understanding its recrystallization behaviour is of high practical importance. The microstructure and texture evolution has been quantified starting from the cold rolled state, with observations being made for increasing levels of recrystallization. In analyzing this data specific attention has been paid to the ‘nucleation¹²’ and growth of specific texture components, i.e. those outlined in Chapter 5 as being important for ridging.

The study of recrystallization in this chapter has been performed on the TD and ND planes. The TD plane is the one that is classically used to characterize recrystallization in ferritic steels [43] [63] [92] [93]. However, it can be estimated (by

¹² The term nucleation is used in this section to describe the earliest stage of recrystallization. It does not imply the formation of a small crystallite caused by fluctuations. In the present case, nucleation corresponds to the development of a nuclei, defined by a small volume having a low dislocation density and surrounded by grain boundaries having misorientations $> 5^\circ$. These are able to grow at the expense of the deformed matrix forming recrystallized grains in the final microstructure [64].

characterization of the dimensions of a deformed grain and the average grain size in the final product) that following 80% reduction a deformed grain is usually replaced by recrystallized grains that pass through its full thickness. In order to have more information about the replacement of a deformed grain by multiple new recrystallized grains, observations were made in the ND plane at the mid-thickness of the sheet. This plane is usually the one that exhibits the most apparent orientation banding in EBSD maps (see section 2.4). From the information gleaned from the ND and TD planes one can extrapolate to understand how recrystallization would appear in the RD plane.

Because the study of recrystallization, especially in the early stages, requires the observation of relatively fine details (one needs to capture features that are on the order of $1\mu\text{m}$ or smaller), the dimensions of the EBSD maps presented in this chapter are smaller than the characteristic dimensions separating hills and valleys in the surface roughness map from a material exhibiting ridging. The maps presented in this chapter have dimensions of $500\text{-}700\ \mu\text{m} // \text{RD} \times 500\text{-}700\ \mu\text{m} // \text{TD}$. This should be contrasted with the 3-4 mm separation between hills (or valleys) in the surface roughness maps shown in chapter 5. Instead of mapping such large continuous maps, several smaller areas were measured at different positions on the prepared surface in order to be statistically representative.

6.2. Effect of Cold Rolling Reduction and Annealing Conditions on Texture and Recrystallization Kinetics

A preliminary study of the evolution of the bulk texture with cold rolling reduction and annealing conditions was performed. Experiments were performed on the annealed AISI 445 hot band after cold rolling to 40%, 60% and 80% reduction. Bulk texture was measured by XRD at mid-thickness according to the procedure presented in Chapter 4. From the XRD pole figure measurements, ODFs were calculated using the software MTEX [152] (Figure 6.1 and Figure 6.2).

As expected [10] [13] [51] [63] [153], increasing the cold rolling reduction leads to a strengthening of the α -fibre with the development of a local maximum between $\{112\}\langle 110\rangle$ and $\{111\}\langle 110\rangle$. The strengthening of the α -fibre is also accompanied by the development of the $\{111\}\langle 110\rangle$ orientations on the γ -fibre (Figure 6.1 and Figure 6.3(a)).

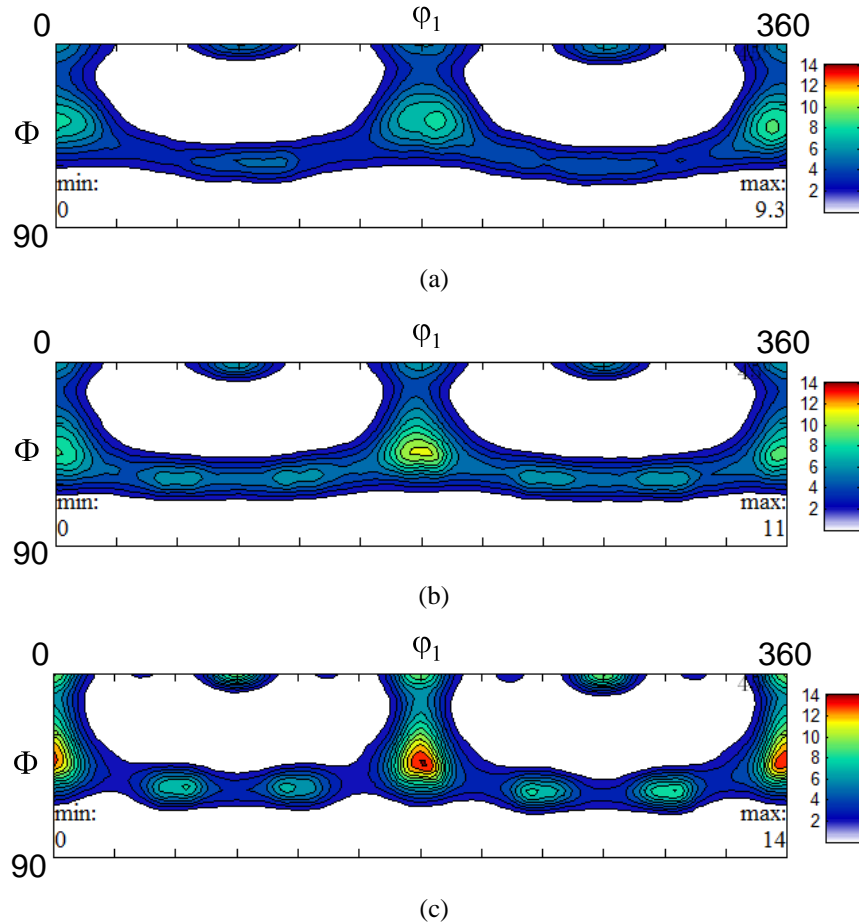


Figure 6.1: Evolution of bulk texture as a function of cold rolling reduction for the AISI 445 annealed hot band. The $\varphi_2=45^\circ$ section of the Euler space with the triclinic symmetry is represented here. The texture measurements were made at the mid-thickness on the ND plane after (a) 40% cold rolling reduction, (b) 60% cold rolling reduction and (c) 80% cold rolling reduction.

Annealing of these cold rolled sheets to full recrystallization was performed in a tube furnace according to the procedure presented in section 4.2.2. The resulting bulk textures, also obtained by XRD measurements on the ND plane, are presented in Figure 6.2. The texture at the centre of the recrystallized sheet changes from the α -fibre + γ -fibre

to a strong γ -fibre. Also as expected from the literature [63] [66] [76], the intensity of the γ -fibre, and especially of the $\{111\}\langle 112\rangle$ orientations in the final fully recrystallized sheet, increases with increasing amount of cold rolling reduction (Figure 6.2 and Figure 6.3(b)).

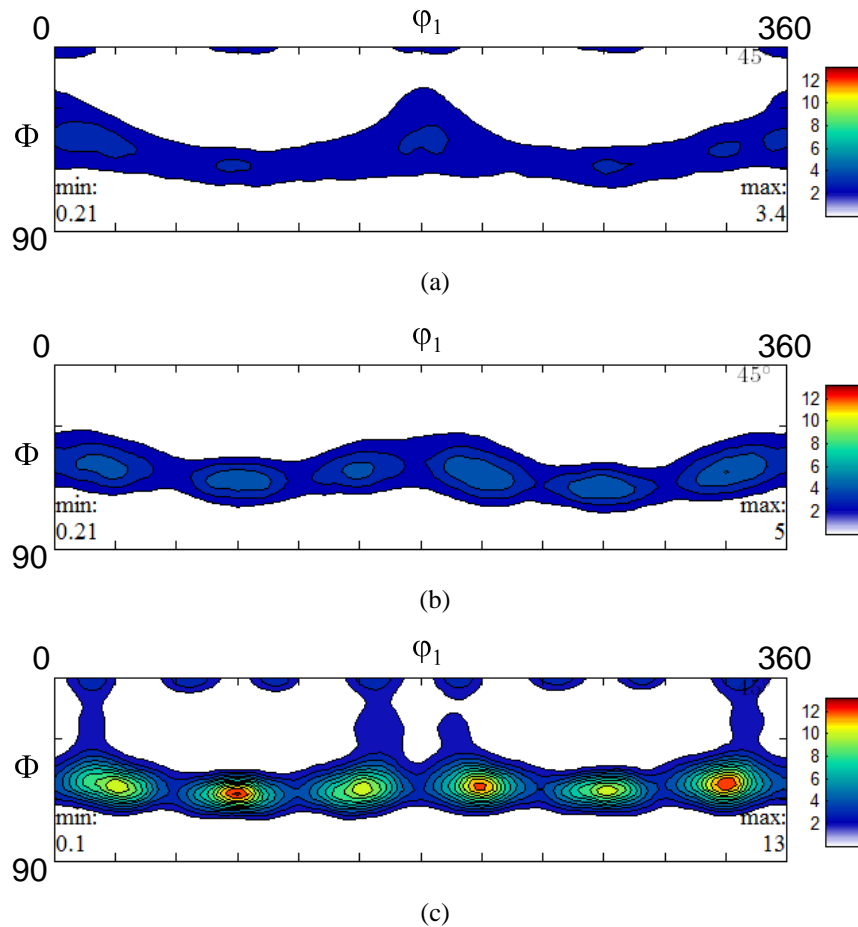


Figure 6.2: Evolution of bulk texture of the fully recrystallized sheet of AISI 445 annealed hot-band following cold rolling and annealing to full recrystallization. The $\phi_2=45^\circ$ section of the Euler space (triclinic symmetry) is represented. XRD measurements were made at mid-thickness on the ND plane. (a) 40% cold rolling reduction, annealed at 1010°C during 110s, (b) 60% cold rolling reduction, annealed at 1010°C during 75s and (c) 80% cold rolling reduction, annealed at 1010°C during 40s. Annealings were performed in the tube furnace.

In order to obtain recrystallization kinetics, samples from each of the three cold rolling reductions were annealed in the Gleeble (see section 4.2.2) at 800°C and 850°C for different times. The fraction recrystallized was measured following the procedure described in section 4.1.1, the results being given in Figure 6.4.

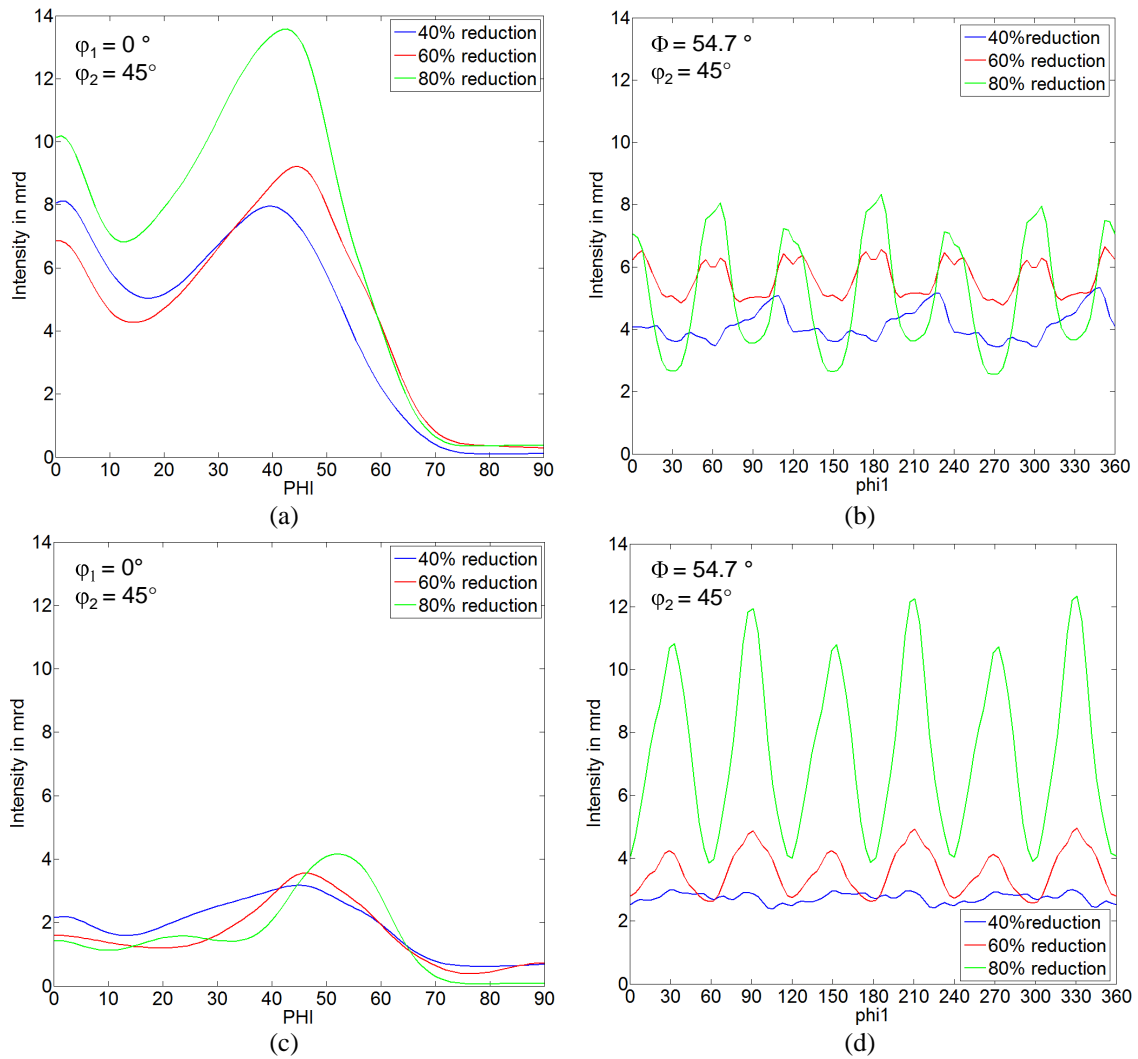
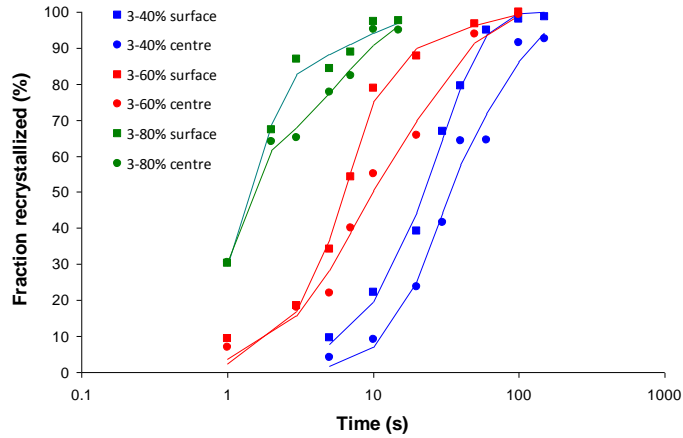
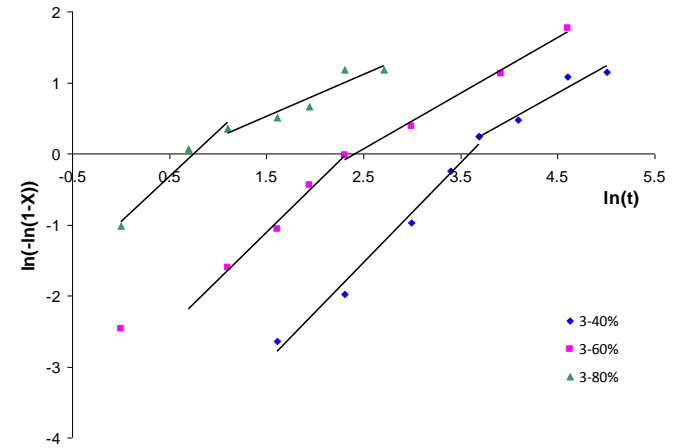


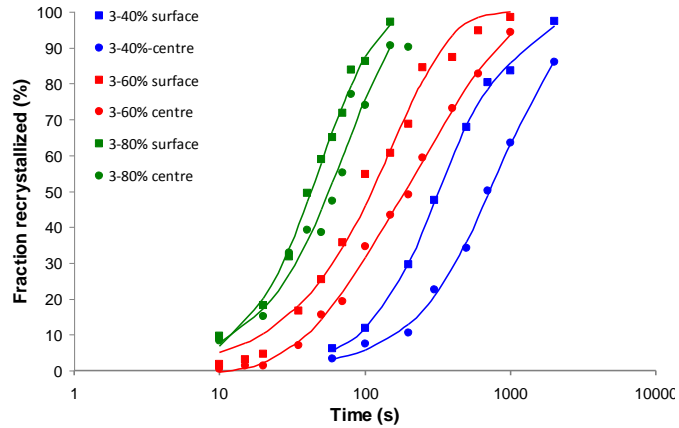
Figure 6.3: Evolution of the intensity along the two common fibre texture in ferritic stainless steels: (a) α -fibre after deformation, (b) γ -fibre after deformation, (c) α -fibre after annealing, and (d) γ -fibre after annealing. The intensity is in multiple of random.



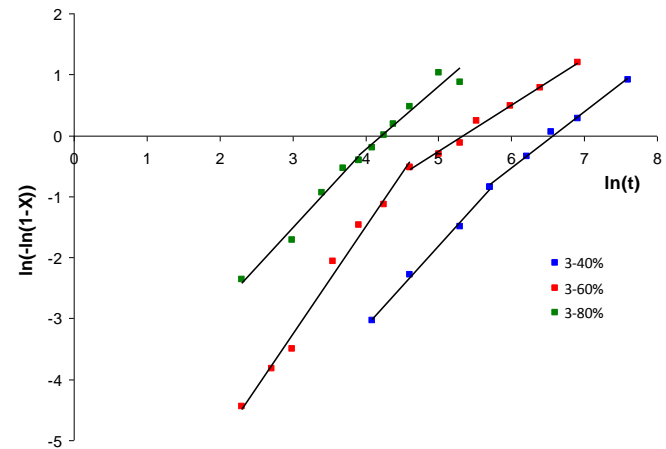
(a)



(b)



(c)



(d)

Figure 6.4: Recrystallization kinetics following 40%, 60% and 80% cold rolling and (a,b) annealed at 850°C and (c,d) 800°C. The solid lines in (a) and (c) show JMAK fits for the data. These fits were obtained using the double log graphs in (b) and (d) [93]. In (b) and (c), X represents the overall fraction recrystallized.

The sluggish recrystallization behaviour typically observed in ferritic stainless steels [63] [71] [90] is also observed in the case of this material. Figure 6.4(b) and Figure 6.4(d) show a plot of $\ln(-\ln(1-X))$, versus log time where X is the fraction recrystallized. When plotted in this way, the JMAK expression $X=1-\exp(-K.t^n)$ [64] plots as a straight line where K and n are expected to be constant for a given annealing temperature. This expression is commonly found to describe the recrystallization kinetics of metals [154] [156] [155]. The data shows a low slope (corresponding to n in the JMAK equation) at high recrystallized fractions (from $n = 1.34 \pm 0.06$ to $n = 0.71 \pm 0.10$ at 850°C, and from $n = 1.46 \pm 0.26$ to $n = 0.91 \pm 0.14$ at 800°C). This is typically associated with the slow recrystallization of α -fibre orientations close to $\{001\}\langle 110 \rangle$ [56] [71] [77].

Based on these results it was decided to perform a more detailed analysis of the microstructure and microtexture evolution on annealing following 80% cold rolling. This choice was made for two reasons. First, it has been suggested based on industrial trials that ridging is more severe for high cold rolling reduction [142]. Second, the results in Figure 6.1 and Figure 6.2 show that strong texture change occurs on annealing following 80% reduction. The origins of these texture changes and how they might contribute to increased ridging behaviour is important from the perspective of controlling ridging industrially

6.3. Annealing of the Annealed Hot Band AISI 445 after Cold Rolling

6.3.1. Methodology

This section deals with the apparition and growth of recrystallized grains from the deformed matrix. As a consequence, it is necessary to first use clear criteria to differentiate between recrystallized and deformed grains to therefore allow the EBSD data to be separated into recrystallized and unrecrystallized subsets. For the purposes of this study, a recrystallized grain was defined as a contiguous set of pixels having an EQAD grain size of at least 5 pixels. A group of pixels satisfying this condition was also required to have an internal misorientation of less than 2.5°, an aspect ratio of less than 3,

and be delimited by grain boundaries having $>5^\circ$ misorientation. These parameters were selected following systematic trials where various combinations of parameters were evaluated. When the internal misorientation threshold was chosen to be smaller than 2.5° , grains identified as recrystallized appeared in the subset containing deformed grains. Alternatively, for a threshold $> 2.5^\circ$, large deformed grains were found to be included in the subset containing recrystallized grains. An aspect ratio of 3 was selected as it was observed that the boundaries of some recrystallized grains were pinned at prior high angle grain boundaries likely due to the presence of precipitate (see [63]) (e.g grain A in Figure 6.5). Some other grains (for instance grain B in Figure 6.5) also appear to have a relatively low internal misorientation but have a very high aspect ratio (larger than 3). Those were considered to be recovered grains, and thus were not considered as recrystallized.

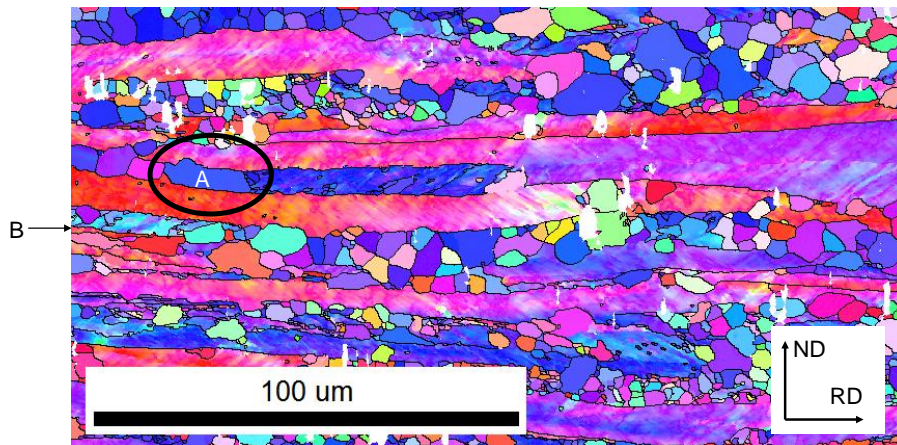


Figure 6.5: Detail of a partially recrystallized microstructure showing a recrystallized grain with high aspect ratio (grain A). Grain B also exhibits low internal misorientation ($<3.5^\circ$) but because of its large aspect ratio, the grain is considered as restored and non recrystallized. The white areas correspond to mis-indexed pixels.

In order to understand how the recrystallization microtexture arises from the deformed state and how it affects the further development of texture leading to the final product (and thus the final ridging properties), it is important to study the orientation relationships between a recrystallized grain and its surrounding deformed grain. This provides information on whether nuclei form in grain interior or grain boundaries and if they form at grain boundaries whether certain grain boundary serve as preferential sites. At higher recrystallization fractions the appearance of particular misorientations can

indicate the growth of grains into deformed grains of a different orientation. The misorientation between neighbouring deformed and recrystallized grains was determined from the EBSD data and the data separated according to the orientation of the recrystallized grains. From this, the correlated Misorientation Distribution Function (MODF) [15] was calculated between neighbouring pixels belonging to a recrystallized grain and to a deformed grain to give the statistical relationship between deformed and recrystallized grains. As a consequence, it is really the local misorientation across the boundary that is measured, not the misorientation between the average orientations of neighbouring deformed and recrystallized grain. The MODF was calculated using the discrete binning calculation method (similar to the method proposed by Matthies et al. [172] for the calculation of ODF), with a bin size of 2° and a Gaussian smoothing of 1° .

The MODF between recrystallized grains and their neighbouring deformed grains is represented in Rodrigues space. Rodrigues space is useful as the Rodrigues vector is directly related to the physical misorientation axis and angle between adjacent grains, and provides an intuitive way to visualize misorientation in a 3-dimensional space. The rotation axis is given by the direction of the 3-dimensional Rodrigues vector and the rotation angle is given by the magnitude of the vector¹³ [15]. For each misorientation, there is a unique point in Rodrigues space. The closer the point is to the centre of Rodrigues space, the smaller the angle of misorientation. Because of cubic symmetry, the fundamental zone of Rodrigues space for misorientations is reduced to the region presented in red in Figure 6.6(a) [15] [157]. For ease of representation, the Rodrigues space (defined by a coordinate system $r_1=[100]$, $r_2=[010]$, $r_3=[001]$) is represented here as section of r_3 (see Figure 6.6(b) for details).

¹³ For a rotation vector \vec{r} and a rotation angle θ , the Rodrigues vector is defined by $\vec{R} = \tan\left(\frac{\theta}{2}\right) \cdot \vec{r}$

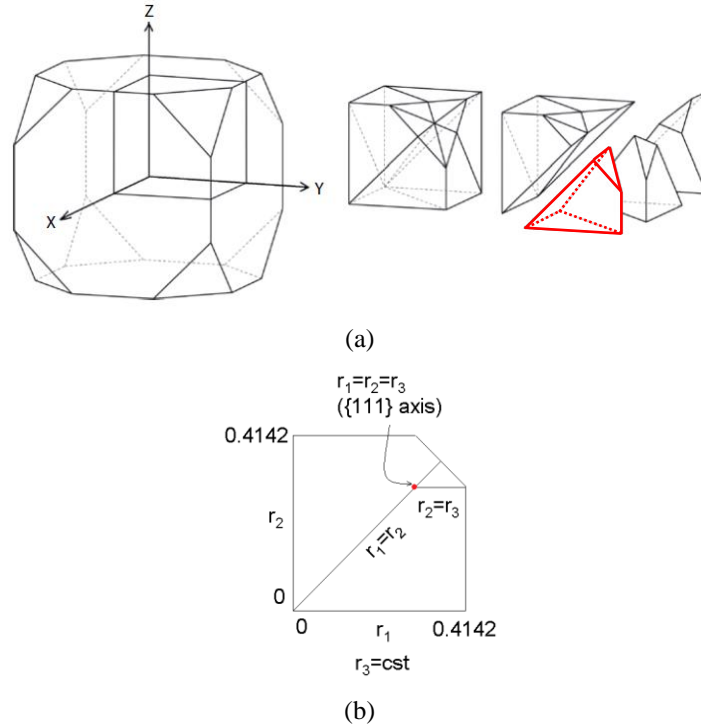


Figure 6.6: Rodrigues space for representation of misorientations. (a) Fundamental zone for cubic symmetry (left), showing also the decomposition of the space into sub-volumes corresponding to the cubic-cubic system (right, in red), from [37]. (b) Example of one of the section of the sub-volume corresponding to the cubic-cubic system showing the characteristic features used in the following sections for the analysis of misorientations ($r_3=0.25$).

For more quantitative measurements, the rotation angles were further divided into three groups: (i) low angle misorientations ($<20^\circ$), (ii) intermediate angle misorientations (between 20° and 40°) and (iii) large angle misorientations ($>40^\circ$).

As mentioned at the end of section 6.2, it was decided to perform a detailed analysis on the material cold rolled 80% and annealed at 800°C . This allowed the full range of recrystallization to be followed (see Figure 6.4). A list of all conditions tested in this section with the corresponding number of maps and fraction recrystallized for each map is presented in Table 6.1. From this table, the full process of recrystallization can be separated in three groups: early stages of recrystallization ($<30\%$), intermediate stages (between 30% and 75%), and end of recrystallization ($>75\%$). These values were chosen based on the features that will be presented in the following sections (characteristics of the MODF for instance).

Table 6.1: Annealing conditions tested for the study of recrystallization at 800°C after 80% cold rolling reduction. The number of measured EBSD maps for each condition and their recrystallized fraction are also indicated. The advancement of recrystallization is also presented (early stage <25%, intermediate stage between 25% and 75%, end stage >75%).

Annealing conditions	Number of maps	Fraction recrystallized	
5s: TD plane	1 (full thickness)	5.6%	Early stage (<30% recrystallized)
10s: ND plane	3	15.6% – 25.0% – 25.2%	
TD plane	1 (full thickness)	20.4%	
20s: TD plane	1 (full thickness)	21.1%	
30s: ND plane	6	47.9% - 51.7% - 63.6% -68.9% - 73.2% - 81.7%	Intermediate stage (30-75% recrystallized)
TD plane	1 (full thickness)	30.6%	
40s: ND plane	2	49.4% - 62.8%	
TD plane	1 (full thickness)	60.3%	
60s: TD plane	1 (full thickness)	66.2%	End stage (>75% recrystallized)
70s: ND plane	4	66.4% (II) - 73.9% (II) 75.7% (III) -79.8% (III)	
80s: TD plane	1 (full thickness)	78.9% (III)	
100s: ND plane	1	82.7% (III)	
200s: ND plane	2	89.0% (III) - 91.4% (III)	

6.3.2. Early Stages of Recrystallization (<30% Recrystallized)

Following cold rolling to 80% reduction and annealing at 800°C, the first evidence of recrystallization was observed after 5s. Two examples of the early stages of recrystallization by EBSD measurements on the TD surface (Figure 6.7) and on the ND surface (Figure 6.8) reveal a heavily deformed microstructure with grains elongated along RD. As expected (see Figure 6.1), the texture of this material is composed of a strong α -fibre accompanied by a weaker γ -fibre. Figure 6.7 and Figure 6.8 also show the separation of data according to the procedure presented in section 6.3.1. The spatial distribution of the first recrystallized grains (using the definition above) form heterogeneously and are restricted to certain regions within the microstructure. The top left hand side of the map (Figure 6.8(a)) contains many more recrystallized grains compared to the central grains having orientations close to $\{001\}\langle 110\rangle$. In particular these first grains form in elongated

features oriented along RD and have a strong $\{111\}\langle 112\rangle$ texture (Figure 6.7(b) and Figure 6.8(b)).

As can be seen on Figure 6.8(a), some recrystallized grains appear within bands (bottom half of the map), while others appear at grain boundaries or in the interior of deformed grains (top half of the map). A closer observation of the bands (Figure 6.9) reveals that their thickness (along RD) is about $5\ \mu\text{m}$ and they are misoriented by $10\text{-}15^\circ$ with regards to the matrix (Figure 6.9(b)). These bands, when viewed on the TD plane, are inclined at angles of $30\text{-}35^\circ$ to the rolling plane. These two observations are fully coherent with the observations of shear bands made in the past [159] [160]. Shear bands have also been reported in the literature as favourable sites for nucleation [59] [161], and were reported as favouring the nucleation of γ -grains within grain interior due to fragmentation [158].

Distinguishing between the last two nucleation sites (near grain boundaries or in the interior of grains) is difficult as growth following nucleation as well as the 2D observation makes identification of the precise nucleation sites difficult. It can however be assumed that recrystallized grains located at least one grain diameter from a grain boundary were formed in the interior of a deformed grain.

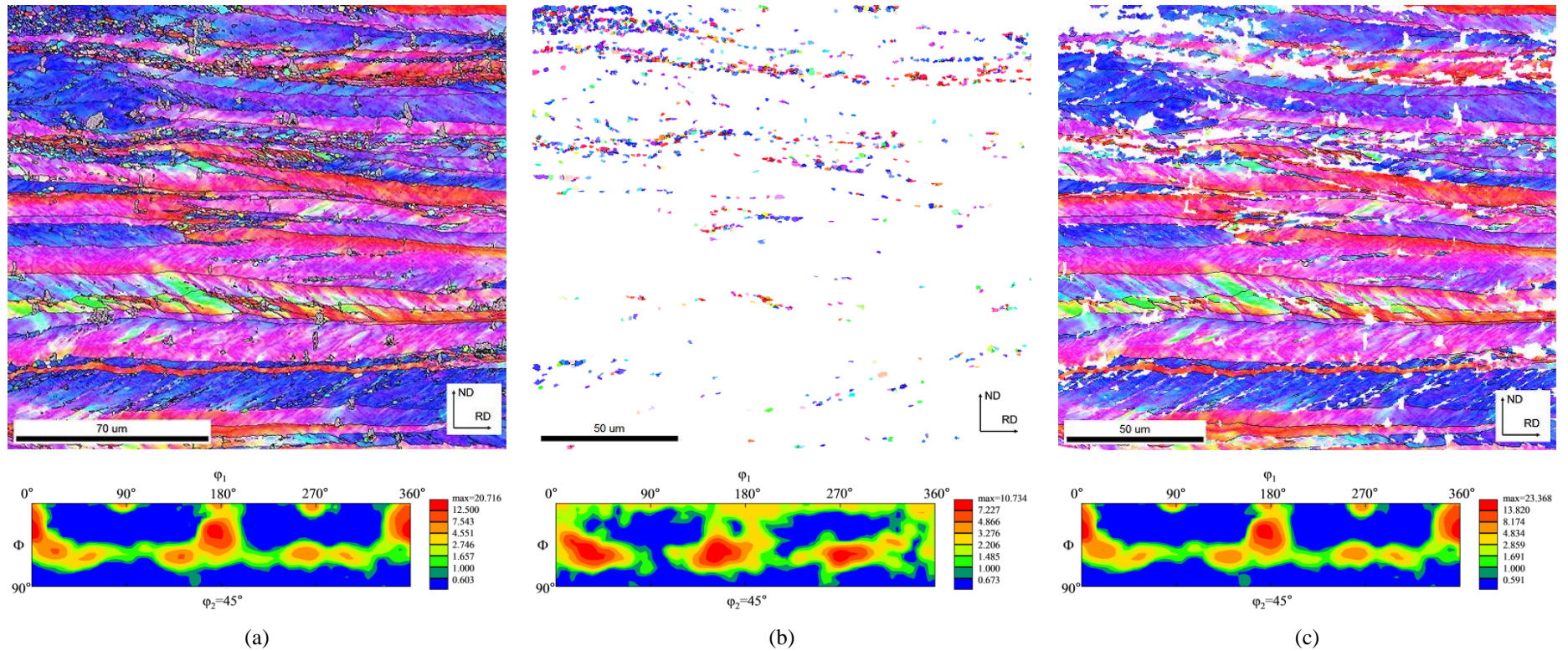


Figure 6.7: Selection of EBSD maps (ND inverse pole figure maps) for the early stages of recrystallization, taken on the TD plane after 80% cold rolling of the annealed hot band and annealing at 800°C for 5s, corresponding to 5.6% recrystallization. (a) full map where white regions are mis-indexed points, such as precipitates, (b) recrystallized grains, (c) deformed grains. Each map is accompanied by its corresponding ODF.

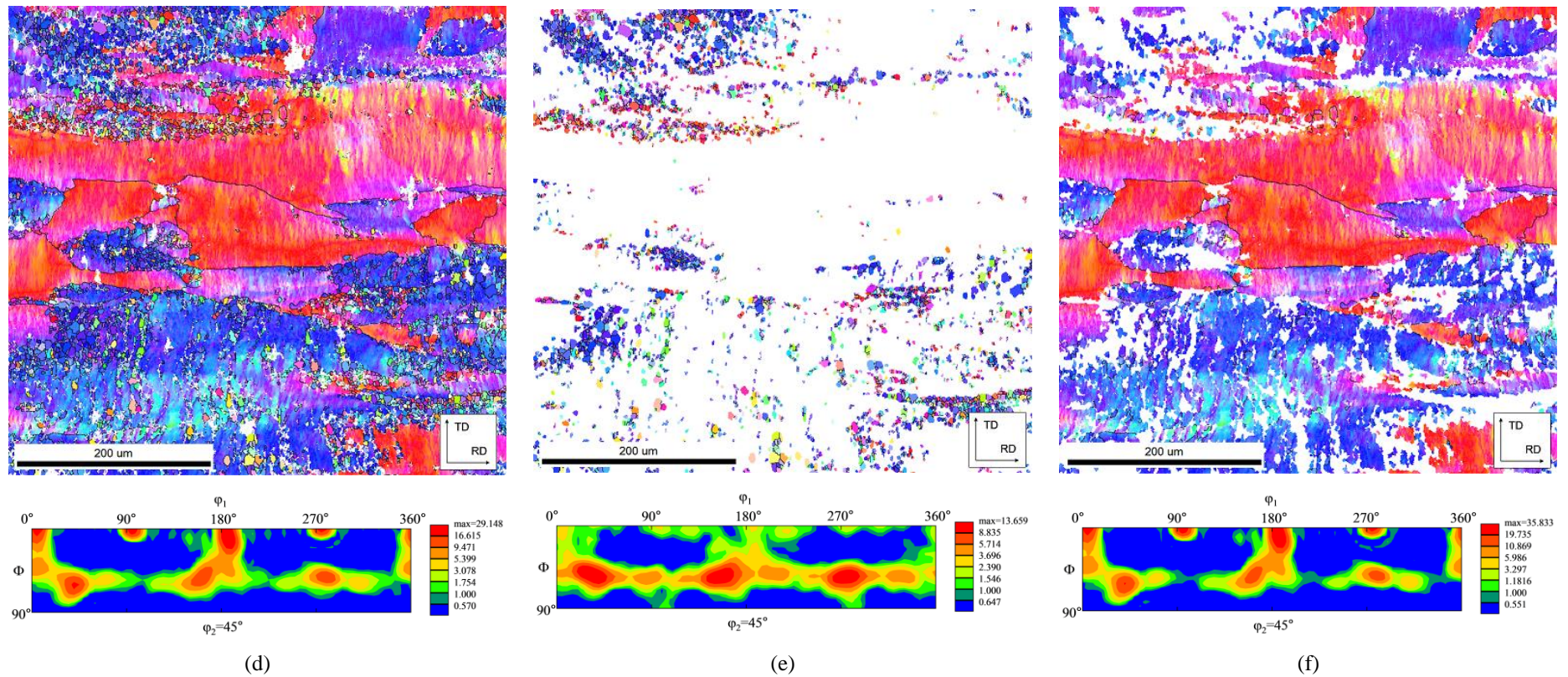


Figure 6.8: Selection of EBSD maps (ND inverse pole figure maps) for the early stages of recrystallization, taken on the ND plane after 80% cold rolling of the annealed hot band and annealing at 800°C for 10s, corresponding to 16.4% recrystallization. (a) full map where white regions are mis-indexed points, such as precipitates, (b) recrystallized grains, (c) deformed grains. Each map is accompanied by its corresponding ODF.

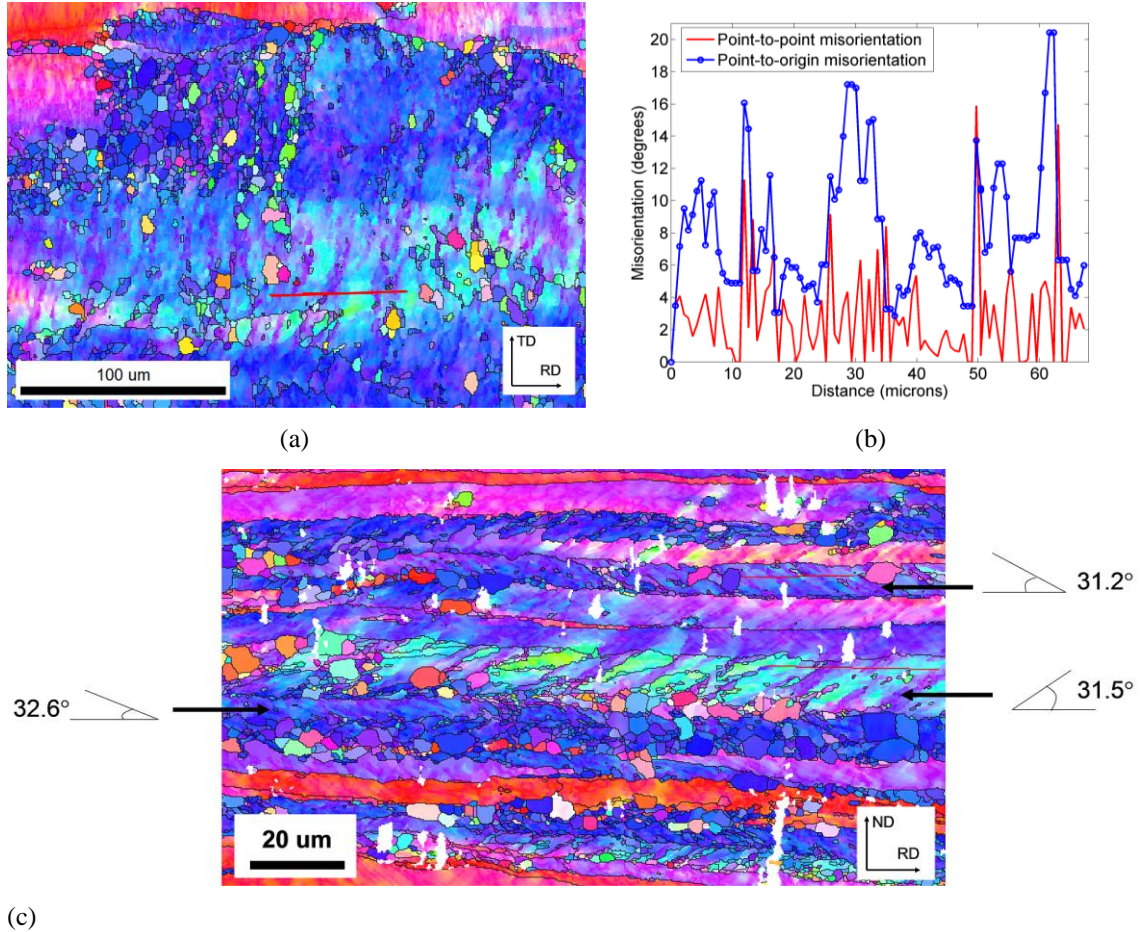


Figure 6.9: (a) Detail from Figure 6.7(d) showing nucleation in bands. The red line is where (b) the misorientation profile across these bands was taken. (c) EBSD map on the TD section showing that these bands are inclined by 30-35° from the RD, in agreement with [159].

Figure 6.7(b) and Figure 6.8(b) reveal that the majority of the first grains to form during recrystallization have orientations close to $\{111\}\langle 112\rangle$. For this reason, it was decided to focus the study of misorientations between these recrystallized grains and their surrounding deformed matrix. Both variants of the $\{111\}\langle 112\rangle$ orientations ($(111)[1-21]$ and $(111)[-1-12]$ and their equivalent orientations) were also studied independently as the importance of individual variants on ridging was already mentioned (see Chapter 5). As seen in Figure 6.10, a large majority of points are found to lie close to the centre of Rodrigues space (close to $(0,0,0)$), meaning that the misorientation between recrystallized $\{111\}\langle 112\rangle$ grains and their neighbouring deformed grains is low. This is seen by plotting a histogram of the misorientation angles (Figure 6.11). The fraction of low

misorientation angle ($<20^\circ$) was calculated to be 46.3% (average over all the EBSD maps corresponding to the early stages of recrystallization).

The $\{111\}<110>$ orientations also represent a major family of recrystallized orientations during the early stages of recrystallization, as can be seen on the ODF in Figure 6.8(b). Similar results to those for $\{111\}<112>$ are observed when the misorientations between the recrystallized $\{111\}<110>$ grains and their surrounding deformed matrix are calculated (one example is given Figure 6.12). Because these two families of orientations represent the majority of the recrystallized orientations in the early stages of recrystallization (maximum intensity of the ODF along the γ -fibre), it can be concluded that there is always a high fraction of grains recrystallizing with an orientation close to that of their parent matrix, providing for a partial memory of where the parent grain was in the structure. With increasing values of r_3 , however, it is found that misorientations exist around one of the four $<111>$ misorientation axis. These correspond to grains which are misoriented by a rotation along the γ -fibre. This result shows that when the misorientation angle between recrystallized grains and their neighbouring deformed grains increases ($>8^\circ$, corresponding to the second section presented in Figure 6.10), the nucleation still happens in γ -fibre oriented grains, with the formation of new grains also belonging to the γ -fibre, but with higher misorientation with regards to the surrounding matrix. This is consistent with the observation that deformed γ -fibre grains are composed of cells that can be highly misoriented [63] [76] and with the observed nucleation of γ -grains within shear bands [158].

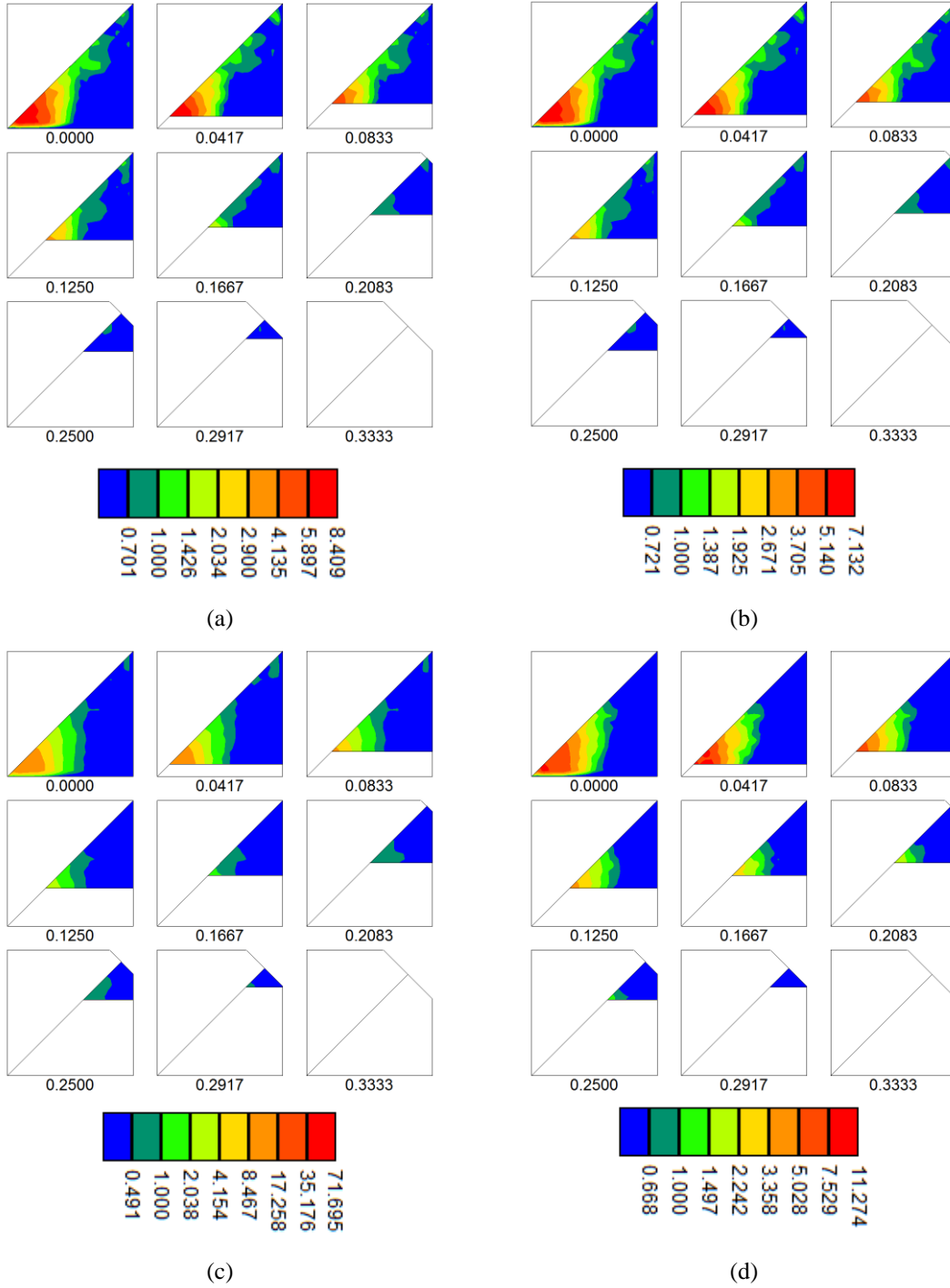


Figure 6.10: Misorientations between recrystallized $\{111\}\langle 112 \rangle$ grains and their deformed neighbours, represented in sections of Rodrigues space for constant r_3 values, for the microstructures presented in Figure 6.8. (a) $(111)[1-21]$ variant for the material annealed 5s (Figure 6.8(a-c)), (b) $(111)[1-12]$ variant for the same material annealed 5s, (c) $(111)[1-21]$ variant for the material annealed 10s (Figure 6.8(d-f)), (d) $(111)[1-12]$ variant for the same material annealed 10s.

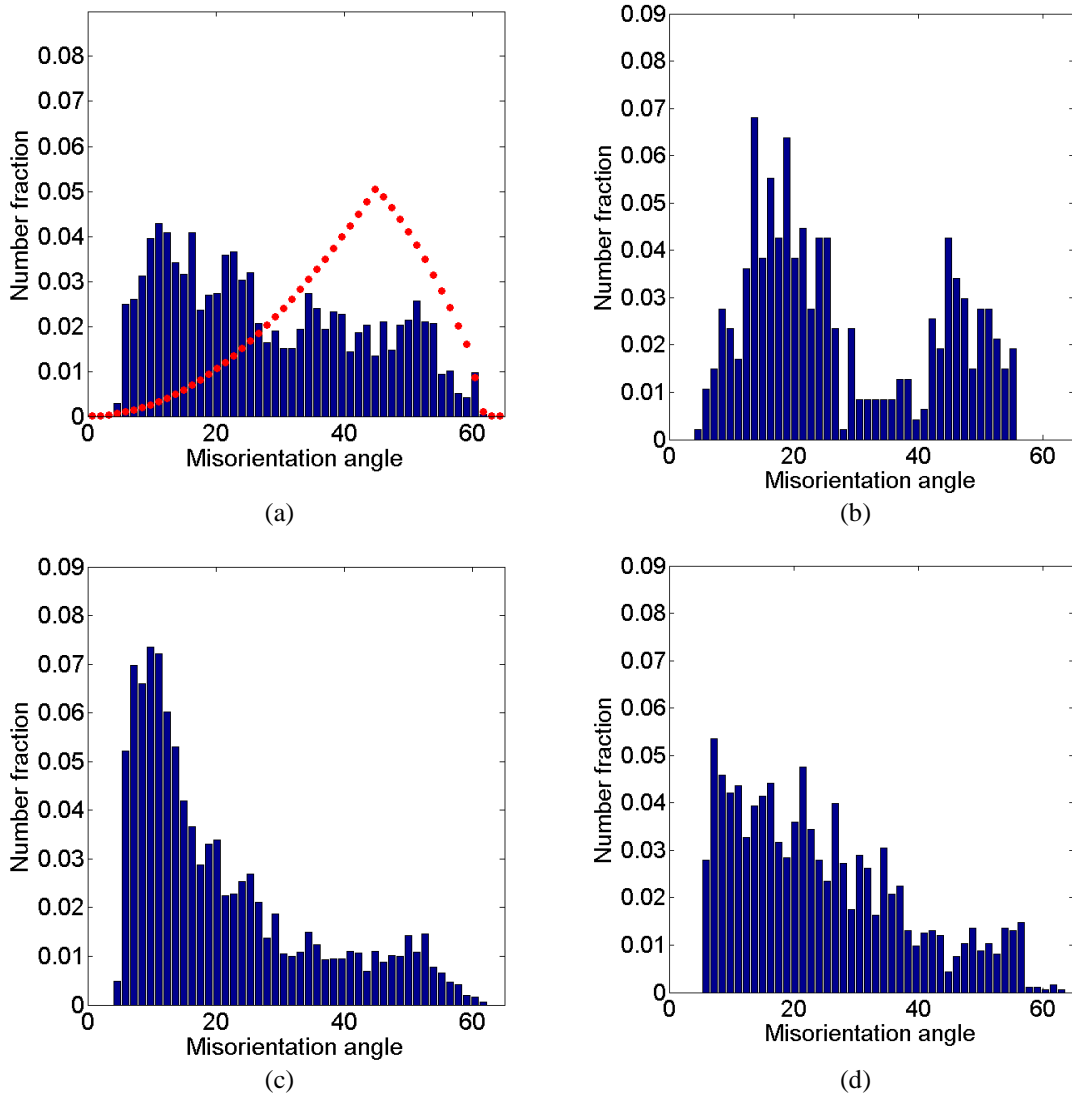


Figure 6.11: (a) to (d) Histograms of the misorientation angles between recrystallized grains and their neighbouring deformed grains, obtained from the data used to calculate the MODFs presented in Figure 6.10 respectively. (a) also presents the MacKenzie plot in red dots (distribution of misorientation angles for a randomly textured polycrystal), showing that the misorientation distribution is non random.

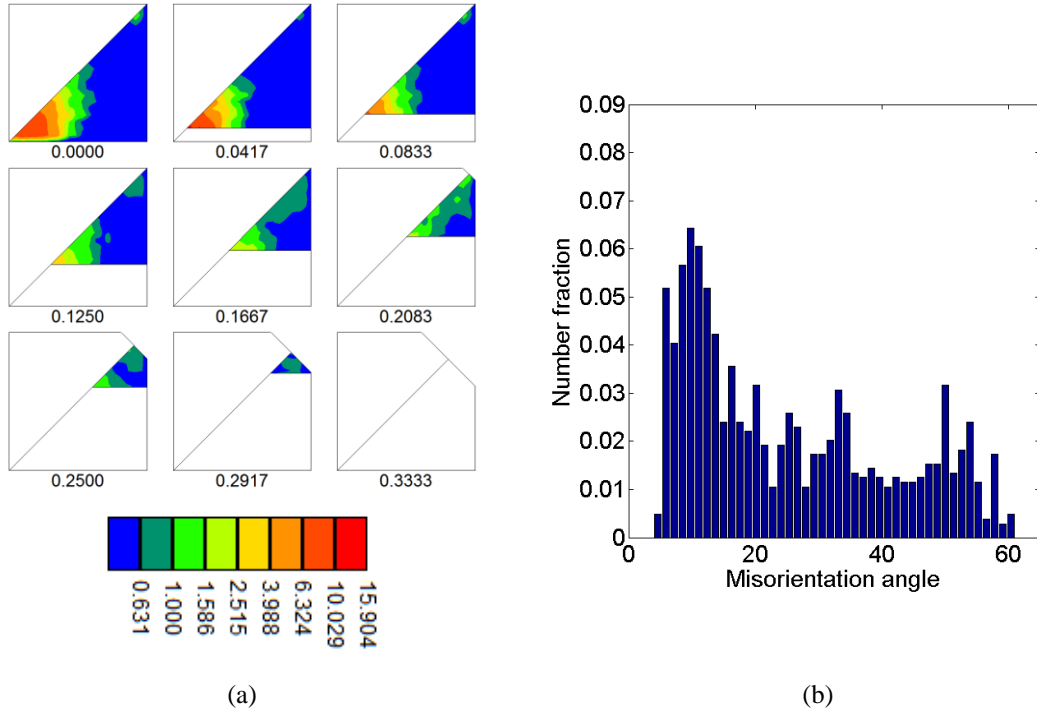


Figure 6.12: Misorientation between recrystallized grains having one of the $\{111\}\langle 110 \rangle$ orientations and their neighbouring deformed grains for the material annealed for 10s (Figure 6.8(d-f)). (a) MODF and (b) histogram of misorientation angles for the $(111)[1-10]$. The results are similar to those presented for the $\{111\}\langle 112 \rangle$ orientations (Figure 6.10 and Figure 6.11).

6.3.3. Intermediate Stages of Recrystallization

At intermediate levels of recrystallization (30%-75% recrystallized), it was observed that the texture of the recrystallized grains continues to predominantly belong to the γ -fibre (Figure 6.13(b) and Figure 6.14(b)). Also, the texture of the remaining deformed regions became sharper and centered on the α -fibre. In particular, the deformed texture was found to be increasingly centered between $\{001\}\langle 110 \rangle$ and $\{112\}\langle 110 \rangle$ (from Figure 6.7(c) and Figure 6.8(c) to Figure 6.13(c) and Figure 6.14(c)). This is consistent with the microstructural features responsible for the slowing of the recrystallization kinetics as noted in section 6.2 [63] [71] [90].

The misorientations between the recrystallized grains and their neighbouring deformed grains exhibits less of a tendency for having a misorientation about the $\langle 111 \rangle$ direction, expressed by a lower intensity of the MODF. As seen in Figure 6.15, for low values of r_3 , the MODF starts to present a spread of intensity along the line $r_1=r_2$, corresponding to a $\langle 110 \rangle$ misorientation axis. This also confirms the fact that there are

new boundaries forming between recrystallized grains and the remaining deformed grains. This result is also seen in the misorientation histograms (Figure 6.16), where the fraction of misorientations with low rotation angle ($<20^\circ$) is significantly lower (21.5% vs 46.3% previously) while the fraction of misorientations with intermediate misorientation angles (between 20° and 40°) increases when compared to Figure 6.11 (from 33.6% to 45.7%).

This type of misorientation ($30\text{-}40^\circ$ around $\{110\}$) has previously been observed in other ferritic steels and has been attributed to the misorientation between recrystallized $\{111\}<112>$ grains and deformed $\{112\}<110>$ grains (whose exact misorientation is 35.6° around $\{17\ 1\ 13\}$) [65]. An example of this specific case is represented in Figure 6.17(a), where two deformed grains are present at the centre of the EBSD map and are surrounded by multiple recrystallized grains consuming them. The pole figures in Figure 6.17(b) reveal that both of the deformed grains have a $\{112\}<110>$ orientation. A selection of the recrystallized grains that are directly in contact with these two deformed grains reveals that they belong to the γ -fibre (Figure 6.17(c)).

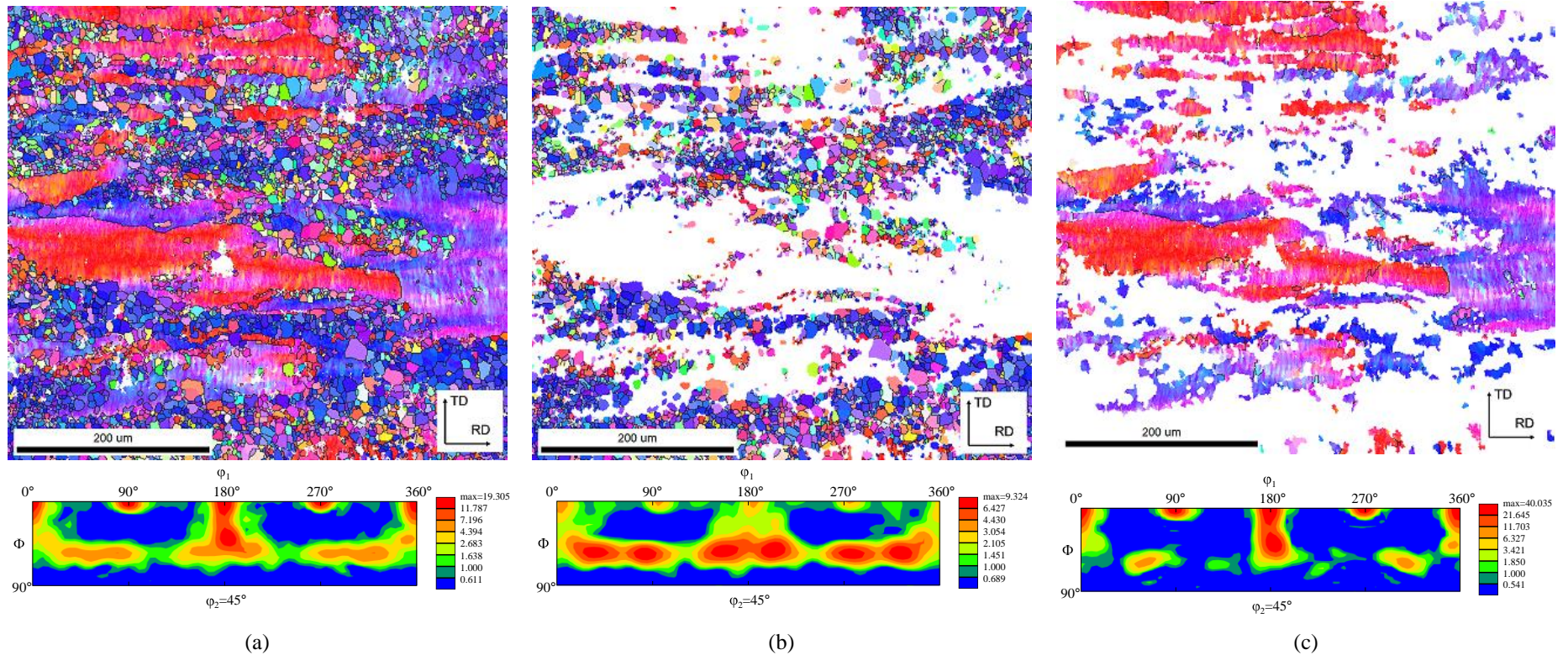


Figure 6.13: Selection of EBSD maps (ND inverse pole figure maps) for the early stages of recrystallization, taken on the ND plane after 80% cold rolling of the annealed hot band and annealing at 800°C for 30s, corresponding to 51.7% recrystallization. (a) full map where white regions are mis-indexed points, such as precipitates, (b) recrystallized grains, (c) deformed grains. Each map is accompanied by its corresponding ODF.

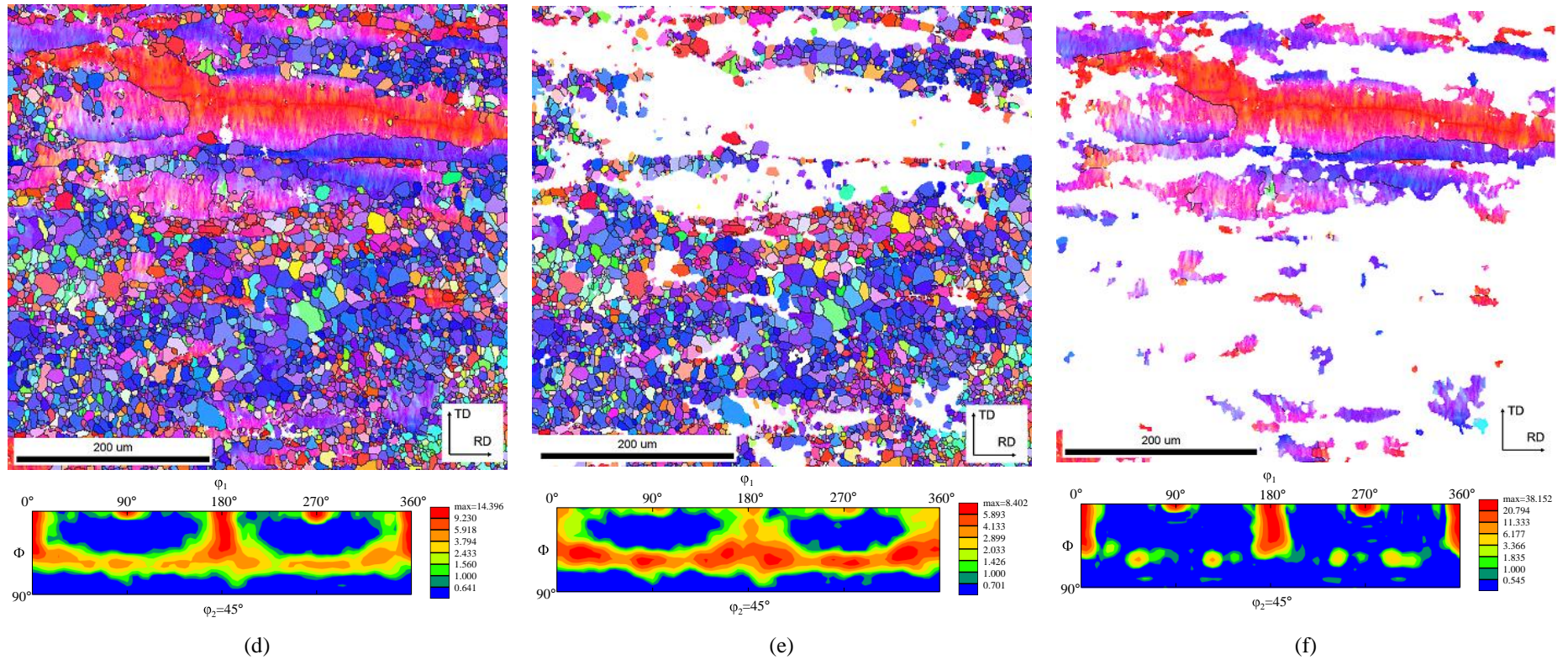


Figure 6.14: Selection of EBSD maps (ND inverse pole figure maps) for the early stages of recrystallization, taken on the TD plane after 80% cold rolling of the annealed hot band and annealing at 800°C for 70s, corresponding to 66.4% recrystallization. (a) full map where white regions are mis-indexed points, such as precipitates, (b) recrystallized grains, (c) deformed grains. Each map is accompanied by its corresponding ODF.

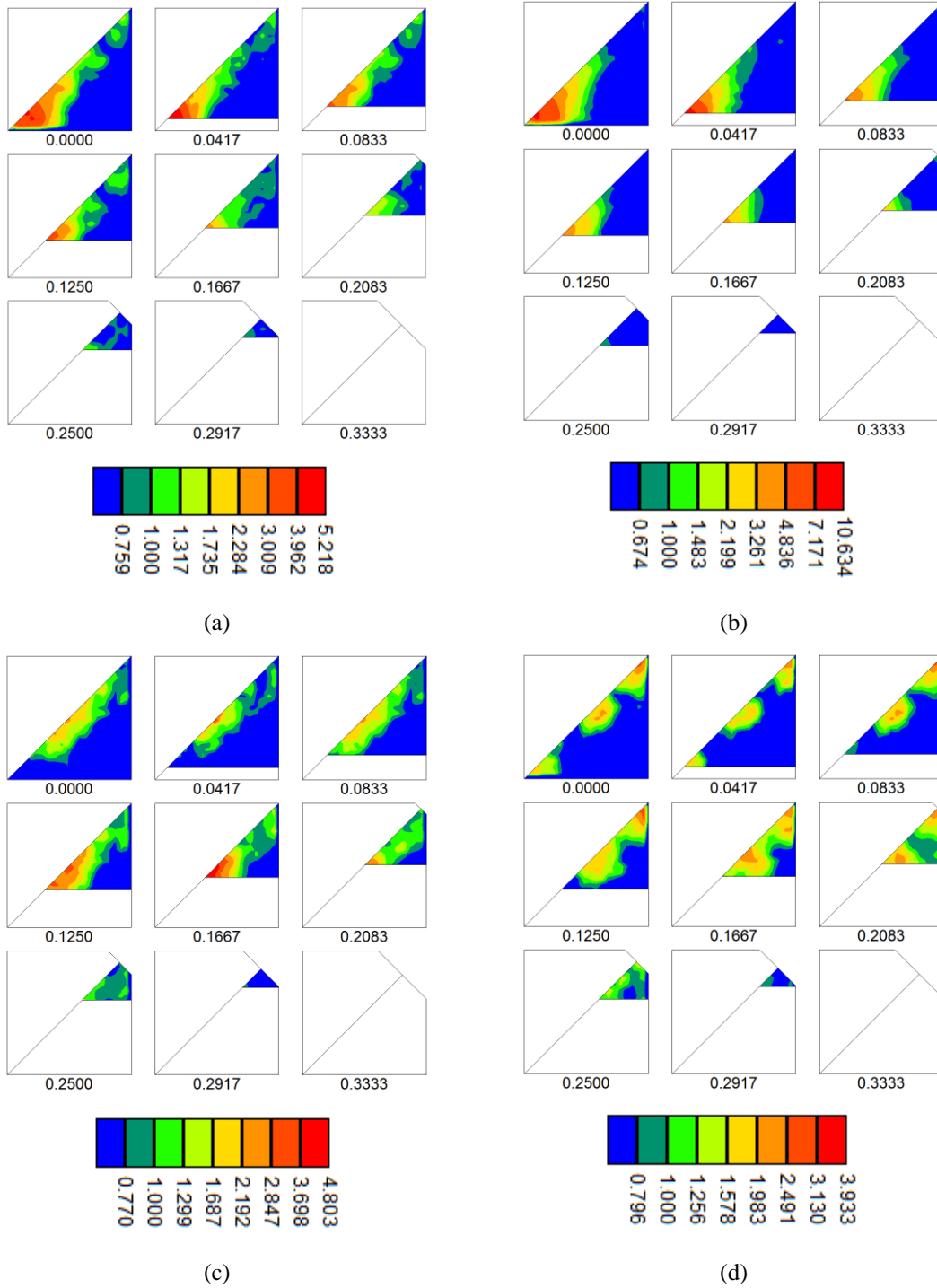


Figure 6.15: Misorientations between recrystallized $\{111\}\langle 112\rangle$ grains and their deformed neighbours, represented in sections of Rodrigues space for constant r_3 values, for the microstructures presented in Figure 6.14. (a) $(111)[1-21]$ variant for the material annealed 30s (Figure 6.14(a-c)), (b) $(111)[-1-12]$ variant for the same material annealed 30s, (c) $(111)[1-21]$ variant for the material annealed 70s (Figure 6.14(d-f)), and (d) $(111)[-1-12]$ variant for the same material annealed 70s.

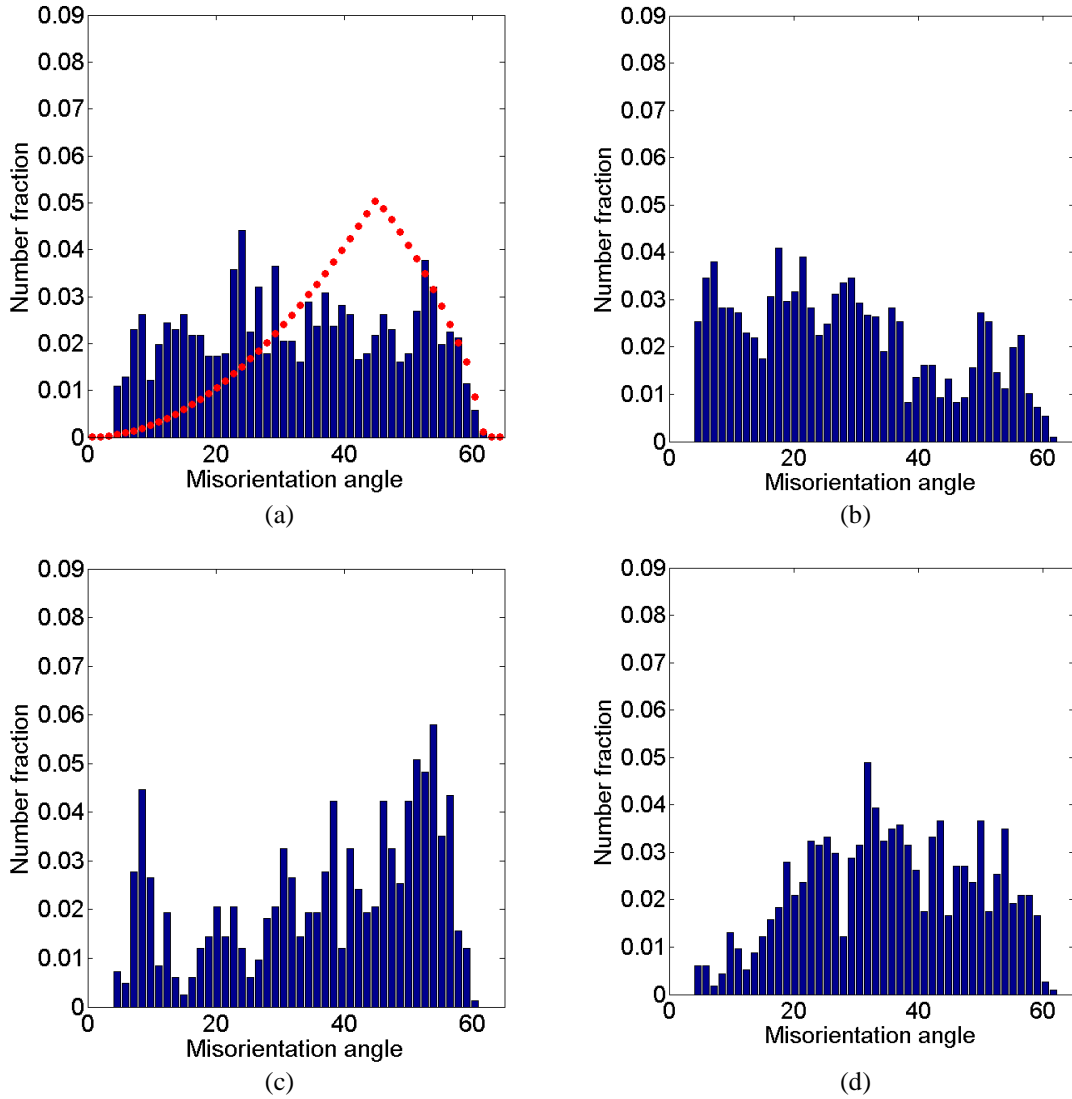


Figure 6.16: (a) to (d) Histograms of the misorientation angles between recrystallized grains and their neighbouring deformed grains, obtained from the data used to calculate the MODFs presented in Figure 6.15 respectively. (a) also presents the MacKenzie plot in red dots (distribution of misorientation angles for a randomly textured polycrystal), showing that the misorientation distribution is non random.

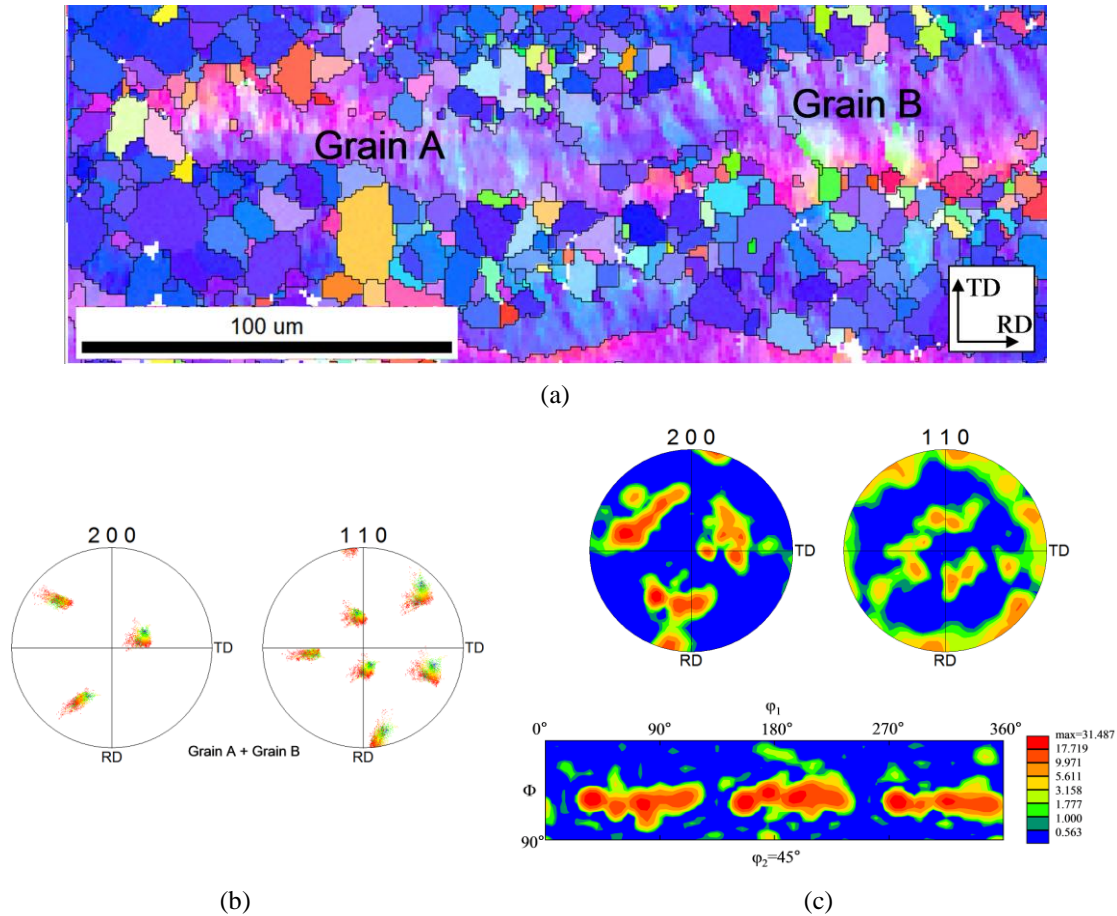


Figure 6.17: Detail of the origins of the 35° around $\{110\}$ misorientation. (a) Inverse pole figure map from the AISI 445 annealed hot band after 80% cold rolling reduction and annealing at 800°C for 30s (63.6% recrystallized) showing deformed grains with a $\{112\}\langle 110\rangle$ orientation, surrounded by recrystallized grains belonging to the γ -fibre. (b) $\{200\}$ and $\{110\}$ pole figures of the deformed grains. (c) Pole Figure and Orientation Distribution Function of the recrystallized grains surrounding the deformed $\{112\}\langle 110\rangle$ grains, showing that these grains belong to the γ -fibre.

6.3.4. End of Recrystallization (>75% Recrystallized)

For the later stages of recrystallization (Figure 6.18 and Figure 6.19), the distribution of misorientations in Rodrigues space (Figure 6.20) becomes significantly different, with a clear tendency towards misorientations of $30\text{-}40^\circ$ around $\langle 110\rangle$. The histogram of misorientations (Figure 6.21) also shows a higher fraction of large misorientation angles ($>40^\circ$) compared to the previous two histograms (53.1 % for the end of recrystallization vs. 20.0% and 32.8% for the early stage (Figure 6.11) and the intermediate stage (Figure 6.16) respectively). Figure 6.18(c) and Figure 6.19(c) also show that the orientations of the remaining deformed grains are not only composed of

$\{112\}\langle 110\rangle$ but rather composed of a continuous α -fibre. The presence of this continuous α -fibre surrounded by recrystallized grains (mainly $\{111\}\langle 112\rangle$ as seen Figure 6.17(c)) can explain the presence of the high fraction of large misorientation axes ($>40^\circ$). Indeed, the misorientation angle between a recrystallized $\{111\}\langle 112\rangle$ grain and a deformed $\{112\}\langle 110\rangle$ is 35.6° , and the misorientation angle between a recrystallized $\{111\}\langle 112\rangle$ grain and a deformed $\{001\}\langle 110\rangle$ is calculated to be 61.2° . All orientations on the α -fibre will therefore present a misorientation angle with surrounding recrystallized grains between 35.6° and 61.2° , which represents an important fraction of the misorientation angles presented in Figure 6.21 (53.1% on average). Recrystallization will then proceed by the full consumption of these remaining grains by the already recrystallized grains. The effect of this on the slowing of recrystallization kinetics has been treated in the model proposed by [93], where the change in fraction of α and γ fibre texture intensity was shown to explain the two-stage recrystallization kinetics.

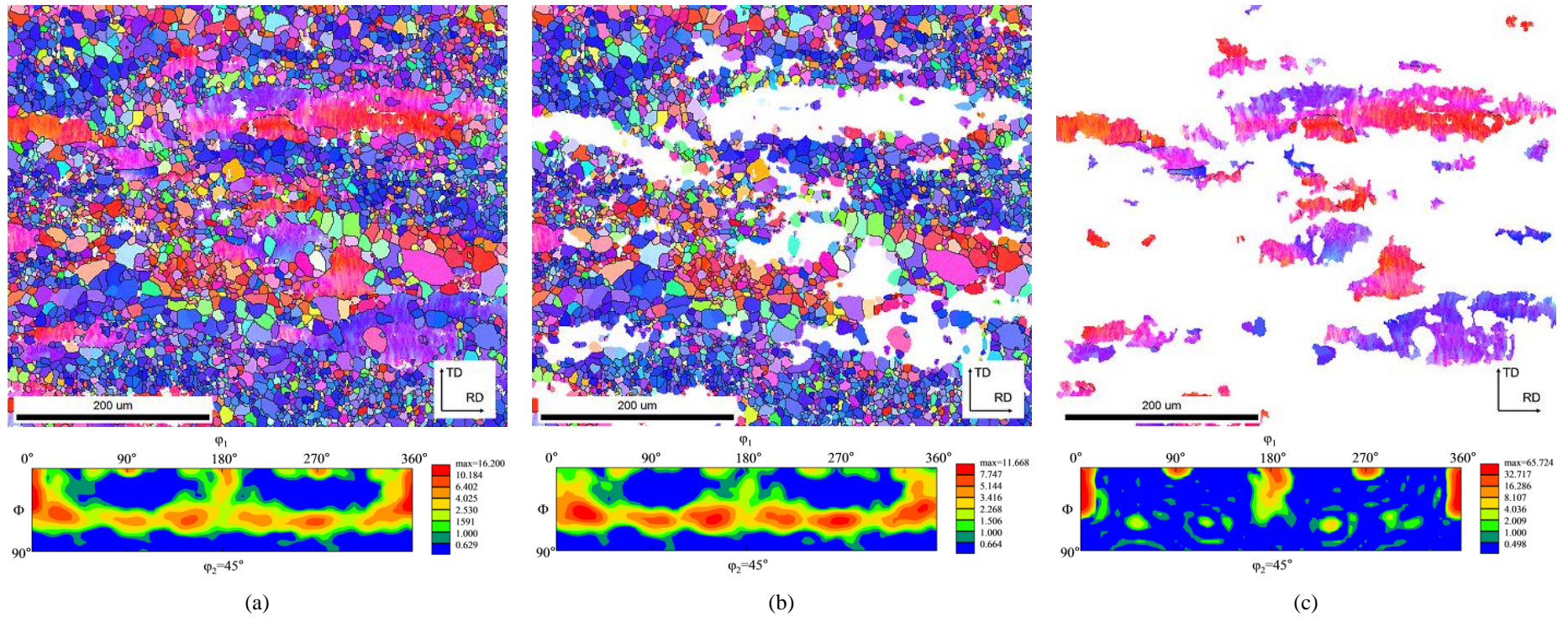


Figure 6.18: Selection of EBSD maps (ND inverse pole figure maps) for the early stages of recrystallization, taken on the TD plane after 80% cold rolling of the annealed hot band and annealing at 800°C for 70s, corresponding to 79.8% recrystallization. (a) full map where white regions are mis-indexed points, such as precipitates, (b) recrystallized grains, (c) deformed grains. Each map is accompanied by its corresponding ODF.

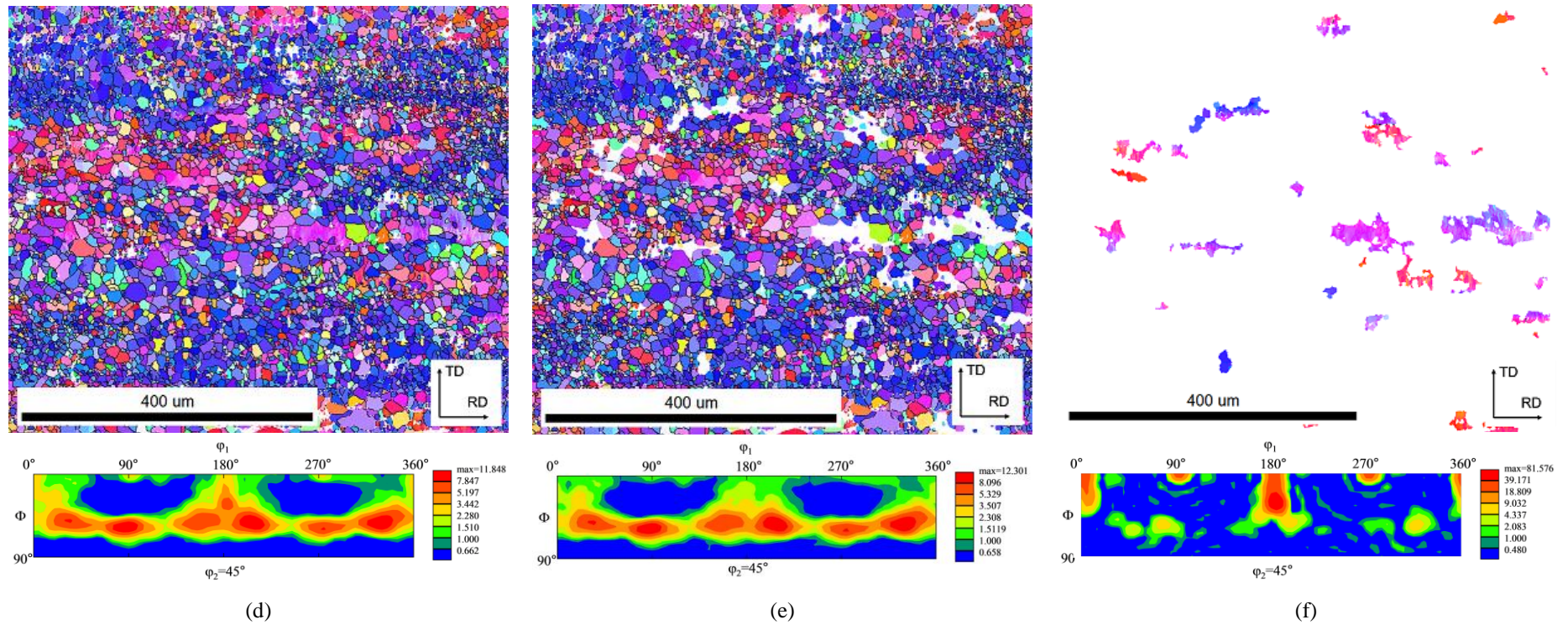


Figure 6.19: Selection of EBSD maps (ND inverse pole figure maps) for the early stages of recrystallization, taken on the TD plane after 80% cold rolling of the annealed hot band and annealing at 800°C for 200s, corresponding to 91.4% recrystallization. (a) full map where white regions are mis-indexed points, such as precipitates, (b) recrystallized grains, (c) deformed grains. Each map is accompanied by its corresponding ODF.

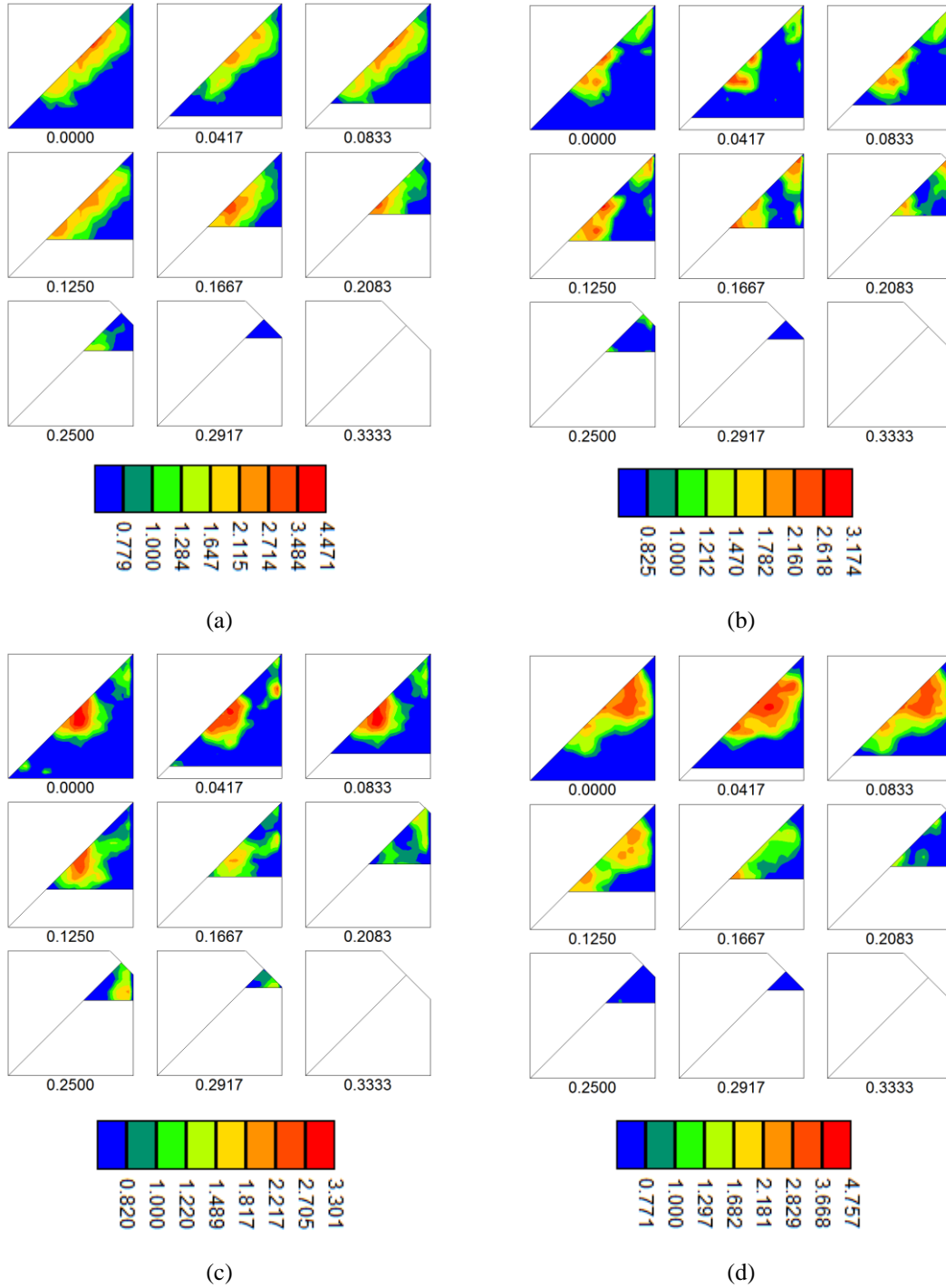


Figure 6.20: Misorientations between recrystallized $\{111\}\langle 112 \rangle$ grains and their deformed neighbours, represented in sections of Rodrigues space for constant r_3 values, for the microstructures presented in Figure 6.19. (a) $(111)[1-21]$ variant for the material annealed 70s (Figure 6.19(a-c)), (b) $(111)[-1-12]$ variant for the same material annealed 70s, (c) $(111)[1-21]$ variant for the material annealed 200s (Figure 6.19(d-f)), (d) $(111)[-1-12]$ variant for the same material annealed 200s.

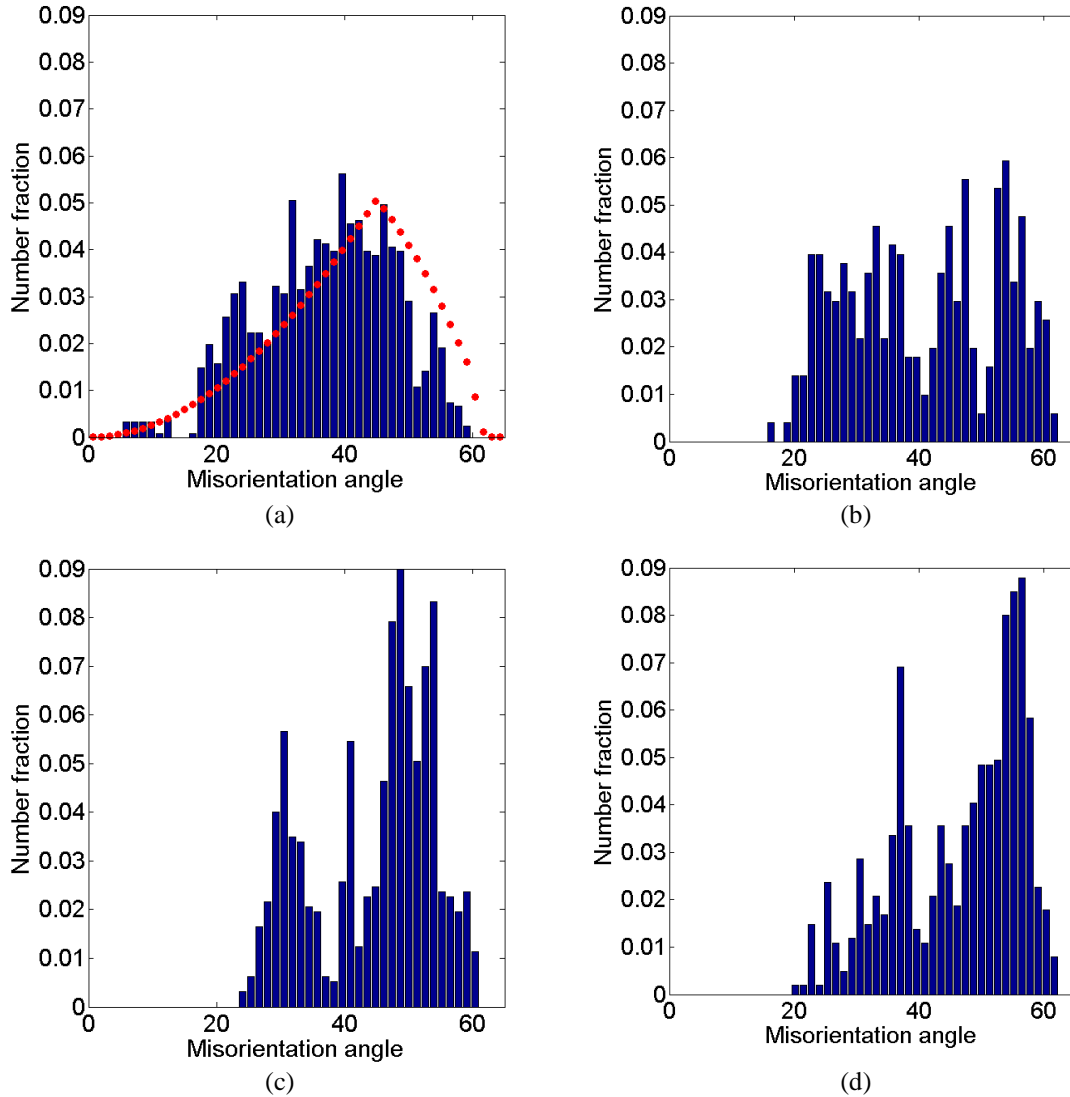


Figure 6.21: (a) to (d) Histograms of the misorientation angles between recrystallized grains and their neighbouring deformed grains, obtained from the data used to calculate the MODFs presented in Figure 6.157 respectively. (a) also presents the MacKenzie plot in red dots (distribution of misorientation angles for a randomly textured polycrystal), showing that the misorientation distribution is non random.

While it was previously known that recrystallization in ferritic stainless steels happens by the replacement of α -fibre grains with γ -fibre grains nucleating in deformed γ -grains ([59] [76] [139] and section 2.5.3), the work presented here provides detailed information that has not been previously reported. There is a clear selection for the nucleation of orientations (in this case $\{111\}\langle 112\rangle$) that form in deformed grains with similar orientations. Other orientations ($\{111\}\langle 110\rangle$) also nucleate in a similar manner but seem to be less predominant (see ODFs Figure 6.7(b) and Figure 6.8(b), Figure

6.13(b) and Figure 6.14(b), Figure 6.18(b) and Figure 6.19(b)). However, this result does not fully describe the process of recrystallization as no comparative measurement is made between different texture components and no information on the nucleation rate or growth rate was obtained.

Extensive work has been carried out in the 1990s to quantitatively measure the relative effects of nucleation and growth rates of grains with specific orientation (for aluminum [162] [163], copper [163] [164] and IF steels [89]) in an attempt to understand the final texture after annealing. With the advances in EBSD techniques, it is now possible to measure large datasets covering thousand of recrystallized grains, leading to reasonable statistical sampling. A more detailed analysis of the nucleation and growth rate of specific orientations was performed here to investigate the development of microstructure and texture during annealing and to explain the formation of the recrystallized texture from the deformed state. Measurements were performed on orientations within $\pm 15^\circ$ of the $\{001\}\langle 110\rangle$, $\{112\}\langle 110\rangle$, $\{111\}\langle 110\rangle$ and $\{111\}\langle 112\rangle$ orientations. These orientations were chosen as they are the most prevalent orientations found in the deformed and recrystallized textures of the material studied here. Several different parameters have been used to characterize nucleation and grain growth:

- The number average grain size: This is the most common parameter reported for microstructure characterization, and is readily available from experimental data.
- The maximum grain size: This parameter, used in [165] for the study of pearlite growth, was argued to be more representative of the actual 3-D size of the grains, as 2-D sections of microstructure rarely truncate grains at their maximum diameter.
- The number fraction of recrystallized grains: Defined as the number of recrystallized grains of a given orientation divided by the total number of recrystallized grains.
- The total area fraction for each of these orientations from the recrystallized subset: this parameter is directly related to the bulk texture of the material.

As seen from Table 6.1, for a given annealing time, a wide range of recrystallized fractions were obtained in this study allowing these parameters to be plotted as a function of the fraction recrystallized instead of annealing time.

Figure 6.22(a) provides information about the process of ‘nucleation’ as it shows the number (fraction) of recrystallized grains of the specified orientation in the microstructure. It shows that grains having near $\{111\}\langle 112\rangle$ orientations appear more numerous compared to other orientations throughout recrystallization. This is consistent with the observations presented in section 6.3.2 as well as observations presented in the literature [89]. Indeed, the number fraction of recrystallized $\{111\}\langle 112\rangle$ grains is at least twice as large as for any other orientation examined (~20% for $\{111\}\langle 112\rangle$, 11% for $\{111\}\langle 110\rangle$, 8-10% for $\{112\}\langle 110\rangle$ and 4% for $\{001\}\langle 110\rangle$). This figure also shows that the number fraction of most texture components is approximately constant during recrystallization. This is also consistent with the observations made by Magnusson et al. on IF steels [89]. The exception is $\{112\}\langle 110\rangle$ which appears to exhibit an increasing number fraction. Although the increase might be considered as negligible (from 8 to 10%), a possible explanation for it can be found using an argument based on stored energy. The $\{112\}\langle 110\rangle$ orientations have been previously considered to have a stored energy in between that of $\{001\}\langle 110\rangle$ (very low stored energy) and $\{111\}\langle 112\rangle$ (larger stored energy) [87]. While the latter orientations classically exhibit an early nucleation (in the sense of an abnormal sub-grain growth compared to the surrounding sub-grains), the former are usually believed to exhibit few nuclei (see section 2.5.3). If one assumes that the time it takes for a subgrain to abnormally grow and be recognized as a new grain is inversely proportional to the stored energy, then the $\{111\}\langle 112\rangle$ deformed grains readily present many nucleation sites, whereas the $\{001\}\langle 110\rangle$ deformed grains present very few nucleation sites (it would take a much longer time for the sub-grains to abnormally grow). As $\{112\}\langle 110\rangle$ orientations have an intermediate stored energy, the nuclei that are initially present as sub-grains are slower to abnormally grow and be recognized as nuclei (using our definition, see section 6.3.1). As a consequence, there is an apparent increase in the number of nuclei with $\{112\}\langle 110\rangle$ orientations due to this delay. Figure 6.22(b) and Figure 6.22(c) provide information related to the growth of grains having specified orientations [162]. The two figures lead to the similar conclusion

that the growth rate of orientations along the γ -fibre are similar and slightly higher than the growth rate of $\{112\}\langle 110\rangle$ orientations. The $\{112\}\langle 110\rangle$ grains exhibit a higher growth rate than the $\{001\}\langle 110\rangle$ grains. As a consequence of these observations, the area fraction of the studied orientations can be ranked from most to least present as followed: $\{111\}\langle 112\rangle > \{111\}\langle 110\rangle > \{112\}\langle 110\rangle > \{001\}\langle 110\rangle$ throughout recrystallization (Figure 6.22(d)).

The comparison between the texture of the first grains to recrystallize (Figure 6.7 and Figure 6.8) and the final product (Figure 6.2) reveals similarities. This observation is classically used to argue that recrystallization is characterized by a nucleation advantage [64] [73] [164]. While this is certainly a major factor in the annealing process of this AISI 445 material, the results provided above show there is also a contribution of growth advantage of orientations on the γ -fibre compared with other orientations (specifically $\{112\}\langle 110\rangle$ and $\{001\}\langle 110\rangle$). The growth advantage has also been observed during the recrystallization of aluminum and copper [64] [163-165].

These two mechanisms provide a qualitative explanation for how the final texture emerges from the deformed material. It does not, however, explain why the texture of the UA-445-R material is different from the texture of the A-445-R material, nor does it explain how groups of grains with similar shearing tendency are formed. To examine this, the spatial distribution of shearing tendency of orientations and how they evolve during recrystallization have to be looked at.

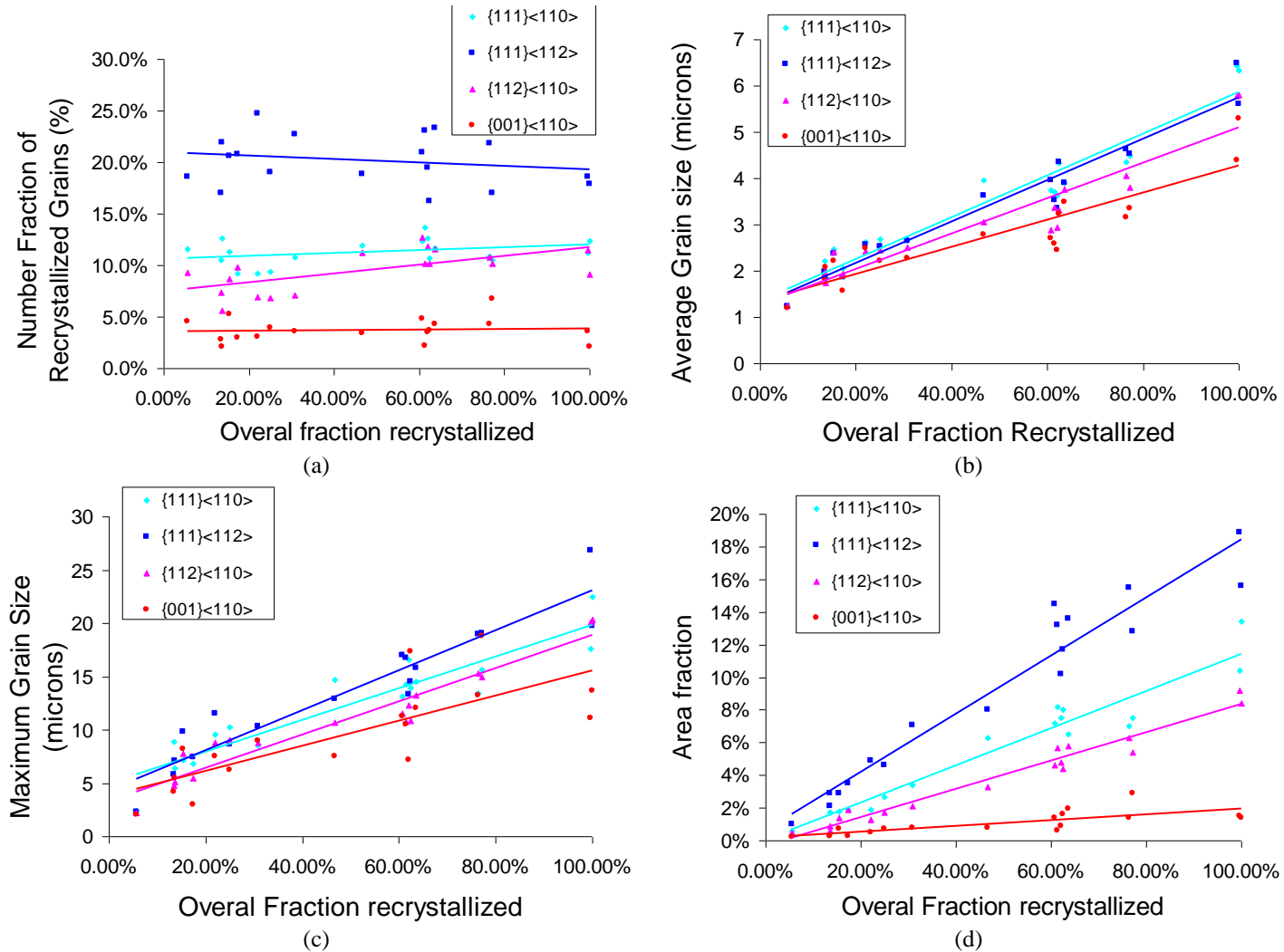


Figure 6.22: Microtexture evolution of specific crystallographic orientation during recrystallization. (a) Number fraction of recrystallized grains, (b) average grains size, (c) maximum grain size and (d) total area fraction, as a function of the overall fraction recrystallized. Solid lines are used only to illustrate trends in the data.

6.4. Influence of Annealing on the Spatially Heterogeneous Distribution of Texture

As chapter 5 showed, both the bulk texture and the spatial distribution of shearing orientations are responsible for ridging. In the case of the AISI 445 annealed hot band, the replacement of the deformation texture by the recrystallization texture composed of a well developed γ -fibre and strong $\{111\}\langle 112\rangle$ orientations clearly reduces ridging compared to the AISI 445 un-annealed hot band or the AISI 409. This material presents the highest $\{111\}\langle 112\rangle$ intensity in the final texture amongst the three materials studied and is also the material that exhibits the lowest ridging. It is thus important to look at the relationship between the apparition and growth of such orientations, their spatial distribution and their effect on ridging.

Starting from the hypothesis that grains with near $\{111\}\langle 112\rangle$ orientations form preferentially (as showed in Figure 6.22(a)), this section will look at how their presence in the microstructure during recrystallization tends to break up the features responsible for ridging. This section will also look at how the different thermomechanical routes influence the final recrystallization behaviour and how this could explain the different ridging behaviour observed in the three materials studied.

The origins of the preferred apparition of $\{111\}\langle 112\rangle$ orientations during the early stages of recrystallization (Figure 6.7 and Figure 6.8) can be found in the structure of the deformed grains. While deformed grains along the α -fibre (and especially orientations between $\{001\}\langle 110\rangle$ and $\{112\}\langle 110\rangle$, e.g Figure 6.23(a)) present a misorientation profile composed of small point-to-point misorientations (average of 1°) that can lead to large point-to-origin misorientation up to 50° over $450\ \mu\text{m}$ (see Figure 6.23(c)), deformed grains belonging to the γ -fibre (for example $\{111\}\langle 112\rangle$, e.g Figure 6.24(a)) exhibit a different behaviour. Firstly, a single grain presents a much lower orientation spread, as can be seen in the pole figures Figure 6.24(b). Secondly, the misorientation profile measured across these grains (along TD) is composed of higher point-to-point misorientations with multiple jumps up to 6° and an average of 2.1° , consistent with a substructure composed of well defined cells that can be highly

disoriented [63] [76]. This type of substructure is usually associated with larger stored energy [73], which can act to drive recrystallization [17] [63] [68] [166].

As a consequence, orientations close to $\{111\}\langle 112\rangle$ are the first to appear as new recrystallized grains. These orientations have been shown to have either no or very low positive or negative out-of-plane shearing tendency (Figure 5.18). Because the deformed γ -fibre grains are composed of multiple well defined cells relatively highly misoriented from each other, some of the cells can be several degrees away from the exact $\{111\}\langle 112\rangle$ orientation. Consequently, from a single deformed γ -grain, recrystallized grains with both shearing tendency (positive and negative) can be generated. As they grow, the newly formed grains will progressively consume their parent grains then the adjacent grains, progressively replacing deformed grains with high shearing tendency (the majority of the deformed grains belong to one of the α -fibres which are known to have a high out-of-plane shearing tendency) by grains with either no shearing tendency (exact $\{111\}\langle 112\rangle$) or very low shearing tendency of both signs.

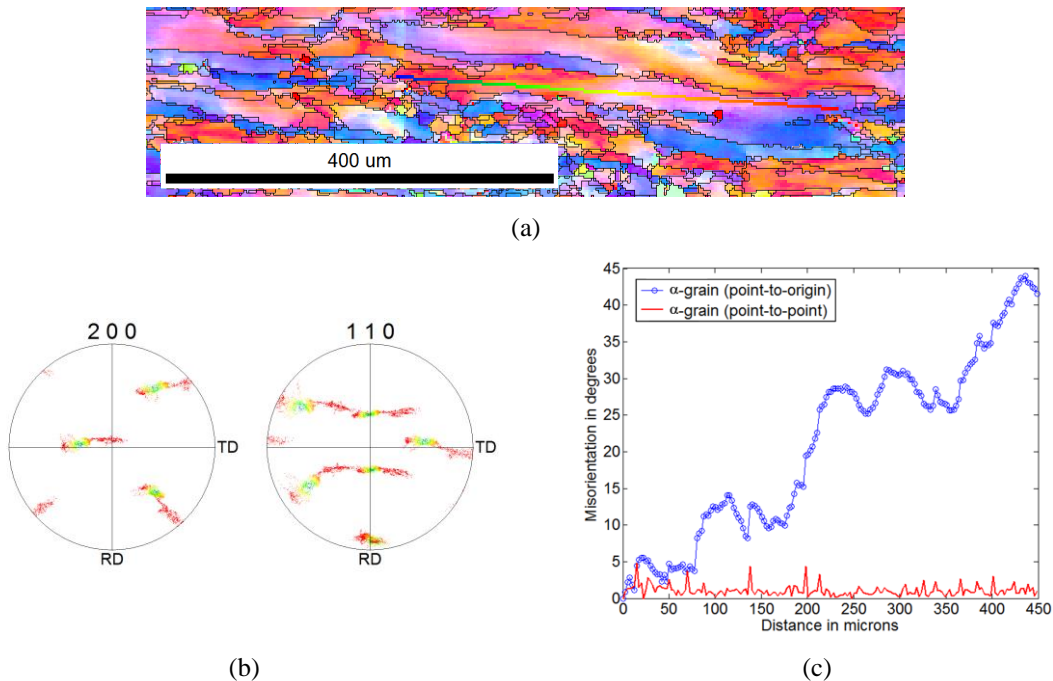


Figure 6.23: (a) Characterization of a deformed grain belonging to the α -fibre. Such grains usually present a large gradient of orientations (b) accompanied by a misorientation profile (c) characterized by small point-to-point misorientations (average 1.1°) that can however add up and generate large misorientation gradients when compared to the point of origin (in this case 50° over $450\ \mu\text{m}$).

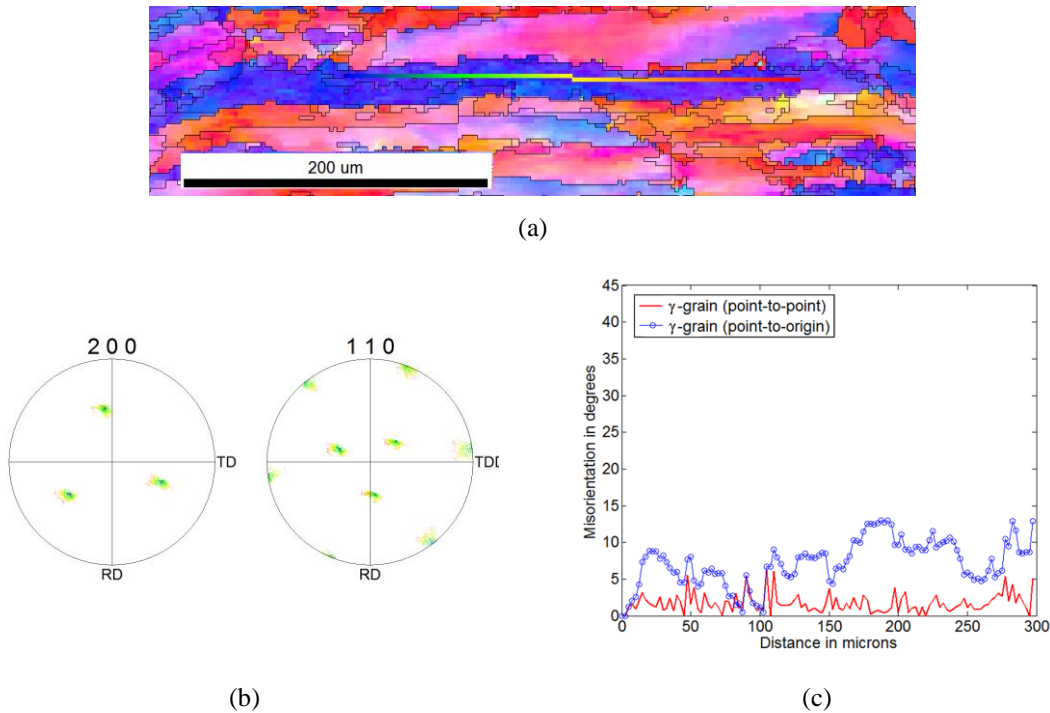


Figure 6.24: (a) Characterization of a deformed grain belonging to the γ -fibre. Such grains usually present little gradient of orientations (b) accompanied by a misorientation profile (c) characterized by larger point-to-point misorientations (average 2.3°). The cumulative profile (with regards to the point of origin) is more chaotic and does not present cumulative misorientation over large distance.

This process breaks up the elongated microstructural features with high shearing tendency developed during rolling by replacing them with multiple new grains with different shearing behaviour of lower intensity, thus reducing the overall intensity of shearing of this specific region of material. A schematic of this process is presented Figure 6.25.

This theoretical description is confirmed by experimental observations. Using the partially recrystallized EBSD maps, it is possible to calculate the shearing tendency of recrystallized grains in a similar manner as what has been presented previously. Using the mean field VPSC model (see section 5.4.4), the out-of-plane shearing tendency was calculated for partially recrystallized microstructures. The VPSC model was used for these calculations for three reasons. First, because of the periodicity on this specific plane (ND plane), grains in the VPFFT model would be assumed to be columnar along ND, which would be a poor assumption. Second, it was seen in section 5.4.4 that the overall spatial distribution or shearing tendency obtained from VPSC or VPFFT are very similar,

and that only fine details differentiate them. Third, this tool is faster than VPFFT and allows for a quick visual representation of the distribution of out-of-plane shearing intensity.

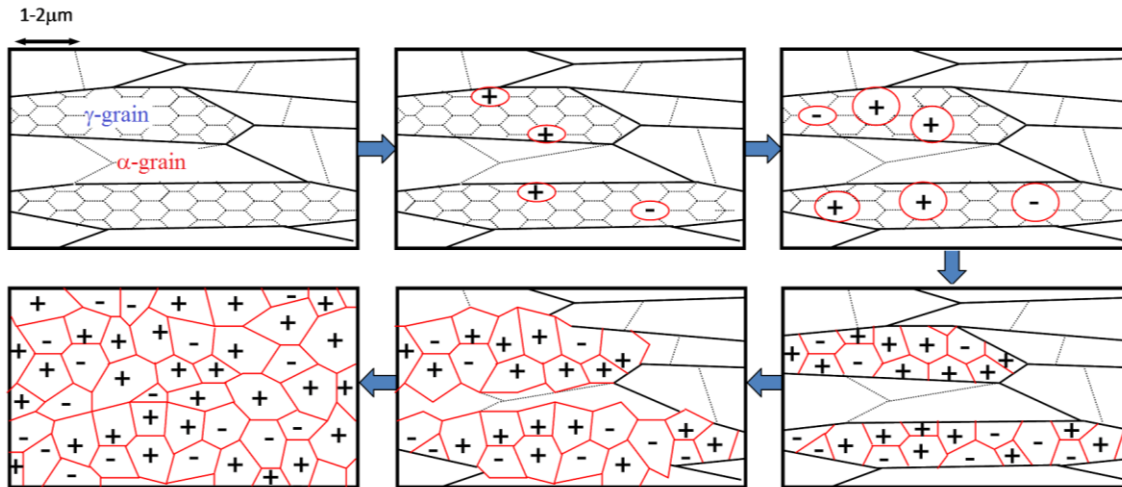


Figure 6.25: Schematic of recrystallization during annealing in ferritic stainless steel and its effect on the spatial distribution of sign of shearing tendency.

It can be seen in Figure 6.26 that during recrystallization, the former deformed grains are replaced by grains with both sign of shearing tendency.

As a consequence, any process which favours the formation of $\{111\}\langle 112 \rangle$ grains will be beneficial for the reduction of ridging. This is confirmed by the comparison between the two AISI 445 materials studied in this work. It was seen in Chapter 5 that the un-annealed hot band presents a much stronger α -fibre texture compared to the annealed hot band (Figure 5.4(d) and Figure 5.6(d)). In addition, the grains in the un-annealed hot band present a pancake shape. As it will be explained, these two conditions favour the formation of a strong α -fibre during cold rolling, at the expense of the γ -fibre

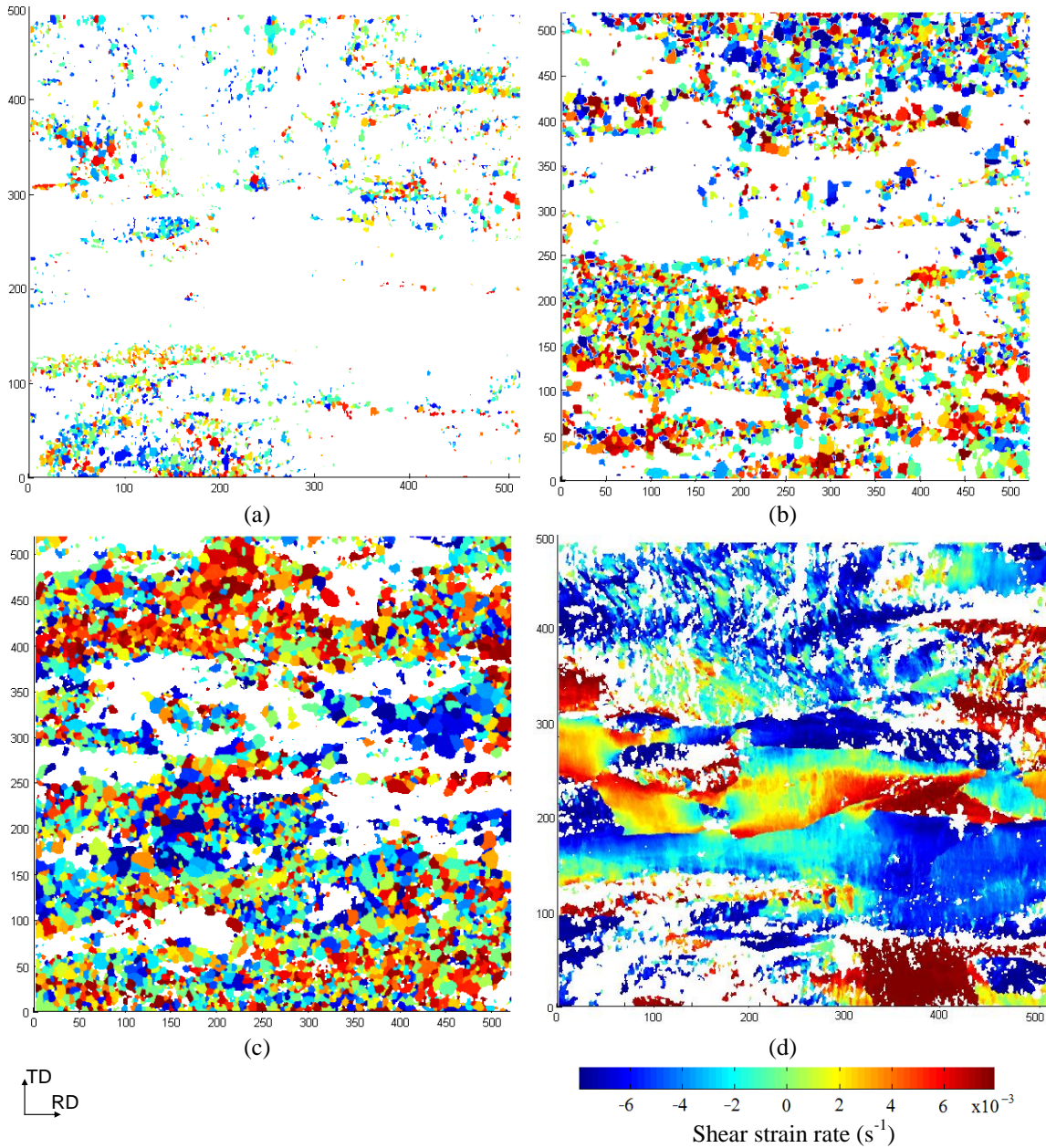


Figure 6.26: Spatial distribution of shear strain rate (s^{-1}) during recrystallization, for recrystallized grains. The intensity was calculated using the method described at the end of section 5.4. The scale on each figure is in μm . (a) is obtained after 15.6% recrystallization, (b) after 49.7% recrystallization and (c) after 73.9% recrystallization. (d) is the intensity of shear strain rate for the deformed grains for the microstructure presented in (a)

It is possible to visualize these effects by calculating the rotation field of various orientations as a function of deformation conditions. For simplifying the observations, it was assumed that the un-annealed hot band was composed of grains with a pancake shape (aspect ratio of 1:10:50 along ND, TD and RD respectively) and embedded in a matrix

composed of a strong α -fibre and weak γ -fibre. The annealed hot band was assumed to be composed of equiaxed grains embedded in a matrix composed of 1000 grains having a random texture. For each condition, plain strain compression up to 1% deformation was simulated using the VPSC model for multiple orientations on a regular grid of Euler space (every 5° along φ_1 and Φ , φ_2 being equal to 45°), assuming a linearization procedure with $n^{\text{eff}}=10$ [149]. For each initial orientation, the final orientation after deformation was estimated and the rotation vector between initial and final orientation was represented back in the Euler section $\varphi_2=45^\circ$. A scaling coefficient of 15 has been applied to the length of the vectors for ease of visualization.

It can be seen in Figure 6.27 that although both cases present similarities, there are also some major differences. In particular, the rotation rates of orientations close to the α -fibre in the case of the un-annealed hot band (Figure 6.27(a)) are much lower towards the γ -fibre (and especially towards the $\{111\}\langle 112\rangle$ orientations, represented by circles taking into account a spread of 15°) compared to the annealed hot band (Figure 6.27(b)). As a consequence, the cold rolling of the AISI 445 un-annealed hot band results in a material containing fewer γ -fibre grains, especially fewer deformed $\{111\}\langle 112\rangle$ grains. Since it has been seen that there is a clear advantage of nucleation of $\{111\}\langle 112\rangle$ grains within deformed $\{111\}\langle 112\rangle$ grains, the number fraction of recrystallizing $\{111\}\langle 112\rangle$ grains will be lower in the case of the un-annealed hot band, providing more room for the recrystallization of other orientations with higher shearing tendency (such as $\{111\}\langle 110\rangle$, $\{112\}\langle 110\rangle$ and $\{223\}\langle 582\rangle$ -like orientations for instance). Because these orientations have both higher intensity for out-of-plane shearing and are associated with a single sign of shearing, both intensity of shearing and clustering of shearing will be enhanced, leading to stronger ridging.

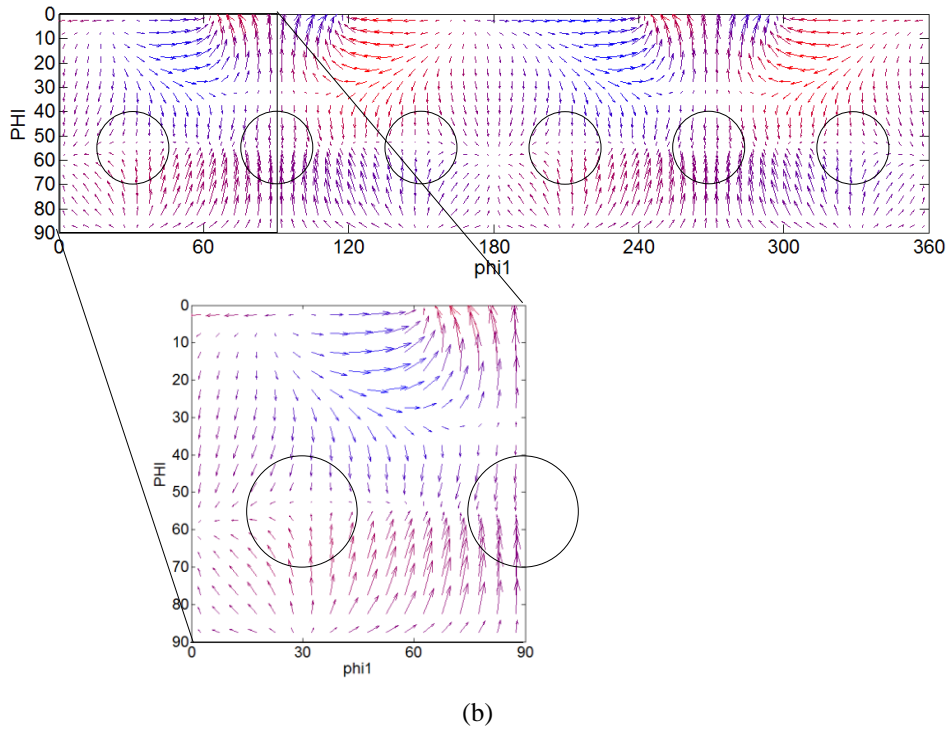
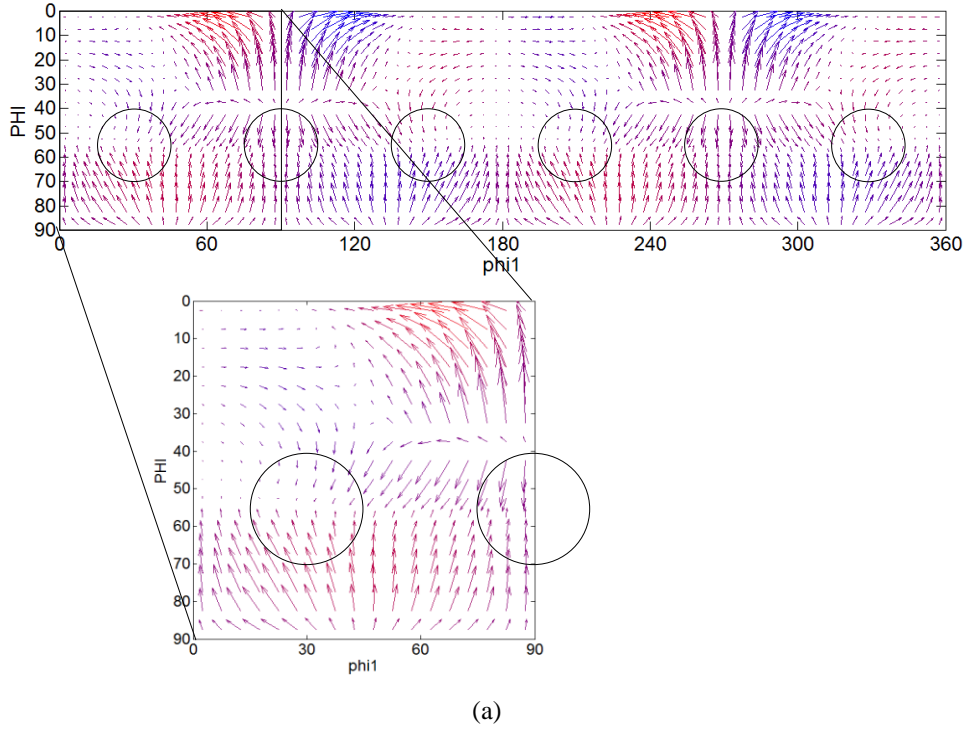


Figure 6.27: Rotation field of orientations during plain strain compression, using the VPSC model with $n^{\text{eff}}=10$. (a) Pancake shaped grains embedded in a deformation texture (strong α -fibre and weak γ -fibre) and (b) equiaxed grains embedded in a random texture. A deformation of 1% was simulated and a scaling factor of 15 was applied for representation. The color corresponds to the change of section for ϕ_2 : blue is for $\phi_2 < 45^\circ$ and red is for $\phi_2 > 45^\circ$

6.5. Conclusion

In this section, the recrystallization behaviour of an AISI 445 annealed hot band after cold rolling was characterized. It was shown that the deformed microstructure, composed mainly of α -fibre grains, was replaced by new grains belonging to the γ -fibre. More precisely, it was shown that there is a clear nucleation advantage of orientations near $\{111\}\langle 112\rangle$ within deformed $\{111\}\langle 112\rangle$. This nucleation advantage is also accompanied by a growth advantage that leads to the texture observed in the final product, i.e. a strong γ -fibre texture with maximum intensity around $\{111\}\langle 112\rangle$. Those orientations have very low or no shearing tendency and new orientations close to $\{111\}\langle 112\rangle$ can possess both positive and negative out-of-plane shear strain rate. A deformed grain, which is more likely to have a strong positive or negative shearing tendency as it belongs to an α -fibre orientation, will thus be replaced by multiple grains with both positive and negative out-of-plane shearing tendency of low intensity. Comparison between the annealed and un-annealed hot band of this material revealed that these conditions are favourable for ridging reduction by decreasing both the intensity and the spatial distribution of shearing tendency. Thus, any step in the process that favours the formation of recrystallized $\{111\}\langle 112\rangle$ grains needs to be followed if one wants to reduce ridging.

Chapter 7: On the Origin of Ridging and the Heredity of Texture and Microstructure

7.1. Introduction

The previous chapters have shown that following cold rolling and annealing, the final sheet product can contain large regions that have a statistically higher proportion of grains with one direction of out-of-plane shearing behaviour than the other (especially visible in the case of the AISI 409). These regions can't be described by a single orientation, nor are they composed of grains all with the same sign of out-of-plane shearing. This was shown to be due to a randomization of both orientation and out-of-plane shearing behaviour caused by recrystallization. In the case of the A-445-R material, it was shown that the recrystallization leads to no visual evidence of such regions in EBSD data. Even when the microstructure doesn't clearly reveal these regions, ridging is still present, although with a lower amplitude. These regions must be developed during processing steps that come well before cold rolling and annealing.

It has been previously observed that when samples were taken from the columnar grain regions of the slab and then processed by hot and cold rolling, the final sheet usually exhibits higher levels of ridging compared to samples from the equiaxed region of the slab [27] [108]. Such observations led some authors ([27] [43]) to the conclusion that ridging is a consequence of the casting. No physical explanation, however, was given to explain why this difference exists between samples taken from the surface and the centre of the slab.

In this section an effort is made to explain this on the basis of texture evolution and grain shape during hot rolling. Starting from the casting, a simplified, semi-quantitative explanation is proposed for the development of microstructure and texture in the final product. This is then discussed in the context of ridging. Rather than attempt to capture all of the complex phenomena occurring during hot rolling, the expected texture evolution occurring during deformation is predicted in plane strain compression. The difference between these results and experimental texture and microstructure

observations are then hypothesized to be a consequence of other phenomena such as continuous dynamic recrystallization.

7.2. Texture and Microstructure Evolution on Roughing

7.2.1. Characterization of the Slab

Microstructural observations of the cast slab (made by the Aperam research centre, Isbergues France), reveal a heterogeneous microstructure through thickness (see Figure 2.23 in the literature review). Columnar grains having dimensions of ~ 2 cm x ~ 2 mm are observed to grow perpendicular to the surfaces of the cast slab. The centre of the slab is populated with more equiaxed grains with an average size of ~ 2 mm. Columnar grains are usually found to have a strong fibre texture characterized by a $\langle 001 \rangle$ direction being parallel to their long axis [43], whereas the equiaxed grains are found to have an almost random texture [99] [103]. The reappearance of a region of columnar grains within the equiaxed region can be attributed to the absence of magnetic stirring in certain regions [105] or by crystal sedimentation [106] (see section 2.5.5).

7.2.2. Roughing

In industrial processing, this slab is reheated to between 1200°C and 1300°C , before being hot rolled (roughing) from its initial thickness (20 cm) to a thickness of 3-4 cm in 5 passes (corresponding to 80% reduction, or an equivalent strain of 1.6), this intermediate product being called the transfer bar (see Figure 2.16).

The microstructure and texture changes during hot rolling are complex due to precipitation, continuous dynamic recrystallization, recovery and plastic strain heterogeneities [167]. Rather than attempt to deal with all of these phenomena, the effect of plain strain compression alone on texture evolution has been simulated. By comparing the predicted texture to the experimental texture inferences can be made about the role of these other mechanisms, particularly continuous dynamic recrystallization.

Texture evolution due to the deformation from the slab to the transfer bar was simulated using VPSC. To mimic the experimental slab, the columnar grain regions were considered to be composed of 720 grains having a strong $\{001\}$ fibre. The orientation of

each grain was determined by choosing the angle φ_1 on a regular grid between 0 and 360° (every 0.5°), Φ randomly between 0 and 5° and $\varphi_2=45^\circ$. The grain shape was set using an aspect ratio of 1:1:10 along RD, TD and ND respectively. The presence of columnar grains oriented along TD, such as those the left hand side of Figure 2.23, were not considered. The resulting texture is presented Figure 7.1(a). The centre of the material was simulated by 1000 equiaxed grains (aspect ratio of 1:1:1) with a random texture (see Figure 7.1(b)).

Roughing was simulated on these two data sets by applying plane strain compression (elongation along direction 1=RD, and reduction of thickness along 3=ND) to a total strain of 1.6 in 5 equal steps of 0.32, assuming a linearization procedure with $n^{\text{eff}}=10$ [149]. The effect of shear introduced by the friction with the surface of the sheet has also been taken into account for the columnar grains, following the procedure presented in [168]. The intensity of the shear strain rate was estimated from the through thickness profile of the equivalent strain [61], assuming that the deformation was purely plain strain at the centre, and was found to be roughly twice the strain rate $\dot{\epsilon}_{11}$ at its maximum ($s=0.8$). The resulting textures after deformation are presented in Figure 7.2. It is expected that an experimentally hot rolled sheet with a gradient of shear through its thickness near the surfaces would present a mixture of the two conditions presented in Figure 7.2(a) and Figure 7.2(b) coming from the behaviour of different layers in the sheet thickness.

The first observation that can be made is that for a given deformation (80% reduction in thickness), the final texture is strongly dependant on the initial state of the material. While the orientations of the columnar grains rotate to the rotated cube positions with a slight extension towards the α -fibre in plain strain compression, and towards the Goss orientation when shear is introduced, the orientations of the equiaxed grains at the centre of the slab rotate more strongly towards the γ -fibre, with maximum intensity around the $\{111\}\langle 110\rangle$ orientations. This texture evolution is coherent with the rotation rate maps presented in Figure 6.27(b), which showed that the $\{111\}\langle 110\rangle$ orientation strongly attracts other orientations. As mentioned earlier (section 2.5.2), the presence of the columnar grains in the central region is an additional source of heterogeneity detrimental for ridging. Indeed, as seen in Figure 7.2, these orientations when deformed

in plain strain compression will rotate towards the rotated cube orientations, which are extremely hard to recrystallize. These columnar grains are even larger than the equiaxed grains, and will keep their very large dimension without recrystallizing, as well as their detrimental orientations.

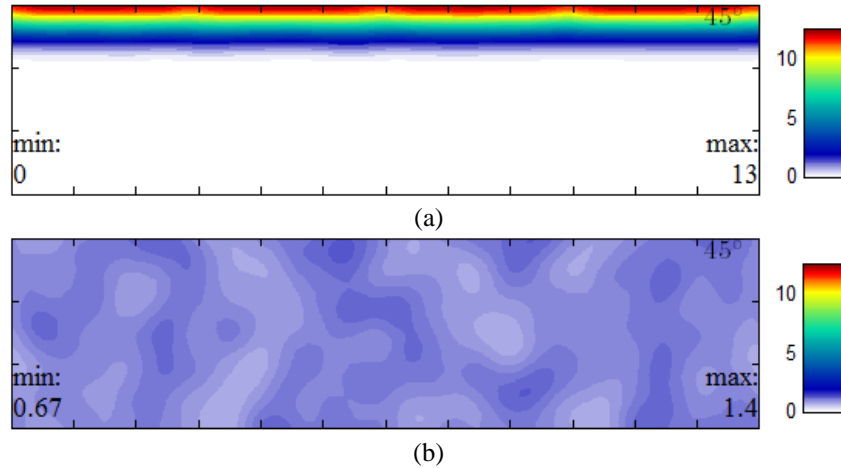


Figure 7.1: Initial ODFs produced for simulating (a) the surface and (b) the centre of the slab, plotted on the $\phi_2=45^\circ$ section of the Euler space using the software MTEX.

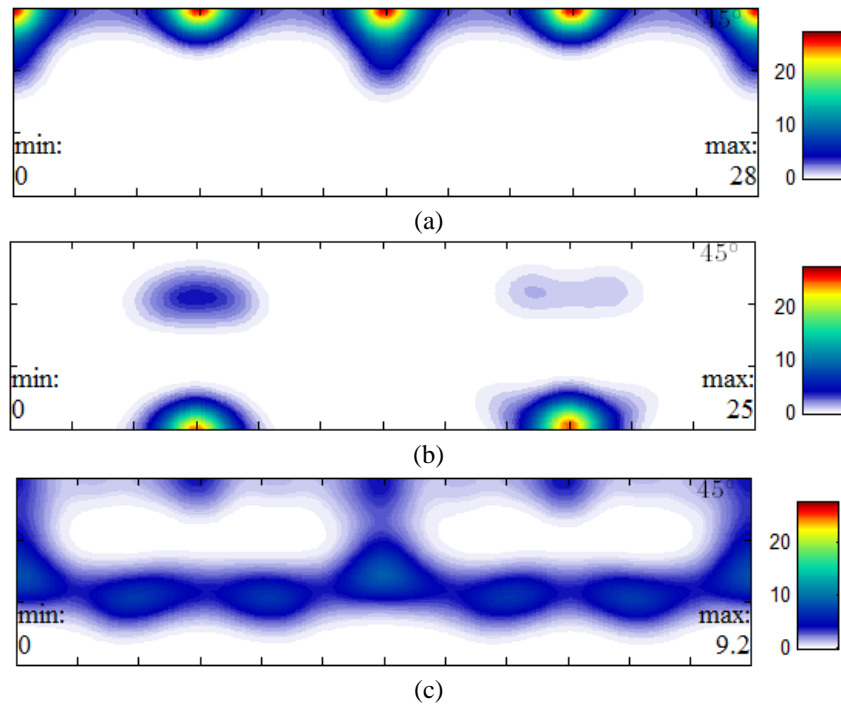


Figure 7.2: Final textures obtained after 5 steps of 0.32 strain (80% rolling) for (a) the surface in plane strain compression, (b) the surface of the slab with introduction of shear, and (c) the centre of the slab in plain strain compression, plotted on the $\phi_2=45^\circ$ section of the Euler space using the software MTEX.

7.2.3. Comparison with the Experimental Transfer Bar

The results of the texture simulations were next compared with a sample taken from an industrial transfer bar of the AISI 445 alloy (provided by Aperam, Isbergues). This material was characterized using EBSD on the transverse plane through the entire thickness (Figure 7.3). Although the dimensions of the measured area do not contain enough grains to make a fully statistical description of the microstructure and texture, it is sufficient to provide a basis for a comparison with the texture simulations.

The transfer bar presents a very heterogeneous microstructure and texture through thickness, this heterogeneity being inherited from the slab. The surfaces are composed of very large and unrecrystallized grains presenting a texture similar to what was predicted by the VPSC simulations (Figure 7.2(a), Figure 7.2(b) and Figure 7.3(b)). The centre of the transfer bar is found to be composed of a mixture of elongated deformed grains and equiaxed recrystallized grains, while the texture is composed of a strong α -fibre and a weaker γ -fibre oriented grains. A more detailed view of the microstructure of the transfer bar on the ND plane at mid thickness is presented in Figure 7.4 (courtesy of Aperam). On this plane, some deformed grains are extremely elongated, reaching dimensions larger than 5.5 mm along RD and up to 1 mm along TD. These are probably grains from the slab that have not been recrystallized yet. Other grains also appear deformed but are smaller (2-3 mm along RD, and about 400 μm along TD). The recrystallized grains are equiaxed and present a grain size varying from 100 μm to 600 μm .

The experimental texture of the central region is quite different from the VPSC predictions. This is due to the phenomena that occur during hot rolling that are not taken into account by the VPSC simulations. During hot rolling, dislocations are stored due to work hardening but because of the high stacking fault energy and high temperature, dislocation climb and glide lead to significant recovery [169]. A detailed description of the phenomenon responsible for recovery for this material is given elsewhere [170]. As a result, the transfer bar is composed of deformed grains with a well defined sub-structure generated by the rearrangement of dislocations into low misorientation walls. It is commonly observed that some of the sub-grains having low dislocation densities grow at the expense of neighbouring sub-grains. Upon reaching a critical size these can bulge into a neighbouring deformed grain having higher stored energy, resulting in the formation of

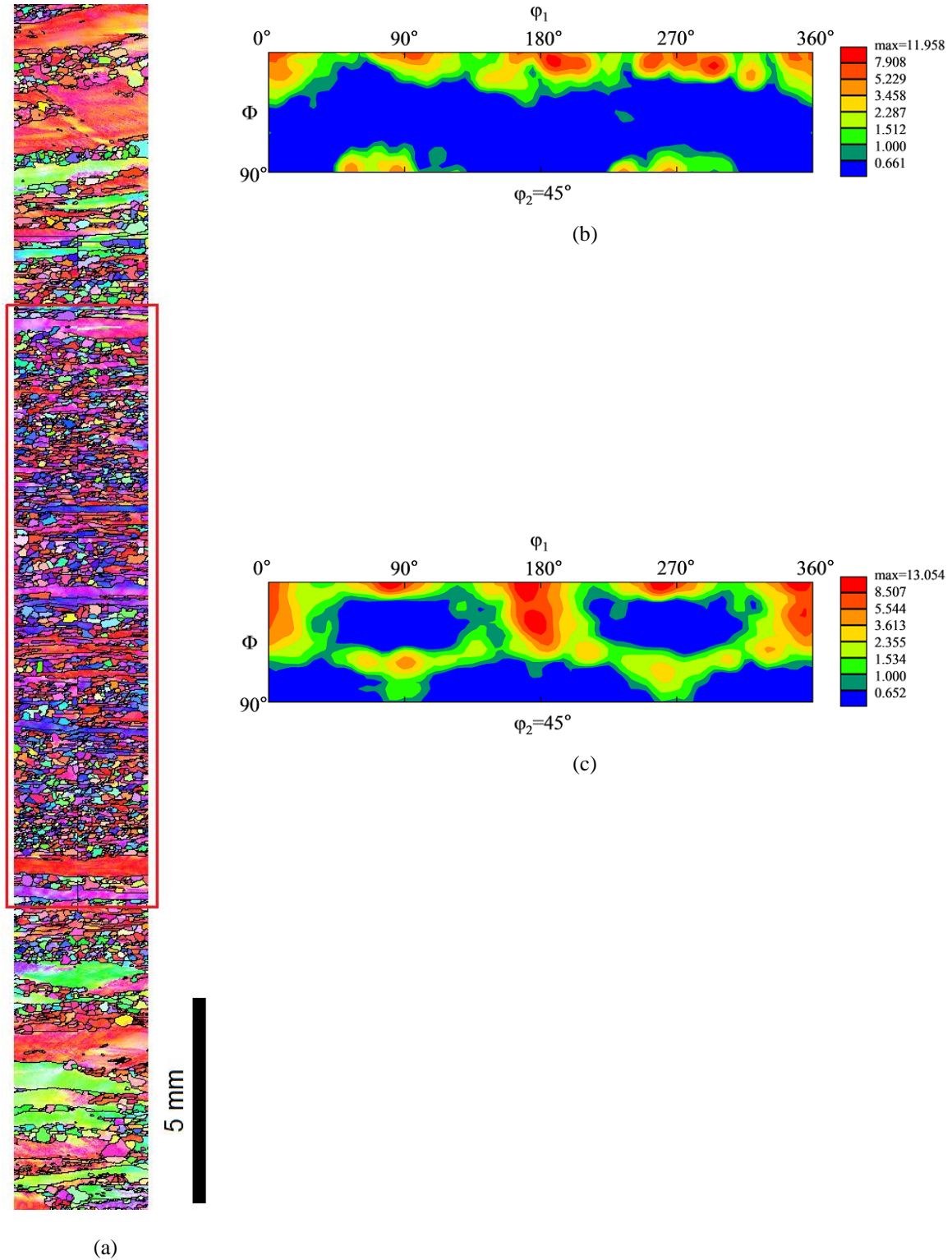


Figure 7.3: EBSD characterization of the transfer bar. (a) Inverse pole figure map of the transverse section (the horizontal direction is RD, the vertical direction is ND), (b) texture of the two surfaces combined and (c) texture of the central region. The centre was considered to be the region surrounded by the red box.

new grains by the strain induced boundary migration (SIBM) mechanism [171]. A detail from Figure 7.3(a) exhibiting bulging is presented in Figure 7.5. In the case of ferritic stainless steels, as mentioned in the literature review, the amount of stored energy depends strongly on orientation. Orientations close to $\{001\}\langle 110\rangle$ and along the α -fibre are usually associated with low stored energy [87]. These orientations thus present favourable conditions for SIBM and are able to consume the orientations that store more energy during deformation (γ -fibre orientations). This results in a decrease of the γ -fibre intensity at the expense of the α -fibre, especially $\{001\}\langle 110\rangle$. This is the exact opposite of what was presented in Chapter 6, where it was argued that static recrystallization favours the development of γ -fibre grains at the expense of the α -fibre grains.

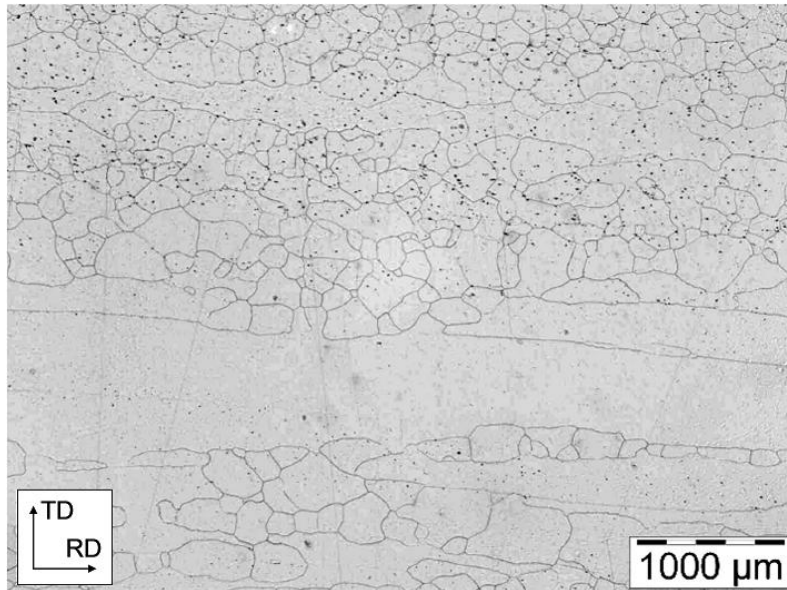


Figure 7.4: Detail of the microstructure of the transfer bar on the sheet plane at mid-thickness, revealing a mixture of large deformed grains and smaller recrystallized grains (courtesy of Aperam, Isbergues).

The important difference between dynamic recrystallization and static recrystallization is that in the former extensive recovery can occur in both α and γ grains leading to the α -fibre grains that can easily grow into the higher energy γ -fibre grains. Annealing following cold deformation on the other hand allows γ -fibre grains to take advantage of the high local misorientations to drive abnormal sub-grain growth. Indeed, some evidence of SIBM (α -fibre grains bulging) can be observed in static

recrystallization but this is much less an important mechanism compared to abnormal sub-grain growth in the γ -fibre oriented grains. In addition to the enhancement of the $\{001\}\langle 110\rangle$ orientations by SIBM, Figure 6.27(b) shows that plain strain compression spreads the $\{001\}\langle 110\rangle$ orientation all along the α -fibre. The combined effect of SIBM and plain strain compression of the α -fibre can thus explain the origins of the strong α -fibre in the transfer bar, in contrast to the VPSC simulations.

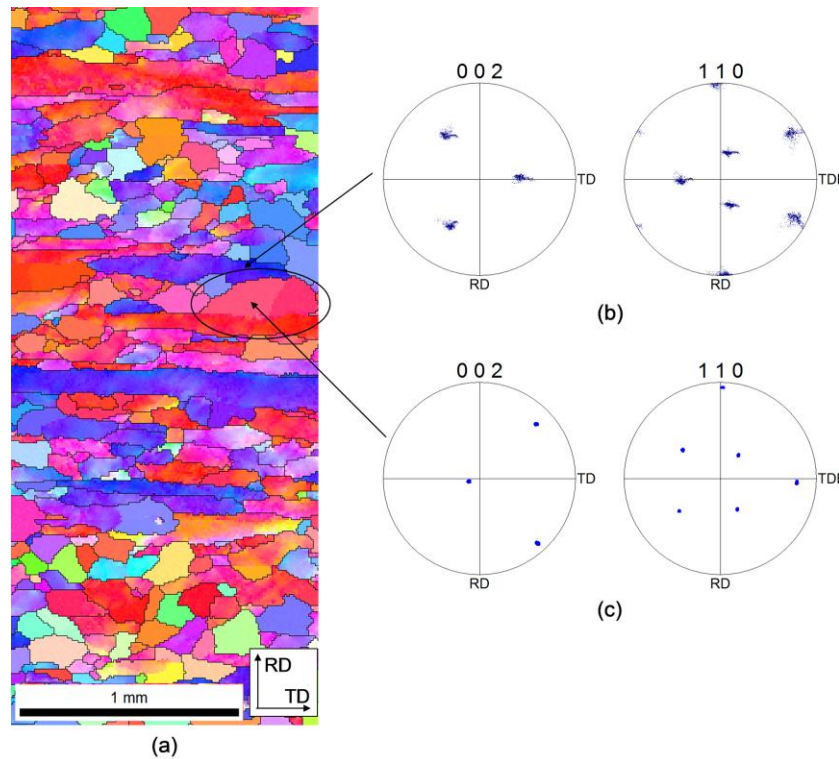


Figure 7.5: Detail from Figure 7.4(a) showing the bulging (circled) of an α -fibre grain close to $\{001\}\langle 110\rangle$ (as indicated by (c)) into an adjacent grains whose orientation is close to $\{111\}\langle 112\rangle$ (as indicated by (b)).

7.3. Relation to Ridging

The hypothetical microstructural evolution proposed above can help us to understand the relationship between processing and ridging. During roughing, the centre of the material changes from a homogeneous structure composed of equiaxed grains having a random texture and a grain size of about 2 mm (similar to half of the wavelength observed on a ridged sheet) to a heterogeneous structure where grains that are still unrecrystallized are surrounded by recrystallized grains. The texture of this material is

composed of a strong α -fibre, these grains having a strong out-of-plane shearing behaviour (Figure 5.18).

Furthermore, the dimension of the recrystallized grains in the transfer bar (between 100 and 600 μm roughly) corresponds to the width of the orientation banding of γ -fibre grains and non γ -fibre grains that are classically observed in the final product (Figure 2.13, Figure 5.2(a), Figure 5.4(a) and Figure 5.6(a)), as highlighted in Figure 7.6.

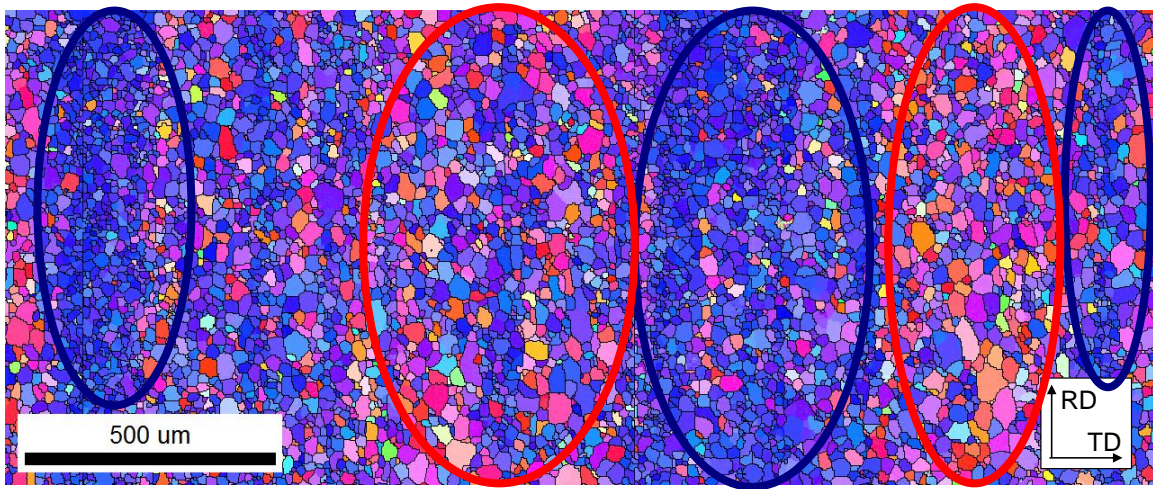


Figure 7.6: Detail from Figure 5.2(a) showing the alternation of bands of grains with γ -fibre orientation (surrounded in blue) and grains with non γ -fibre orientations (surrounded in red).

Based on these observations one can propose the following hypothesis for the origin and heredity of microstructure and texture evolution important for ridging. A grain (~ 2 mm in size) initially present in the slab with a random orientation (e.g. Figure 7.7 top) will see its orientation rotate during roughing towards one of the α -fibres while being elongated along RD (e.g. Figure 7.7 centre). This grain can remain fully deformed (yellow grain), and thus keep its large aspect ratio (several mm or even cm along RD, and about 1-2 mm along TD), or be replaced by a set of new grains by recrystallization. These recrystallized grains will have orientations closely related to the original orientation on the α -fibre and whose dimension varies between 100 and 600 μm (red and blue grains). From the transfer bar, the finishing steps of hot rolling will further enhance this microstructure. The still un-recrystallized grains (yellow grain) will be further elongated, while the texture (α -fibre orientations) will be strengthened during rolling (according to

Figure 6.27). The equiaxed recrystallized grains from the transfer bar, while still being included in a group of grains that are all originated from a single previous grain from the slab, will develop an elongated structure that will eventually lead to the orientations banding of γ -fibre grains and non γ -fibre grains that are observed in the final product (e.g. Figure 7.6). According to Figure 6.27, if these grains are slightly away from the $\{001\}\langle 110\rangle$ orientations, they will rotate towards $\{111\}\langle 112\rangle$ orientations during plain strain compression, and will thus recrystallize first during the final annealing step, forming the bands of γ -grains observable in the final product. The other grains from the hot band that do not rotate towards $\{111\}\langle 112\rangle$ will either be consumed by the growing $\{111\}\langle 112\rangle$ recrystallized grains (and will be part of the γ -fibre grains bands) or will be replaced by grains with a more random set of orientations (forming the bands of non γ -fibre grains visible on Figure 7.6).

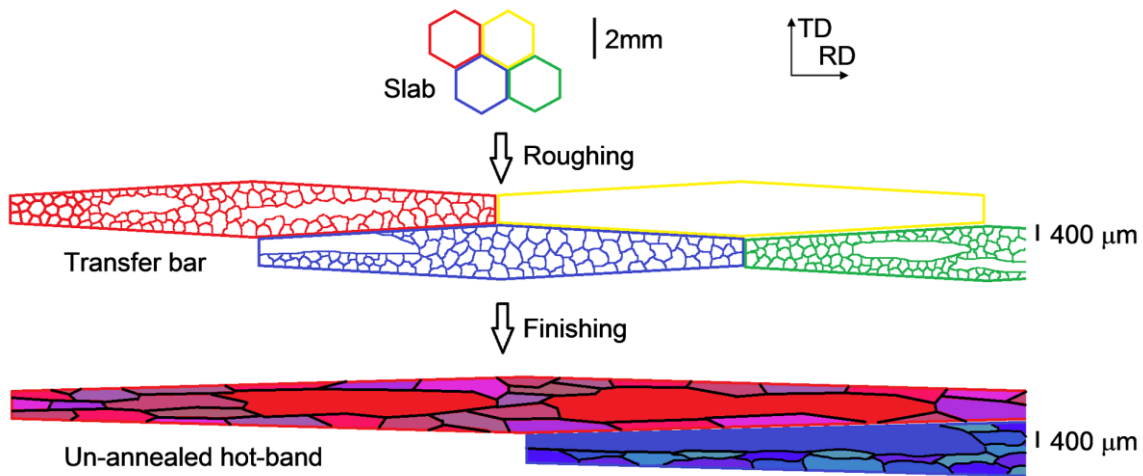


Figure 7.7: Schematic of the microstructure (and texture) evolution during hot rolling, from the slab to the un-annealed hot band.

For the columnar grains, the shift towards the α -fibre is even more pronounced. Furthermore, due to the low stored energy of these orientations and as discussed in the previous section, fragmentation by recrystallization is harder in these grains which prefer to grow by SIBM. A potential proof for this is seen in Figure 7.3, where these grains are still highly deformed. As a consequence, there is less randomization of microstructure and texture due to recrystallization and the elongated grains having high out-of-plane

shearing tendency formed during roughing are not removed, leading to a stronger ridging. The lack of fragmentation of the columnar grains (especially those within the equiaxed grain region) could also be part of the reason for the presence of large areas of grains having similar out-of-plane shearing behaviour in some final products (e.g. 409 grade). By remaining unrecrystallized, these grains keep the high out-of-plane shearing behaviour they acquire during roughing for a longer time during the rest of the process.

From all these observations and hypothesis, it appears that ridging is really a multi-scale problem, where different levels of spatial non-random distribution of features (such as out-of-plane shearing behaviour or orientations), are present. As seen in Figure 7.8, the hills and valleys on a final deformed sample (bottom) are the result of the through thickness deformation of multiple layers of material initially composed of bands of γ -fibre grains and non γ -fibre grains (centre). These bands are themselves composed of multiple grains whose shearing behaviour is not necessarily of a single sign (top). This points to the importance of looking at the through thickness behaviour, and not only at the ND plane as it is commonly found in the literature, for ridging prediction as mentioned in Chapter 5.

From an industrial point of view, the results presented in chapter 5, 6 and 7 show that the reduction of ridging can be achieved by a better spatial randomisation of the out-of-plane shearing tendency. During the final annealing, it was shown to be effectively done by the recrystallization of $\{111\}\langle 112 \rangle$ orientations. Steps in the upstream process that enhance the recrystallization of these orientations have thus to be favoured. One way of doing so is to suppress the formation of columnar grains [27] [108]. The presence of an equiaxed casting does not, however, guarantee low or no ridging (since samples taken from the equiaxed region of the cast slab also exhibit ridging). What is of primary importance is to prevent the formation of a strong α -fibre during the deformation steps. During cold rolling, it was observed that cross rolling [49] and multiple steps of cold rolling and annealing [17] [96] were efficient in reducing the intensity along the α -fibre, although these processing steps are not industrially attractive. During hot rolling, the α -fibre is strengthened by high recovery and SIBM, which consume the γ -fibre grains that store more energy during deformation. It can be suggested that lower amount of recovery

by decreasing the roughing temperature would prevent such an extensive strengthening of the α -fibre (similarly to the decrease in finishing temperature discussed in section 2.5.6).

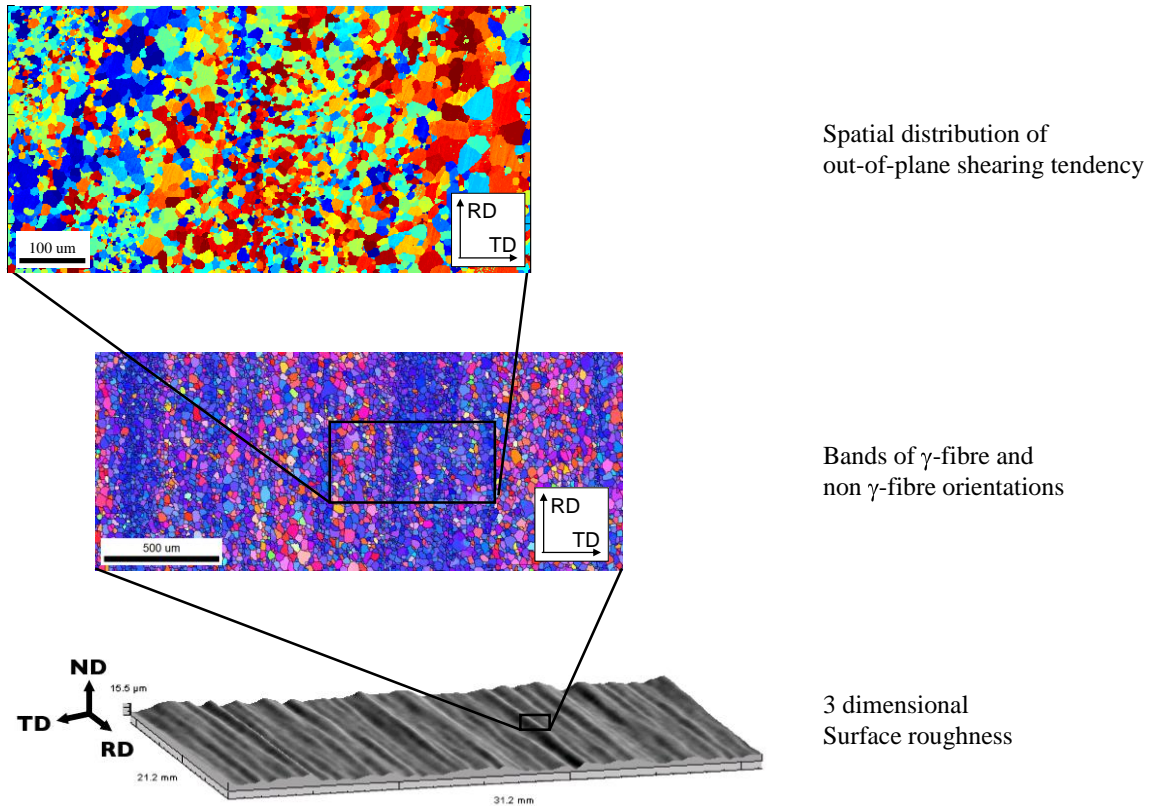
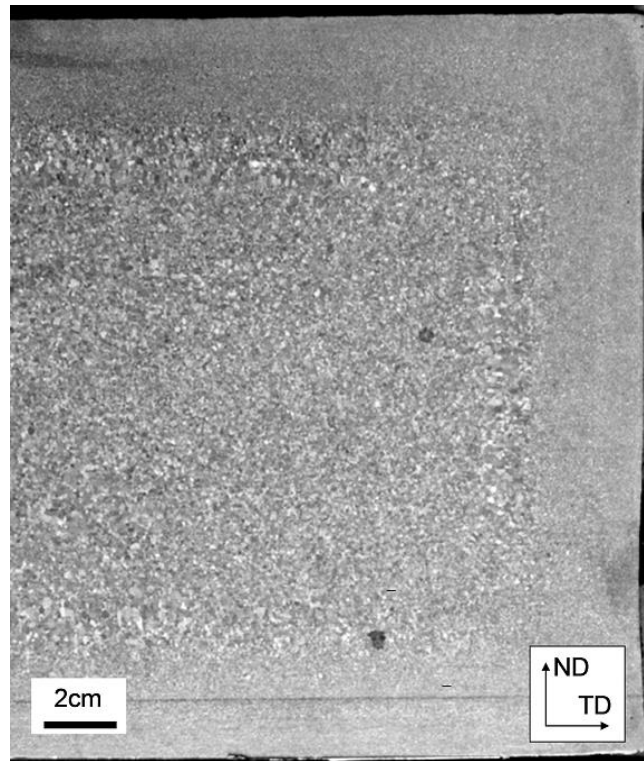


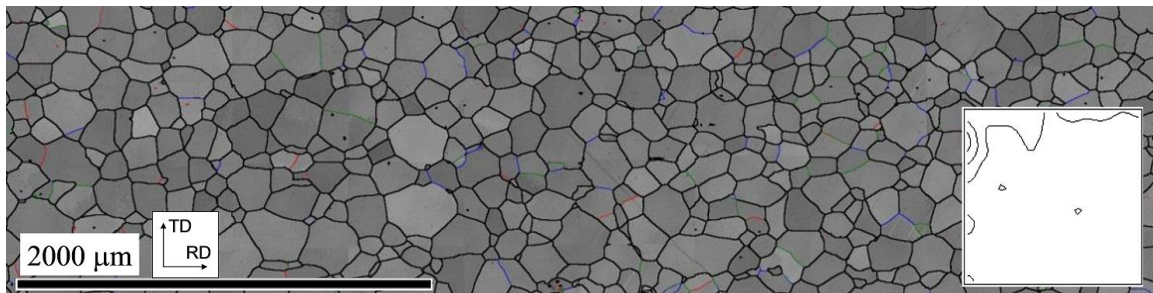
Figure 7.8: Multi-scale schematic characterization of ridging in the final product.

There exist limitations, however, on the temperature for hot rolling in order to prevent excessive load on the rolling mills due to the large reductions per pass. Furthermore, the fragmentation of the initial grains from the cast slab reduces the elongation of these grains while providing more favourable condition for the development of future γ -fibre grains (as explained above). It can thus be suggested that a better recrystallization during hot rolling (or a well recrystallized transfer bar) is favourable. The addition of Ti has been industrially shown to be particularly attractive (grade AISI 445 E2). First, the columnar region is completely absent in the cast slab structure (Figure 7.9(a), provided by Aperam, Isbergues). Second, it was observed that the recrystallization kinetics during hot rolling are much higher than those of the same

grade containing no Ti, leading to a fully recrystallized transfer bar with a very weak α -fibre intensity compared to our material, see Figure 7.9(b) [170].



(a)



(b)

Figure 7.9: (a) Microstructure of the cast slab for the grade AISI 445 E2 showing no columnar grains, figure provided by Aperam, Isbergues. (b) Band contrast EBSD map on the ND plane at mid-thickness and its corresponding texture on the section $\phi_2=45$ of the Euler space using orthotropic sample symmetry. The contours represent intensities of 2, 3 and 4, from [170].

In this work, the difference was explained in terms of texture, the grade E1 containing a stronger α -fibre during hot deformation, which leads to a lower rate of nucleation of recrystallized grains. It was also observed by our industrial partner that this

Ti, Nb-stabilized grade also exhibit a much lower ridging. The mechanisms responsible for these differences are, however, still unknown, and further work is required.

7.4. Conclusion

The aim of this section was to provide a general idea of the possible origins of ridging relative to the industrial processing schedule. It was proposed that roughing was responsible for generating large areas composed of similarly shearing grains. During this processing step, a combination of deformation and annealing leads to the fragmentation of the initial grain, while still retaining a ‘memory’ of its initial out-of-plane shearing behaviour through the similarity between its orientation and that of its parent matrix. Fragmentation leads to the formation of smaller grains whose orientations are related to the initial orientation of the grain from the slab (mainly α -grains). These grains, upon further rolling reduction and annealing steps, are responsible for the orientation banding (γ -fibre bands and non γ -fibre bands) classically observed by EBSD on the final product.

It was also shown that the removal of the regions containing columnar grains, although beneficial for the reduction of ridging, does not prevent its development. A better control of the microstructure and texture in the central region of the cast slab should be an aim. It is suggested that a fully recrystallized transfer bar with low α -fibre intensity would promote a better recrystallization of $\{111\}\langle 112\rangle$ orientations during the final annealing, accompanied by a better spatial randomization of out-of-plane shearing behaviour. Addition of Ti and optimization of the roughing temperature and their relation to texture and microstructure evolution during the process are two potential parameters to examine.

Chapter 8: Conclusions and Future Work

8.1. Conclusions

Although the topic of ridging of ferritic stainless steels has been studied for the past 50 years, the lack of a clear definition of what is responsible for this phenomenon has made it difficult to correlate the surface roughness developed during deformation to microstructure. The work presented in this thesis provides a more precise description of the features responsible for ridging, and suggests a possible explanation for how the full thermo-mechanical process schedule (from the slab to the final product) impacts on ridging severity.

The full-field crystal plasticity VPFPT simulations performed as part of this work highlight a number of important concepts. First, they pointed out the importance of looking at the through thickness sections (RD plane) to evaluate ridging. Previous studies have almost exclusively focused on studies in the ND plane where through-thickness effects can not be assessed. It was also possible in this way to identify the differences in the spatial distribution of grains with various out-of-plane shear strain rates. The interactions between neighbouring grains were found to reduce the intensity of out-of-plane shearing, especially for grains aligned along ND. Importantly, the VPFPT simulations also provided a way of explaining the different ridging behaviour of the three materials studied. Results showed that differences in ridging behaviour could be explained by both the non-random distribution of out-of-plane shearing orientations (difference between the AISI 409 and the AISI 445) and by the bulk texture itself (difference between the two AISI 445 materials). A methodology that allows for the two different effects to be separated was developed by statistically evaluating the non-randomness distribution of out-of-plane shearing behaviour along TD. From this work, a simplified computer program that takes an input microstructure from EBSD and predicts the out-of-plane shearing tendency distribution for a given product was developed and transmitted to the industrial sponsors of this project. This work has also led to a better understanding of the evolution of microstructure and texture during the annealing of the cold rolled sheet. A detailed EBSD analysis showed that annealing after cold rolling typically reduces the tendency for ridging due to the replacement of large α -fibre grains

with finer γ -fibre grains. More specifically, it was shown that the final texture was composed mainly by $\{111\}\langle 112\rangle$ recrystallized grains due to both a nucleation advantage and growth advantage of this orientation. This favoured texture component is beneficial for ridging as the exact $\{111\}\langle 112\rangle$ orientation has no shearing tendency. Due to the spread of orientation around the exact $\{111\}\langle 112\rangle$ component, however, there is a spatial randomization of the out-of-plane shearing tendency. Indeed, it was shown that grains with both positive and negative out-of plane shear strain rate can nucleate and grow out of a single deformed $\{111\}\langle 112\rangle$ grain. Comparison between the un-annealed and the annealed hot bands of the AISI 445 material revealed that the lower ridging behaviour in the final product coming from the annealed hot band is the result of a stronger γ -fibre relative to the α -fibre (and especially $\{111\}\langle 112\rangle$) before and after cold rolling, caused by the extra annealing of the hot band.

These results suggest that the ridging originates in the processes occurring prior to cold rolling. With this in mind, an attempt was made to understand the effect of the entire process schedule on microstructure, texture and the final ridging severity. Based on observations of the cast slab, of the transfer bar and using crystal plasticity simulations, a hypothesis has been proposed to explain the heredity of microstructure and texture that favours ridging. It has been argued that continuous dynamic recrystallization during hot rolling favours the α -fibre orientations that are detrimental for ridging. It has also been suggested that grain shape can influence the evolution of texture in a small but perhaps important way. Finally, it is believed that the spacing between ridges in the final product is determined by the dimensions of the microstructure in the cast slab and that, although an initial grain from the cast slab can be fragmented during hot rolling, there is a memory of its out-of-plane shearing behaviour throughout the process.

8.2. Future Work

The work presented in this thesis has improved our understanding of the relationship between deformation, annealing and ridging in ferritic stainless steels. This work also raises new questions that should be investigated.

1. The surface roughness predictions obtained from the full-field crystal plasticity model used here came from two-dimensional EBSD maps. This assumes that the grains are infinite in length and columnar along RD. While the effect of the grain shape and size along this direction has been estimated previously using a mean field approach [41], a more complete description is still required. This could be investigated by means of a parametric study using the VPFIT model on synthetic microstructures. These simulations would be performed so as to estimate the effect of the spatial non-homogeneous distribution of out-of-plane shearing parallel to the RD on the surface roughness (amplitude and corrugation spacing) associated with ridging.
2. Further work on microstructure and texture evolution during hot rolling (roughing and finishing) is required to confirm the hypotheses proposed in Chapter 7. Understanding the development of texture and the refinement of microstructure during this processing step is required if one wants to improve the processing route in order to favour steps that can both break up the elongated features responsible for banding of shearing behaviour, and lead to a better recrystallization of the hot band. This has been looked at in a recent Ph.D. thesis [170], however this work did not explicitly attempt to describe texture evolution on hot rolling. This needs to be predicted in order to understand the heredity of texture and microstructure through the entire process.
3. This thesis showed that an efficient way of reducing ridging was the introduction of $\{111\}\langle 112 \rangle$ orientations during annealing. In some cases, this process is so efficient that regions of material composed of grains having similar out-of-plane shearing are not easily observable without using the sort of statistical test introduced here. Ridging, however, still occurs in such materials, although its amplitude is low. This is of interest for steel manufacturers as it can direct them to concrete ideas for changes in the upstream thermo-mechanical process that can favour the formation of such orientations in the final annealing. Furthermore, the

hypothesis made here that the spacing between corrugations is determined by the grain size in the slab should give some incentive to modify the microstructure of the slab. As mentioned in section 7.3 the introduction of Ti was shown to effectively modify the slab and the transfer bar microstructures, resulting in very low ridging. The mechanism by which Ti influences ridging is, however, still unclear. Further work is required to evaluate its effect on microstructure and texture change during the process.

4. The origins of the shifted γ -fibre orientations (such as $\{223\}\langle 582\rangle$), which appear during annealing of cold rolled sheet having a strong α -fibre texture, remain unclear. Depending on the processing history, these orientations can end up being a dominant texture component in the final product, although they do not represent a major component of the texture of the deformed material. Because these orientations have a strong out-of-plane shearing intensity, a more detailed analysis of the mechanisms responsible for the nucleation and growth of these orientations is required.

Bibliography

- [1] M. B. Cortie, "History and Development of Ferritic Stainless-Steels." *Journal of the South African Institute of Mining and Metallurgy* 93, no. 7 (1993), pp. 165–176.
- [2] J.-H. Schmitt, "Some Examples of Stainless Steel Use in the Automotive Industry." *Key Engineering Materials* 230–232 (2002), pp. 17–22.
- [3] J. A. Douthett, *Automotive engineering International* 103, no. 11 (1995), pp. 45-49.
- [4] J. Charles, J.-D. Mithieux, P.-O. Santacreu, and L. Peguet, "The ferritic stainless family: the appropriate answer to nickel volatility?" *Revue De Metallurgie-Cahiers D Informations Techniques* 106, no. 3 (2009), pp. 124–139.
- [5] www.aperam.com
- [6] P. Lacombe, B. Baroux, G. Beranger Ed, *Stainless Steels* (1993), Les editions de physique, Les Ulis.
- [7] ASTM Standard A240, (2013), "Specification for Chromium and Chromium-Nickel Stainless Steel Plate, Sheet, and Strip for Pressure Vessels and for General Applications," ASTM International, West Conshohocken, PA.
- [8] DIN EN 10088-2, (2005), "Stainless steels - Part 2: Technical delivery conditions for sheet/plate and strip of corrosion resisting steels for general purposes," Deutsches Institut Fur Normung E.V. (German National Standard).
- [9] W. B. Hutchinson, "Development and Control of Annealing Textures in Low-carbon Steels." *International Metals Reviews* 29, no. 1 (1984), pp. 25–42.
- [10] R. K. Ray, J. J. Jonas, and R. E. Hook, "Cold rolling and annealing textures in low carbon and extra low carbon steels." *International Materials Reviews* 39, no. 4 (1994), pp. 129–172.
- [11] K. M. Lee, M.-Y. Huh, S. Park, and O. Engler, "Effect of Texture Components on the Lankford Parameters in Ferritic Stainless Steel Sheets." *ISIJ International* 52, no. 3 (2012), pp. 522–529.
- [12] F. Emren, U. Vonschlippenbach, and K. Lucke, "Investigation of the Development of the Recrystallization Textures in Deep Drawing Steels by Odf Analysis." *Acta Metallurgica* 34, no. 11 (1986), pp. 2105–2117.
- [13] D. Raabe, and K. Lücke, "Textures of Ferritic Stainless-Steels." *Materials Science and Technology* 9, no. 4 (1993), pp. 302–312.
- [14] U. F. Kocks, C. N. Tomé, and H.-R. Wenk, "Texture and Anisotropy: Preferred Orientations in Polycrystals and Their Effect on Materials Properties." (2000) Cambridge University Press.

- [15] O. Engler, and V. Randle, *Introduction to Texture Analysis: Macrotecture, Microtexture, and Orientation Mapping*. CRC Press (2010).
- [16] Y. B. Park, D. N. Lee, and G. Gottstein, "Evolution of Recrystallization Textures from Cold Rolling Textures in Interstitial Free Steel." *Materials Science and Technology* 13, no. 4 (1997), pp. 289–298.
- [17] M. Y. Huh, and O. Engler, "Effect of intermediate annealing on texture, formability and ridging of 17%Cr ferritic stainless steel sheet." *Materials Science and Engineering a-Structural Materials Properties Microstructure and Processing* 308, no. 1–2 (2001), pp. 74–87.
- [18] S. Mishra, C. Darmann, and K. Lücke, "On the Development of the Goss Texture in Iron-3-Percent Silicon." *Acta Metallurgica* 32, no. 12 (1984), pp. 2185–2201.
- [19] Y. Shimizu, Y. Ito, and Y. Iida, "Formation of the Goss Orientation Near the Surface of 3-Pct Silicon Steel During Hot-Rolling." *Metallurgical Transactions a-Physical Metallurgy and Materials Science* 17, no. 8 (1986), pp. 1323–1334.
- [20] H. C. Chao, "Mechanism of Ridging in Ferritic Stainless Steels." *ASM Transactions Quarterly* 60, no. 1 (1967): 37–49.
- [21] H. Takechi, H. Kato, T. Sunami, and T. Nakayama, "Mechanism of Ridging Formation in 17 Percent-Chromium Stainless Steel Sheets." *Transactions of the Japan Institute of Metals* 8, no. 4 (1967), pp. 233–239. Copyright [1967 Takechi]. This material is reproduced with permission of John Wiley & Sons, Inc.
- [22] R. N. Wright, "Anisotropic Plastic-Flow in Ferritic Stainless-Steels and Roping Phenomenon." *Metallurgical Transactions* 3, no. 1 (1972), pp. 83–91.
- [23] C. W. Sinclair, J.-D. Mithieux, F. Chassagne, Unpublished work, Aperam research centre, 2002
- [24] R. N. Wright, "The Direction of Tensile Strain and the 'roping' Phenomenon in Ferritic Stainless Steels." *Metallurgical and Materials Transactions A* 7, no. 9 (1976), pp. 1385–1388.
- [25] H. C. Chao, "Discussion of 'the Direction of Tensile Strain and "roping" Phenomenon in Ferritic Stainless Steels'." *Metallurgical Transactions A* 8, no. 6 (1977), pp. 1009–1010.
- [26] G. J. Baczynski, R. Guzzo, M. D. Ball, and D. J. Lloyd, "Development of roping in an aluminum automotive alloy AA6111." *Acta Materialia* 48, no. 13 (2000), pp. 3361–3376.
- [27] H. J. Shin, J. K. An, S. H. Park, and D. N. Lee, "The effect of texture on ridging of ferritic stainless steel." *Acta Materialia* 51, no. 16 (September 15, 2003), pp. 4693–4706.

- [28] D. V. Wilson, W. T. Roberts, and P. M. B. Rodrigues, "Effect of Grain Anisotropy on Limit Strains in Biaxial Stretching .1. Influence of Sheet Thickness and Grain-Size in Weakly Textured Sheets." *Metallurgical Transactions a-Physical Metallurgy and Materials Science* 12, no. 9 (1981), pp. 1595–1602.
- [29] K. Sztwiertnia, J. Pospiech, and T. Rostek, "Topological Aspects of Ridging Phenomenon in Ferritic Stainless Steel." *Proc. of Int. Conf. on Stainless Steels* (1999), pp. 647–653.
- [30] K. Bethke, M. Holscher, and K. Lücke, "Local Orientation Investigation on the Ridging Phenomenon in Fe 17-Percent Cr Steel." In *Proceedings of the 10th International Conference on Textures of Materials, Pts 1 and 2 - ICOTOM-10*, (1994), edited by H. J. Bunge, Vol. 157, pp. 1137–1144. Zurich-Uetikon: Transtec Publications Ltd.
- [31] D. V. Wilson, W. T. Roberts, and P. M. B. Rodrigues, "Effects of Grain Anisotropy on Limit Strains in Biaxial Stretching .2. Sheets of Cubic Metals and Alloys with Well-Developed Preferred Orientations." *Metallurgical Transactions a-Physical Metallurgy and Materials Science* 12, no. 9 (1981), pp. 1603–1611.
- [32] P. D. Wu, D. J. Lloyd, A. Bosland, H. Jin, and S. R. MacEwen, "Analysis of roping in AA6111 automotive sheet." *Acta Materialia* 51, no. 7 (2003), pp. 1945–1957.
- [33] N. J. Wittridge, and R. D. Knutsen, "Characterization of Microstructure and Texture Evolution in AISI 430 Ferritic Stainless Steel - Analysis of the Surface Ridging Phenomenon." *Thermomechanical Processing in Theory, Modelling & Practice*, ASM, no. 390 (1997).
- [34] J. D. Defilippi, and H. Chao, "Effect of Chromium and Molybdenum Segregation on Ridging Behavior of Type-434 Stainless Steel." *Metallurgical Transactions* 2, no. 11 (1971), pp. 3209–3216.
- [35] S. Keijiro, and S. Asami, "Ridging Phenomenon Related to the Undulated Segregation-pattern on Transverse Section in Ferritic Stainless Steel." *Transactions of the Iron and Steel Institute of Japan* 24, no. 5 (1984), pp. 359–364.
- [36] M. Brochu, T. Yokota, and S. Satoh, "Analysis of grain colonies in type 430 ferritic stainless steels by electron back scattering diffraction (EBSD)." *ISIJ International* 37, no. 9 (1997), pp. 872–877.
- [37] O. Engler, M. Y. Huh, and C. N. Tomé, "Crystal-plasticity analysis of ridging in ferritic stainless steel sheets." *Metallurgical and Materials Transactions a-Physical Metallurgy and Materials Science* 36A, no. 11 (2005), pp. 3127–3139.
- [38] J. F. Peck, and D. A. Thomas, "A Study of Fibrous Tungsten and Iron." *Transactions of the Metallurgical Society of Aime* 221, no. 6 (1961), pp. 1240–1247.
- [39] W. F. Hosford, "Microstructural Changes During Deformation of (011) Fiber-Textured Metals." *Transactions of the Metallurgical Society of AIME* 230, no. 1 (1964): 12–15.
- [40] D. Raabe, and K. Lücke, "Annealing Textures of BCC Metals." *Scripta Metallurgica Et Materialia* 27, no. 11 (1992), pp. 1533–1538.

- [41] C. W. Sinclair, “Embedded grain rotation and roping of stainless steel.” *Metallurgical and Materials Transactions a-Physical Metallurgy and Materials Science* 38A, no. 10 (2007), pp. 2435–2441.
- [42] G. Lefebvre, C. W. Sinclair, R. A. Lebensohn, and J.-D. Mithieux, “Accounting for local interactions in the prediction of roping of ferritic stainless steel sheets.” *Modelling and Simulation in Materials Science and Engineering* 20, no. 2 (2012).
- [43] S. H. Park, K. Y. Kim, Y. D. Lee, and C. G. Park, “Evolution of microstructure and texture associated with ridging in ferritic stainless steels.” *ISIJ International* 42, no. 1 (2002), pp. 100–105.
- [44] P. D. Wu, H. Jin, Y. Shi, and D. J. Lloyd, “Analysis of ridging in ferritic stainless steel sheet.” *Materials Science and Engineering a-Structural Materials Properties Microstructure and Processing* 423, no. 1–2 (2006), pp. 300–305.
- [45] P. D. Wu, and D. J. Lloyd, “Correlation of roping and texture in AA6111 automotive sheet.” *Modelling and Simulation in Materials Science and Engineering* 13, no. 6 (September 2005), pp. 981–991.
- [46] P. D. Wu, D. J. Lloyd, and Y. Huang, “Correlation of ridging and texture in ferritic stainless steel sheet.” *Materials Science and Engineering a-Structural Materials Properties Microstructure and Processing* 427, no. 1–2 (2006), pp. 241–245.
- [47] R. A. Lebensohn, and C. N. Tomé, “A Self-Consistent Anisotropic Approach for the Simulation of Plastic-Deformation and Texture Development of Polycrystals - Application to Zirconium Alloys.” *Acta Metallurgica Et Materialia* 41, no. 9 (1993), pp. 2611–2624.
- [48] C. N. Tomé, and R. A. Lebensohn, VPSC Version7c (2011), Los Alamos National Laboratory, USA
- [49] M. Y. Huh, J. H. Lee, S. H. Park, O. Engler, and D. Raabe, “Effect of through-thickness macro and micro-texture gradients on ridging of 17%Cr ferritic stainless steel sheet.” *Steel Research International* 76, no. 11 (2005), pp. 797–806. Copyright [2005 Huh]. This material is reproduced with permission of John Wiley & Sons, Inc.
- [50] D. Raabe, and K. Lücke, “Texture and Microstructure of Hot Rolled Steel.” *Scripta Metallurgica Et Materialia* 26, no. 8 (April 15, 1992), pp. 1221–1226.
- [51] M. Holscher, D. Raabe, and K. Lücke, “Rolling and Recrystallization Textures of Bcc Steels.” *Steel Research* 62, no. 12 (1991), pp. 567–575.
- [52] S. H. Hong, and D. N. Lee, “Recrystallization textures in cold-rolled Ti bearing IF steel sheets.” *ISIJ International* 42, no. 11 (2002), pp. 1278–1287.
- [53] W. B. Hutchinson, “Recrystallisation Textures in Iron Resulting from Nucleation at Grain Boundaries.” *Acta Metallurgica* 37, no. 4 (1989), pp. 1047–1056.

- [54] D. Vanderschueren, N. Yoshinaga, and K. Koyama, "Recrystallisation of Ti IF steel investigated with electron back-scattering pattern (EBSP)." *Isij International* 36, no. 8 (1996), pp. 1046–1054.
- [55] I. Samajdar, B. Verlinden, P. Van Houtte, and D. Vanderschueren, "gamma-fibre recrystallization texture in IF-steel: an investigation on the recrystallization mechanisms." *Materials Science and Engineering a-Structural Materials Properties Microstructure and Processing* 238, no. 2 (1997), pp. 343–350.
- [56] I. Samajdar, B. Verlinden, P. Van Houtte, and D. Vanderschueren, "Recrystallisation kinetics in IF-steel: A study on the sluggish recrystallisation behaviour." *Scripta Materialia* 37, no. 6 (1997), pp. 869–874.
- [57] I. Samajdar, B. Verlinden, and P. Van Houtte, "Development of recrystallization texture in IF-steel: An effort to explain developments in global texture from microtextural studies." *Acta Materialia* 46, no. 8 (1998), pp. 2751–2763.
- [58] L. Lesne, H. Regle, and J. H. Driver. "A Study of the Recrystallization Mechanisms in Doped Ultra-High Purity Iron." *Materials Transactions Jim* 41, no. 1 (2000), pp. 91–94.
- [59] B. J. Duggan, Y. Y. Tse, G. Lam, and M. Z. Quadir, "Deformation and Recrystallization of Interstitial Free (IF) Steel." *Materials and Manufacturing Processes* 26, no. 1 (2011), pp. 51–57.
- [60] W. Du, L.-Z. Jiang, Q.-S. Sun, Z.-Y. Liu, and X. ZHANG, "Effect of Hot Band Annealing Processes on Microstructure, Texture and r-Value of Ferritic Stainless Steel." *Journal of Iron and Steel Research, International* 17, no. 7 (2010), pp. 58–62.
- [61] D. Raabe, "On the influence of the chromium content on the evolution of rolling textures in ferritic stainless steels." *Journal of Materials Science* 31, no. 14 (1996), pp. 3839–3845.
- [62] C. W. Sinclair, F. Robaut, L. Maniguet, J.-D. Mithieux, J.-H. Schmitt, and Y. Brechet, "Recrystallization and texture in a ferritic stainless steel: an EBSD study." *Advanced Engineering Materials* 5, no. 8 (2003), pp. 570–574.
- [63] C. W. Sinclair, J.-D. Mithieux, J.-H. Schmitt, and Y. Brechet, "Recrystallization of stabilized ferritic stainless steel sheet." *Metallurgical and Materials Transactions a-Physical Metallurgy and Materials Science* 36A, no. 11 (2005), pp. 3205–3215.
- [64] F. J. Humphreys, and M. Hatherly, *Recrystallization and Related Annealing Phenomena* (2004), 2nd ed. Pergamon.
- [65] D. Raabe, and K. Lücke, "Selective Particle Drag During Primary Recrystallization of Fe-Cr Alloys." *Scripta Metallurgica Et Materialia* 26, no. 1 (1992), pp. 19–24.

- [66] A. Ferreira Filho, C. Herrera, N. B. de Lima, R. L. Plaut, and A. F. Padilha, "Texture evolution of ferritic (AISI 430) stainless steel strips during cold rolling, annealing and drawing." In *THERMEC 2006, Pts 1-5* (2007), edited by T. Chandra, K. Tsuzaki, M. Militzer, and C. Ravindran, Vol. 539–543, pp. 4926–4931. Stafa-Zurich: Trans Tech Publications Ltd.
- [67] H. Yan, H. Bi, X. Li, and Z. Xu, "Microstructure and texture of Nb plus Ti stabilized ferritic stainless steel." *Materials Characterization* 59, no. 12 (2008), pp. 1741–1746.
- [68] H. Liu, Z. Liu, and G. Wang, "Texture Development and Formability of Strip Cast 17% Cr Ferritic Stainless Steel." *ISIJ International* 49, no. 6 (2009), pp. 890–896.
- [69] J. Mola, I. Jung, J. Park, D. Chae, and B. C. de Cooman, "Ridging Control in Transformable Ferritic Stainless Steels." *Metallurgical and Materials Transactions a-Physical Metallurgy and Materials Science* 43A, no. 1 (2012), pp. 228–244.
- [70] Y. Inokuti, and R. D. Doherty, "Transmission Kossel Study of the Structure of Compressed Iron and Its Recrystallization Behaviour." *Acta Metallurgica* 26, no. 1 (1978), pp. 61–80.
- [71] D. Raabe, "Investigation of the Orientation Dependence of Recovery in Low-Carbon Steel by Use of Single Orientation Determination." *Steel Research* 66, no. 5 (1995), pp. 222–229.
- [72] I. Samajdar, B. Verlinden, and P. Van Houtte, "Developments in Macro and Micro Texture During Plane Strain Channel Die Compression of IF Steel." *ISIJ International* 38, no. 7 (1998), pp. 759–765.
- [73] I. L. Dillamore, C. J. E. Smith, and T. W. Watson, "Oriented Nucleation in the Formation of Annealing Textures in Iron." *Metal Science* 1, no. 1 (1967), pp. 49–54.
- [74] I. L. Dillamore, P. L. Morris, C. J. E. Smith, and W. B. Hutchinson, "Transition Bands and Recrystallization in Metals." *Proceedings of the Royal Society of London. A. Mathematical and Physical Sciences* 329, no. 1579 (1972), pp. 405–420.
- [75] R. L. Every, and M. Hatherly, "*Oriented nucleation in low carbon steels*". *Texture* 1, no. 3 (1974), pp. 183–194.
- [76] H. Réglé, "*Mechanisms of microstructure and texture evolution during recrystallisation of ferritic steels sheets*." Proceedings of the first joint international conference Recrystallization and Grain Growth (2001) Edited by G. Gottstein and D. A. Molodov. Berlin: Springer-Verlag Berlin., pp. 707–717
- [77] H. Réglé, "Evolution Mechanisms of Texture and Microstructure During Recrystallization of Ferritic Steel Sheets." *Revue De Métallurgie* 100, no. 09 (2003), pp. 883–890.
- [78] B. L. Li, A. Godfrey, Q. C Meng, Q. Liu, and N Hansen, "Microstructural Evolution of IF-steel During Cold Rolling." *Acta Materialia* 52, no. 4 (2004), pp. 1069–1081.

- [79] O. Castelnau, T. Ungar, A. Miroux, T. Chauveau, and B. Bacroix, "Orientation dependent intragranular stored energy in polycrystalline Ti-IF steel." In *European Powder Diffraction, Pts 1 and 2*, (2000), edited by R. Delhez and E. J. Mittemeijer, Vol. 321–324, pp. 720–725. Stafa-Zurich: Trans Tech Publications Ltd.
- [80] N. Rajmohan, Y. Hayakawa, J. A. Szpunar, and J. H. Root, "Neutron Diffraction Method for Stored Energy Measurement in Interstitial Free Steel." *Acta Materialia* 45, no. 6 (1997), pp. 2485–2494.
- [81] B. Bacroix, A. Miroux, and O. Castelnau, "Simulation of the Orientation Dependence of Stored Energy During Rolling Deformation of Low Carbon Steels." *Modelling and Simulation in Materials Science and Engineering* 7, no. 5 (1999), pp. 851–864.
- [82] J. J. Jonas, and L.S. Tóth, "Modelling Oriented Nucleation and Selective Growth During Dynamic Recrystallization." *Scripta Metallurgica Et Materialia* 27, no. 11 (1992), pp. 1575–1580.
- [83] Y. Hayakawa, and J. A. Szpunar, "Modeling of texture development during recrystallization of interstitial free steel." *Acta Materialia* 45, no. 6 (1997), pp. 2425–2434.
- [84] N. Tsuji, K. Tsuzaki, and T. Maki, "Effect of Initial Orientation on the Recrystallization Behavior of Solidified Columnar Crystals in a 19-Percent Cr Ferritic Stainless-Steel." *ISIJ International* 33, no. 7 (1993), pp. 783–792.
- [85] N. Tsuji, K. Tsuzaki, and T. Maki, "Effects of Rolling Reduction and Annealing Temperature on the Recrystallization Structure of Solidified Columnar Crystals in a 19% Cr Ferritic Stainless Steel." *ISIJ International* 34, no. 12 (1994), pp. 1008–1017.
- [86] M. Matsuo, "Texture Control in the Production of Grain Oriented Silicon Steels." *ISIJ International* 29, no. 10 (1989), pp. 809–827.
- [87] W. B. Hutchinson, "Deformation Microstructures and Textures in Steels." *Philosophical Transactions of the Royal Society of London. Series A: Mathematical, Physical and Engineering Sciences* 357, no. 1756 (1999), pp. 1471–1485. Copyright [1999 Hutchinson]. This material is reproduced with permission of John Wiley & Sons, Inc.
- [88] R. D. Doherty, D. A. Hughes, F. J. Humphreys, J. J. Jonas, D. J. Jensen, M. E. Kassner, W. E. King, T. R. McNelley, H. J. McQueen, and A. D. Rollett, "Current Issues in Recrystallization: a Review." *Materials Science and Engineering: A* 238, no. 2 (1997), pp. 219–274.
- [89] H. Magnusson, D. J. Jensen, and B. Hutchinson, "Growth rates for different texture components during recrystallization of if steel." *Scripta Materialia* 44, no. 3 (2001), pp. 435–441.
- [90] A. Miroux, H. Réglé, and B. Bacroix, "Effect of cold rolling level on recrystallization textures in low carbon steel sheets - Modelling." In *Texture and Anisotropy of Polycrystals* (1998), edited by R. A. Schwarzer, Vol. 273–275, pp. 433–438. Zurich-Uetikon: Transtec Publications Ltd.

- [91] J. S. Hinton, and J. H. Beynon, "Restoration processes during hot deformation in the delta-ferrite and austenite dual phase region of AISI430 ferritic stainless steel." *ISIJ International* 47, no. 10 (2007), pp. 1465–1474.
- [92] C. W. Sinclair, D. Weygand, J. Lepinoux, and Y. Brechet, "Simulating the topology of recrystallization in stabilized ferritic stainless steels." In *Recrystallization and Grain Growth, Pts 1 and 2* (2004), edited by B. Bacroix, J. H. Driver, R. LeGall, C. Maurice, R. Penelle, H. Regle, and L. Tabourot, Vol. 467-470, pp. 671–676. Zurich-Uetikon: Trans Tech Publications Ltd.
- [93] G. Lefebvre, S. Shahandeh, C. W. Sinclair, M. Militzer, J.-D Mithieux, and J. Laigo, "Spatially Inhomogeneous Recrystallization in Ferritic Stainless Steels." *Materials Science Forum* 715–716 (2012), pp. 866–871.
- [94] T. Tsuchiyama, R. Hirota, K. Fukunaga, and S. Takaki, "Ridging-free Ferritic Stainless Steel Produced Through Recrystallization of Lath Martensite." *ISIJ International* 45, no. 6 (2005), pp. 923–929.
- [95] H. Miyaji, and S. Watanabe, "Effect of the Distribution of Martensite Phase in a Hot-Rolled Sheet on the Ridging Phenomenon in 17Cr Stainless Steel." *J. Japan. Inst. Metals* 39, no. 2 (1975), pp. 194–198.
- [96] J. Raulet, "Effect of multiple recrystallizations on formability and texture of the F17R Ferritic Stainless Steel." (2003), Internship Ugine & Alz (now Aperam), Isbergues, France.
- [97] T. Sheppard, and P. Richards, "Roping Phenomena in Ferritic Stainless-Steels." *Materials Science and Technology* 2, no. 7 (July 1986), pp. 693–699.
- [98] A. Le Bon, and P. Hug, *The book of steel*, Intercept Ed., (1996), pp. 1207
- [99] M. F. Littmann, "Development of Improved Cube-on-Edge Texture from Strand Cast 3pct Silicon-Iron." *Metallurgical Transactions A* 6, no. 5 (1975), pp. 1041–1048.
- [100] N. Tsuji, K. Tsuzaki, and T. Maki, "Effect of Initial Orientation on the Cold-Rolling Behavior of Solidified Columnar Crystals in a 19-Percent Cr Ferritic Stainless-Steel." *Isij International* 32, no. 12 (1992), pp 1319–1328.
- [101] J. K. Brimacombe, "The Challenge of Quality in Continuous Casting Processes." *Metallurgical and Materials Transactions B* 30, no. 4 (1999), pp. 553–566.
- [102] J. P. Birat, and J. P. Larrecq, *The book of steel*, Intercept Ed., (1996), pp. 1185-1206.
- [103] Y. Liu, Y. Yang, H. Bi, and L. Zuo, "The Hereditary Feature for Preferred Orientation in Ferritic Stainless Steel." In *Manufacturing Science and Engineering, Pts 1-5* (2010), edited by Z. Jiang and C. L. Zhang, Vol. 97–101, pp. 897–900. Stafa-Zurich: Trans Tech Publications Ltd.
- [104] J. Hamada, Y. Matsumoto, F. Fudanoki, and S. Maeda, "Effect of Initial Solidified Structure on Ridging Phenomenon and Texture in Type 430 Ferritic Stainless Steel Sheets." *ISIJ International* 43, no. 12 (2003), pp. 1989–1998.

- [105] J. C. Kim, J. J. Kim, J. Y. Choi, J. H. Choi, and S. K. Kim, "Control of columnar-to-equiaxed transition in continuous casting of 16% Cr stainless steel." *Metallurgia Italiana* no. 9 (2009), pp. 43–48.
- [106] J. P. Liang, C. J. Song, L. X. Wang, Z. J. Li, and Q. J. Zhai, "Study on Macrostructure Refinement of 12 wt-%Cr Ferritic Stainless Steel Slabs by TiN Nucleation." *Materials Technology: Advanced Performance Materials* 27, no. 4 (2012), pp. 333–336.
- [107] E. Pouillard, and B. Osdoit, "Influence of Composition and Hot Rolling Conditions on Susceptibility to Zoning in Steels with 17 Percent Chromium." *Revue De Metallurgie* 63, no. 9 (1966), pp. 679–690.
- [108] S. H. Park, K. Y. Kim, Y. D. Lee, and C. G. Park, "Initial orientation dependence of texture evolution in ferritic stainless steels." In *Proceedings of the 12th International Conference on Textures of Materials, ICOTOM-12*, (1999), edited by J. A. Szipunar, pp. 1095–1144.
- [109] P. A. Davidson, "Magnetohydrodynamics in Materials Processing." *Annual Review of Fluid Mechanics* 31, no. 1 (1999), pp. 273–300.
- [110] W. C. Winegard, and B. Chalmers, "Supercooling and Dendritic Freezing in Alloys." *Transactions of the American Society for Metals* 46 (1954), pp. 1214–1224.
- [111] K. A. Jackson, J. D. Hunt, D. R. Uhlmann, and T. P. Seward, "On Origin of Equiaxed Zone in Castings." *Transactions of the Metallurgical Society of AIME* 236, no. 2 (1966), pp. 149–158.
- [112] K. Murakami, and T. Okamoto, "Formation of Equiaxed Zone in Castings." *Metal Science* 18, no. 2 (1984), pp. 103–111.
- [113] S. I. Chung, and J. K. Yoon, "Numerical analysis of effect of electromagnetic stirring on solidification phenomena in continuous casting." *Ironmaking & Steelmaking* 23, no. 5 (1996), pp. 425–432.
- [114] H. Takeuchi, H. Mori, Y. Ikehara, T. Komano, and T. Yanai, "The Effects of Electromagnetic Stirring on Solidification Structure of Continuously Cast Sus430-Stainless Steel Slabs." *Transactions of the Iron and Steel Institute of Japan* 21, no. 2 (1981), pp. 109–116.
- [115] T. Sawatani, T. Ashiura, M. Wakamatsu, H. Yoshimura, M. Ishii, and A. Yamamoto, "Development of continuous annealing process for 17% Cr stainless steel strip." *Nippon steel technical report. Overseas* no. 21, pp. 275–290.
- [116] H. Takeuchi, Y. Ikehara, T. Yanai, and S. Matsumura, "Quality Improvement of Continuously Cast Stainless-Steel Blooms Through Electromagnetic Stirring." *Transactions of the Iron and Steel Institute of Japan* 18, no. 6 (1978), pp. 352–360.
- [117] C.-X. Shi, G.-G. Cheng, Z.-J. Li, and P. Zhao, "Solidification Structure Refining of 430 Ferrite Stainless Steel With TiN Nucleation." *Journal of Iron and Steel Research, International* 15, no. 3 (2008), pp. 57–60.

- [118] M. Aksoy, V. Kuzucu, and M.H. Korkut, “The Influence of Strong Carbide-forming Elements and Homogenization on the Wear Resistance of Ferritic Stainless Steel.” *Wear* 211, no. 2 (1997), pp. 265–270.
- [119] V. Kuzucu, M. Aksoy, and M. H. Korkut, “The effect of strong carbide-forming elements such as Mo, Ti, V and Nb on the microstructure of ferritic stainless steel.” *Journal of Materials Processing Technology* 82, no. 1–3 (1998), pp. 165–171.
- [120] H. Yan, H. Bi, X. Li, and Z. Xu, “Precipitation and mechanical properties of Nb-modified ferritic stainless steel during isothermal aging.” *Materials Characterization* 60, no. 3 (2009), pp. 204–209.
- [121] C. Wang, H. Gao, Y. Dai, X. Ruan, J. Wang, and B. Sun, “Grain Refining of 409L Ferritic Stainless Steel Using Fe-Ti-N Master Alloy.” *Metallurgical and Materials Transactions a-Physical Metallurgy and Materials Science* 41A, no. 7 (2010), pp. 1616–1620.
- [122] E. Pouillard, and B. Osdoit, “Mechanism of Banding in Ferritic Steels with 17 Percent Cr.” *Revue De Metallurgie-Cahiers D Informations Techniques* 66, no. 11 (1969), pp. 763–769.
- [123] K. Kimura, A. Yamamoto, T. Takeshita, J. Harase, “Hot Recrystallization Behavior of SUS 430 Stainless Steel”, Nippon Steel Technical Report N°71 (1996).
- [124] B. K. Jha, P. Jha, and C. D. Singh, “Process technology for the continuous hot band annealing of 17%Cr ferritic stainless steel.” *Journal of Materials Engineering and Performance* 11, no. 2 (2002), pp. 180–186.
- [125] Y. Uematsu, , and K. Yamazaki, “Effects of Hot-Rolling Conditions on Hot Rolled Microstructures and Ridging Properties in 17-Percent-Cr Ferritic Stainless-Steel.” *Tetsu to Hagane-Journal of the Iron and Steel Institute of Japan* 78, no. 4 (1992), pp. 632–639.
- [126] W. Johnson, and G. Needham, “Further Experiments in Asymmetrical Rolling.” *International Journal of Mechanical Sciences* 8, no. 6 (1966), pp. 443–455.
- [127] R. Lapovok, D. Orlov, I. B. Timokhina, A. Pougis, L. S. Tóth, P. D. Hodgson, A. Haldar, and D. Bhattacharjee, “Asymmetric Rolling of Interstitial-Free Steel Using One Idle Roll.” *Metallurgical and Materials Transactions a-Physical Metallurgy and Materials Science* 43A, no. 4 (2012), pp. 1328–1340.
- [128] L. S. Tóth, B. Beausir, D. Orlov, R. Lapovok, and A. Haldar, “Analysis of Texture and R Value Variations in Asymmetric Rolling of IF Steel.” *Journal of Materials Processing Technology* 212, no. 2 (February 2012), pp. 509–515.
- [129] R. Roumina, and C. W. Sinclair, “Deformation Geometry and Through-Thickness Strain Gradients in Asymmetric Rolling.” *Metallurgical and Materials Transactions A* 39, no. 10 (2008), pp. 2495–2503.

- [130] I. Salvatori, M. Lubrano, E. Petrone, A. Montanari, and G. Porcu, *Metallurgical Impact of Hot Asymmetric Rolling on Grain Refinement*. Warrendale: Minerals, Metals & Materials Soc, 2008.
- [131] T. Siegmund, E. Werner, and F. D. Fischer, "The Irreversible Deformation of a Duplex Stainless Steel Under Thermal Cycling." *Materials Science and Engineering: A* 169, no. 1–2 (1993), pp. 125–134.
- [132] M. Fukuda, "The Effect of Carbon Content against γ Value-Cold Reduction Relations in Steel Sheets." *Tetsu to Hagane-Journal of the Iron and Steel Institute of Japan* 53, no. 4 (1967), pp. 559–561.
- [133] K. Suzuki, S. Asami, and K. Suzuki, "Formation of Ridging Related to the Banded Segregation Pattern of Cr and C on Ferritic Stainless Steel Sheet." *Transactions of the Iron and Steel Institute of Japan* 23, no. 9 (1983), pp. 731–737.
- [134] K. Suzuki, S. Asami, and K. Suzuki, "Microsegregation of Chromium and Carbon and Ridging Phenomenon in 18 Cr Stainless Steel Sheets." *Transactions of the Iron and Steel Institute of Japan* 24, no. 1 (1984), pp 1–6.
- [135] High-Strength Structural and High-Strength Low-Alloy Steels, *Properties and Selection: Irons, Steels, and High-Performance Alloys*, Vol 1, *ASM Handbook*, ASM International (1990), pp. 389–423.
- [136] J. K. Kim, Y. H. Kim, S. H. Uhm, J. S. Lee, and K. Y. Kim, "Intergranular Corrosion of Ti-stabilized 11 Wt% Cr Ferritic Stainless Steel for Automotive Exhaust Systems." *Corrosion Science* 51, no. 11 (2009), pp. 2716–2723.
- [137] M. O. H. Amuda, and S. Mridha, "An Overview of Sensitization Dynamics in Ferritic Stainless Steel Welds." *International Journal of Corrosion* 2011 (2011), pp. 1–9.
- [138] R. E. Hook, A. J. Heckler, and J. A. Elias, "Texture in Deep Drawing Columbium (Nb)-treated Interstitial-free Steels." *Metallurgical Transactions A* 6, no. 9 (1975), pp. 1683–1692.
- [139] R. H. Goodenow, and J. F. Held, "Recrystallization of Low-carbon Titanium Stabilized Steel." *Metallurgical Transactions* 1, no. 9 (1970), pp. 2507–2515.
- [140] P. R. Mould, and J. M. Gray, "Plastic Anisotropy of Low-carbon, Low-manganese Steels Containing Niobium." *Metallurgical Transactions* 3, no. 12 (1972), pp. 3121–3132.
- [141] C. W. Sinclair, C. R. Hutchinson, and Y. Bréchet, "The Effect of Nb on the Recrystallization and Grain Growth of Ultra-High-Purity α -Fe: A Combinatorial Approach." *Metallurgical and Materials Transactions A* 38, no. 4 (2007), pp. 821–830.
- [142] P. Dernoncourt, Note Technique CRI, "Influence de l'épaisseur finale sure le roping du AISI430", 2001.
- [143] R. A. Lebensohn, "N-site Modeling of a 3D Viscoplastic Polycrystal Using Fast Fourier Transform." *Acta Materialia* 49, no. 14 (2001), pp. 2723–2737.

- [144] H. Moulinec, and P. Suquet, “A Fast Numerical-Method for Computing the Linear and Nonlinear Mechanical-Properties of Composites.” *Comptes Rendus De L Academie Des Sciences Serie Ii* 318, no. 11 (1994), pp.1417–1423.
- [145] H. Moulinec, and P. Suquet, “A Numerical Method for Computing the Overall Response of Nonlinear Composites with Complex Microstructure.” *Computer Methods in Applied Mechanics and Engineering* 157, no. 1–2 (1998), pp. 69–94.
- [146] R. A. Lebensohn, R. Brenner, O. Castelnau, and A. D. Rollett, “Orientation Image-based Micromechanical Modelling of Subgrain Texture Evolution in Polycrystalline Copper.” *Acta Materialia* 56, no. 15 (2008), pp. 3914–3926.
- [147] A. Prakash, and R. A. Lebensohn, “Simulation of Micromechanical Behavior of Polycrystals: Finite Elements Versus Fast Fourier Transforms.” *Modelling and Simulation in Materials Science and Engineering* 17, no. 6 (2009).
- [148] R. A. Lebensohn, M. Montagnat, P. Mansuy, P. Duval, J. Meysonnier, and A. Philip, “Modeling Viscoplastic Behavior and Heterogeneous Intracrystalline Deformation of Columnar Ice Polycrystals.” *Acta Materialia* 57, no. 5 (2009), pp. 1405–1415.
- [149] R. A. Lebensohn, and C. N. Tomé, “A Self-consistent Viscoplastic Model: Prediction of Rolling Textures of Anisotropic Polycrystals.” *Materials Science and Engineering: A* 175, no. 1–2 (1994), pp. 71–82.
- [150] R. A. Lebensohn, P. A. Turner, J. W. Signorelli, G. R. Canova, and C. N. Tomé, “Calculation of Intergranular Stresses Based on a Large-strain Viscoplastic Self-consistent Polycrystal Model.” *Modelling and Simulation in Materials Science and Engineering* 6, no. 4 (1998), pp. 447–465.
- [151] B. Raesisinia, “Modelling the Effect of Grain Size Distribution on the Mechanical Response of Metals” (2008), PhD. Thesis, The University of British Columbia, Vancouver, B.C.
- [152] R. Hielsche, and H. Schaeben, “A Novel Pole Figure Inversion Method: Specification of the MTEX Algorithm.” *Journal of Applied Crystallography* 41, no. 6 (2008), pp. 1024–1037.
- [153] A. J. Heckler, and W. G. Granzow, “Crystallite Orientation Distribution Analysis of the Cold Rolled and Recrystallization Textures in Low-carbon Steels.” *Metallurgical Transactions* 1, no. 8 (August 1, 1970), pp. 2089–2094.
- [154] M. Avrami, “Kinetics of Phase Change I - General Theory.” *Journal of Chemical Physics* 7, no. 12 (1939) pp. 1103–1112.
- [155] M. Avrami, “Kinetics of Phase Change. II Transformation - Time Relations for Random Distribution of Nuclei.” *Journal of Chemical Physics* 8, no. 2 (1940), pp. 212–224.
- [156] W. A. Johnson, and R. F. Mehl, “Reaction Kinetics in Processes of Nucleation and Growth.” *Transactions of the American Institute of Mining and Metallurgical Engineers* 135 (1939), pp. 416–442.

- [157] A. Heinz, and P. Neumann, “Representation of Orientation and Disorientation Data for Cubic, Hexagonal, Tetragonal and Orthorhombic Crystals.” *Acta Crystallographica Section A* 47 (1991), pp. 780–789.
- [158] M. R. Barnett, “Role of In-grain Shear Bands in the Nucleation of $\langle 111 \rangle$ //ND Recrystallization Textures in Warm Rolled Steel.” *ISIJ International* 38, no. 1 (1998), pp. 78–85.
- [159] M. R. Barnett, and J. J. Jonas, “Influence of Ferrite Rolling Temperature on Microstructure and Texture in Deformed Low C and IF Steels.” *ISIJ International* 37, no. 7 (1997), pp. 697–705.
- [160] M. D. Z. Quadir, and B. J. Duggan, “Shear Band Thickening During Rolling of Interstitial Free Steel.” *ISIJ International* 46, no. 10 (2006), pp. 1495–1499.
- [161] J. J. Jonas, “Effects of Shear Band Formation on Texture Development in Warm-rolled IF Steels.” *Journal of Materials Processing Technology* 117, no. 3 (2001), pp. 293–299.
- [162] D. J. Jensen, “Growth of Nuclei with Different Crystallographic Orientations During Recrystallization.” *Scripta Metallurgica Et Materialia* 27, no. 5 (1992), pp. 533–538.
- [163] D. J. Jensen, “Growth-Rates and Misorientation Relationships Between Growing Nuclei Grains and the Surrounding Deformed Matrix During Recrystallization.” *Acta Metallurgica Et Materialia* 43, no. 11 (1995), pp. 4117–4129.
- [164] R. A. Vandermeer, and D. J. Jensen, “Quantifying Recrystallization Nucleation and Growth Kinetics of Cold-worked Copper by Microstructural Analysis.” *Metallurgical and Materials Transactions A* 26, no. 9 (1995), pp. 2227–2235.
- [165] J. W. Cahn, and W. C. Hagel. “Divergent Pearlite in a Manganese Eutectoid Steel.” *Acta Metallurgica* 11, no. 6 (1963): 561–574.
- [166] F. Scholz, J. H. Driver, and E. Woldt, “The stored energy of cold rolled ultra high purity iron.” *Scripta Materialia* 40, no. 8 (1999), pp. 949–954.
- [167] T. R de Oliveirs, “Effet du niobium et du titane sur la déformation a chaud d’aciers inoxydables ferritiques stabilisés” (2003), PhD thesis, Ecoles des Mines de St-Etienne.
- [168] O. Engler, M. Y. Huh, and C. N. Tomé. “A Study of through-Thickness Texture Gradients in Rolled Sheets.” *Metallurgical and Materials Transactions a-Physical Metallurgy and Materials Science* 31, no. 9 (2000), pp. 2299–2315.
- [169] G. Glover, and C. M. Sellars, “Recovery and Recrystallization During High Temperature Deformation of A-iron.” *Metallurgical Transactions* 4, no. 3 (1973), pp. 765–775.
- [170] G. Jacquet, “ Etude de la cinétique de recrystallization au cours du laminage à chaud d’aciers inoxydables ferritiques stabilisés” (2013), PhD thesis, Ecoles des Mines de St-Etienne.

Bibliography

- [171] J. E. Bailey, and P. B. Hirsch, "The Recrystallization Process in Some Polycrystalline Metals." *Proceedings of the Royal Society of London. Series A. Mathematical and Physical Sciences* 267, no. 1328 (1962), pp. 11–30.
- [172] S. Matthies, and G. W. Vinel, "On Some Methodical Developments Concerning Calculations Performed Directly in the Orientation Space." *Proceedings of the 10th International Conference on Textures of Materials, Pts 1 and 2 - ICOTOM-10* (1994), edited by H. J. Bunge, Vol. 157, pp. 1641–1646. Zurich-Uetikon: Transtec Publications Ltd.
- [173] K. J. Stout, P. J. Sullivan, W. P. Dong, E. Mainsah, N. Luo, T. Mathia, and H. Zahouani, "The development of methods for the characterization of roughness in three dimension.", Commission of the European Communities, Printed in Univ. of Birmingham, Report EUR 15178 EN, (1993).
- [174] M. Hansen, K. Anderko, "Constitution of Binary Alloys 2E" (1958) © McGraw-Hill Education.

Appendix A: Experimental surface roughness measurements

Here, the methodology used for experimental surface roughness measurements is presented as well as the procedures used for statistical repeatability and the effect of the polynomial correction.

On a deformed sample, the surface roughness was measured along TD, at three different locations along the gauge length of the sample, each profile being 4 cm away from each other, such as represented in Figure A.1. Each roughness measurement at a given position was repeated three time.

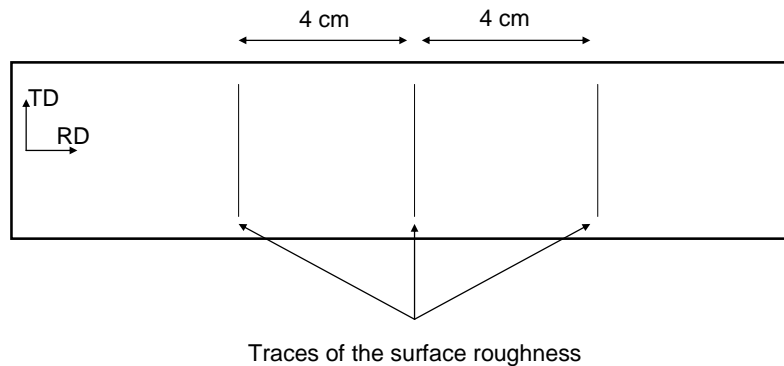


Figure A.1: Schematic of the surface roughness measurements on the surface of a deformed sample.

From this raw surface roughness profile, a correction is applied (see section 4.1.4). The effect of the polynomial correction is presented here between a 6th order polynomial plane and a 8th order polynomial plane (previously used in the industry and currently used, respectively). Figure A.2 presents an example of a raw surface roughness and the two polynomial functions obtained using a least square fit (for the AIS 409 material).

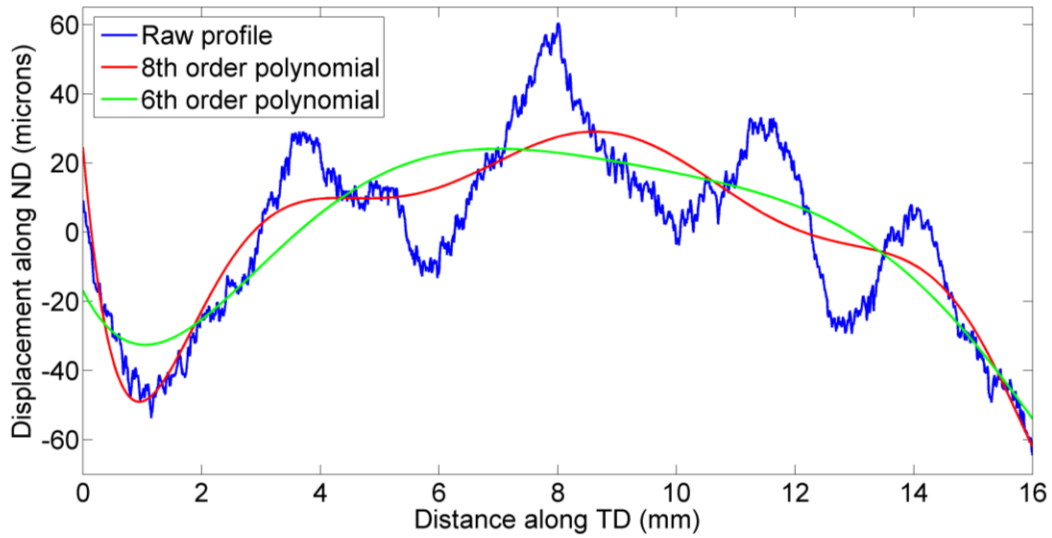


Figure A.2: Raw data for a surface roughness measurement of the AISI 409 material, and polynomial fits (6th order and 8th order).

The raw data is then corrected by each polynomial plane and the filter previously introduced is applied. The resulting surface roughness profiles after filtering are presented in Figure A.3.

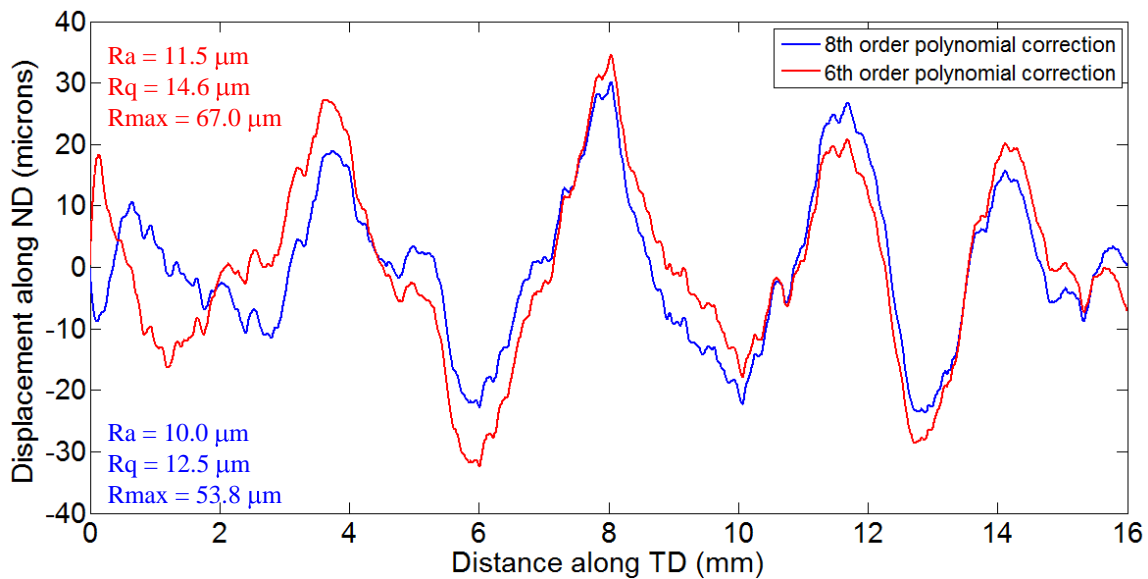


Figure A.3: Final surface roughness profiles after correction by the two polynomial fits and filtering. Also included are the amplitude parameters using the same color code as the corresponding curves.

It is seen from this figure that increasing the degree of the polynomial correction does not change the overall aspect of the final curve. It does, however, decrease the three amplitude parameters (R_a , R_q and R_{max}). This result is expected since a higher polynomial correction would fit better the raw curve, and thus the difference between the raw curve and the fit decreases. This result shows that the correction can strongly influence the absolute value of the roughness parameters.

The repeatability has been tested by measuring the surface roughness three times at each position. In each case, the values for R_a , R_q and R_{max} were found to be extremely close to each other. An example is given in Table A.1 for the AISI 409 material. Results were identical for the two other materials.

Table A.1: Characterization of the repeatability of surface roughness measurement on R_a , R_q and R_{max}

	R_a	R_q	R_{max}
Scan 1	11.48	14.61	66.98
Scan 2	11.59	14.66	67.16
Scan 3	11.60	14.67	66.86
Average	11.56	14.65	67.00
Standard deviation	0.06	0.04	0.15

Appendix B: Input for VPFFT simulations

This section presents the inputs used for the VPFFT simulations, with a focus on boundary conditions and on slip activity (including hardening).

In the input file ‘fft.in’, the deformation is controlled by the velocity gradient $\dot{u} = \frac{\partial u}{\partial t}$, corresponding to a tension along the rolling direction (direction 3), which is converted into a strain by the introduction of a time increment imposed to achieve the final deformation (in this case, 0.01).

In the input file ‘bcc.sx3’, the activity of slip system is defined. The three families of slip system are presented, as well as the hardening function for each system, described by an extended Voce law $\hat{\tau}^s = \tau_0^s + (\tau_1^s + \theta_1^s \Gamma)(1 - \exp(-\Gamma \frac{|\theta_0^s|}{|\tau_1^s|}))$. In this equation, θ_0 and θ_1 are the initial hardening rate and the asymptotic hardening rate. In our case, these parameters were set to non-zero values. However, since there is one single step of deformation, there is no effect of hardening of a slip system for the following steps.

Appendix B: Input for VPFFT simulations

```

2          number of phases (nph)
32768     number of Fourier points (should be npts1*npts2*npts3)
1. 1. 1.   RVE dimensions (delt)
* name and path of microstructure file (filetext)
microstructure
*INFORMATION ABOUT PHASE #1
0          igas(iph)
* name and path of single crystal file (filecrys) (dummy if igas(iph)=1)
bcc.sx3
*INFORMATION ABOUT PHASE #2
1          igas(iph)
* name and path of single crystal file (filecrys) (dummy if igas(iph)=1)
bcc.sx3
*INFORMATION ABOUT TEST CONDITIONS
* boundary conditions
0  1  1      iudot | flag for vel.grad.
1  0  1      | (0:unknown-1:known)
1  1  1      | DO NOT CHANGE
|
-0.5  0.  0.   udot | vel.grad
0.  -0.5  0.   |
0.  0.  1      |
|
1  0  0      iscau | flag for Cauchy
1  0      | DO NOT CHANGE
0      |
|
0.  0.  0.   scauchy | Cauchy stress
0.  0.   |
0.   |
* other
0.01      eqincr (if ictrl>=0) or tdot (if ictrl=-1)
-1        ictrl (1-6: strain comp, 0: VM eq, -1: tdot)
*INFORMATION ABOUT RUN CONDITIONS
1         nsteps
0.000000001  err
100      itmax
0         IRECOVER read grain states from STRESS.IN (1) or not (0)?
0         ISAVE write grain states in STRESS.OUT (1) or not (0)?
1         IUPDATE update tex & RVE dim (1) or not (0)?
0         IUPHARD
1         IWTEX
1         IWFIELDS

```

Figure B1: Definition of the deformation and boundary conditions for the VPFFT simulations in the `fft.in` input file.

Appendix B: Input for VPFPT simulations

```

SLIP SYSTEMS FOR CUBIC CRYSTAL
CUBIC      icryst
1. 1. 1.  crystal axes (cdim(i))
2      nmodesx (total # of modes listed in the file)
2      nmodes  (# of modes to be used in the calculation)
1 2      mode(i) (label of the modes to be used)
{110}<111> SLIP
1 12 10 1.0 0.0 0      modex,nsmx,nrsx,gamd0x,twshx,isectwx
11.0 11.0 15.5 430.0 110.0  tau0xf,tau0xb,tau1x,thet0,thet1
1.0 1.0 1.0          hselfx,hlatex
0 1 1 1 1 -1  slip (n-b)
1 0 1 1 1 -1
1 -1 0 1 1 -1
0 1 -1 1 -1 -1
1 0 1 1 -1 -1
1 1 0 1 -1 -1
0 1 1 1 -1 1
1 0 -1 1 -1 1
1 1 0 1 -1 1
0 1 -1 1 1 1
1 0 -1 1 1 1
1 -1 0 1 1 1
{112}<111> SLIP
2 12 10 1.0 0.0 0      modex,nsmx,nrsx,gamd0x,twshx,isectwx
11.0 11.0 15.5 430.0 110.0  tau0xf,tau0xb,tau1x,thet0,thet1
1.0 1.0 1.0          hselfx,hlatex
-2 1 -1 -1 -1 1  slip (n-b)
1 -2 -1 -1 -1 1
1 1 2 -1 -1 1
-2 -1 -1 -1 1 1
1 2 -1 -1 1 1
1 -1 2 -1 1 1
2 1 -1 1 -1 1
-1 -2 -1 1 -1 1
-1 1 2 1 -1 1
2 -1 -1 1 1 1
-1 2 -1 1 1 1
-1 -1 2 1 1 1

```

Figure B2: Definition of the activity of slip systems and hardening law in the bcc.sx3 input file.